UNIVERSITÀ DEGLI STUDI DI MILANO
Facoltà di Scienze MM. FF. NN.
Dipartimento di Fisica
Dottorato di Ricerca in Fisica – XII Ciclo

TESI DI DOTTORATO

di ENRICO PIOTTO

Search for neutral Higgs bosons in $e^+e^- \rightarrow H\nu\overline{\nu}$ channel with DELPHI detector at LEP 2

Coordinatore: **Ch.mo Prof. ANTONINO PULLIA**
Tutore: **Ch.mo Prof. GUIDO VEGNI**

ANNO ACCADEMICO 1998 - 1999

Alla piccola Iride,

a Ugo,

alla loro storia.

Contents

"Maria montesque pollicere coepit"
Sallustio

Introduction

The Standard Model has been tremendously successful in predicting the properties of new particles and the structure of the basic interactions. In many of its facets it has been tested to an accuracy significantly better than 0.1 percent.

The most important aspect of the Standard Model which has not yet been verified experimentally is the Higgs sector. The Standard Model without the Higgs boson is incomplete since it predicts massless fermions and gauge bosons. Furthermore, the electroweak radiative corrections to observables such as the $W^{\pm}$ and Z^0 boson masses would be infinite in the absence of Higgs boson.

In the first chapter I will show how the simplest solution, corresponding to the introduction of a $SU(2)_L$ doublet of Higgs bosons, cures these defects. This simple solution inside the Standard Model is fascinating, but there are a variety of nagging theoretical problems which cannot be solved without the introduction of some new physics. There is no understanding of masses or why there are three generations of quarks and leptons. Neither the fundamental parameters, masses and couplings, nor the symmetry pattern are accounted for: these elements are merely built into the model. Moreover when radiative correction on the Higgs mass are computed, an unnatural method to suppress divergences must be introduced. Supersymmetry is, at present, many theorists' favourite candidate for new physics beyond the Standard Model. The Higgs sector in Supersymmetry theory becomes more complicated and I will review it in section 1.5.1.1.

The search for Higgs boson(s) and for new physics is one of the main goals of the progressive increase of the centre-of-mass energy ($\sqrt{s}$) in the second phase of LEP (LEP2). Since 1995 LEP has been running at centre-of-mass energies above the Z^0 pole. Data were collected at $\sqrt{s}$ =130-136 GeV in 1995, at $\sqrt{s}$ =161 GeV and $\sqrt{s}$ =172 GeV in 1996, at $\sqrt{s}$ =183 GeV in 1997 and at $\sqrt{s}$ =189 GeV in 1998. In the first two years of LEP2 running relatively low luminosity samples ($\mathcal{L} \sim 10$ pb^{-1} per energy) were collected. A sample of about 50 pb^{-1} was collected at $\sqrt{s}$ =183 GeV and 158 pb^{-1} at 189 GeV. In 1999 the centre of mass energy has reached 200 GeV and the aims for the future are to go as high as possible in $\sqrt{s}$, with $\sqrt{s}$ = 204 GeV foreseen for the last year.

In the analysis described in this thesis, Higgs bosons are searched for in the final states with neutrinos: $e^+e^- \to H\nu\overline{\nu}$. They come from the Higgs-strahlung process: $e^+e^- \to Z^0H$ with $Z^0 \to \nu\overline{\nu}$, or from the W^+W^- fusion process: $e^+e^- \to W^+W^-\nu_e\overline{\nu_e} \to H\nu\overline{\nu}$. All Higgs boson decays are considered.

The branching ratio for these final states is of the order of 20% and they are the second most likely final states for Higgs production at e^+e^- colliders in the LEP2 centre of mass energy. Their characteristics are a high value of missing energy and the presence of two acoplanar jets. This is a very peculiar signature which places the $e^+e^- \to H\nu\overline{\nu}$ channel among the preferred ones for Higgs hunting.

This thesis is organised as follows. In the first chapter I will provide an exhaustive description of the Higgs boson sector and its properties both in the Standard Model and in the Minimal Supersymmetric extension of the Standard Model. Higgs production mechanisms at LEP are examined.

The second chapter contains a brief description of the LEP accelerator and the DELPHI detector. Since many publications exist in the literature I will give only a summary. I dwell on the microvertex detector because I had the possibility to contribute to its running during 1999 data taking.

Emphasis is placed in chapter 3 on the alignment of the DELPHI detector since part of my PhD activities were dedicated to this task, which, during my PhD, has constituted a challenge in the effort to improve the detector performances.

The Higgs search made in this thesis is pursued in two steps. The data collected during 1998 at centre of mass energy of 189 GeV are analysed. First of all (chapter 4) a sequential series of cuts is applied in order to select a sample of events with an increase in signal over background ratio. Then (chapter 5) the likelihood ratio method is adopted to discriminate between signal and background events. There are two irreducible background processes: $e^+e^- \to Z^0Z^0$ with one Z^0 decaying into neutrinos, and $e^+e^- \to Z^0\gamma\gamma$ with the two photons in the beam pipe. The latter (which is called the double radiative return to the Z^0) represents a non-negligible background in the $e^+e^- \to H\nu\overline{\nu}$ channel. I was then motivated by a careful analysis of this process which was not previously studied. As a result the first preliminary world measurement of the cross section has been performed.

Since no evidence for a Higgs signal has been found, it is possible to set a lower limit on the mass of the Higgs boson. In chapter 6 I will extensively described the method used to define the limit and the limit itself will be computed. A detailed study of systematic error sources has been done and the total systematic error has been introduced in the limit derivation.

Finally, since at the moment of writing this thesis, $\simeq$140 pb^{-1} have been collected during 1999 data taking, a preliminary analysis of these data has been performed (chapter 7). Due to the Standard Model parameter fit indication of a light Higgs boson, at each LEP energy step a great expectation is present and the data are immediately analysed.

Chapter 1

Phenomenology

In the framework of the Standard Model, it is foreseen the existence of a particle called "Higgs boson". The Standard Model without the Higgs boson is incomplete since it predicts massless fermions and gauge bosons. Furthermore, the electroweak radiative corrections to observables such as the $W^{\pm}$ and Z^0 boson masses would be infinite if there were no Higgs boson. In this chapter I will describe why such particle has been introduced, and I will review its general properties. The Standard Model has been successful in predicting the properties of new particles and the structure of the basic interactions. However there are some theoretical problems which cannot be solved without the introduction of new physics. I will show the reasons why Supersimmatry must be introduced and I will describe the properties of the Higgs boson in the framework of Supersymmetry theory. The Higgs analysis, that is the subject of this thesys, has been driven by properties here reviewed.

1.1 Standard Model

In this first section I briefly recall the properties of Standard Model. For a complete review see for example [1].

Experimental observations of the weak interaction lead to classification of particles into doublets and singlets of a representation of the symmetry group $SU(2)$:

$$\begin{array}{ccc} \begin{pmatrix} \nu_e \\ e \end{pmatrix}_L & \begin{pmatrix} \nu_\mu \\ \mu \end{pmatrix}_L & \begin{pmatrix} \nu_\tau \\ \tau \end{pmatrix}_L \\ \\ e_R & \mu_R & \tau_R \end{array} \tag{1.1}$$

for leptons, and

$$\begin{array}{ccc} \begin{pmatrix} u \\ d' \end{pmatrix}_L & \begin{pmatrix} c \\ s' \end{pmatrix}_L & \begin{pmatrix} t \\ b' \end{pmatrix}_L \\ \\ u_R, d'_R & c_R, s'_R & t_R, b'_R \end{array} \tag{1.2}$$

for quarks.

Indexes L and R stand for helicity Left and Right. The same classification is applied to antiparticles with the exchange of L with R.

This classification reflects the existence of an underlying symmetry: the weak isospin symmetry. The weak isospin is a conserved quantum number in weak interactions and the $SU(2)$ is a representation of isospin symmetry.

The index $'$ (prime) indicates the eigenstates of the weak interaction: they are connected with mass eigenstates by the Cabibbo-Kobayashi-Maskawa mixing matrix (CKM):

$$\begin{pmatrix} d' \\ s' \\ b' \end{pmatrix} = \begin{pmatrix} V_{ud} & V_{us} & V_{ub} \\ V_{cd} & V_{cs} & V_{cb} \\ V_{td} & V_{ts} & V_{tb} \end{pmatrix} \begin{pmatrix} d \\ s \\ b \end{pmatrix} \tag{1.3}$$

This matrix is described by complex elements, but unitarity constraint and the arbitrarity in definition of quark fields leave only four free parameters: three real angles and a complex phase.

Quantum numbers of elementary particles are summarised in tables 1.1 and 1.2

lepton	T	T_3	Q	Y
ν_e	1/2	1/2	0	-1
e_L^-	1/2	-1/2	-1	-1
e_R^-	0	0	-1	-2

Table 1.1: *Quantum numbers of leptons*

quark	T	T_3	Q	Y
u_L	1/2	1/2	2/3	1/3
d_L	1/2	-1/2	-1/3	1/3
u_R	0	0	2/3	4/3
d_R	0	0	-1/3	-2/3

Table 1.2: *Quantum numbers of quarks*

Hypercharge Y is related to electric charge Q and to weak isospin T by:

$$Q = T_3 + \frac{Y}{2} \tag{1.4}$$

The hypercharge operator is the generator of $U(1)_Y$ symmetry group and isospin operators are the generators of $SU(2)_L$ symmetry group. The ElectroWeak interaction is a gauge theory based on $SU(2)_L \times U(1)_Y$ symmetry group. To have local gauge invariance, gauge fields are associated to these operators: a triplet $W^a_{a=1,2,3}$ is associated to weak isospin, and a single field B is associated to hypercharge.

Quarks have an additional quantum number: the colour. It may have three different values: red, yellow, blue. Colour charge cannot be observed: only colour singlet states can be viewed

The Standard Model (SM) lagrangian is given by:

$$\mathcal{L}_{SM} = \mathcal{L}_{fermions} + \mathcal{L}_{gauge} + \mathcal{L}_{Higgs} + \mathcal{L}_{mass} \tag{1.5}$$

In the following sections each of the previous four contributions will be described with particular interest for the Higgs field lagrangian.

1.1.1 Fermion fields lagrangian

$$\begin{aligned}
\mathcal{L}_{fermions} &= \mathcal{L}_{leptons} + \mathcal{L}_{quarks} && (1.6)\\
&= \sum_{families}\left[\begin{pmatrix} \overline{\nu_e} & \overline{e} \end{pmatrix}_L \gamma^\mu D_{\mu L} \begin{pmatrix} \nu_e \\ e \end{pmatrix}_L + \overline{e_R}\gamma^\mu D_{\mu R} e_R\right] && (1.7)\\
&+ \sum_{families}\left[\begin{pmatrix} \overline{u} & \overline{d} \end{pmatrix}_L \gamma^\mu D_{\mu L} \begin{pmatrix} u \\ d \end{pmatrix}_L + \overline{q_R}\gamma^\mu D_{\mu R} q_R\right]
\end{aligned}$$

where:

$$\begin{aligned}
D_{\mu L} &= \partial_\mu - ig\vec{T}\vec{W}_\mu - ig'\frac{Y}{2}B_\mu && (1.8)\\
D_{\mu R} &= \partial_\mu - ig'\frac{Y}{2}B_\mu
\end{aligned}$$

are the covariant derivatives; $\overline{f} = f^\dagger\gamma^0$ and f is the fermion field; $\vec{T} = |T|\vec{\sigma}$ with $\sigma^a_{a=1,2,3}$ Pauli matrices; γ^μ are the Dirac matrices; g and g' are the coupling constants of fermions to gauge fields W and B which appear in derivatives to maintain local gauge invariance. $W^a_{a=1,2,3}$ and B are not the physical fields which are a linear combination of them:

$$\begin{aligned}
W^\pm_\mu &= \frac{1}{\sqrt{2}}\left(W^1_\mu \mp iW^2_\mu\right) && (1.9)\\
\begin{pmatrix} A_\mu \\ Z_\mu \end{pmatrix} &= \begin{pmatrix} \cos\theta_W & \sin\theta_W \\ -\sin\theta_W & \cos\theta_W \end{pmatrix}\begin{pmatrix} B_\mu \\ W^3_\mu \end{pmatrix} && (1.10)
\end{aligned}$$

where

$$\begin{aligned}
\sin\theta_W &= \frac{g'}{\sqrt{g^2+g'^2}} && (1.11)\\
\cos\theta_W &= \frac{g}{\sqrt{g^2+g'^2}} && (1.12)
\end{aligned}$$

Gauge bosons masses are:

$$
\begin{aligned}
m_A &= 0 && (1.13)\\
m_W &= \frac{1}{2}vg && (1.14)\\
m_Z &= \frac{1}{2}v\sqrt{g^2+g'^2} && (1.15)
\end{aligned}
$$

From the previous equations:

$$\rho = \frac{m_W^2}{m_Z^2\cos^2\theta_W} = 1 \tag{1.16}$$

which has been verified with great precision [5]:

$$\rho_{exp} = 1.0012 \pm 0.0022 \tag{1.17}$$

Once the electromagnetic coupling constant (electric charge) is defined by:

$$e = g\sin\theta_W = g'\cos\theta_W \tag{1.18}$$

it is possible to rewrite the electroweak lagrangian for the interaction of fermions as:

$$\mathcal{L}_{fermions} = \mathcal{L}_{e.m.} + \mathcal{L}_{c.c.} + \mathcal{L}_{n.c.} \tag{1.19}$$

where:

- Electromagnetic interaction:

$$\mathcal{L}_{e.m.} = -\sum_{families} e\left(-\overline{e}\gamma^\mu e + \frac{2}{3}\overline{u}\gamma^\mu u - \frac{1}{3}\overline{d}\gamma^\mu d\right)A_\mu \tag{1.20}$$

  It is possible to note the electric charge $(-1; \frac{2}{3}; -\frac{1}{3})$ of fermions $(e; u; d)$ as the coupling constants to photon field A_μ

- weak interaction by charge current:

$$
\begin{aligned}
\mathcal{L}_{c.c.} &= \sum_{families}\frac{g'}{\sqrt{2}}\left(\overline{\nu_e}\gamma^\mu\frac{1-\gamma^5}{2}eW_\mu^+ + \overline{e}\gamma^\mu\frac{1-\gamma^5}{2}\nu_e W_\mu^-\right) && (1.21)\\
&+ \sum_{families}\frac{g'}{\sqrt{2}}\left(\overline{u}\gamma^\mu\frac{1-\gamma^5}{2}dW_\mu^+ + \overline{d}\gamma^\mu\frac{1-\gamma^5}{2}uW_\mu^-\right)
\end{aligned}
$$

  which couples left handed states with W^+ and W^- bosons.

- weak interactions by neutral current:

$$\mathcal{L}_{n.c.} = \sum_{fermions} -\frac{1}{2}\frac{1}{\sqrt{g^2+g'^2}}\overline{f}\gamma^\mu\left(\frac{g_{V_f}+g_{A_f}\gamma^5}{2}\right)fZ_\mu \tag{1.22}$$

  which couples fermions to the Z^0 boson by a combination of axial and vector components with strengths g_{A_f} and g_{V_f} whose values are summarised in table 1.3

fermions		g_{V_f}	g_{A_f}
leptons	ν_e,ν_μ,ν_τ	$g^2 + g'^2$	$g^2 + g'^2$
	e,μ,τ	$3g^2 - g'^2$	$-g^2 - g'^2$
quarks	u,c,t	$-\frac{5}{3}g^2 + g'^2$	$g^2 + g'^2$
	d,s,b	$\frac{1}{3}g^2 - g'^2$	$-g^2 - g'^2$

Table 1.3: *Vector and axial coupling constants for leptons and quarks*

1.1.2 Gauge fields lagrangian

Fields W and B are introduced on covariant derivatives to save local gauge invariance under $SU(2)_L \times U(1)_Y$. To complete the lagrangian for gauge fields it is necessary to introduce the kinematic term:

$$\mathcal{L}_{gauge} = -\frac{1}{4}W^a_{\mu\nu}W^{\mu\nu}_a - \frac{1}{4}B_{\mu\nu}B^{\mu\nu} \tag{1.23}$$

where field tensors are given by.

$$W^a_{\mu\nu} = \partial_\mu W^a_\nu - \partial_\nu W^a_\mu + g\epsilon^{abc}W_{b\mu}W_{c\nu} \tag{1.24}$$

$$B_{\mu\nu} = \partial_\mu B_\nu - \partial_\nu B_\mu \tag{1.25}$$

In this way a self coupling term for W fields is present.

The lagrangian $\mathcal{L} = \mathcal{L}_{fermions} + \mathcal{L}_{gauge}$ gives a description of a gauge-invariant and renormalizable unified theory of weak and electromagnetic interactions. However all leptons and gauge bosons till this point have zero mass. The addition of an *ad hoc* mass term:

$$m_f\overline{f}f \tag{1.26}$$

spoils the $SU(2) \times U(1)$ symmetry. This follows since expression 1.26 can be written as:

$$m_f\overline{f}\left(\frac{1+\gamma_5}{2} + \frac{1-\gamma_5}{2}\right)f = m_f\left[\overline{f_L}f_R + \overline{f_R}f_L\right] \tag{1.27}$$

but $\overline{f_R}$ and f_R are isoscalars under $SU(2) \times U(1)$, while $\overline{f_L}$ and f_L are isospinors and so $\overline{f_R}f_L$ is not invariant under $SU(2)_L$ operations.

Similarly it is not possible to add a mass term for gauge bosons without spoiling the symmetry. And, it is worthwhile to note, the gauge invariance is indispensable to have a renormalizable theory.

Spontaneous symmetry breaking and Higgs mechanism are the instruments to overcome the problems.

1.2 Spontaneous symmetry breaking and Higgs mechanism

The idea is to introduce a scalar field to add mass to fermions and gauge bosons. (in the following the different possibilities to have one or more multiplets of a scalar field will be treated)

To understand how it works, let consider the simple case of a gauge massless field A_μ

$$\mathcal{L}(A) = -\frac{1}{4}F_{\mu\nu}F^{\mu\nu} \tag{1.28}$$

where $F_{\mu\nu} = \partial_\mu A_\nu - \partial_\nu A_\mu$

To add the mass term for the gauge field without breaking the gauge invariance, a term for a scalar field ϕ is added to the lagrangian:

$$\mathcal{L}(\phi) = (D_\mu\phi)^*(D^\mu\phi) - V(\phi) \tag{1.29}$$

where the potential is given by:

$$V(\phi) = \mu^2\phi^*\phi + \lambda(\phi^*\phi)^2 \tag{1.30}$$

with $\mu^2 < 0$ and $\lambda > 0$. Note that $\mathcal{L} = \mathcal{L}(\phi) + \mathcal{L}(A)$ is invariant under gauge transformation:

$$\begin{array}{rcl} \phi & \rightarrow & (1 + ig\chi(x))\phi \\ A_\mu & \rightarrow & A_\mu - \partial\chi(x) \end{array} \tag{1.31}$$

if covariant derivative is used: $D_\mu = \partial_\mu + igA_\mu$.

The potential $V(\phi)$ has a minimum at $\phi = ve^{i\theta}/\sqrt{2}$ with $v = \sqrt{-\mu^2/\lambda}$ at a value which does not follow the potential symmetry. It is possible to compute the perturbative excitations around this minimum (spontaneous symmetry breaking) with the substitution

$$\phi = (\frac{v + H(x)}{\sqrt{2}})e^{i\theta} \tag{1.32}$$

(where $H(x)$ is a real field). Since the lagrangian density is invariant under global phase transformation $\phi(x) \rightarrow \phi(x)e^{i\theta}$, the value of θ is not significant and one can take $\theta = 0$. Then the lagrangian becomes:

$$\begin{array}{rcl} \mathcal{L} & = & \frac{1}{2}[(\partial_\mu - igA_\mu)(v + H)][(\partial_\mu + igA_\mu)(v + H)] + \\ & & \frac{1}{2}\mu^2(v + H)^2 - \frac{1}{4}\lambda(v + H)^4 - \frac{1}{4}F_{\mu\nu}F^{\mu\nu} \end{array} \tag{1.33}$$

In the previous equation some terms are of particular interest:

- $g^2v^2A_\mu A^\mu$: mass term for gauge field
- $\lambda v^2 H$: mass term for scalar field
- $vg^2HA^\mu A_\mu$ and $g^2H^2A^\mu A_\mu$: interactions of scalar field H with gauge field
- λH^4 and $v\lambda H^2$ self-interactions of scalar field.

We have shown that by spontaneous symmetry breaking and Higgs mechanism, without explicitly breaking the gauge invariance, it is possible to add a mass term for the gauge field. As a "by product" a scalar massive field H appears: the Higgs boson.

1.2.1 Higgs mechanism in Minimal Standard Model

The Higgs mechanism can be applied using as scalar field multiplets of $SU(2)_L \times U(1)_Y$ group (under some conditions specified later). The simplest choice is a doublet ($T = 1/2$) with hypercharge $Y = 1$:

$$\Phi = \begin{pmatrix} \phi^+ \\ \phi^0 \end{pmatrix} = \begin{pmatrix} (\phi_1 + i\phi_2)/\sqrt{2} \\ (\phi_3 + i\phi_4)/\sqrt{2} \end{pmatrix} \tag{1.34}$$

where ϕ_i are real fields.

Lagrangian for scalar field and potential are the same as 1.29 and 1.30, and the covariant derivative has the form:

$$D_\mu = i\partial_\mu - g\vec{T} \cdot \vec{W}_\mu - g' \frac{Y}{2} B_\mu \tag{1.35}$$

Perturbative expansion is computed around $\Phi_0 = \frac{1}{\sqrt{2}} \begin{pmatrix} 0 \\ v \end{pmatrix}$:

$$\Phi(x) = \frac{e^{i\sigma(x)/v}}{\sqrt{2}} \begin{pmatrix} 0 \\ v + H(x) \end{pmatrix} \tag{1.36}$$

the $\sigma(x)$ fields are the Goldstone bosons. At the end of the computation, mass terms appear for W_μ, Z_μ and H fields (while A_μ stays massless) and three degrees of freedom are absorbed by longitudinal polarisation of $W^\pm$ and Z^0.

Higgs boson mass is equal to $v\sqrt{2\lambda}$ and it is not predicted by the model.

A prediction for v can be obtained by the correspondence between this model and the effective theory of charge currents at low energy:

$$v = \left(G_F \sqrt{2}\right)^{-\frac{1}{2}} \simeq 246 GeV \tag{1.37}$$

1.2.2 General scalar sector

The previous choice of a doublet is called minimal (MSM). A *priori* other multiplets can be used to produce the Higgs mechanism, and moreover a more complex structure of the scalar sector could explain the difference between fermion masses and can give a new source of CP violation. Actually in the MSM the CP violation source is included in the complex phase inside the CKM mixing matrix. However this source is not enough to explain the asymmetry between matter and antimatter in the universe [2]. Models in which the scalar sector has more than a doublet give new sources of CP asymmetry and make possible the baryogenesis at the scale of the weak interaction.

So there are a lot of reasons to introduce a more complex structure in the scalar sector of MSM. There are, of course, also some constraints to be explained later.

Let us introduce the general possibility of N multiplets Φ_i with isospin T_i and hypercharge Y_i:

$$\Phi_i = \begin{pmatrix} \phi_{i,1}(T_i) \\ \phi_{i,2}(T_i-1) \\ \vdots \\ \phi_{i,j}(T_{i,j}) \\ \vdots \\ \phi_{i,2T_i+1}(-T_i) \end{pmatrix} \tag{1.38}$$

where each $\phi_{i,j}$ has electric charge: $Q_{i,j} = T^3_{i,j} + \frac{Y}{2}$ ($T^3_{i,j}$ being the third component of weak isospin of $\phi_{i,j}$).

Mass term for gauge bosons appears in developing the term in the lagrangian

$$|\sum_i \left(\partial_\mu - g\vec{T}\cdot\vec{W}_\mu - g'\frac{Y}{2}B_\mu\right)\Phi_i|^2 \tag{1.39}$$

if, and only if, at least one of the components of one multiplet Φ_i has an expectation value on vacuum not equal to zero:

$$< 0|\Phi_i|0 > = < \Phi_i >_0 = \begin{pmatrix} 0 \\ \vdots \\ 0 \\ 1 \\ 0 \\ \vdots \\ 0 \end{pmatrix} \tag{1.40}$$

In order that the vacuum state is invariant under local transformation of $U(1)_{em}$ group, it is necessary that non null components of $< \Phi_i >_0$ are electrically neutral.

Developing 1.39, the masses of gauge bosons have the following expressions:

$$m_W^2 = \frac{g^2}{2}\sum_i v_i^2\left[T_i(T_i+1) - (\frac{Y_i}{2})^2\right] \tag{1.41}$$

$$m_Z^2 = \frac{g^2}{\cos\theta_W{}^2}\sum_i v_i^2(\frac{Y_i}{2})^2 \tag{1.42}$$

The number of massive scalar bosons (after absorption of three degree of freedom in the longitudinal polarisation of massive gauge bosons) is equal to $2\sum_{i=1}^N(2T_i+1)-3$. Vacuum mean value is:

$$2\sum_{i=1}^N v_i^2\left[T_i(T_i+1) - (\frac{Y_i}{2})^2\right] \simeq (246GeV)^2 \tag{1.43}$$

1.2.3 Constraints on scalar sector

Constraints on the structure of scalar multiplets come from two different considerations:

- the gauge bosons mass relation $\rho = \frac{m_W^2}{m_Z^2 \cos^2\theta_W} = 1$ must be verified at zero order of quantic corrections;
- the generation mechanism of fermion masses where the neutral currents with change of quark flavour (FCNC) at tree level must be avoided .

Let us examine both constraints.

1.2.3.1 Relation $\rho = 1$

In the case of N multiplets (T_i, Y_i) the general expression for ρ is:

$$\rho = \frac{\sum_{i=1}^{N} v_i^2 \left[T_i(T_i+1) - (\frac{Y_i}{2})^2\right]}{\sum_{i=1}^{N} v_i^2 (\frac{Y_i}{2})^2} \tag{1.44}$$

The relation $\rho = 1$ can be verified if each multiplet verifies:

$$T_i(T_i+1) = 3(\frac{Y_i}{2})^2 \tag{1.45}$$

The simplest possibilities are the singlets $(T = 0, Y = 0)$ and doublets $(T = 1/2, Y = \pm 1)$. Singlets are usually used with other multiplets, in particular the doublets (it is the case of some supersymmetric extension of MSM)

Also the representation $(T = 3, Y = 4)$ called *septet*, gives $\rho = 1$ but its complex structure makes it unlikely.

Another way to have $\rho = 1$ is by adjusting v_i values. For example, if a triplet with hypercharge $Y_1 = 2$ and a triplet with $Y_2 = 0$ are used:

$$\rho = \frac{v_1^2 + 2v_2^2}{2v_1^2} \tag{1.46}$$

using $v_1^2 = 2v_2^2$ gives $\rho = 1$. However, this way of doing things seems artificial.

Unitarity of ρ implies a scalar sector with at least a doublet. It is possible to add a triplet which will give a ρ value slightly different from one. In this case the experimental value of ρ will constrain the vacuum mean value of the triplet depending on its hypercharge [3]. A recent analysis gives [4]:

$$|v_{1,Y}| < 0.03 |v_{\frac{1}{2},1}| \tag{1.47}$$

where $Y = 0$ or $Y = \pm 2$ and $v_{\frac{1}{2},1}$ is the vacuum mean value of the doublet. But a low value of $v_{1,Y}$ contradicts the role of scalar multiplets which needs vacuum mean value different from zero to break the electroweak symmetry. For this reason, this structure is not likely.

Another possibility [4] is to add at the singlet of MSM a triplet of real fields ($Y = 0$) and a triplet of complex fields ($Y = 2$). Unitarity of ρ is assured if vacuum mean value of the two triplets are equal. Also this possibility seems unlikely.

Consequently the constraint $\rho = 1$ (which is given by the experiments with great precision), leads to a scalar sector made by doublet and singlet (MHDM: "Multiple Higgs Doublets Models"). This is the simplest and most likely solution which does not require any other condition.

1.2.3.2 Mass lagrangian and suppression of FCNC

As was shown in 1.26 it is not possible to add a fermion mass term in the form $m_f\overline{f}f$ without explicitly breaking the symmetry.

Once the scalar sector is added, it can be used to overcome the problem. If the scalar sector has a doublet Φ with hypercharge $Y = \pm 1$ the following term can be built (G_f is a coupling constant):

$$G_f\left[(\overline{f}_L\Phi)f_R + \overline{f_R}(\Phi^\dagger f_L)\right] \tag{1.48}$$

which is invariant under $SU(2)$ operations.

In the case of MSM there are three families of leptons and quarks and, moreover, the possibility of quark flavour mixing must be taken into account. This mixing is expressed in the frame of the MSM by the Cabibbo Kobayashi Maskawa matrix. As was mentioned above this matrix is unitary: this reflects the absence at tree level of transitions $d \leftrightarrow s$, $s \leftrightarrow b$, $d \leftrightarrow b$ which implies the absence of neutral currents with change of flavour (FCNC). Taking into account all these facts, the mass lagrangian becomes:

$$\begin{aligned}
\mathcal{L}_{mass} &= \mathcal{L}^{leptons}_{mass} + \mathcal{L}^{quarks}_{mass} && (1.49)\\
&= \sum_{families}\left[G_e(\overline{e}_L\Phi)e_R + G_e(\overline{e}_R\Phi^c)e_L\right] + h.c.\\
&+ \sum_{i,j}\left[G'_{i,j}(\overline{Q_{iL}}\Phi)d'_{jR} + G_{i,j}(\overline{Q_{iL}}\Phi^c)u_{jR}\right] + h.c.\\
& && (1.50)
\end{aligned}$$

where

- $\Phi = \begin{pmatrix} \phi^+ \\ \phi^0 \end{pmatrix}$
- $\Phi^c = \begin{pmatrix} \phi^{0*} \\ -\phi^- \end{pmatrix}$
- $Q_{iL} = \begin{pmatrix} u \\ u \end{pmatrix}_{iL}$

- G and G' are 3×3 matrices
- i, j specify the families
- The $'$ indicates the eigenstates of weak interaction (connected to mass eigenstates as specified in 1.3)

After symmetry breaking and perturbative expansion of Φ near its minimum, the quark masses lagrangian becomes:

$$\left(1 + \frac{H(x)}{v}\right) \sum_{i,j} \left(\overline{u_{iL}} M_{ij} u_{jR} + \overline{d'_{iL}} M'_{ij} d'_{jR}\right) + h.c. \tag{1.51}$$

where $M = \frac{v}{\sqrt{2}} G$ and $M' = \frac{v}{\sqrt{2}} G'$. Once these matrices are diagonalized, the lagrangian for quark masses becomes:

$$\left(1 + \frac{H(x)}{v}\right) \left(m_u \overline{u} u + m_d \overline{d} d + \cdots\right) \tag{1.52}$$

In the lagrangian there is no term of flavour change like $H\overline{d}s$. This is due to the fact that the diagonalisation of M and M' implies the diagonalization of G and G'

This is not the case for theory different from MSM. We can consider, for example, the case of scalar sector made by two doublets Φ_1 and Φ_2 with hypercharge $Y_{1,2} = 1$. The lagrangian for mass term of quarks is:

$$\mathcal{L}^{quarks}_{mass} = \sum_{i,j} \left[G'^{(1)}_{ij} (\overline{Q_{iL}} \Phi_1) d'_{jR} + G'^{(2)}_{ij} (\overline{Q_{iL}} \Phi_2) d'_{jR}\right] + h.c. \tag{1.53}$$

After spontaneous symmetry breaking it gives the following terms

$$\sum_{ij} \left(1 + \frac{H_1(x)}{v_1}\right) \left(\overline{d'_{iL}} M'^{(1)}_{ij} d'_{jR}\right) + \sum_{ij} \left(1 + \frac{H_2(x)}{v_2}\right) \left(\overline{d'_{iL}} M'^{(2)}_{ij} d'_{jR}\right) + h.c. \tag{1.54}$$

where v_i and H_i are respectively the vacuum mean value and the massive field associated to doublet Φ_i. The mixing matrix to be diagonalized is:

$$M' = M'^{(1)} + M'^{(2)} = \frac{v_1}{\sqrt{2}} G'^{(1)} + \frac{v_2}{\sqrt{2}} G'^{(2)} \tag{1.55}$$

It is evident that diagonalization of M' does not imply diagonalization of each of $G'^{(1)}$ and $G'^{(2)}$ and so the interaction between scalar fields and quarks does not necessarily preserve flavour. Since experimental measurements constrain the absence of FCNC at tree level, the scalar sector should be built in such a way that FCNC are absent at order zero of quantum corrections.

In the MHDM there are a lot of possibilities to do this, but the most elegant one relies on a theorem proved by Glashow and Weinberg [6] [7] which states that: *scalar fields do not induce FCNC if and only if all quarks with the same electric charge:*

- *have the same irreducible representation of $SU(2)_L$ (doublets or singlets in the MSM)*
- *have the same quantum number T_3*
- *take mass from coupling to only one Higgs doublet*

Actually, terms with FCNC disappear if, for quarks of same charge, mass matrix M is proportional to interaction matrix G, that is M is defined by only one scalar doublet. This condition is equivalent to the request of an additional discrete symmetry, whose definition is model dependent (it will be given later for models with two doublets).

In the MHDM there are five [8] different ways to couple Higgs doublets to fermions respecting conditions of the above theorem. They are summarised in table 1.4 in which it is specified also to which doublet each quark couples.

fermions	models				
	I	I'	II	II'	III
u,c,t	Φ_1	Φ_1	Φ_1	Φ_1	Φ_1
d,s,b	Φ_1	Φ_1	Φ_2	Φ_2	Φ_2
e,μ,τ	Φ_1	Φ_2	Φ_1	Φ_2	Φ_3

Table 1.4: *Five ways to couple Higgs doublets to fermions respecting conditions for suppression of FCNC defined by Glashow and Weinberg*

If, for example, we consider the two doublets model II in which doublet Φ_1 (Φ_2) couples to quarks u (d), the lagrangian for quark mass becomes:

$$\sum_{i,j}\left[G'^{(1)}_{i,j}(\overline{Q_{iL}}\Phi_1)d'_{jR}+G^{(2)}_{i,j}(\overline{Q_{iL}}\Phi_2)u'_{jR}\right]+h.c. \tag{1.56}$$

and diagonalization of the mass matrix implies diagonalization of G and G'.

We have shown that the request of unitarity of ρ and absence of FCNC at tree level favour extensions of MSM made by at least two doublets of $SU(2)_L$ group with, eventually, singlets; and that fermions couple to three different doublets (at maximum) in five different ways. The desire for simplicity and a limited number of free parameters from the scalar sector favour the case of two doublets.

1.2.4 Two doublets models

The interest to investigate these models, relays on the fact that the Minimal Supersymmetric extension of Standard Model is made by a two doublets model.

Let us call Φ_1 and Φ_2 two doublets of $SU(2)_L$ made by complex scalar fields with hypercharge $Y_{1,2} = 1$:

$$\Phi_1 = \begin{pmatrix} \phi_1^+ \\ \phi_1^0 \end{pmatrix} = \begin{pmatrix} \varphi_1 + i\varphi_2 \\ \varphi_3 + i\varphi_4 \end{pmatrix} \tag{1.57}$$

$$\Phi_2 = \begin{pmatrix} \phi_2^+ \\ \phi_2^0 \end{pmatrix} = \begin{pmatrix} \varphi_5 + i\varphi_6 \\ \varphi_7 + i\varphi_8 \end{pmatrix} \tag{1.58}$$

The choice of $Y(\Phi_1) = Y(\Phi_2) = 1$ is arbitrary: two doublets Φ_1 and Φ_2' with $Y(\Phi_1) = -Y(\Phi_2') = 1$ can be used. In this case Φ_2' can be obtained from Φ_2 with an isospin rotation: $\Phi_2' = i\sigma_2\Phi_2$.

The most general potential built with these two doublets is [9]:

$$\begin{aligned} V(\Phi_1,\Phi_2) = & - \mu_1^2(\Phi_1^\dagger\Phi_1) - \mu_2^2\Phi_2^\dagger\Phi_2 - \left(\mu_{12}^2\Phi_1^\dagger\Phi_2 + h.c.\right) \\ & + \lambda_1(\Phi_1^\dagger\Phi_1)^2 + \lambda_2(\Phi_2^\dagger\Phi_2)^2 + \lambda_3(\Phi_1^\dagger\Phi_1\Phi_2^\dagger\Phi_2) + \lambda_4(\Phi_1^\dagger\Phi_2\Phi_2^\dagger\Phi_1) \\ & + \frac{1}{2}\left[\lambda_5(\Phi_1^\dagger\Phi_2)^2 + h.c.\right] + \left[(\lambda_6\Phi_1^\dagger\Phi_1 + \lambda_7\Phi_2^\dagger\Phi_2)(\Phi_1^\dagger\Phi_2) + h.c.\right] \end{aligned} \tag{1.59}$$

where λ_i are complex numbers. This potential has terms proportional to $\Phi_1^\dagger\Phi_2$ which are responsible of CP violation: more precisely if λ_5 is real and non-zero, there is CP violation if one of three parameters μ_{12}, λ_6 or λ_7 is not equal to zero. In this case there are two kinds of CP violation:

- *spontaneous violation*: if $\lambda_5 > 0$ and μ_{12}, λ_6, λ_7 are real, then there is CP violation if there is a phase ξ between vacuum mean values of the two doublets:

$$< \Phi_1 >_0 = \begin{pmatrix} 0 \\ v_1 \end{pmatrix} \text{ and } < \Phi_2 >_0 = \begin{pmatrix} 0 \\ v_2 e^{i\xi} \end{pmatrix}$$

- *explicit violation*: at least one of μ_{12}, λ_6, λ_7 is complex and so the phase ξ appears.

Until this point there is no FCNC suppression. To achieve this there must exist one of the following *discrete symmetries*:

$$\Phi_1 \to -\Phi_1, \qquad \Phi_2 \to \Phi_2 \tag{1.60}$$

$$d_{iR} \to d_{iR} \qquad \textit{or} \qquad d_{iR} \to -d_{iR} \qquad u_{iR} \to u_{iR} \tag{1.61}$$

where i is index of families. Symmetry associated to transformation $d_{iR} \to d_{iR}$ is verified by models I where all quarks couple to the same doublet; the other symmetry is verified by models II where quarks u and d couple to different scalar doublets.

Potential 1.59 is invariant under 1.60 if μ_{12}, λ_6, λ_7 are all equal to zero. In this case there is no more source of CP violation in the scalar sector. To obtain CP violation inside the scalar potential without having FCNC at tree level, there are a lot of possibilities [9]. For example invariance under 1.60 can be broken "softly" by the term $\mu_{12}^2(\Phi_1^\dagger\Phi_2)$.

In the following we consider only the case in which the symmetry to assure the suppression of FCNC is exact and then the scalar potential has no terms with CP violation. In this case the potential can be written as:

$$\begin{aligned} V(\Phi_1,\Phi_2) &= \lambda_1(\Phi_1^\dagger\Phi_1 - v_1^2)^2 + \lambda_2(\Phi_2^\dagger\Phi_2 - v_2^2)^2 \\ &+ \lambda_3[(\Phi_1^\dagger\Phi_1 - v_1^2) + (\Phi_2^\dagger\Phi_2 - v_2^2)]^2 \\ &+ \lambda_4(\Phi_1^\dagger\Phi_1\Phi_2^\dagger\Phi_2 - \Phi_1^\dagger\Phi_2\Phi_2^\dagger\Phi_1) \\ &+ \lambda_5[\mathcal{RE}(\Phi_1^\dagger\Phi_2)]^2 + \lambda_6[\mathcal{IM}(\Phi_1^\dagger\Phi_2)]^2 \end{aligned} \tag{1.62}$$

where all λ_i are real positive numbers.

Since in the Higgs mechanism, three degrees of freedom of scalar fields are absorbed by longitudinal polarisation of gauge bosons when they aquired mass, in the two doublets model the remaining five degrees of freedom lead to the existence of five Higgs bosons:

- two neutral bosons: H, h with quantum numbers $J^{CP} = 0^{++}$
- one neutral boson : A with quantum numbers $J^{CP} = 0^{+-}$
- two charged bosons: $H^\pm$, with quantum numbers $J^P = 0^+$

Masses of these bosons are functions of λ_i and v_i and an important parameter of the model is the ratio between vacuum expectation values of the doublets:

$$\tan\beta = \frac{v_2}{v_1} \tag{1.63}$$

The expressions for Higgs boson masses can be obtained by minimising the potential 1.62 around $\langle\varphi_3\rangle = v_1$, $\langle\varphi_7\rangle = v_2$ and $\langle\varphi_i\rangle = 0$ for $k \neq 3, 7$ and then the mass eigenstates are obtained diagonalising the mass matrix $\mathcal{M}$ given by:

$$\mathcal{M}_{ij} = \frac{1}{2}\frac{\partial^2 V}{\partial\varphi_i\partial\varphi_j}. \tag{1.64}$$

1.2.4.1 Neutral sector

In this sector the real components of fields (φ_3 and φ_7) are decoupled from imaginary components (φ_4 and φ_8). Let us look to the corresponding matrixes:

- the matrix for the imaginary components of the field is:

$$M^i = \lambda_6 \begin{pmatrix} v_1^2 & -v_1v_2 \\ -v_1v_2 & v_2^2 \end{pmatrix} \tag{1.65}$$

The eigenvalue 0 has as eigenstate the Goldstone boson G (absorbed to give the longitudinal polarization to Z boson) defined by:

$$G = \sqrt{2}[\mathcal{IM}(\phi_1^0)\cos\beta + \mathcal{IM}(\phi_2^0)\sin\beta] \tag{1.66}$$

The other eigenvalue $m_A = \lambda_6(v_1^2 + v_2^2)$ is the mass of A boson described by the eigenstate:

$$A = \sqrt{2}[-\mathcal{IM}(\phi_1^0)\sin\beta + \mathcal{IM}(\phi_2^0)\cos\beta] \tag{1.67}$$

- the matrix for the real components of the field is:

$$M^r = \lambda_6 \begin{pmatrix} 4v_1^2(\lambda_1+\lambda_3) + v_2^2\lambda_5 & (4\lambda_3+\lambda_5)v_1v_2 \\ (4\lambda_3+\lambda_5)v_1v_2 & 4v_2^2(\lambda_2+\lambda_3) + v_1^2\lambda_5 \end{pmatrix} \tag{1.68}$$

It can be diagonalized by a rotation of angle α:

$$\tan\alpha = \frac{2M_{12}^r}{M_{11}^r - M_{22}^r} \tag{1.69}$$

The eigenstates are the two Higgs bosons:

$$\begin{aligned} H &= \sqrt{2}[(\mathcal{RE}(\phi_1^0) - v_1)\cos\alpha + (\mathcal{RE}(\phi_2^0) - v_2)\sin\alpha] \\ h &= \sqrt{2}[-(\mathcal{RE}(\phi_1^0) - v_1)\sin\alpha + (\mathcal{RE}(\phi_2^0) - v_2)\cos\alpha] \end{aligned} \tag{1.70}$$

The masses of the two bosons are:

$$m_{H,h}^2 = \frac{1}{2}[M_{11}^r + M_{22}^r \pm \sqrt{(M_{11}^r - M_{22}^{r2}M_{12}^{r2})}] \tag{1.71}$$

1.2.4.2 Charged sector

In this sector the real components of fields (φ_1 and φ_5) are decoupled from imaginary components (φ_2 and φ_6). The two corresponding matrixes are equal and they are expressed by:

$$M = \lambda_4 \begin{pmatrix} v_1^2 & -v_1v_2 \\ -v_1v_2 & v_2^2 \end{pmatrix} \tag{1.72}$$

The eigenvalues equal to 0 are associated to the Goldstone bosons absorbed to give the longitudinal polarisation of W^+ and W^-. The other eigenvalue is the mass of the two charged Higgs bosons:

$$m_{H^\pm}^2 = \lambda_4(v_1^2 + v_2^2) \tag{1.73}$$

The eigenstates are:

$$\begin{aligned} G^\pm &= \phi_1^\pm\cos\beta + \phi_2^\pm\sin\beta \\ H^\pm &= -\phi_1^\pm\sin\beta + \phi_2^\pm\cos\beta \end{aligned} \tag{1.74}$$

1.3 The Standard Model Higgs properties

In section 1.2.1 it has been shown that a single Higgs particle fits in the Standard Model. In the following there will be a review of its properties.

1.3.1 Higgs mass limits

There exist indirect considerations which constraint upper an lower values of the Higgs mass [10].

1.3.1.1 Unitarity

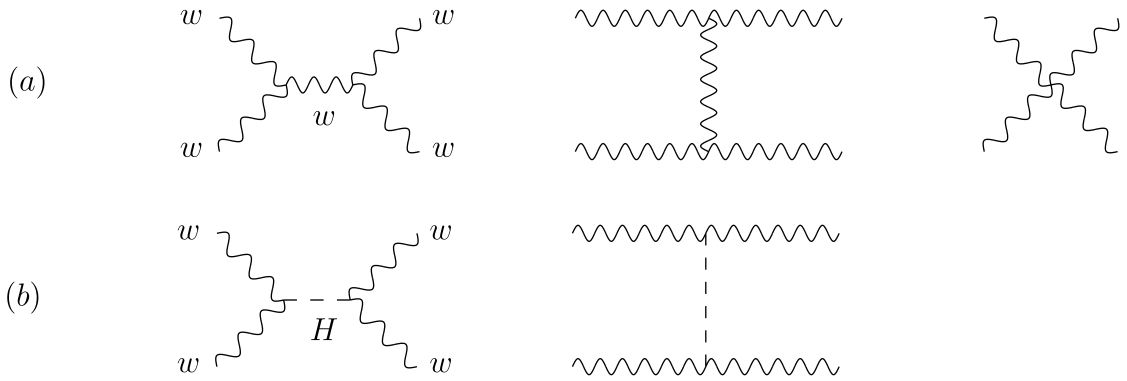

Figure 1.1: *Generic diagrams of elastic ww scattering: (a) pure gauge-boson dynamics, and (b) Higgs-boson exchange.*

Models which have cross sections rising with s will eventually violate perturbative unitarity. To see this we consider $2 \to 2$ elastic scattering. The cross section can be written as

$$\begin{aligned} \sigma &= \frac{8\pi}{s}\sum_{l=0}^{\infty}\sum_{l'=0}^{\infty}(2l+1)(2l'+1)a_l a_l^* \\ &\quad \cdot \int_{-1}^{1} d\cos\theta P_l(\cos\theta)P_{l'}(\cos\theta) \\ &= \frac{16\pi}{s}\sum_{l=0}^{\infty}(2l+1) \mid a_l \mid^2 \end{aligned} \tag{1.75}$$

where a_l is the spin l partial wave and P_l are the Legendre polynomials.

The optical theorem gives,

$$\sigma = \frac{1}{s} Im\Big[\mathcal{A}(\theta = 0)\Big] = \frac{16\pi}{s}\sum_{l=0}^{\infty}(2l+1) \mid a_l \mid^2 . \tag{1.76}$$

This immediately yields the unitarity requirement:

$$| a_l |^2 = Im(a_l). \tag{1.77}$$

One statement of unitarity is the requirement that

$$| Re(a_l) | < \frac{1}{2}. \tag{1.78}$$

As a demonstration of unitarity restrictions we consider the scattering of longitudinal gauge bosons, $w^+w^- \rightarrow w^+w^-$ in which also the contribution coming from Higgs particle is taken into account (figure 1.1). Constructing the $J = 0$ partial wave in the limit $m_w^2 << s$

$$\begin{aligned} a_0^0(\omega^+\omega^- \rightarrow \omega^+\omega^-) &\equiv \frac{1}{16\pi s}\int_{-s}^{0} | \mathcal{A} | \, dt \\ &= -\frac{G_F m_H^2}{8\sqrt{2}\pi}\Big[2 + \frac{m_H^2}{s - m_H^2} - \frac{m_H^2}{s}\log\Big(1 + \frac{s}{m_H^2}\Big)\Big]. \end{aligned} \tag{1.79}$$

If we go to very high energy, $s >> m_H^2$, then Eq. 1.79 has the limit

$$a_0^0(\omega^+\omega^- \rightarrow \omega^+\omega^-) \longrightarrow_{s>>m_H^2} -\frac{G_F m_H^2}{4\pi\sqrt{2}}. \tag{1.80}$$

Applying the unitarity condition, $| Re(a_0^0) | < \frac{1}{2}$ gives the restriction

$$m_H < 860\ GeV. \tag{1.81}$$

This does not mean that the Higgs boson cannot be heavier that 860 GeV, it simply means that for heavier masses perturbation theory is not valid.

The Higgs boson therefore plays a fundamental role in the theory since it cuts off the growth of the partial wave amplitudes and makes the theory unitary.

We can apply the alternate limit to Eq. 1.79 and take the Higgs boson much heavier than the energy scale. In this limit[13]

$$a_0^0(\omega^+\omega^- \rightarrow \omega^+\omega^-) \longrightarrow_{s<<m_H^2} \frac{G_F s}{16\pi\sqrt{2}}. \tag{1.82}$$

Again applying the unitarity condition we find,

$$\sqrt{s_c} < 1.8\ TeV \tag{1.83}$$

s_c denotes the scale at which perturbative unitarity is violated. Eq. 1.83 is the basis for the statement: there must be new physics on the TeV scale. It implies that, without a Higgs boson, there must be new physics which restores perturbative unitarity somewhere below an energy scale of 1.8 TeV.

1.3.1.2 Triviality

In a scalar potential for a complex $SU(2)_L$ Higgs doublet, after spontaneous symmetry breaking, the quartic coupling can then be related to the physical Higgs boson mass,

$$\lambda = \frac{m_H^2}{2v^2} \quad . \tag{1.84}$$

As with all couplings in a gauge theory, the quartic coupling, λ, evolves with the energy scale, Q. The basic contributions are depicted in Fig. 1.2. The Higgs loop itself gives rise to an indefinite increase of the coupling while the fermionic top-quark loop, with increasing top mass, drives the coupling to smaller values, finally even to values below zero.

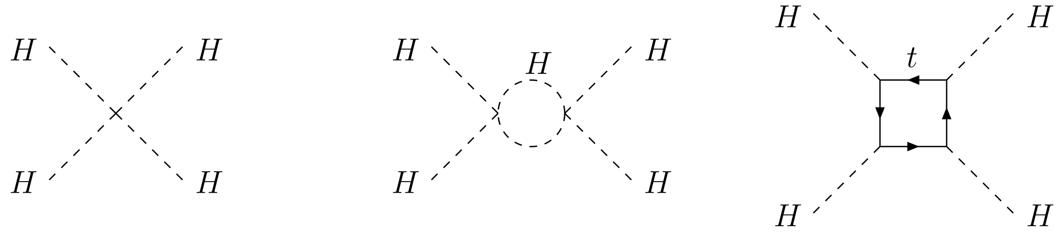

Figure 1.2: *Diagrams generating the evolution of the Higgs self-interaction λ.*

For large λ, (and neglecting for now the effects of gauge couplings and the top quark), the evolution is roughly,

$$Q\frac{d\lambda}{dQ} \sim \frac{3\lambda^2}{4\pi^2} \quad . \tag{1.85}$$

This equation is easily solved for $\lambda(Q)$,

$$\frac{1}{\lambda(Q)} \sim \frac{1}{\lambda(\Lambda)} - \frac{3}{4\pi^2}\log\left(\frac{Q}{\Lambda}\right). \tag{1.86}$$

The requirement that the coupling, λ, be finite up to some large scale, Λ, (*i.e.* that there be no Landau pole), then gives an upper bound on the Higgs mass,

$$m_H^2 < \frac{8\pi^2 v^2}{3\log(\Lambda/m_H)} \sim \frac{8\pi^2 v^2}{3\log(\Lambda/v)} \quad . \tag{1.87}$$

This bound is the solid line in figure 1.3. If Λ goes to infinity, the Higgs boson mass goes to zero, along with λ, and so the theory becomes non-interacting or trivial.

Everything done so far is for a theory with only scalars. The physics changes when one couples the theory to fermions and gauge bosons. Since the Higgs coupling to fermions is proportional to the fermion mass, the only relevant fermion is the top quark. When we include the top quark and the gauge bosons, Eq. 1.85 becomes[12]

$$Q\frac{d\lambda}{dQ} = \frac{1}{16\pi^2}\Big[12\lambda^2 + 6\lambda(\sqrt{2}m_t/v)^2 - 3(\sqrt{2}m_t/v)^4 - \frac{3}{2}\lambda(3g^2 + g'^{\,2}) + \frac{3}{16}(2g^4 + (g^2 + g'^{\,2})^2)\Big] \tag{1.88}$$

where g and g' are the $SU(2)_L$ and $U(1)$ coupling constants, respectively. The important physics point is the opposite signs between the various terms. For a heavy Higgs boson , $\lambda > \sqrt{2}m_t/v, g, g'$, and

$$\frac{d\lambda}{dQ} \sim \frac{\lambda}{16\pi^2}\Big[12\lambda + 6(\sqrt{2}m_t/v)^2 - \frac{3}{2}(3g^2 + g'^{\,2})\Big]. \tag{1.89}$$

There is a critical value of λ which depends on the top quark mass,

$$\lambda_c \equiv \frac{1}{8}(3g^2 + g'^{\,2}) - \frac{(\sqrt{2}m_t/v)^2}{2} \tag{1.90}$$

for which there is no evolution of the scalar coupling constant [14]. If $m_H > m_H^c \equiv \sqrt{2\lambda_c}v$ then the quartic coupling blows up and the theory is non-perturbative. If we require that the theory be perturbative (i.e., the Higgs quartic coupling be finite) at all energy scales below some unification scale ($\sim 10^{16}$ GeV) then an upper bound on the Higgs mass is obtained as a function of the top quark mass. If a Higgs boson were found which was heavier than this bound, it would require that there be some new physics below the unification scale. We see that the inclusion of the top quark into the evolution equations for the scalar coupling has changed the bounds on the Higgs mass considerably.

1.3.1.3 Vacuum stability

Another limit for the quartic coupling also gives an interesting limit on the Higgs boson mass. For small λ, the evolution with energy is

$$Q\frac{d\lambda}{dQ} \sim \frac{1}{16\pi^2}\Big[\frac{3}{4}(g^4 + 2g^2g'^2 + 3g'^4) - 12(\frac{m_t}{v})^4\Big] \quad , \tag{1.91}$$

The large value of the top quark mass tends to drive the quartic coupling negative, thus destabilizing the potential. Eq. 1.91 can be solved for $\lambda(Q)$,

$$\lambda(Q) \sim \lambda(\Lambda) + \frac{\frac{3}{4}(g^4 + 2g^2g'^2 + 3g'^4) - 12\frac{m_t}{v}^4}{16\pi^2}\log\Big(\frac{Q}{\Lambda}\Big) \quad . \tag{1.92}$$

The requirement that the quartic coupling be always positive yields a lower bound on the Higgs boson mass,[15]

$$m_H^2 > \frac{v^2}{8\pi^2}(12\frac{m_t}{v}^4 - \frac{3}{4}(g^4 + 2g^2g'^2 + 3g'^4))\log\Big(\frac{\Lambda}{m_H}\Big) \quad . \tag{1.93}$$

This bound is the dot-dashed curve of figure 1.3. Including the 2-loop evolution of all couplings and summing the large logarithms gives a lower bound on the Higgs mass slightly below that of Eq. 1.93.

The two bounds on the Higgs boson mass from the scale dependence of the potential are shown in figure 1.3 For any given scale Λ, the allowed region for the Higgs boson mass is quite restricted. For example, if there is no new physics beyond that of the Standard Model before the Planck scale, the allowed range is roughly,

$$70\ GeV < m_H < 170\ GeV \tag{1.94}$$

which is the *intermediate mass Higgs boson range.*

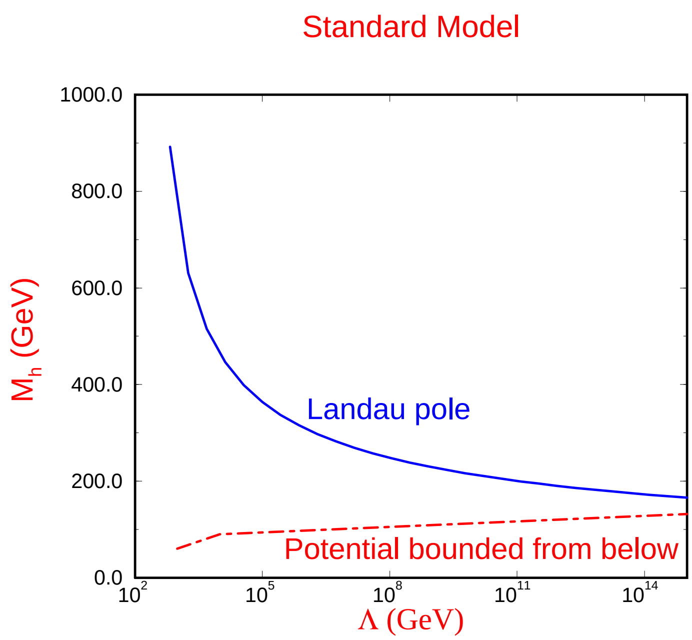

Figure 1.3: *Theoretically allowed mass region for the Higgs boson as a function of the scale of new physics, Λ. The region above the solid line is forbidden because the quartic coupling, $\lambda(\Lambda)$, has a Landau pole. The region below the dot-dashed line is forbidden because the scalar potential is unbounded from below, $\lambda(\Lambda) < 0$.*

1.3.1.4 Estimation of Higgs mass from electroweak data

Indirect evidence for a light Higgs boson comes from the precision measurements at LEP and elsewhere [19]. Indeed, the fact that the SM is renormalizable only after including the top and Higgs particle in the loop corrections, shows that the electroweak observables should be sensitive to these particle masses.

The QED coupling at the Z boson mass scale plays an important role in the prediction of m_H. This fact has stimulated a lot of activity on the exact determination of $(\Delta\alpha)_h$, which is the five-flavour hadronic contribution to the QED vacuum polarization at $q^2 = m_Z^2$. The most phenomenological analyses rely on the use of all the available experimental data on the hadron production in $e^+ e^-$ annihilation and on perturbative QCD (pQCD). In this approach the perturbative QCD computations are used only in the high energy tail ($E \geq 40$ GeV) of dispersion integral. The reference value in this approach is

$$(\Delta\alpha)_h^{EJ} = 0.02804 \pm 0.00065 \ . \tag{1.95}$$

In the recent past the hadronic contribution to the vacuum polarization has been the subject of several new investigations that advocate the use of pQCD computation down to an energy scale of the order of 1 GeV. In this theory , the various analyses differ on the energy value at which to start applying pQCD and on the amount of theoretical inputs used to evaluate the experimental data. The common characteristic of these studies with respect to the most phenomenological ones is to obtain a smaller central value for $(\Delta\alpha)_h$ with a reduced uncertainty. The most stringent result of these analyses is

$$(\Delta\alpha)_h^{DH} = 0.02784 \pm 0.00026 \tag{1.96}$$

At the moment there is no definite argument for choosing one or other of the two approaches. The results are absolutely compatible with each other. However, the numerical difference between central values and uncertainties is such that it prevents an easy estimation of the effect of choosing one value instead of the other. For these reasons the results are presented for the values of $(\Delta\alpha)_h$ given by $(\Delta\alpha)_h^{EJ}$ and $(\Delta\alpha)_h^{DH}$ separately as can be seen in figure 1.4.

1.3.2 Higgs branching ratios

1.3.2.1 Decays to fermion pairs

The dominant decays of the intermediate mass Higgs boson are into fermion- antifermion pairs. In the Born approximation, the width into charged lepton pairs is

$$\Gamma(H \to l^+l^-) = \frac{G_F m_l^2}{4\sqrt{2}\pi} m_H \beta_l^3 \quad , \tag{1.97}$$

where $\beta_l \equiv \sqrt{1 - 4m_l^2/m_H^2}$ is the velocity of the final state leptons. The Higgs boson decay into quarks is enhanced by the color factor $N_c = 3$ and also receives significant QCD corrections,

$$\Gamma(H \to q\overline{q}) = \frac{3G_F m_q^2}{4\sqrt{2}\pi} m_H \beta_q^3 \left(1 + \frac{4}{3}\frac{\alpha_s}{\pi}\Delta_h^{QCD}\right) \quad , \tag{1.98}$$

where the QCD correction factor, Δ_h^{QCD}, can be found in [16].

For the intermediate mass Higgs boson, the $\mathcal{O}(\alpha_s)$ corrections decrease the decay width for $H \to b\overline{b}$ by about a factor of 2.

The electroweak radiative corrections to $H \to q\overline{q}$ are not significant and amount to only a few percent [17]. These can be neglected in comparison with the dominant QCD corrections.

The branching ratios for the dominant decays to fermion- antifermion pairs are shown in figure 1.5. The decrease in the $H \to f\overline{f}$ branching ratios at $m_H \sim 150\ GeV$ is due to the turn-on of the WW^* decay channel. For most of the region below the W^+W^- threshold, the Higgs decays almost entirely to $b\overline{b}$ pairs.

1.3.2.2 Decays to gauge boson pairs

The decay of the Higgs boson to gluons arises through fermion loops,[18]

$$\Gamma_0(H \to gg) = \frac{G_F \alpha_s^2 m_H^3}{64\sqrt{2}\pi^3} \mid \sum_q F_{1/2}(\tau_q) \mid^2 \tag{1.99}$$

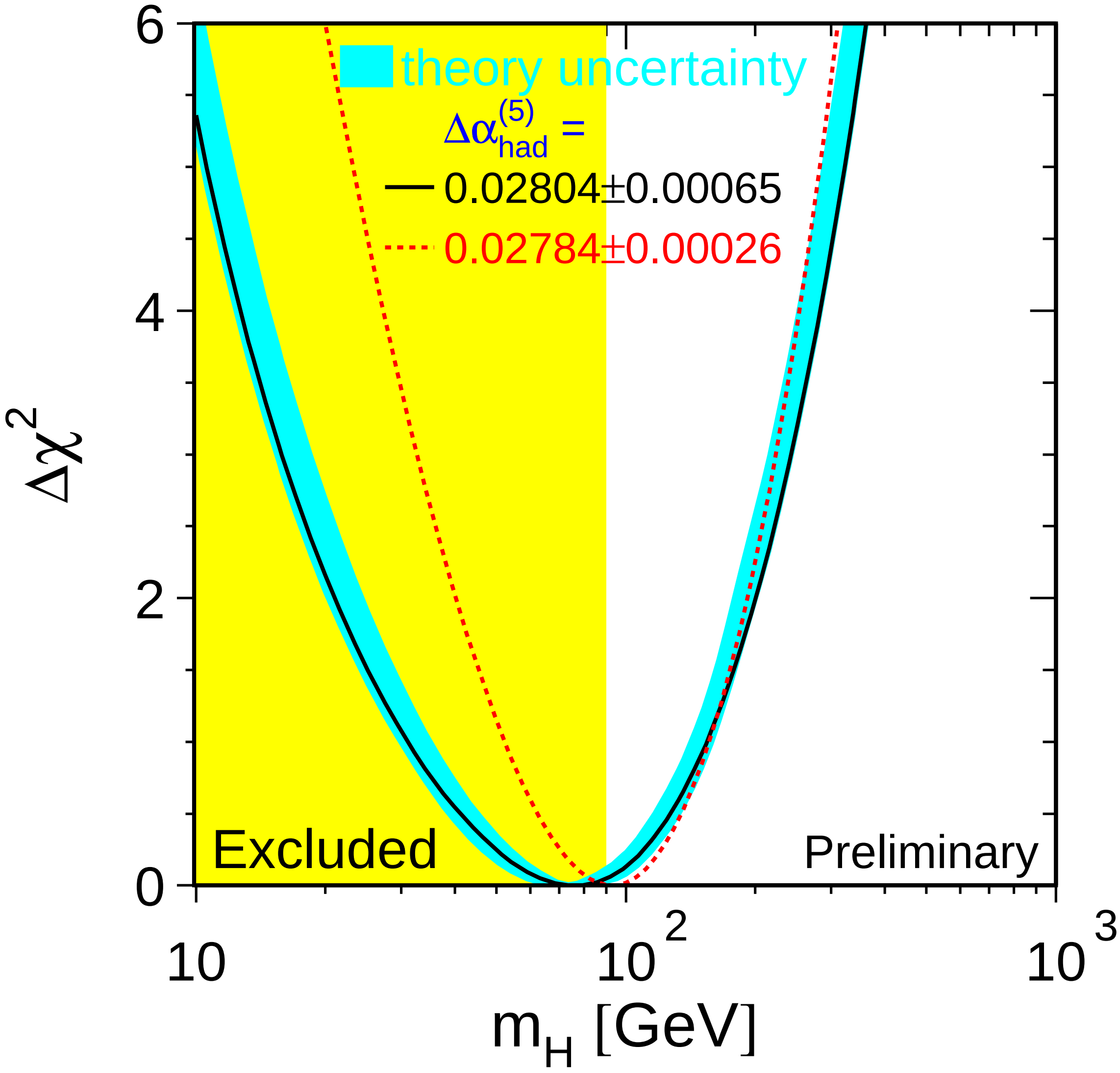

Figure 1.4: *$\Delta\chi^2 = \chi^2 - \chi^2_{min}$ versus m_H. The lines are the results of the fit using all data and the two different values of $(\Delta\alpha)_h$; the band represents an estimate of the theoretical error due to missing higher order corrections. The shadow band shows the 95% CL exclusion limit on m_H from direct searches.*

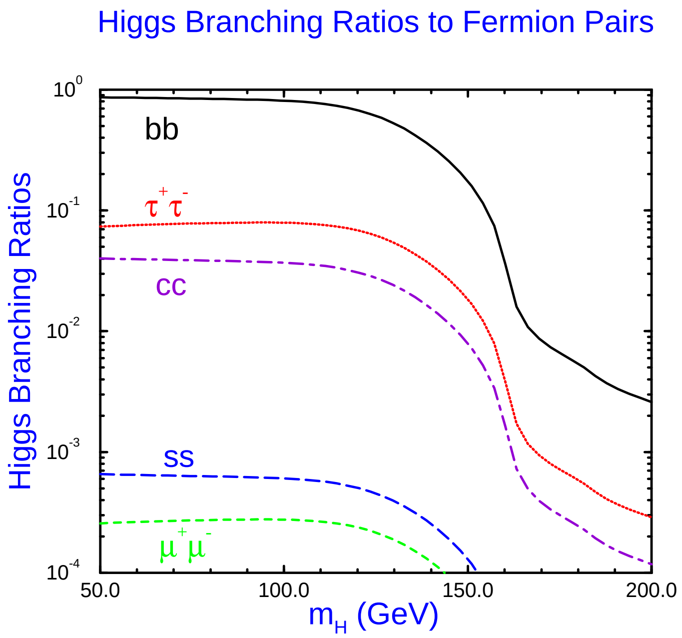

Figure 1.5: *Branching ratios of the Standard Model Higgs boson to fermion-antifermion pairs, including QCD radiative corrections.*

where $\tau_q \equiv 4m_q^2/m_H^2$ and $F_{1/2}(\tau_q)$ is defined by:

$$F_{1/2}(\tau_q) \equiv -2\tau_q \Big[1 + (1 - \tau_q) f(\tau_q)\Big] \quad . \tag{1.100}$$

The function $f(\tau_q)$ is given by:

$$f(\tau_q) = \begin{cases} \left[\sin^{-1}\left(\sqrt{1/\tau_q}\right)\right]^2, & \text{if } \tau_q \geq 1 \\ -\frac{1}{4}\left[\log\left(\frac{x_+}{x_-}\right) - i\pi\right]^2, & \text{if } \tau_q < 1, \end{cases} \tag{1.101}$$

with

$$x_\pm = 1 \pm \sqrt{1 - \tau_q}. \tag{1.102}$$

In the limit in which the quark mass is much less than the Higgs boson mass,

$$F_{1/2} \rightarrow \frac{2m_q^2}{m_H^2} \log^2\left(\frac{m_q}{m_H}\right). \tag{1.103}$$

On the other hand, for a heavy quark, $\tau_q \rightarrow \infty$, and $F_{1/2}(\tau_q)$ approaches a constant,

$$F_{1/2} \rightarrow -\frac{4}{3}. \tag{1.104}$$

It is clear that the dominant contribution to the gluonic decay of the Higgs boson is from the top quark loop.

The intermediate mass Higgs boson can also decay to vector boson pairs VV^*, ($V = W^\pm, Z$), with one of the gauge bosons off-shell. The widths, summed over all available channels for $V^* \to f\overline{f}$ are: [20]

$$\begin{aligned}\Gamma(H\to ZZ^*) &= \frac{g^4 m_H}{2048(1-x_W)^2\pi^3}\Big(7-\frac{40}{3}x_W+\frac{160}{9}x_W^2\Big)F\Big(\frac{m_Z}{m_H}\Big)\\ \Gamma(H\to WW^*) &= \frac{3g^4 m_H}{512\pi^3}F\Big(\frac{m_W}{m_H}\Big)\end{aligned} \tag{1.105}$$

where $x_W \equiv \sin^2\theta_W$ and

$$\begin{aligned}F(x) \;\equiv\; & -\mid 1-x^2\mid\Big(\frac{47}{2}x^2-\frac{13}{2}+\frac{1}{x^2}\Big)-3\Big(1-6x^2+4x^4\Big)\mid\ln(x)\mid\\ & +3\frac{1-8x^2+20x^4}{\sqrt{4x^2-1}}\cos^{-1}\Big(\frac{3x^2-1}{2x^3}\Big)\quad .\end{aligned} \tag{1.106}$$

These widths can be significant when the Higgs boson mass approaches the real W^+W^- and ZZ thresholds, as can be seen in figure 1.6. The WW^* and ZZ^* branching ratios grow rapidly with increasing Higgs mass and above $2m_W$, the rate for $H\to W^+W^-$ is close to 1. The decay to ZZ^* is roughly an order of magnitude smaller than the decay to WW^* over much of the intermediate mass Higgs range due to the smallness of the neutral current couplings as compared to the charged current couplings.

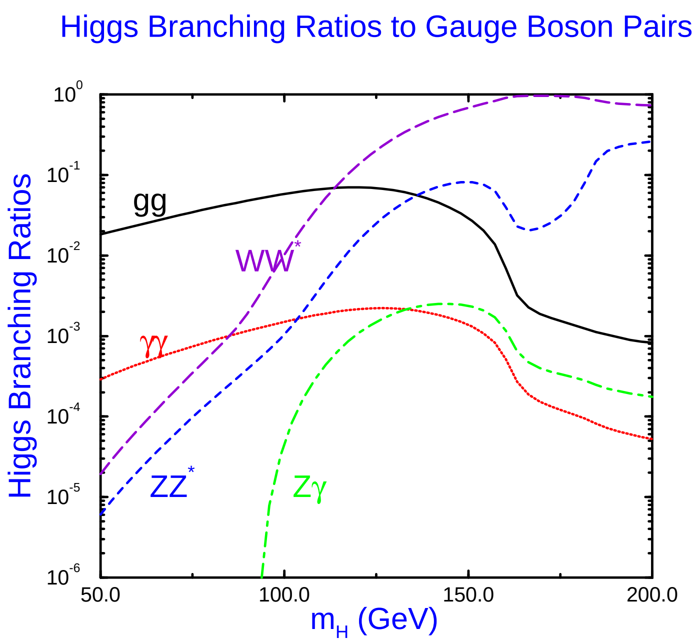

Figure 1.6: *Branching ratios of the Standard Model Higgs boson to gauge boson pairs. The rates to WW^* and ZZ^* must be multiplied by the appropriate branching ratios for W^* and Z^* decays to $f\overline{f}$ pairs.*

The decay $H \rightarrow \gamma\gamma$ is an important mode for the Higgs search at the LHC, since the hadronic decays suffer of high backgrounds. At lowest order, the branching ratio is, [21]

$$\Gamma(H \rightarrow \gamma\gamma) = \frac{\alpha^2 G_F}{128\sqrt{2}\pi^3} m_H^3 \mid \sum_i N_{ci} Q_i^2 F_i(\tau_i) \mid^2 \tag{1.107}$$

where the sum is over fermions and $W^{\pm}$ bosons with $F_{1/2}(\tau_q)$ given in equation 1.100, and

$$F_W(\tau_W) = 2 + 3\tau_W[1 + (2 - \tau_W) f(\tau_W)] \quad . \tag{1.108}$$

$\tau_W = 4m_W^2/m_H^2$, $N_{Ci} = 3$ for quarks and 1 otherwise, and Q_i is the electric charge in units of e. The function $f(\tau_q)$ is given in Eq. 1.101. The $H \rightarrow \gamma\gamma$ decay channel clearly probes the possible existence of heavy charged particles. (Charged scalars, such as those existing in SUSY models, would also contribute to the rate)[18].

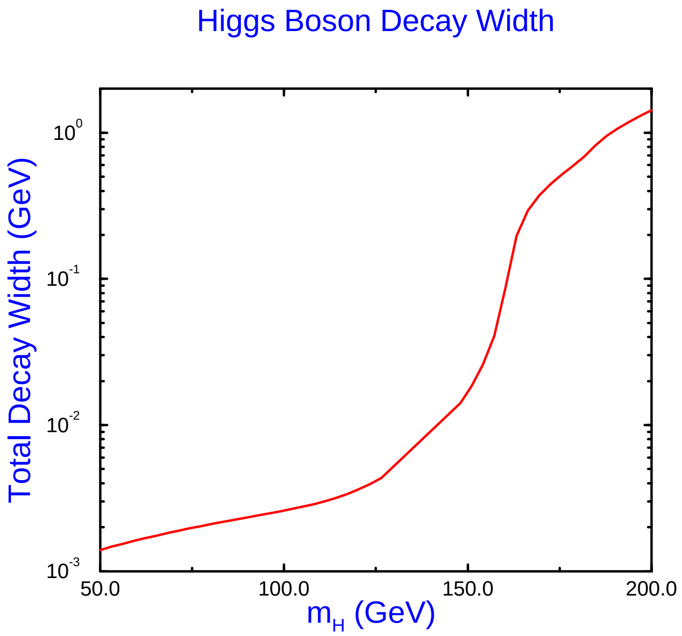

Figure 1.7: *Total Higgs boson decay width in the Standard Model, including QCD radiative corrections.*

The $H \rightarrow \gamma\gamma$ branching ratio is the dotted line in figure 1.6.

The total width for the intermediate mass Higgs boson is shown in figure 1.7. Below $m_H \sim 150\ GeV$, the Higgs boson is quite narrow with $\Gamma_H < 10\ MeV$. As the WW^* and ZZ^* channels become accessible, the width increases rapidly with $\Gamma_H \sim 1\ GeV$ at $m_H \sim 200\ GeV$.

1.3.3 Higgs production in e^+e^- collisions

Since the analysis I porsued is based on data collected at LEP, I review the production mechanism in e^+e^- collisions

1.3.3.1 $e^+e^- \rightarrow ZH$

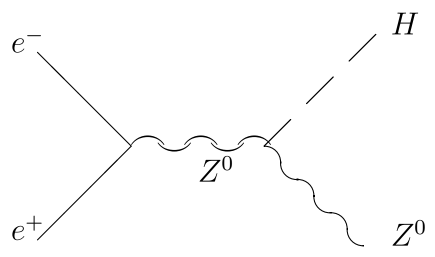

Figure 1.8: *Higgs-strahlung process*

At LEPII, the primary production mechanism for the Standard Model Higgs boson is $e^+e^- \rightarrow ZH$ (see figure 1.8), in which a physical Z boson is produced [22]. The cross section is (see figure 1.9),

$$\hat{\sigma}(e^+e^- \rightarrow HZ) = \frac{\pi\alpha^2\lambda_{ZH}^{1/2}[\lambda_{ZH} + 12\frac{m_Z^2}{s}][1 + (1 - 4\sin^2\theta_W)^2]}{192 s \sin^4\theta_W \cos^4\theta_W (1 - m_Z^2/s)^2} \tag{1.109}$$

where

$$\lambda_{ZH} \equiv (1 - \frac{m_H^2 + m_Z^2}{s})^2 - \frac{4m_H^2 m_Z^2}{s} \tag{1.110}$$

The electroweak radiative corrections are quite small at LEPII energies [17]. Photon bremsstrahlung can be important however since it is enhanced by a large logarithm, $\log(s/m_e^2)$. Photon radiation significantly reduces the ZH production rate from the Born cross section as shown in figure 1.10.

1.3.3.2 Higgs production in vector boson fusion, $VV \rightarrow H$

In e^+e^- collisions the Higgs boson can also be produced by W^+W^- fusion,[18, 23]

$$e^+e^- \rightarrow W^+W^-\nu\overline{\nu} \rightarrow H\nu\overline{\nu}, \tag{1.111}$$

and by ZZ fusion (see figure 1.11),

$$e^+e^- \rightarrow ZZe^+e^- \rightarrow He^+e^-. \tag{1.112}$$

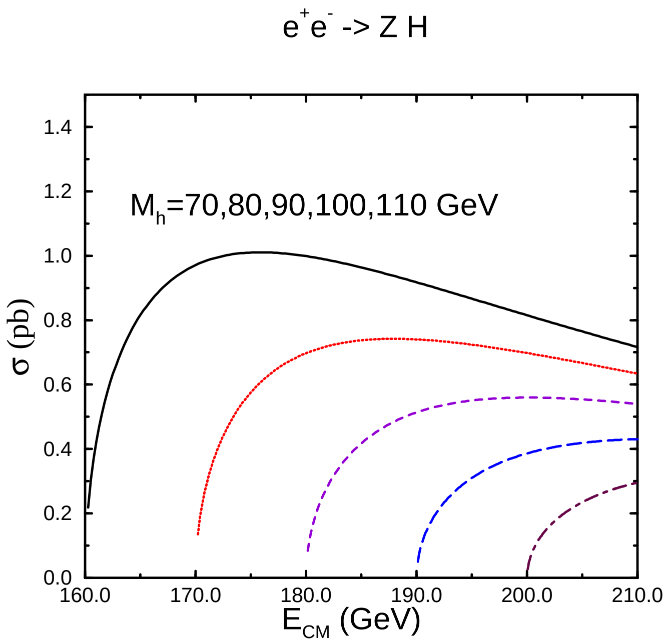

Figure 1.9: *Born cross section for $e^+e^- \to ZH$ as a function of the center of mass energy, E_{CM}, and for various values of the Higgs boson mass.*

The fusion cross sections are found, [24]

$$\sigma_{VVh} = \frac{G_F^3 m_V^4}{64\sqrt{2}\pi^3} \int_{\frac{m_H^2}{s}}^1 dx \int_x^1 \frac{dy}{(1+s(y-x)/M_V^2)^2} \Big((v^2+a^2)^2 f(x,y) + 4v^2a^2 g(x,y) \Big) \tag{1.113}$$

where,

$$\begin{aligned} f(x,y) &= \left(\frac{2x}{y^3} - \frac{1+2x}{y^2} + \frac{2+x}{2y} - \frac{1}{2}\right)\left(\frac{w}{1+w} - \log(1+w)\right) + \frac{x}{y^2}\frac{w^2(1-y)}{1+w} \\ g(x,y) &= \left(-\frac{x}{y^2} + \frac{2+x}{2y} - \frac{1}{2}\right)\left(\frac{w}{1+w} - \log(1+w)\right) \\ w &\equiv \frac{y(sx - m_H^2)}{m_V^2 x} \end{aligned} \tag{1.114}$$

and $v = a = \sqrt{2}$ for $e^+e^- \to W^+W^-\nu\overline{\nu} \to \nu\overline{\nu}H$ and $v = -1 + 4\sin^2\theta_W,\ a = -1$ for $e^+e^- \to ZZe^+e^- \to e^+e^-H$.

The ZZ fusion cross section is an order of magnitude smaller than the W^+W^- fusion process due to the smaller neutral current couplings.

The size of the various contributions to the cross section for the final state $e^+e^- \to H\nu\nu$ is shown in figure 1.12: the interference term between different contributions is also taken into account.

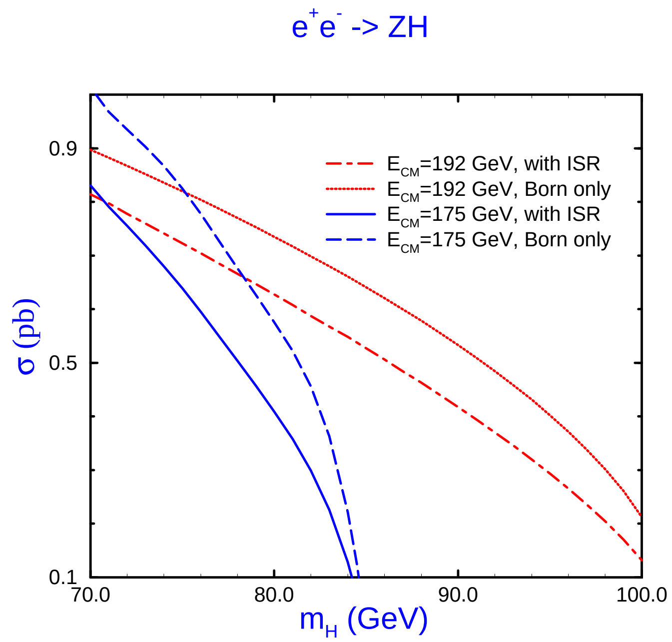

Figure 1.10: *Effects of initial state radiation(ISR) on the process $e^+e^- \to ZH$. The curves labelled "Born only" do not include the photon radiation while those labelled "with ISR" include it.*

Figure 1.11: *Fusion processes*

1.4 Why the Supersymmetry?

The Standard Model has been confirmed by experiemental measurements to a precision which arrives in some cases to the order of 0.1 %. In the present data there is no significant evidence for departures from the Standard Model, no convincing hint of new physics comes from precise measurements neither from search analysis. In such situation, why new theories should be advocated? The argument against the simplest version of the Standard Model is theoretical and arises when radiative corrections to the Higgs boson mass are computed. At one loop, the quartic self-interactions of the Higgs boson generate a quadratically divergent contribution to the Higgs boson mass

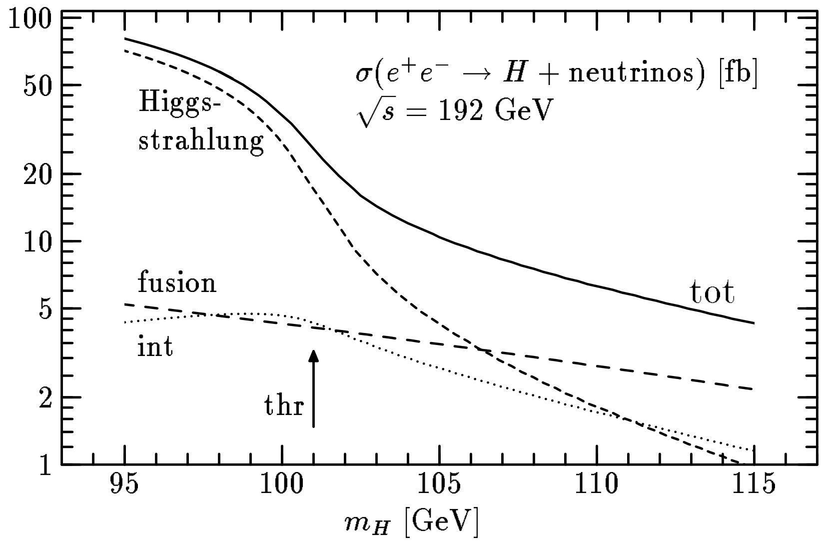

Figure 1.12: *Higgs-strahlung (dashed) and WW fusion (long-dashed) processes for Higgs production (without radiative corrections). The solid line shows the total cross section including (dotted line) the interference term.*

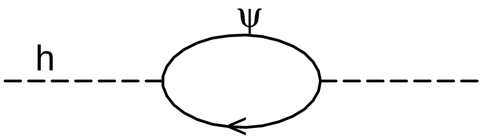

Figure 1.13: *Higgs mass renormalization from a fermion loop.*

which must be cancelled by a mass counterterm. This counterterm must be fine tuned at each order in perturbation theory. The quadratic growth of the Higgs boson mass beyond tree level in perturbation theory is one of the driving motivations behind the introduction of supersymmetry, which cures this problem.

In the following there will be a brief description of how this happens.

Consider a theory with a single fermion f ,with mass m_F , coupled (with constant λ_F)to a massive Higgs scalar with mass m_S,

$$\mathcal{L}_\phi = \overline{f}(i\gamma^\mu\partial_\mu)f + \mid \partial_\mu\phi \mid^2 - m_S^2 \mid \phi \mid^2 - \left(\frac{\lambda_F}{2}\overline{f}f\phi + \text{h.c.}\right) \quad . \tag{1.115}$$

Assume that this lagrangian leads to spontaneous symmetry breaking and so $\phi = (H+v)/\sqrt{2}$, with H the physical Higgs boson. Consider the renormalization of the scalar mass from a fermion loop (figure 1.13)

$$-i\Sigma_S(p^2) = \left(\frac{-i\lambda_F}{\sqrt{2}}\right)^2 (i)^2(-1) \int \frac{d^4k}{(2\pi)^4} \frac{Tr[(k+m_F)((k-p)+m_F)]}{(k^2-m_F^2)[(k-p)^2-m_F^2]} \quad . \tag{1.116}$$

Integrating with a momentum space cutoff Λ we find the contribution to the Higgs mass, $(\delta m_H^2)_a \equiv \Sigma_S(m_S^2)$,

$$\begin{aligned}(\delta m_H^2)_a &= -\frac{\lambda_F^2}{8\pi^2}\Big[\Lambda^2 + (m_S^2 - 6m_F^2)\log\Big(\frac{\Lambda}{m_F}\Big) \\ &\quad +(2m_F^2 - \frac{m_S^2}{2})\Big(1 + I_1\Big(\frac{m_S^2}{m_F^2}\Big)\Big)\Big] + \mathcal{O}\Big(\frac{1}{\Lambda^2}\Big),\end{aligned} \tag{1.117}$$

where $I_1(a) \equiv \int_0^1 dx \log(1 - ax(1-x))$. The Higgs boson mass diverges quadratically.

In the Standard Model, the physical Higgs boson mass, m_H, must be less than around 1 TeV (as has been shown in section 1.2.3), we have the result,

$$m_H^2 = m_{H,0}^2 + \delta m_H^2 + \text{counterterm}, \tag{1.118}$$

where the counterterm must be adjusted to a precision of 1 part in 10^{15} in order to cancel the quadratically divergent contributions to δm_H^2. This adjustment must be made at each order in perturbation theory. This is known as the *hierarchy problem*.

The quadratic divergence can be renormalized by adjusting the cut-off. There is nothing formally wrong with this fine tuning. Most theorists, however, regard this solution as unattractive. On the other hand, the problem of quadratic divergence arises only when one attempts to import a physical significance to the cut-off Λ.

Let us see which is the effect of scalar particles on the Higgs mass renormalization. We introduce two complex scalar fields, ϕ_1 and ϕ_2 with masses m_{s1} and m_{s2}, interacting with the Standard Model Higgs boson, H,

$$\begin{aligned}\mathcal{L} &= \mid \partial_\mu\phi_1 \mid^2 + \mid \partial_\mu\phi_2 \mid^2 - m_{s_1}^2 \mid \phi_1 \mid^2 - m_{s_2}^2 \mid \phi_2 \mid^2 \\ &\quad +\lambda_S \mid \phi \mid^2 \Big(\mid \phi_1 \mid^2 + \mid \phi_1 \mid^2 \Big) + \mathcal{L}_\phi \quad .\end{aligned} \tag{1.119}$$

From the diagram of figure 1.14, we find the contribution to the Higgs mass renormalization,

$$\begin{aligned}(\delta m_H^2)_b &= -\lambda_S \int \frac{d^4k}{(2\pi)^4}\Big[\frac{i}{k^2 - m_{s_1}^2} + \frac{i}{k^2 - m_{s_2}^2}\Big] \\ &= \frac{\lambda_S}{16\pi^2}\Big\{2\Lambda^2 - 2m_{s_1}^2\log\Big(\frac{\Lambda}{m_{s_1}}\Big) - 2m_{s_2}^2\log\Big(\frac{\Lambda}{m_{s_2}}\Big)\Big\} \\ &\quad +\mathcal{O}\Big(\frac{1}{\Lambda^2}\Big).\end{aligned} \tag{1.120}$$

From Eqs. 1.117 and 1.120, we see that if

$$\lambda_S = \lambda_F^2, \tag{1.121}$$

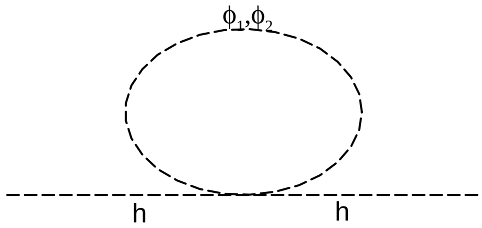

Figure 1.14: *Higgs mass renormalization from scalar loops.*

the quadratic divergences coming from these two terms cancel each other. The cancellation occurs independent of the masses, m_F and m_{s_i}, and of the magnitude of the couplings λ_S and λ_F.

In the Standard Model, one could attempt to cancel the quadratic divergences in the Higgs boson mass by balancing the contribution from the Standard Model Higgs quartic coupling with that from the top quark loop in exactly the same manner as above. This approach would give a prediction for the Higgs boson mass in terms of the top quark mass. However, since there is no symmetry to enforce this relationship, this attempt to cancel quadratic divergences must fail at 2− loops.

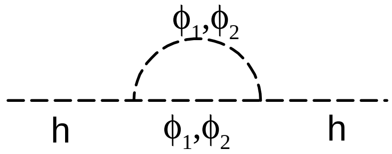

Figure 1.15: *Higgs mass renormalization from scalar loops.*

After the spontaneous symmetry breaking, Eq. 1.119 also leads to a cubic interaction shown in figure 1.15. These graphs give a contribution to the Higgs mass renormalization, although they are not quadratically divergent.

$$\begin{aligned}(\delta m_H^2)_c &= \frac{\lambda_S^2 v^2}{16\pi^2}\left\{-1+2\log\left(\frac{\Lambda}{m_{s_1}}\right)-I_1\left(\frac{m_H^2}{m_{s_1}^2}\right)\right\} \\ &+ \frac{\lambda_S^2 v^2}{16\pi^2}\left\{-1+2\log\left(\frac{\Lambda}{m_{s_2}}\right)-I_1\left(\frac{m_H^2}{m_{s_2}^2}\right)\right\}++\mathcal{O}\left(\frac{1}{\Lambda^2}\right).\end{aligned} \tag{1.122}$$

Combining the three contributions to the Higgs mass and assuming $\lambda_S = \lambda_F^2$ and $m_{s_1} = m_{s_2}$, we find no quadratic divergences in the Higgs mass renormalization,

$$(\delta m_H^2)_{tot} = \frac{\lambda_F^2}{4\pi^2}\left\{m_{s_1}^2\log\left(\frac{\Lambda}{m_{s_1}}\right)-m_F^2\log\left(\frac{\Lambda}{m_F}\right)\right\}+\mathcal{O}\left(\frac{1}{\Lambda^2}\right). \tag{1.123}$$

If the mass splitting between the fermion and scalar is small, $\delta m^2 \equiv m_F^2 - m_{s_1}^2$, then we have the approximate result,

$$(\delta m_H^2)_{tot} = \frac{\lambda_F^2}{4\pi^2}\delta^2 \quad . \tag{1.124}$$

Therefore, as long as the mass splitting between scalars and fermions is small, no unnatural cancellations will be required and the theory can be considered natural. In this manner, a theory with nearly degenerate fermions and scalars and carefully adjusted couplings solves the hierarchy problem.

1.5 Supersymmetry

In the previous section we saw that if the fermion and scalar couplings of a theory are carefully adjusted, it is possible to cancel the quadratically divergent contributions to the Higgs boson mass. In order for this cancellation to persist to all orders in perturbation theory it must be the result of a symmetry. This symmetry is the *supersymmetry*.

Supersymmetry is a symmetry which relates the masses and couplings of particles of differing spin, (in the above example, fermions and scalars). The particles are combined into a superfield, which contains fields differing by one-half unit of spin [25]. The simplest example, the scalar superfield, contains a complex scalar, S, and a two-component Majorana fermion, ζ. (A Majorana fermion, ζ, is one which is equal to its charge conjugate, $\zeta^c = \zeta$.) The supersymmetry completely specifies the allowed interactions. In this simple case, the lagrangian is

$$\begin{aligned}\mathcal{L} &= -\partial_\mu S^* \partial^\mu S - i\overline{\zeta}\overline{\sigma}^\mu \partial_\mu \zeta - \frac{1}{2}m(\zeta\zeta + \overline{\zeta\zeta}) \\ &\quad -cS\zeta\zeta - c^* S^* \overline{\zeta\zeta} - \mid mS + cS^2 \mid^2,\end{aligned} \tag{1.125}$$

(where $\overline{\sigma}^\mu \equiv (1, -\vec{\sigma})$, $\vec{\sigma}$ are the Pauli matrices, and c is an arbitrary coupling constant.) This lagrangian is invariant (up to a total derivative) under supersymmetry transformations which take the scalar into the fermion and viceversa. The scalar self interactions of Eq. 1.125,

$$V(S, S^*) = \mid mS + cS^2 \mid^2 \tag{1.126}$$

yield a potential which is positive definite, which is a general feature of an unbroken supersymmetric theory. An unbroken supersymmetric theory has its minimum at $\langle V \rangle = 0$.

Since the scalar and fermion interactions have the same coupling, the cancellation of quadratic divergences occurs automatically, as in Eq. 1.121. This lagrangian contains both a scalar and a fermion of equal mass. Supersymmetry connects particles of differing spin, but with all other characteristics the same. That is, they have the same quantum numbers and the same mass. In other words, in a theory with unbroken supersymmetry particles in a superfield have the same masses and quantum numbers and differ by 1/2 unit of spin .

Supersymmetry must be a broken symmetry: in fact there are no candidate supersymmetric scalar partners for any of the fermions in the experimentally observed spectrum. A non-zero mass splitting between the particles of a superfield is a signal for supersymmetry breaking.

1.5.1 The Minimal supersymmetric exstension of Standard Model: MSSM

The MSSM respects the same $SU(3) \times SU(2)_L \times U(1)_Y$ gauge symmetries as does the Standard Model. The particles necessary to construct the minimal supersymmetric version of the Standard Model are shown in tables 1.5 and 1.6 in terms of the superfields, (which are denoted by a hat). Since there are no candidates for supersymmetric partners of the observed particles, we must double the entire spectrum, placing the observed particles in superfields with new postulated superpartners. There are quark and lepton superfields for all 3 generations and in table 1.5 only the members of the first generation are presented. The superfield $\hat{Q}$ thus consists of an $SU(2)_L$ doublet of quarks:

$$Q = \begin{pmatrix} u \\ d \end{pmatrix}_L \tag{1.127}$$

and their scalar partners which are also in an $SU(2)_L$ doublet,

$$\tilde{Q} = \begin{pmatrix} \tilde{u}_L \\ \tilde{d}_L \end{pmatrix} \quad . \tag{1.128}$$

Similarly, the superfield $\hat{U}^c$ ($\hat{D}^c$) contains the right-handed up (down) anti-quark, $\overline{u}_R$ ($\overline{d}_R$), and its scalar partner, $\tilde{u}_R^*$ ($\tilde{d}_R^*$). The scalar partners of the quarks are called squarks. Each quark has 2 scalar partners, one corresponding to each quark chirality. The leptons are contained in the $SU(2)_L$ doublet superfield $\hat{L}$ which contains the left-handed fermions,

$$L = \begin{pmatrix} \nu \\ e \end{pmatrix}_L \tag{1.129}$$

and their scalar partners,

$$\tilde{L} = \begin{pmatrix} \tilde{\nu}_L \\ \tilde{e}_L \end{pmatrix} \quad . \tag{1.130}$$

Finally, the right-handed anti-electron, $\overline{e}_R$, is contained in the superfield $\hat{E}^c$ and has a scalar partner $\tilde{e}_R^*$. The scalar partners of the leptons are termed sleptons.

The $SU(3) \times SU(2)_L \times U(1)_Y$ gauge fields all obtain Majorana fermion partners in a SUSY model. The $\hat{G}^a$ superfield contains the gluons, $G^{a\mu}$, and their partners the gluinos, $\tilde{g}^a$; $\hat{W}_i$ contains the $SU(2)_L$ gauge bosons, W_i^μ and their fermion partners, $\tilde{\omega}_i$ (winos); and $\hat{B}$ contains the $U(1)_Y$ gauge field, B^μ, and its fermion partner, $\tilde{b}$ (bino). The usual notation is to denote the supersymmetric partner of a fermion or gauge field with the same letter, but with a tilde over it.

Superfield	SU(3)	$SU(2)_L$	$U(1)_Y$	Particle Content
$\hat{Q}$	3	2	$\frac{1}{6}$	(u_L, d_L), $(\tilde{u}_L, \tilde{d}_L)$
$\hat{U}^c$	$\overline{3}$	1	$-\frac{2}{3}$	$\overline{u}_R$, $\tilde{u}_R^*$
$\hat{D}^c$	$\overline{3}$	1	$\frac{1}{3}$	$\overline{d}_R$, $\tilde{d}_R^*$
$\hat{L}$	1	2	$-\frac{1}{2}$	(ν_L, e_L), $(\tilde{\nu}_L, \tilde{e}_L)$
$\hat{E}^c$	1	1	1	$\overline{e}_R$, $\tilde{e}_R^*$
$\hat{H}_1$	1	2	$-\frac{1}{2}$	$(H_1, \tilde{h}_1)$
$\hat{H}_2$	1	2	$\frac{1}{2}$	$(H_2, \tilde{h}_2)$

Table 1.5: *Chiral Superfields of the MSSM*

Superfield	SU(3)	$SU(2)_L$	$U(1)_Y$	Particle Content
$\hat{G}^a$	8	1	0	G^μ, $\tilde{g}$
$\hat{W}^i$	1	3	0	W_i^μ, $\tilde{\omega}_i$
$\hat{B}$	1	1	0	B^μ, $\tilde{b}$

Table 1.6: *Vector Superfields of the MSSM*

1.5.1.1 The Higgs sector in MSSM

The Standard Model contains a single $SU(2)_L$ doublet of scalar particles. In the supersymmetric extension of the Standard Model, this scalar doublet acquires a SUSY partner which is an $SU(2)_L$ doublet of Majorana fermion fields, $\tilde{h}_1$ (the Higgsinos), which contribute to the triangle $SU(2)_L$ and $U(1)_Y$ gauge anomalies. Since the fermions of the Standard Model have exactly the right quantum numbers to cancel these anomalies, it follows that the contribution from the fermionic partner of the Higgs doublet remains uncancelled [26]. Since gauge theories cannot have anomalies, these contributions must be cancelled. The simplest way is to add a second Higgs doublet with precisely the opposite $U(1)_Y$ quantum numbers as the first Higgs doublet. In a SUSY model, this second Higgs doublet will also have fermionic partners, $\tilde{h}_2$, and the contributions of the fermion partners of the two Higgs doublets to gauge anomalies will precisely cancel each other, leaving an anomaly free theory. It is easy to check that the fermions of Table 1 satisfy the conditions for anomaly cancellation:

$$Tr(Y^3) = Tr(T_{3L}^2 Y) = 0 \quad . \tag{1.131}$$

The cancellation of quadratic divergences in the Higgs boson mass renormalization comes from the complete set of particles contained in the MSSM [27]. Now gauge bosons, gauginos, Higgs self-interactions, Higgsinos, fermions, and sfermions all contribute. The cancellation of quadratic divergences in this case uses the fact that the trace of the hypercharge generator over the particle spectrum vanishes [28]. In order not to have large contributions of the form of Eq. 1.124, SUSY particles must have masses below about 1 TeV.

We have shown in section 1.2.3 that the relation $\rho = \frac{m_W^2}{m_Z^2 \cos^2\theta_W} = 1$ and the absence of FCNC favour extension of the Standard Model with a Higgs sector made by at least two doublets and eventually singlets, and in addition in section 1.2.4 we saw how the same constraints help in writing the potential.

Using different considerations here we arrived to the conclusion that the Supersimmetry requires two doublets in the Higgs sector. Two Higgs doublets are also required in order to give both the up and down quarks masses in a SUSY theory. The requirement that there be at least 2 $SU(2)_L$ Higgs doublets is a feature of all models with weak scale supersymmetry.

Moreover, Supersymmetry imposes the following constraints on the tree-level values of the quartic couplings λ_i:

$$\begin{aligned} \lambda_1 = \lambda_2 &= \frac{1}{4}(g^2 + g'^2)\,, & \lambda_3 &= \frac{1}{4}(g^2 - g'^2)\,, \\ \lambda_4 &= -\frac{1}{2}g^2\,, & \lambda_5 = \lambda_6 &= \lambda_7 = 0\,. \end{aligned} \tag{1.132}$$

1.6 The MSSM Higgs properties

1.6.1 Higgs mass relations

Considering the relations in equations 1.132, the expressions given in sections 1.2.4.1 and 1.2.4.2 take the following form.

The squared masses for the CP-odd and charged Higgs states are

$$\begin{aligned} m_A^2 &= m_{12}^2(\tan\beta + \cot\beta)\,, \\ m_{H^\pm}^2 &= m_A^2 + m_W^2\,, \end{aligned} \tag{1.133}$$

and the tree-level neutral CP-even mass matrix is given by

$$\mathcal{M}^r = \begin{pmatrix} m_A^2 \sin^2\beta + m_Z^2\cos^2\beta & -(m_A^2 + m_Z^2)\sin\beta\cos\beta \\ -(m_A^2 + m_Z^2)\sin\beta\cos\beta & m_A^2\cos^2\beta + m_Z^2\sin^2\beta \end{pmatrix}. \tag{1.134}$$

The eigenvalues of $\mathcal{M}^r$ are the squared masses of the two CP-even Higgs scalars

$$m_{H^0,h^0}^2 = \frac{1}{2}\left(m_A^2 + m_Z^2 \pm \sqrt{(m_A^2 + m_Z^2)^2 - 4m_Z^2 m_A^2 \cos^2 2\beta}\right). \tag{1.135}$$

and the CP-even Higgs mixing angle α is determined by

$$\cos 2\alpha = -\cos 2\beta \left(\frac{m_A^2 - m_Z^2}{m_H^2 - m_h^2}\right), \qquad \sin 2\alpha = -\sin 2\beta\left(\frac{m_H^2 + m_h^2}{m_H^2 - m_h^2}\right). \tag{1.136}$$

From these results:

$$\cos^2(\beta - \alpha) = \frac{m_h^2(m_Z^2 - m_h^2)}{m_A^2(m_H^2 - m_h^2)}\,. \tag{1.137}$$

Thus, in the MSSM, two parameters (chosen to be m_A and $\tan\beta$) fix all other tree-level Higgs sector parameters.

Equation 1.135 implies the following tree-level sum rule:

$$m_h^2 + m_H^2 = m_A^2 + m_Z^2 \,. \tag{1.138}$$

In addition, a number of important mass inequalities can be derived from the expressions for the tree-level Higgs masses obtained above:

$$\begin{aligned} m_h &\leq m_A|\cos 2\beta| \leq m_A \\ m_h &\leq m_Z|\cos 2\beta| \leq m_Z \\ m_H &\geq (m_A^2 \sin^2 2\beta + m_Z^2)^{1/2} \geq m_Z \\ m_H &\geq (m_Z^2 \sin^2 2\beta + m_A^2)^{1/2} \geq m_A \\ m_{H^\pm} &\geq m_W \end{aligned} \tag{1.139}$$

Of particular note is the tree-level upper bound of the mass of the lightest CP-even Higgs boson, $m_h \leq m_Z|\cos 2\beta|$. When radiative corrections are included, the light Higgs mass upper bound may increase significantly. In the one-loop leading logarithmic approximation (assuming $m_A \gtrsim m_Z$) [29],

$$m_h^2 \lesssim m_Z^2 \cos^2\beta + \frac{3g^2 m_t^4}{8\pi^2 m_W^2} \ln\left(\frac{m_{\tilde{t}}^2}{m_t^2}\right) , \tag{1.140}$$

where $m_{\tilde{t}}$ is the (approximate) common mass of the top-squarks.

There exist in literature [30, 31] the leading one-loop and two-loop calculations. As shown in equation 1.140 the corrections depend on the spectrum of particles in the top sector and on the mixing between $\tilde{t}_L$ and $\tilde{t}_R$. The results are shown in figure 1.16.

1.6.2 Higgs branching ratios

1.6.2.1 Decays to fermion pairs

Supersymmetry imposes a particular structure on the coupling of the Higgs bosons to the fermions. In particular, one Higgs doublet (before symmetry breaking) couples exclusively to down-type fermions and the other Higgs doublet couples exclusively to up-type fermions. As a result, the charged Higgs boson coupling to fermion pairs (with all particles pointing into the vertex) is given by

$$g_{H^- t\bar{b}} = \frac{g}{2\sqrt{2}m_W} \left[m_t \cot\beta\,(1+\gamma_5) + m_b \tan\beta\,(1-\gamma_5)\right] , \tag{1.141}$$

where the effects of intergenerational mixing (which depends in the same way on the Cabibbo-Kobayashi-Maskawa mixing matrix as the weak charged current couplings) have been omitted. The neutral Higgs bosons couplings to $f\bar{f}$ are flavor diagonal, and

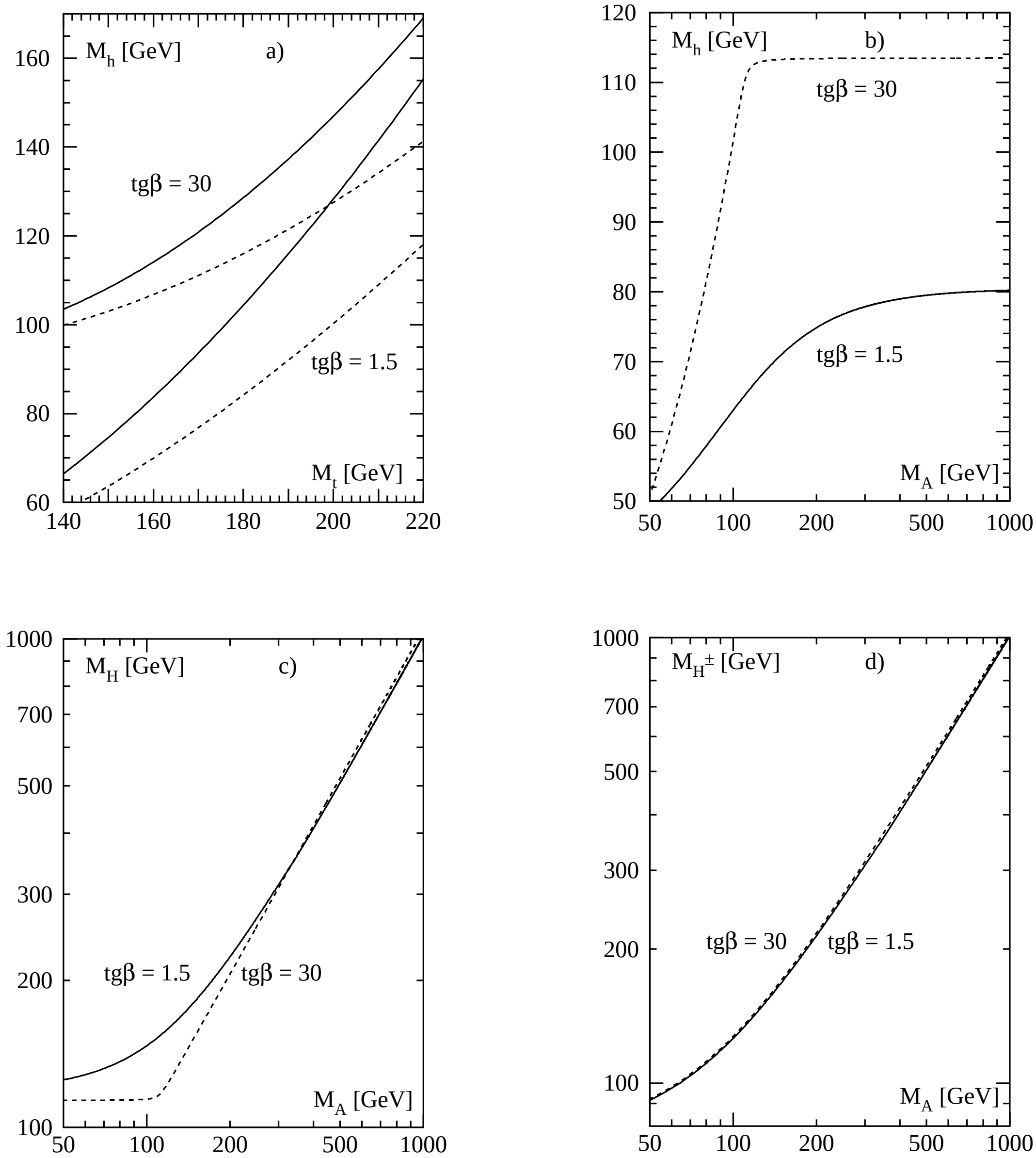

Figure 1.16: *(a) The upper limit on the light scalar Higgs pole mass in the MSSM as a function of the top quark mass for two values of* $\tan\beta = 1.5, 30$*; the common squark mass has been chosen as* $M_S = 1$ *TeV. The full lines correspond to the case of maximal mixing and the dashed lines to vanishing mixing in top sector. The pole masses of the Higgs bosons* $h, H, H^{\pm}$*, are shown as a function of the pseudoscalar Higgs* A *mass in (b–d) for two values of* $\tan\beta = 1.5, 30$ *in the vanishing mixing hypothesis.*

are listed below relative to the Standard Model values and can be seen in figures 1.17 and 1.18:

$$\begin{aligned}
hb\bar{b}: &\quad -\tfrac{\sin\alpha}{\cos\beta} &&= \sin(\beta-\alpha) - \tan\beta\cos(\beta-\alpha)\,,\\
ht\bar{t}: &\quad \tfrac{\cos\alpha}{\sin\beta} &&= \sin(\beta-\alpha) + \cot\beta\cos(\beta-\alpha)\,,\\
Hb\bar{b}: &\quad \tfrac{\cos\alpha}{\cos\beta} &&= \cos(\beta-\alpha) + \tan\beta\sin(\beta-\alpha)\,,\\
Ht\bar{t}: &\quad \tfrac{\sin\alpha}{\sin\beta} &&= \cos(\beta-\alpha) - \cot\beta\sin(\beta-\alpha)\,,\\
Ab\bar{b}: &\quad \gamma_5\tan\beta\,, &&\\
At\bar{t}: &\quad \gamma_5\cot\beta\,, &&
\end{aligned} \tag{1.142}$$

where the γ_5 indicates a pseudoscalar coupling.

All tree-level couplings discussed above are modified by radiative corrections. In a first approximation, one can consider the modifications to the couplings that arise through the renormalization of the CP-even Higgs mixing angle α. The parameter $\tan\beta$ is by assumption an input parameter. The most significant implication of this procedure is the renormalization of $\cos(\beta-\alpha)$, shown in figure 1.19, which governs many of the couplings listed above. However, this approximation clearly misses some of the radiative corrections that arise from the radiatively corrected three-point (and four-point) vertex functions. In most cases, these corrections are not expected to be large.

1.6.2.2 Decays to gauge boson pairs

The couplings of the two CP-even Higgs bosons to W and Z pairs are given by

$$\begin{aligned}
g_{hVV} &= g_V m_V \sin(\beta-\alpha)\,,\\
g_{HVV} &= g_V m_V \cos(\beta-\alpha)\,,
\end{aligned} \tag{1.143}$$

where

$$g_V \equiv \begin{array}{ll} g, & V=W,\\ g/\cos\theta_W, & V=Z. \end{array} \tag{1.144}$$

The strengths of the trilinear couplings of one gauge boson to two Higgs bosons are:

$$\begin{aligned}
g_{hAZ} &= \frac{g\cos(\beta-\alpha)}{2\cos\theta_W}\,,\\
g_{HAZ} &= \frac{-g\sin(\beta-\alpha)}{2\cos\theta_W}\,.
\end{aligned} \tag{1.145}$$

All the vector boson–Higgs boson couplings cannot vanish simultaneously. From the expressions above, we see that the following tree-level sum rules must hold separately

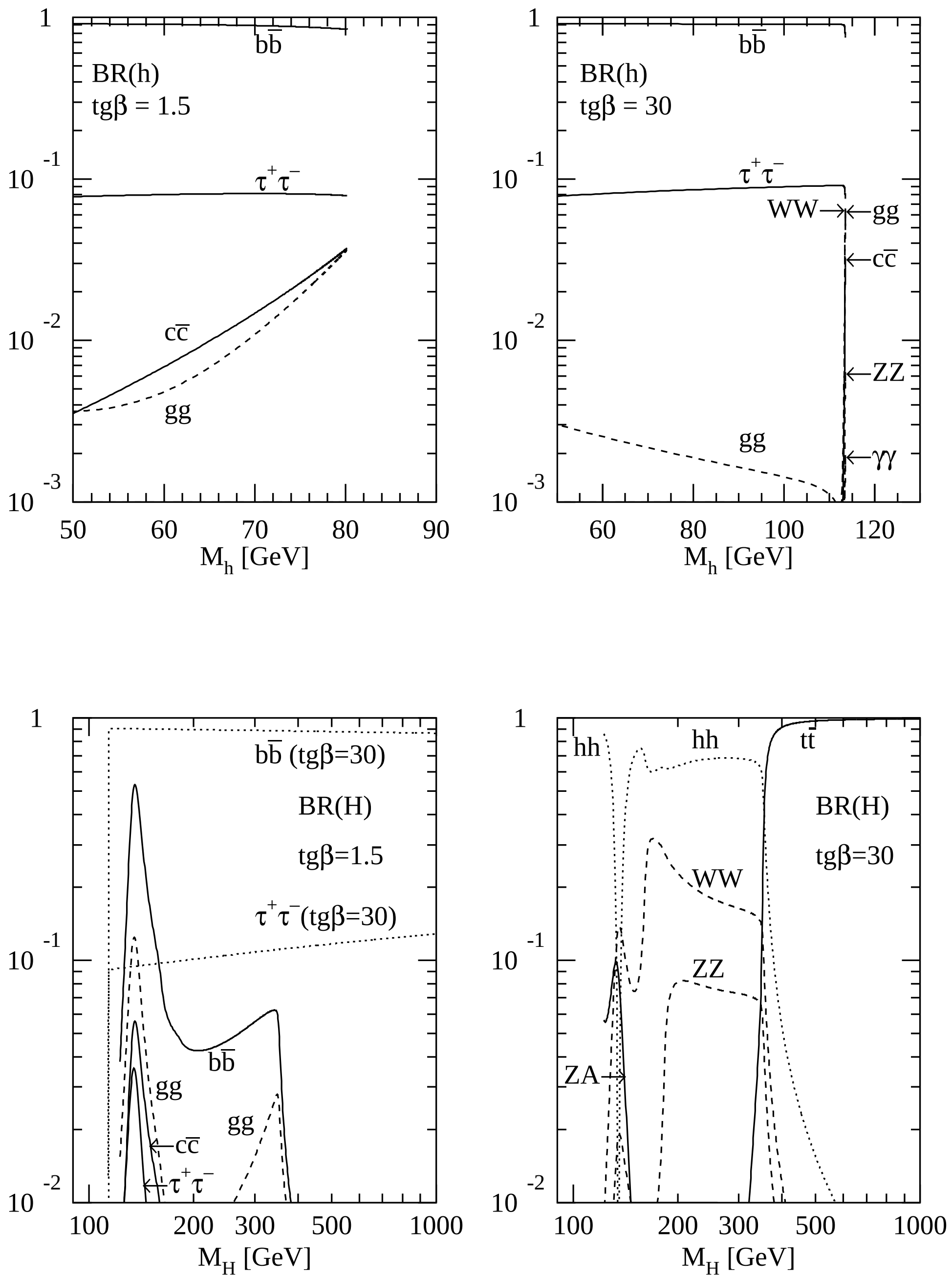

Figure 1.17: *Branching ratios of the MSSM Higgs bosons h, H for non-SUSY decay modes as a function of the masses for two values of $\tan\beta = 1.5, 30$ and vanishing mixing. The common squark mass has been chosen as $M_S = 1$ TeV.*

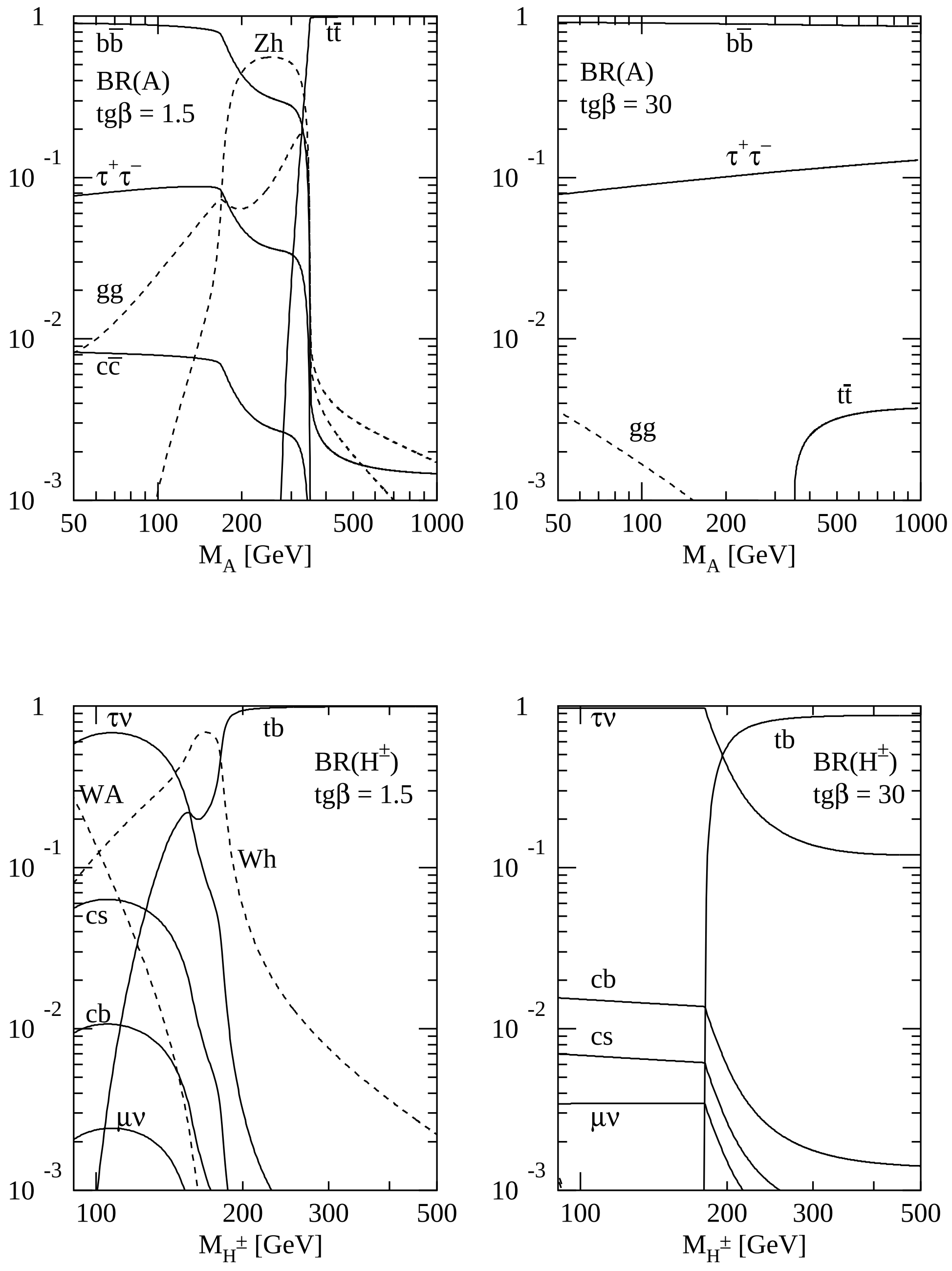

Figure 1.18: *Branching ratios of the MSSM Higgs bosons $A, H^\pm$ for non-SUSY decay modes as a function of the masses for two values of $\tan\beta = 1.5, 30$ and vanishing mixing. The common squark mass has been chosen as $M_S = 1$ TeV.*

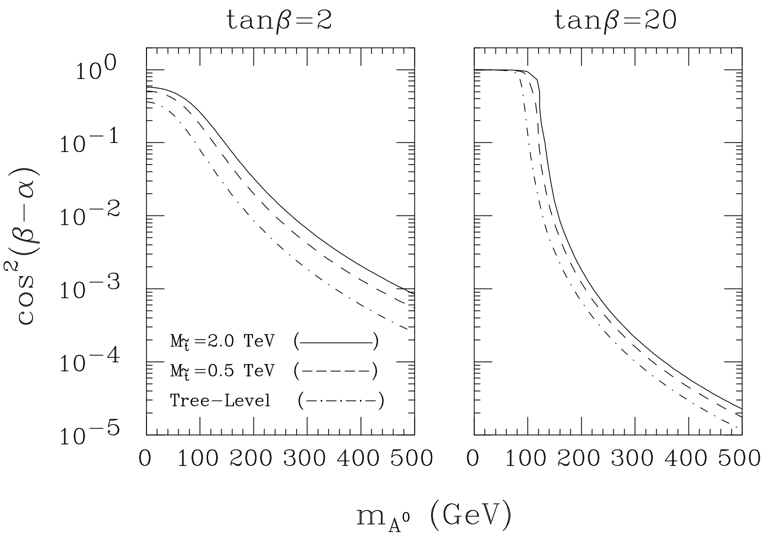

Figure 1.19: *The value of* $\cos^2(\beta-\alpha)$ *is shown as a function of* m_A *and* $\tan\beta$. *The tree-level prediction is depicted by the dot-dashed line. The solid and dashed lines include the effects of the renormalization-group-improved radiatively-corrected CP-even Higgs squared mass matrix for two different choices of the (common) top-squark mass.*

for $V = W$ and Z:

$$\begin{aligned} g^2_{HVV} + g^2_{hVV} &= g^2_V m^2_V \,, \\ g^2_{hAZ} + g^2_{HAZ} &= \frac{g^2}{4\cos^2\theta_W} \,. \end{aligned} \tag{1.146}$$

Moreover, if we focus on a given CP-even Higgs state, we note that its couplings to VV and AV cannot be simultaneously suppressed, since eqs. (1.143)–(1.145) imply that

$$g^2_{HZZ} + 4m^2_Z g^2_{HA^0Z} = \frac{g^2 m^2_Z}{\cos^2\theta_W} \,, \tag{1.147}$$

for $H = h$ or H. Similar considerations also hold for the coupling of h and H to $W^\pm H^\mp$.

We can summarize the above results by noting that the coupling of h and H to vector boson pairs or vector–scalar boson final states is proportional to either $\sin(\beta-\alpha)$ or $\cos(\beta-\alpha)$ as indicated below. These proportional factors relate the corresponding SM coupling to the MSSM ones.

See also figures 1.17 and 1.18.

1.6.3 Higgs production in e^+e^- collisions

- Neutral Higgs bosons

$\cos(\beta-\alpha)$	$\sin(\beta-\alpha)$
HW^+W^-	hW^+W^-
HZZ	hZZ
ZAh	ZAH
$W^\pm H^\mp h$	$W^\pm H^\mp H$
$ZW^\pm H^\mp h$	$ZW^\pm H^\mp H$
$\gamma W^\pm H^\mp h$	$\gamma W^\pm H^\mp H$

Table 1.7: *Couplings of MSSM Higgs bosons to gauge bosons respect to the SM couplings*

The main production mechanisms of neutral Higgs bosons are Higgs-strahlung process and associated pair production, as well as the fusion processes:

$$
\begin{array}{lll}
(a)\ \text{Higgs–strahlung:} & e^+e^- \xrightarrow{Z} & Z + h/H \\
(b)\ \text{Pair production :} & e^+e^- \xrightarrow{Z} & A + h/H \\
(c)\ \text{Fusion processes :} & e^+e^- \xrightarrow{WW} & \overline{\nu_e}\,\nu_e\ + h/H \\
 & e^+e^- \xrightarrow{ZZ} & e^+e^- + h/H
\end{array}
$$

The CP-odd Higgs boson A cannot be produced in fusion processes to leading order. The cross sections for the four Higgs-strahlung and pair production processes can be expressed as

$$
\begin{aligned}
\sigma(e^+e^- \to Z + h/H) &= \sin^2/\cos^2(\beta-\alpha)\ \sigma_{SM} \\
\sigma(e^+e^- \to A + h/H) &= \cos^2/\sin^2(\beta-\alpha)\ \bar{\lambda}\ \sigma_{SM}\ ,
\end{aligned} \tag{1.148}
$$

where σ_{SM} is the SM cross section for Higgs-strahlung and the coefficient

$$\bar{\lambda} \sim \lambda_{Aj}^{3/2}/[\lambda_{Zj}^{1/2}(12m_Z^2/s + \lambda_{Zj})] \tag{1.149}$$

with $j = h, H$ and

$$\lambda_{ij} = [1-(m_i+m_j)^2/s][1-(m_i-m_j)^2/s] \tag{1.150}$$

accounts for the suppression of the P-wave Ah/H cross sections near the threshold.

- Charged Higgs bosons
  At e^+e^- colliders the dominant process is:

$$e^+e^- \to (\gamma, Z^*) \to H^+H^-$$

The production cross sections are shown in figure 1.20

1.7 SM Higgs or MSSM Higgs?

For the Standard Model Higgs boson ($h_{\rm SM}$), at tree-level, the Higgs quartic self-coupling is related to its mass: $\lambda = m^2_{h_{\rm SM}}/2v^2$. This means that one cannot take $m_{h_{\rm SM}}$ arbitrarily large without the attendant growth in λ. That is, the heavy Higgs limit in the Standard Model exhibits non-decoupling. In the MSSM, the non-minimal Higgs boson masses can be taken large at fixed Higgs self-couplings. More generally, such behavior can arise in models that possess one (or more) off-diagonal squared-mass parameters in addition to the diagonal scalar squared-masses. When the off-diagonal squared-mass parameters are taken large, the heavy Higgs states decouple, while both light and heavy Higgs bosons remain weakly-coupled. In this decoupling limit, exactly one neutral CP-even Higgs scalar remains light, and its properties are precisely those of the (weakly-coupled) Standard Model Higgs boson. That is, $h \simeq h_{\rm SM}$, with $m_h \sim \mathcal{O}(m_Z)$, and all other non-minimal Higgs states are significantly heavier than m_h. Squared-mass splittings of the heavy Higgs states are of $\mathcal{O}(m_Z^2)$, which means that all heavy Higgs states are approximately degenerate, with mass differences of order m_Z^2/m_A (where m_A is approximately equal to the common heavy Higgs mass scale). In contrast, if the non-minimal Higgs sector is weakly coupled but far from the decoupling limit, then h is not separated in mass from the other Higgs states. In this case, the properties of h differ significantly from those of $h_{\rm SM}$.

In the MSSM, the decoupling limit corresponds to the limit of $m_A \gg m_Z$. In this case, the tree-level Higgs masses take on a particularly simple form

$$\begin{aligned}
m_h^2 &\simeq m_Z^2 \cos^2 2\beta \,, \\
m_H^2 &\simeq m_A^2 + m_Z^2 \sin^2 2\beta \,, \\
m_{H^\pm}^2 &= m_A^2 + m_W^2 \,, \\
\cos^2(\beta - \alpha) &\simeq \tfrac{m_Z^4 \sin^2 4\beta}{4m_A^4} \,.
\end{aligned} \tag{1.151}$$

A number of consequences are immediately apparent. First, $m_A \simeq m_H \simeq m_{H^\pm}$, up to corrections of $\mathcal{O}(m_Z^2/m_A)$. Second, $\cos(\beta-\alpha) \simeq 0$ up to corrections of $\mathcal{O}(m_Z^2/m_A^2)$. One can also check that when $\cos(\beta-\alpha) = 0$, the h couplings to vector boson pairs and fermion pairs, and the $(h)^3$ and $(h)^4$ self-couplings all reduce to the corresponding Standard Model couplings of $h_{\rm SM}$.

It may happen that the first Higgs state to be discovered will be experimentally indistinguishable from the Standard Model Higgs boson. This occurs in many theoretical models that exhibit the decoupling of heavy scalar states. As noted above, in the decoupling limit the lightest Higgs state, h, is a neutral CP-even scalar with properties nearly identical to those of the $h_{\rm SM}$.

The channel exploited in this thesis is: $e^+e^- \to h\nu\nu$ and, from what has been shown, the h particlex can be the Standard Higgs boson h_{SM}, or the lightest MSSM h.

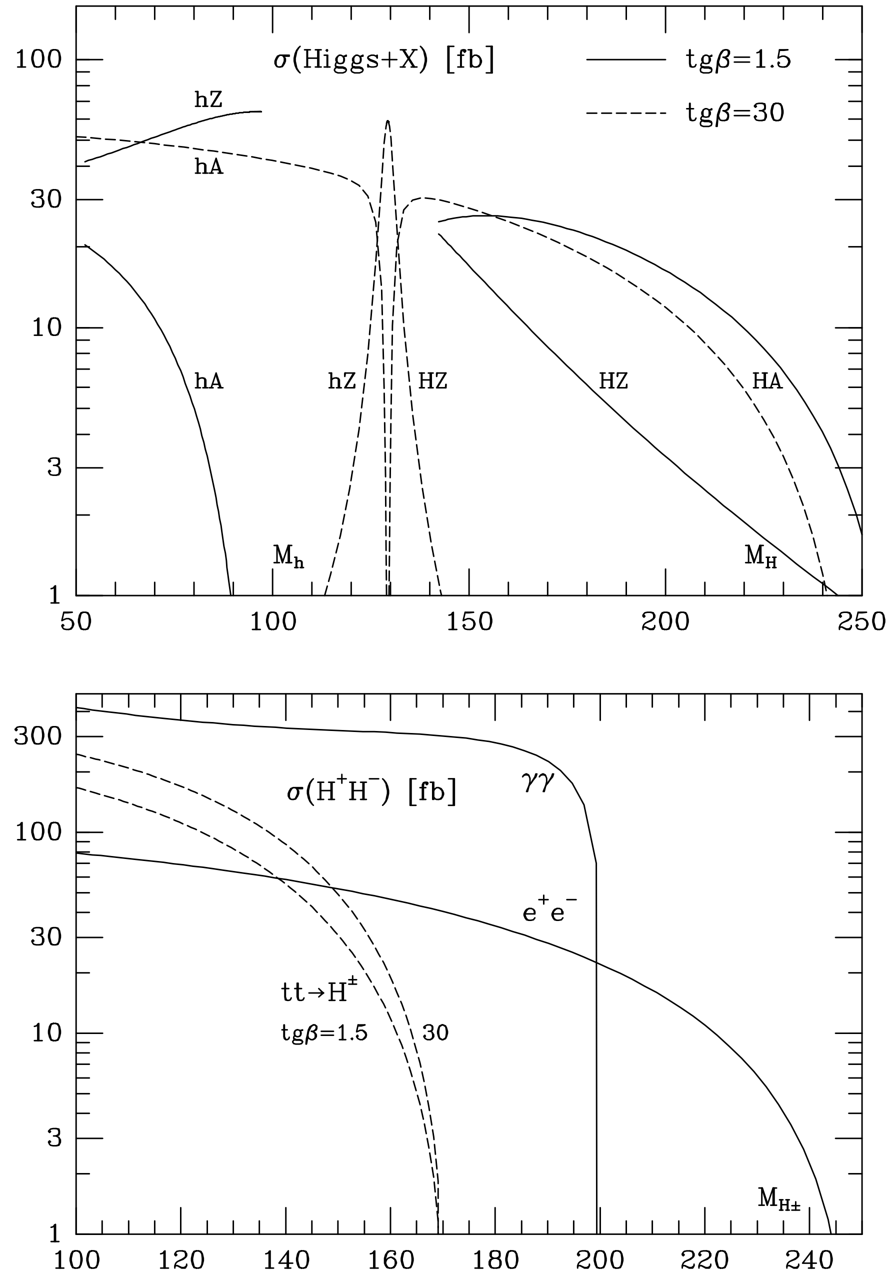

Figure 1.20: *Production cross sections of MSSM Higgs bosons at $\sqrt{s} = 500$ GeV: Higgs-strahlung and pair production; upper part: neutral Higgs bosons, lower part: charged Higgs bosons.*

Chapter 2

The LEP accelerator and DELPHI experiment

In the sections of this chapter there will be a description of the LEP accelerator and of the DELPHI experiment. A complete description can be found in [32] and [33].

2.1 Introduction

LEP is an electron-positron collider situated at C.E.R.N. laboratory in Geneva (Switzerland). Its main goal is the detailed study of the electroweak interaction, both by performing precision measurements of the relevant physical quantities and by searching for unexpected features. LEP was operated in its phase I (from 1989 to 1995) at a centre-of-mass energy very close to the Z^0 mass. After this the energy was raised. At the Z^0 pole, very large statistics were accumulated (about 24 million Z^0's), and very precise measurements and tests of the electroweak theory could be performed. The increase of the centre-of-mass energy started in November 1995. The threshold for the production of pairs of $W^\pm$ bosons was reached, and $W^\pm$ pairs were produced for the first time at LEP in the summer of 1996, at a centre-of-mass energy of about 161 GeV. This second phase will hopefully take LEP to an energy of 204 GeV foreseen for the summer of 2000. The accelerator will be described in some more detail in the first part of the present chapter.

Four experiments - ALEPH, DELPHI, L3 and OPAL - are installed at LEP in the crossing points of the two beams . The detection systems are, in their global geometry, largely determined by the characteristics of the machine and, thus, rather similar. They are essentially 4π detectors surrounding the interaction point. The global structure and main components are closely related to the general physics goals and also have a large number of common features in the different experiments. Since the aim is to achieve an analysis as complete as possible of the final state, they are general purpose detectors formed by layers of subdetectors with very different characteristics. The detection systems will be described in the second part of the chapter. Although the features common to all the detectors will be emphasised, the description will be centered on the DELPHI detector and in particular in the aspects that are more relevant for the present analysis.

2.2 The LEP collider

An accelerator can be characterised essentially by the following aspects [63]:

- type of colliding particles,
- dimensions and geometry,
- centre-of-mass energy ($\sqrt{s}$),
- luminosity ($\mathcal{L}$).

At LEP (Large Electron Positron collider) bunches of electrons and positrons with the same energy (E) and opposite momenta collide in interaction points surrounded by the detection systems. In this kind of collisions all the beam energy is available in the centre-of-mass ($\sqrt{s} = 2E$). Furthermore, since the laboratory frame is also the centre-of-mass frame the outgoing particles are essentially symmetrically distributed with respect to the collision point.

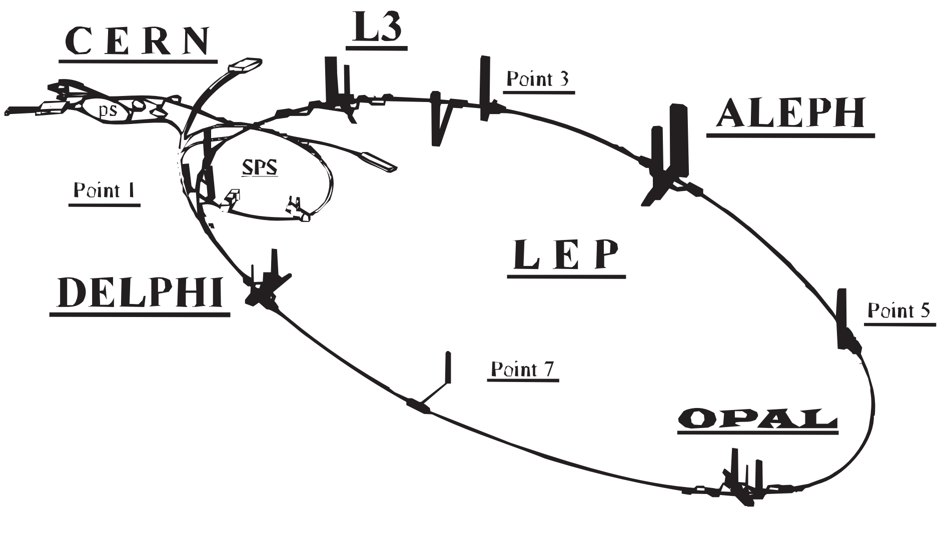

Figure 2.1: *Overview of the LEP collider, showing the four LEP experiments.*

The LEP is schematically shown in figure 2.1. The accelerator is situated about 100 m below the ground and has a perimeter of 26.6 km. It is formed by 8 linear sectors of about 100 m connected by curved regions. The energy lost by synchrotron radiation in the curved sectors is proportional to E^4/R and, thus, determined by the energy and the curvature radius R. The shape of the accelerator constitutes an equilibrium between the amount of energy radiated in the curved sectors and their high engineering costs.

The design energy of an accelerator is essentially determined by the physics goals. At LEP these were the massive production of Z^0 bosons in its phase I, the production of $W^{\pm}$ pairs in a second phase, and, finally, the exploration of the highest possible energy regions, in the search for new physics.

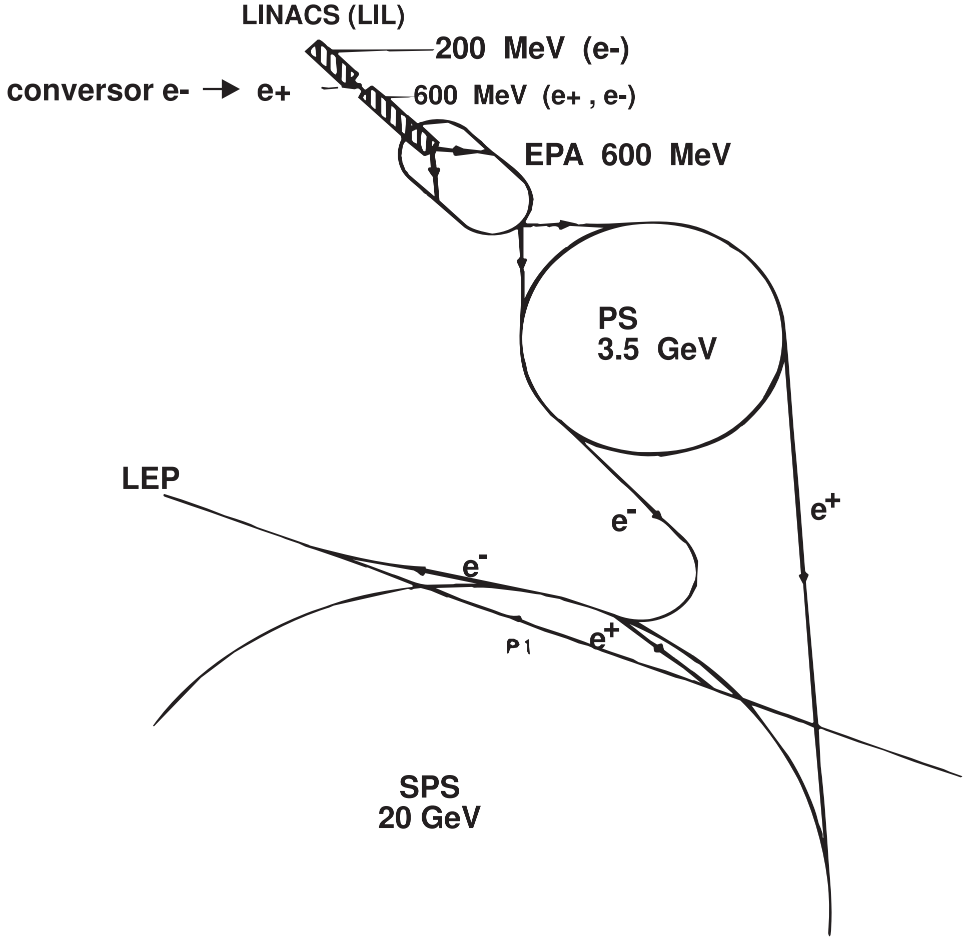

Figure 2.2: *The LEP acceleration and injection chain, using other accelerators existing at CERN.*

The acceleration of electrons and positrons to such high energies requires a complex chain that uses the other accelerators available at CERN. The LEP acceleration chain is shown in figure 2.2. The positrons are produced by the collision of 200 MeV electrons with a tungsten target. Electrons and positrons are then accelerated to 600 MeV at the LIL (Linear Injector-LEP) and accumulated in the storage ring EPA (Electron-Positron Accumulator). When the currents reach a certain value the beams are injected in the PS (Proton Synchrotron) where they are accelerated to a maximum energy of 3.5 GeV and then in the SPS (Super Proton Synchrotron) where they reach an energy of about 20 GeV. They are finally injected in LEP and accelerated to the desired energy. The acceleration is done in the straight sections of the tunnel using radio frequency cavities, while dipole magnets guide the beams through the curved sections. Once the energy is stable the beams are focused in order to decrease their cross-section in the interaction regions. The focusing is performed by superconducting quadrupole and sextupole magnets situated a few meters away from the interaction points.

The other important parameter in an accelerator is the luminosity. The luminosity is defined as the number of beam particles that cross the collision region per unit of area per second. Thus, the event rate $\dot{N}$ for a physical process of cross-section σ will be:

$$\dot{N} = \mathcal{L}\sigma. \tag{2.1}$$

This event rate can be written as:

$$\dot{N} = n_b f \frac{N_+ N_-}{S} \sigma, \tag{2.2}$$

where n_b is the number of bunches per cycle, $N_\pm$ are the number of particles per bunch in each beam, f is the revolution frequency and S is the cross-section of the bunches. Assuming that the bunch profiles are gaussian in the plane perpendicular to the beam ($S = 4\pi\sigma_x\sigma_y$, where $\sigma_{x,y}$ are the transverse dimensions of the beam) and that the number of particles in bunches of opposite beams is the same, the luminosity can be written in terms of the beam parameters as:

$$\mathcal{L} = \frac{n_b f N^2}{4\pi\sigma_x\sigma_y}. \tag{2.3}$$

where $N = N^+ = N^-$. The number of particles per bunch is of the order of 10^{11}. The number of bunches per beam and per cycle at LEP is either 4 or 8, depending on the running conditions. At LEP 2 the bunches can in addition be divided in bunchlets of particles. To n_b=4 corresponds an interval between collisions of $\sim 22\mu s$. Equation 2.3 shows that a higher luminosity can be achieved essentially by increasing the intensity of the beams or by decreasing their transverse dimensions. The main limitations are the synchrotron radiation and beam-beam interaction effects. Namely, when the beam currents exceed a certain limit the dimension of the bunches starts to increase due to the effects of one beam on the particles of the opposite beam, which can cause deflection. The luminosity achieved was $\sim 10^{31} cm^{-2}s^{-1}$ at LEP 1 and $\sim 10^{32} cm^{-2}s^{-1}$ at LEP 2.

Since the luminosity relates the event rate of a given process with its cross-section, an accurate measurement of the luminosity is important in the determination of cross-sections and other quantities derived from them. At LEP the luminosity is measured using equation 2.1 by obtaining the event rate for a high statistics process whose cross-section is theoretically known with great precision. This process is Bhabha dispersion ($e^+e^- \to e^+e^-$). The luminosity integrated over a certain period will be given by:

$$L = \int_{\Delta t} \mathcal{L} = \frac{N}{\sigma_{eff}} \tag{2.4}$$

where $N = N^{meas} - N^{back}$ is the number of events after background subtraction and the effective cross-section $\sigma_{eff} = \sigma\varepsilon_a\varepsilon$ is obtained from the theoretical cross-section (σ) by correcting for the effects of geometrical acceptance (ε_a) and Bhabha identification efficiency (ε). The computation of such factor requires a very accurate simulation of the detector used as a luminometer.

2.3 The DELPHI detector

The LEP detectors cover as much as possible of the solid angle around the interaction point and are forward-backward and azimuthally symmetric, reflecting the fact that the outgoing particles are essentially symmetrically emitted in the laboratory frame.

DELPHI [33] is formed by a cylinder (barrel region) closed by two endcaps that constitute the forward regions of the detector. Figure 2.3 shows the present layout of the barrel and of one endcap. The cartesian and cylindric coordinate systems used in DELPHI are shown in figure 2.4. The z axis is defined along the direction of the electron beam, the x axis points towards the centre of LEP and the y axis points upwards. The polar angle with respect to the z axis is θ and the azimuthal angle around the z axis ϕ is defined with respect to the x axis. The radius in the transverse plane is $R = \sqrt{x^2 + y^2}$. The barrel covers roughly the θ region from $40°$ to $140°$.

The main goal of the detection systems at LEP is to characterise as completely as possible the different final states. This requires:

- the capability of measuring the kinematic properties of the final state particles,
- the capability of identifying the detected particles,
- hermeticity, to guarantee that no information about the final state is lost,
- an efficient event selection system (trigger),
- a fast data acquisition system (minimizing the dead time) and software tools for event reconstruction and visualization,
- the capability of performing an accurate luminosity measurement.

Each of these topics will be discussed below. The measurement of the properties of the final state particles and the identification of leptons, photons and hadrons implies the presence of a number of subdetectors, with very different characteristics and goals. The information from the different subdetectors is associated by specific event reconstruction software tools. To avoid information losses, it is important that the detector is hermetic, detecting all the visible final state particles, and that the acquisition system is fast and equipped with an efficient trigger system, with a high rejection rate for spurious (non physical) events. The layout of the detector is the subject of the next few sections.

2.3.1 Detection principles

Particle detectors of all kinds are based on the way particles interact with matter. For charged particles, interaction with matter takes place essentially by:

- bremsstrahlung radiation,
- ionization,

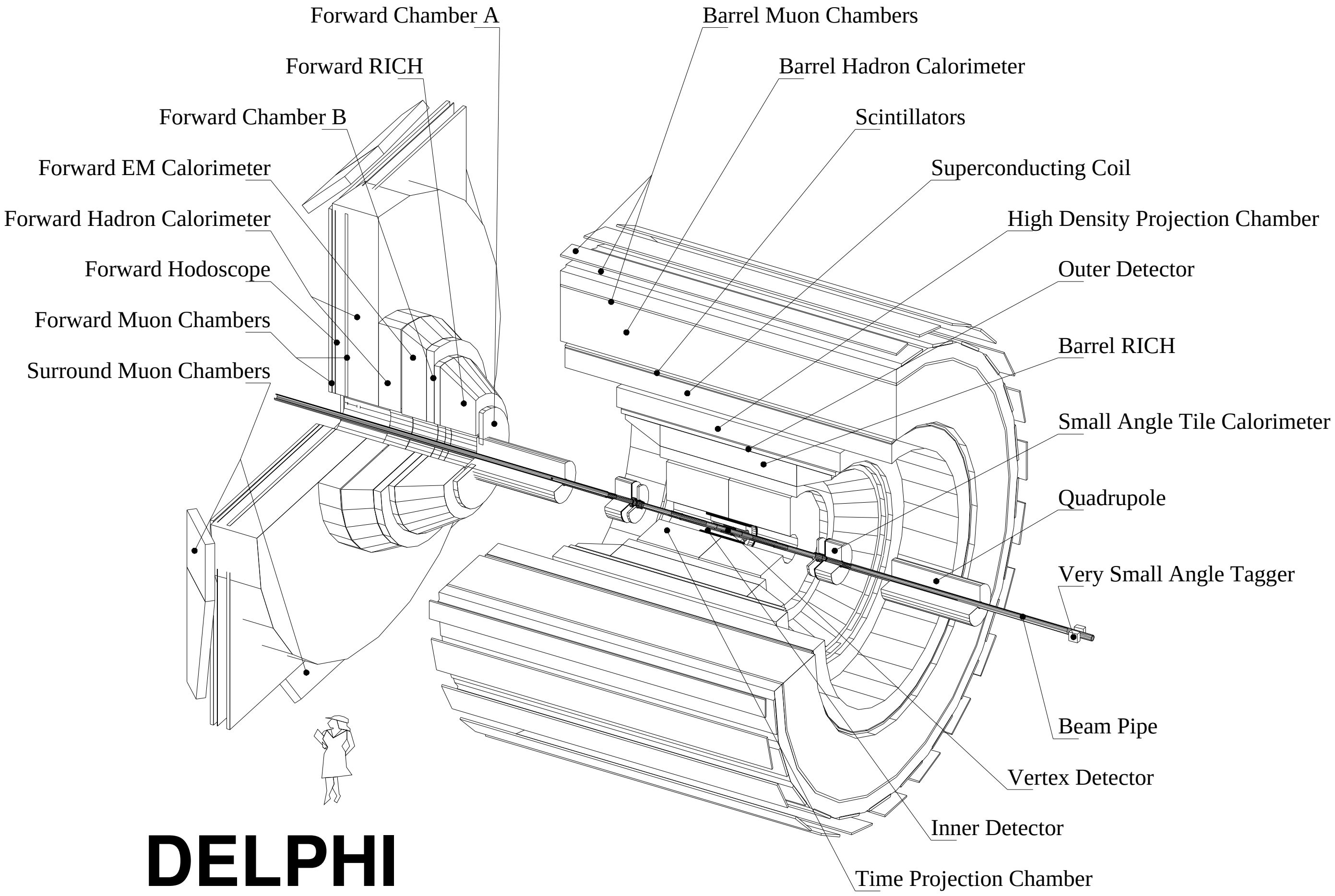

Figure 2.3: *A perspective view of the DELPHI detector, showing the layout of the barrel region and of one endcap.*

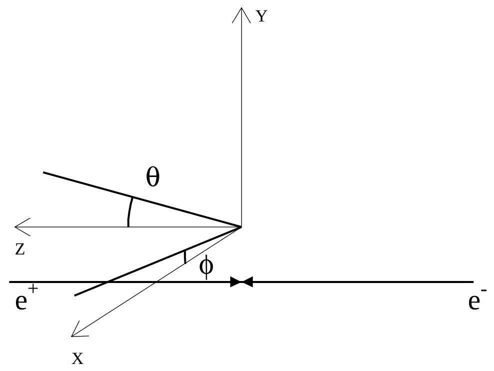

Figure 2.4: *Coordinate systems used in DELPHI.*

- nuclear reactions.

The relative importance of the different processes depends essentially on the particle type and on its energy.

Figure 2.5 summarises some aspects of the interaction of particles with matter that are most relevant for the present case. For electrons above 10-100 MeV, due to their low mass value, the dominant interaction process is bremsstrahlung. Muons and pions are, at the relevant energies, minimum ionizing particles (mip's). Hadrons interact mostly with the atomic nuclei of the materials they cross. For photons with energies above 10-100 MeV the dominant effect is the production of e^+e^- pairs. These will emit bremsstrahlung photons which will again convert in e^+e^- pairs, resulting in an electromagnetic shower. Neutrinos interact only through the weak interaction and are not recorded in the kind of detection systems described here. The muons are the most penetrating of the detected particles, since they are minimum ionizing particles at the relevant energies, have much smaller bremsstrahlung losses than electrons due to their higher mass and do not undergo strong interaction.

Particle detectors measure essentially positions, velocities, energies, charges and ionization energy losses. Completely different types of detectors, based on different working principles, are used for the various purposes. The reconstruction of the trajectory, energy and momentum of a particle by connecting the information from the different subdetectors is an elaborated task performed by specific software tools briefly described below.

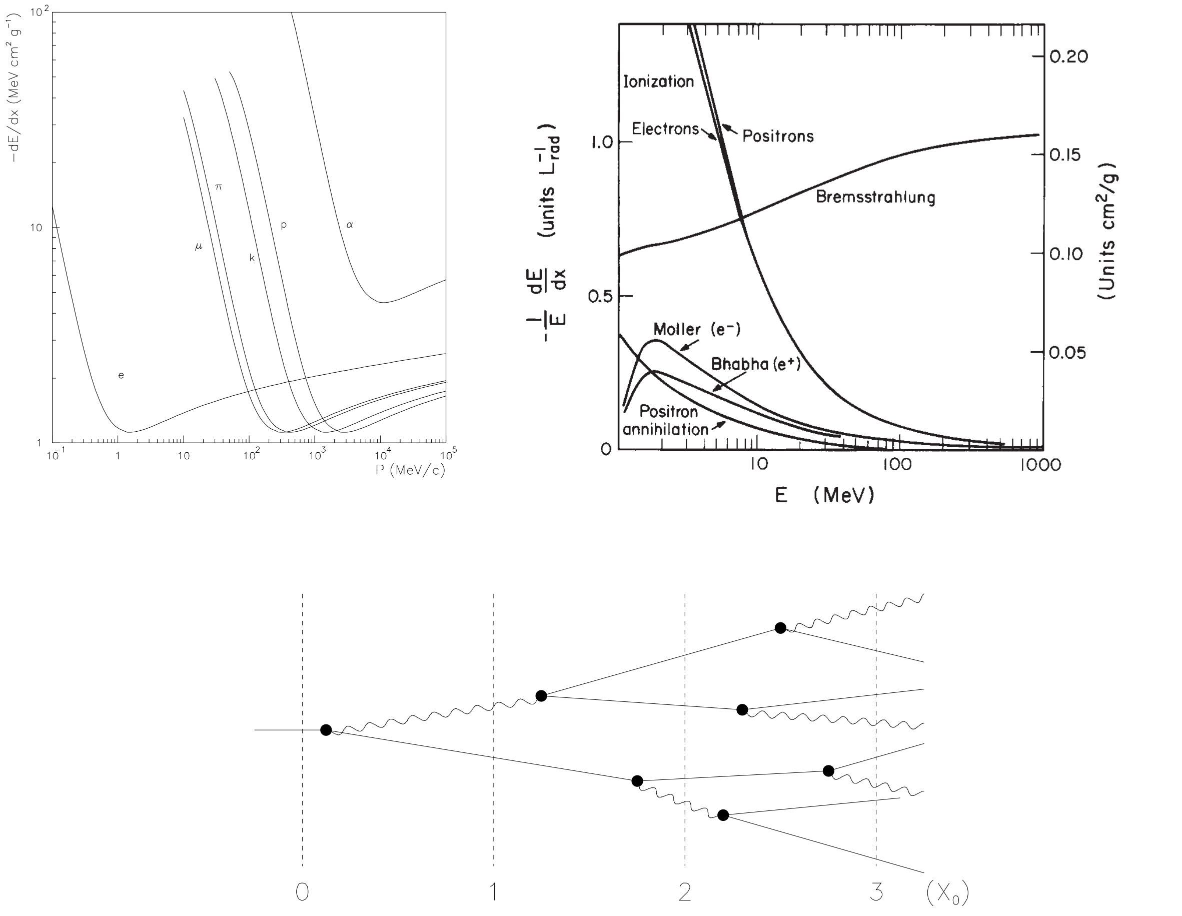

Figure 2.5: **(a)** *Ionization losses of different types of particles in lead as a function of their momenta;* **(b)** *interaction of electrons with matter;* **(c)** *schematic representation of the development of an electromagnetic shower.*

2.3.1.1 Tracking

The positions and trajectories of charged particles can be measured using the ionization effect produced in a medium by their passage. In the presence of a magnetic field, the trajectory of the particle allows the determination of its momentum and charge. In a tracking detector the particles have a minimal energy loss. The two main types of tracking devices are gas chambers and semiconductor detectors.

Basically, in a gas chamber the ionization caused by the passage of a particle in a gas is recorded. In the presence of an electric field, the ionization electrons are detected in the anodes (wires) and the positive ions are detected in the cathodic pads. The signal in the anodes is proportional to the deposited energy. The existence of many wires and the segmentation of the cathodes allow for position information. There is a wide range of detectors based on this working principle, with very different shapes and goals. Particularly important At LEP are the drift chambers of large dimensions (for example, time projection chambers). In such a drift chamber the ionization electrons are drifted over a low field region before reaching the amplification region where the anodes are placed. The cathode segmentation gives transverse position information, while the third dimension is given by the drift time of the electrons. The signals in the wires give successive measurements of the ionization energy loss (dE/dx).

Semiconductor detectors work as solid-state ionization chambers. A charged particles creates electron-hole pairs on its way through a semiconducting material. High electric fields are generated for the collection of the charges. The dimensions of a semiconducting strip can be of the order of some tens of microns. Semiconductor detectors can give precise position information and are generally used to obtain position information very close to the interaction point. This is crucial for the identification of long lived particles, as discussed below.

2.3.1.2 Calorimetry

Calorimeters can measure the energy of charged and neutral particles. This measurement requires that the particles are fully absorbed in the detector, to ensure containment of the energy. A calorimeter must have:

- a medium where the interaction probability of the particle is large, able to cause the deposition of essentially all the particle energy within a reasonable distance,
- an active medium able to produce a recordable signal in response to the deposition of a certain amount of energy.

The two functions are performed by the same material in homogenous calorimeters and by two different materials in sampling calorimeters. In the second case the passive media is in general a high atomic number material where most of the energy is deposited, while only a small fraction of the energy (proportional to the total energy) will be detected by the active material.

Electromagnetic and hadron calorimeters have as common feature the fact that the particle is made to shower in order to fully deposit its energy. They have some basic differences resulting from the fact that they aim to measure the energy of distinct types of particles, which interact with matter in a very different way.

The parameter used to describe the longitudinal development of an electromagnetic shower is the radiation length (X_0), defined as:

$$\left(\frac{dE}{dx}\right)_{rad} = -\frac{E}{X_0}. \tag{2.5}$$

This parameter obviously depends on the material that is used. For electrons in lead the radiation length is of the order of 0.5 cm. The radiation length determines both the choice and the extension of the passive material in a calorimeter. At the LEP energies, about 20 to 30 radiation lengths are needed to contain an electromagnetic shower.

Hadronic showers result essentially from nuclear interaction and their longitudinal development is characterized in terms of interaction length (λ). The length of an electromagnetic calorimeter usually corresponds to a fraction of λ, while about 7λ are needed in order to contain 95% of an hadronic shower.

Since the number of secondary particles produced in a shower is proportional to the initial energy, the resolution of calorimeters improves with the energy:

$$N_{sec} \propto E \Rightarrow \frac{\sigma(E)}{E} \sim \frac{\sigma(N)}{N} \sim \frac{1}{\sqrt{(N)}} \sim \frac{1}{\sqrt{(E)}} . \tag{2.6}$$

Calorimeters can also give position information if they have transverse segmentation. The transverse development of an electromagnetic shower is essentially due to the emission of non collinear bremsstrahlung photons and to multiple Coulomb scattering in the media crossed. In the latter the energy loss is negligible but the direction of the particle is changed.

This kind of detector has the great advantage of being sensitive to both neutral and charged particles. Calorimeters are, for example, the only source of position information for photons. Highly segmented calorimeters can give detailed information on the shape of the shower. The choice of the ideal granularity takes into account the transverse dimensions of the shower. The amount of energy deposited in the neighboring towers can give some information about the impact point of the particle within a given tower.

2.3.2 The subdetector layers

In short, the main layers of the LEP detectors are (starting from the interaction point):

- the tracking detectors, measuring trajectories, momenta, charges and ionization losses,
- the electromagnetic calorimeters, measuring the energy of electrons and photons,
- the hadron calorimeters, measuring the energy of hadrons,

- the muon chambers, detecting the particles that were able to reach the outer part of the detector.

At least the central part of the detector has to be inside a magnetic field, to allow the measurement of momenta and charges. The tracking system usually includes very precise position information close to the interaction point. Particle identification can be performed combining the information from the different subdetectors (see section 2.3.4) or using the specific detectors that are present for this purpose, like the Čerenkov detectors. Specific detectors are also used to measure the luminosity by counting the number of Bhabha events. They are placed in the very forward region of the detectors because the cross-section of this process is peaked at very low polar angles. Subdetector with the main goal of reinforcing the global hermeticity may be present. These will be discussed separately (see section 2.3.5).

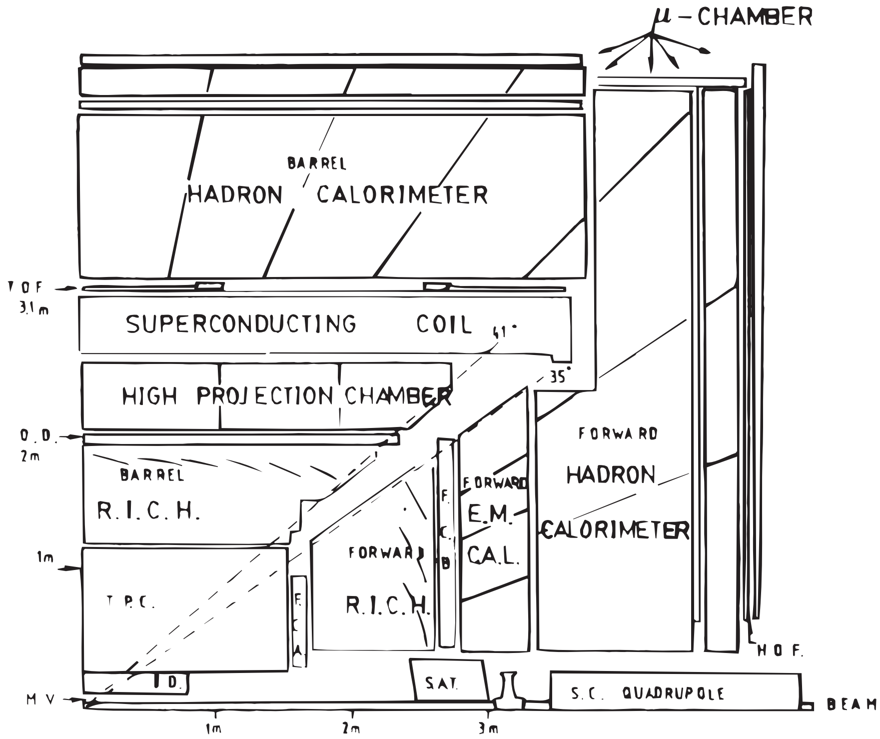

Figure 2.6: *Longitudinal view of the DELPHI detector.*

Each layer of the DELPHI detector will be shortly described below. A longitudinal profile of the detector is shown in figure 2.6.

2.3.2.1 Tracking system

The DELPHI tracking system is segmented into a relatively large number of tracking devices:

- **Vertex detector (VD)**
  The next section is dedicated to it.

- **Inner detector (ID)**
The ID covers the polar angle region between 15° and 165°. It has two distinct parts. The inner part is a drift chamber divided in 24 azimuthal sectors, each sector having 24 anode wires. It gives a maximum of 24 $R\phi$ measurements per track with a typical resolution of $\Delta(R\phi) \simeq 90$ μm. The outer part is formed by 5 concentric layers of proportional chambers which perform fast ($t < 3$ μs) $R\phi$ measurements that participate in the first level trigger. Information on the z coordinate is also available due to the small stereo angle of 2 layers.

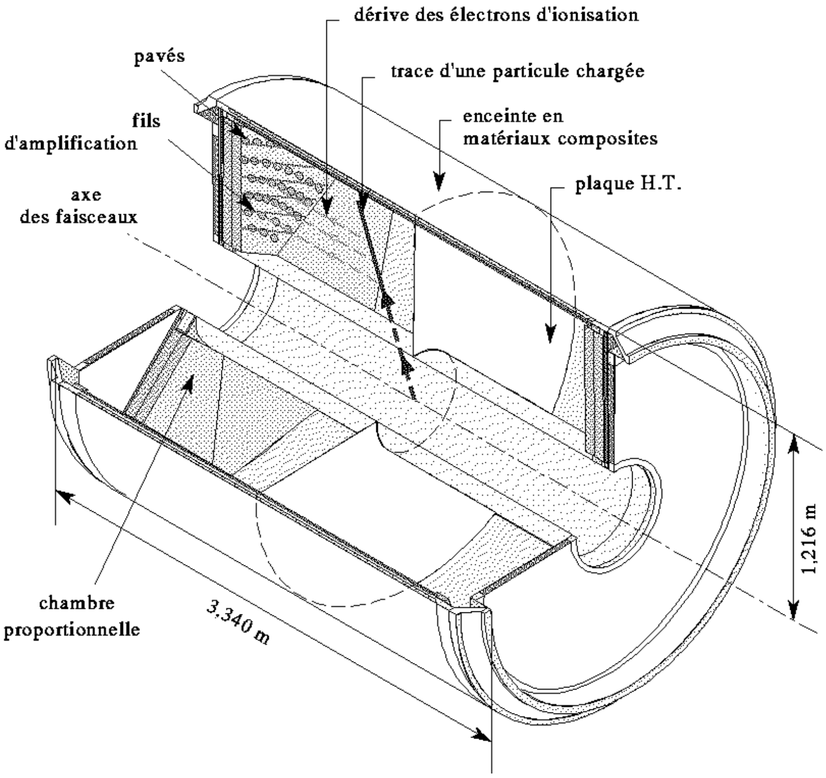

Figure 2.7: *Schematic view of the DELPHI TPC.*

- **Time projection chamber (TPC)**
The TPC, the main tracking device of DELPHI, is a drift chamber of large dimensions covering the polar angle region between 20° and 160°. It is formed by a cylinder with an inner radius of 35 cm and an outer radius of 111 cm, filled with an argon/methane mixture (80 %/20 %) at the pressure of 1 atm. In the central part of the detector ($z = 0$) a high voltage plane divides the cylinder into two drift volumes both 130 cm long. Both end plates are divided in 6 $R\phi$ sectors ($6\times60°$), each sector containing 192 wires and 16 circular cathode pad rows. The detector is schematically shown in figure 2.7. The TPC provides 3 dimensional position information (R, ϕ, z) with a good resolution ($\Delta(R\phi) \simeq 230$ μm and $\Delta z \simeq 0.9$ mm). In about 82% of the covered polar angle region it provides up

to 16 3-dimensional position measurements per track. It also provides up to 192 dE/dx measurements. This information is crucial for particle identification in the low momentum region. It participates in the second level trigger.

- **Outer detector (OD)**
  The outer detector is about 2 m away from the interaction point and covers the polar angle region between 42° and 138°. It has 24 modules, each consisting of 145 drift tubes disposed in 5 layers. It performs a good resolution $R\phi$ measurement ($\Delta(R\phi) \simeq 110\ \mu$m). The difference in drift time to both ends gives a fast measurement of z ($\Delta z \simeq 3.5$ cm). It participates in the first level trigger.

- **Forward chambers A and B (FCA and FCB)**
  These two tracking chambers are placed in the forward region of the detector, about 1 m away from each other. The FCA covers the polar angle regions $11° < \theta < 32°$ and $148° < \theta < 169°$, while for the FCB the acceptance regions are $11° < \theta < 36°$ and $144° < \theta < 169°$. They are essentially sets of drift tubes.

- **Barrel, forward and surrounding muon chambers (MUC=MUB+MUF+MUS)**
  The muon chambers are sets of drift chambers placed in the outermost part of DELPHI. They provide (good resolution) $R\phi$ information and z information for muons. They are crucial for muon identification, since muons are essentially the only particles reaching these detectors.

As mentioned, the presence of a magnetic field is crucial for the determination of the momentum and charge of particles. In DELPHI a superconducting solenoid placed in the barrel region, between the electromagnetic and the hadron calorimeters, provides a field ($\vec{B}$) of 1.2 Tesla essentially uniform and parallel to the beam axis (z). This induces a curvature in the trajectory of the particle in the xy plane. The relation between the transverse (xy plane) momentum of a particle and its radius of curvature (r) is:

$$p_T[GeV/c] = 0.3B[T]r[m]. \tag{2.7}$$

2.3.2.2 Calorimeters

The DELPHI calorimeters reflect the emphasis put, in the design of the detector, on having subdetectors with a high granularity, giving detailed position information and (as far as possible) 3-dimensional spatial information. The calorimeters are the barrel and the forward electromagnetic calorimeters, the hadron calorimeter, covering both the barrel and the forward region of the detector, and a very forward electromagnetic calorimeter which is also the DELPHI luminometer.

- **High density projection chamber (HPC)**
  The HPC is the barrel region electromagnetic calorimeter of DELPHI. It is a sampling calorimeter of lead (passive medium) and a gaseous mixture (active medium). It covers the polar angle region $41.5\ ° < \theta < 138.5°$. It has a high

transversal and longitudinal segmentation, providing 3-dimensional reconstruction of the electromagnetic cascades. The HPC consists of 144 modules organized in 6 rings of 24 modules. Each module has 10 layers of lead separated by gas chambers. The resolution of the HPC is given by:

$$\frac{\sigma_E}{E(GeV)} = \frac{(29 \pm 7.8\%)}{\sqrt{E(GeV)}} \oplus (6.9 \pm 0.6\%). \tag{2.8}$$

The position resolution for photons in the HPC is $\Delta\theta = 1.1$ mrad and $\Delta\phi = 3.1$ mrad. Its total depth is about $18X_0/sin\theta$.

- **Forward electromagnetic calorimeter (FEMC)**
  The FEMC is a homogenous highly segmented ($1^\circ \times 1^\circ$) calorimeter formed by 2×4532 blocks of *leadglass* with the shape of truncated pyramids disposed in 2 layers. The Čerenkov light is read out by triodes. It covers the angular region $10^\circ < \theta < 35.5^\circ$ and the complementary region $144.5^\circ < \theta < 170^\circ$. The energy resolution of the FEMC is given by:

$$\frac{\sigma_E}{E(GeV)} = \frac{(20 \pm 9\%)}{\sqrt{E(GeV)}} \oplus (4.7 \pm 1.5\%). \tag{2.9}$$

  It gives fast ($t \sim 3\mu s$) trigger information. Its depth amounts to about 20 radiation lengths (X_0). The material placed in front of the calorimeter amounts to about $2X_0$.

- **Hadron calorimeter (HCAL)**
  The HCAL is an iron/gas sampling calorimeter assuring the measurement of the hadronic energy both in the barrel and in the forward regions. The barrel part covers the polar angle region $43^\circ < \theta < 137^\circ$, while the forward part covers the region $10^\circ < \theta < 52^\circ$ and complementary $132^\circ < \theta < 170^\circ$. In the barrel the resolution can be parameterized as

$$\frac{\sigma_E}{E(GeV)} = 0.21 \oplus \frac{1.12}{\sqrt{E(GeV)}}. \tag{2.10}$$

  In the forward region it was estimated to be about $2/\sqrt{E}$. The depth of the hadron calorimeter corresponds to about 6 interaction lengths. The iron acts simultaneously as the magnet return yoke.

- **Small angle tile calorimeter (STIC)**
  The STIC is a sampling electromagnetic calorimeter formed by 49 lead-scintillator layers, giving a total of 27 radiation lengths. The light produced in the scintillator is collected by wave length shifter (WLS) fibers and read out by tetrodes. The STIC covers the very forward region of DELPHI, $2^\circ < \theta < 10^\circ$ and $170^\circ < \theta < 178^\circ$, and performs a very precise luminosity measurement. The scintillator planes in the STIC layers 8 and 15 were replaced by silicon microstrip detectors giving precise information on the direction of the showers. Two scintillator planes are placed in front of the calorimeter, providing electron/photon separation.

2.3.2.3 Specific subdetectors

- **Ring imaging Čerenkov detectors (RICH=RIB+RIF)**
  In a RICH the Čerenkov light produced by charged particles travelling faster than the speed of light in the medium they cross is detected. The threshold velocity for a particle to radiate is $\beta = 1/n$, where n is the refractive index of the material. Above threshold, the photons are radiated at an angle that is directly related to the velocity of the particle: $cos\theta_c = 1/\beta n$. This velocity measurement, when combined with a momentum measurement, identifies the particle by its mass. The detector can be used in veto mode and in ring identification mode. The RICH has two radiators (liquid and gas) of different refractive index and is designed to provide optimal pion-kaon-proton separation in both the low and high momentum regions. The RIB and the RIF cover the barrel and forward region of the detector, respectively.

- **Time of flight detectors (TOF and HOF)**
  These detectors are constituted by scintillator planes placed in the barrel (TOF) and forward (HOF) regions of the detector. Given their fast response, they are used in the first level trigger. They are also useful in rejecting cosmic background.

- **Very small angle tagger (VSAT)**
  The VSAT performs a second measurement of the DELPHI luminosity. It is a tungsten/silicon detector with a depth of 24 radiation lengths and a very limited geometrical acceptance: $0.29° < \theta < 0.4°$ and the complementary region $179.6° < \theta < 197.71°$ for $\Delta\phi = \pm 45°$ around $\phi = 0°$ and $\phi = 180°$.

2.3.3 The vertex detector (VD)

The VD consists of three layers of microstrips in the central part, extended by two layers of ministrips and two layers of pixel detectors in each forward region (Very Forward Tracker, VFT). The task of the barrel vertex detector is to enable the reconstruction of primary and secondary vertices with high spatial resolution. The VFT is a self sufficient tracking detector close to the interaction region to cover polar angles below 25^o. The combined silicon detectors cover polar angles $10^o < \theta < 170^o$. The micro and ministrip detectors were fully upgraded and installed for the running period in 1996. The pixel detector was completed for the data taking period in 1997. With a total sensitive area of 1.78 m^2 the DELPHI experiment contains the largest silicon vertex detector currently existing (see figure 2.8).

2.3.3.1 The microstrip vertex detector

The microstrip vertex detector consists of three layers of microstrip detector modules with two-coordinate readout. The modules are placed at average radii of 6.6, 9.2, 10.6 cm, chosen to provide optimal track resolution by maximum lever arm and closest possible distance to the beam pipe. The configuration of the layers is shown in figure 2.9.

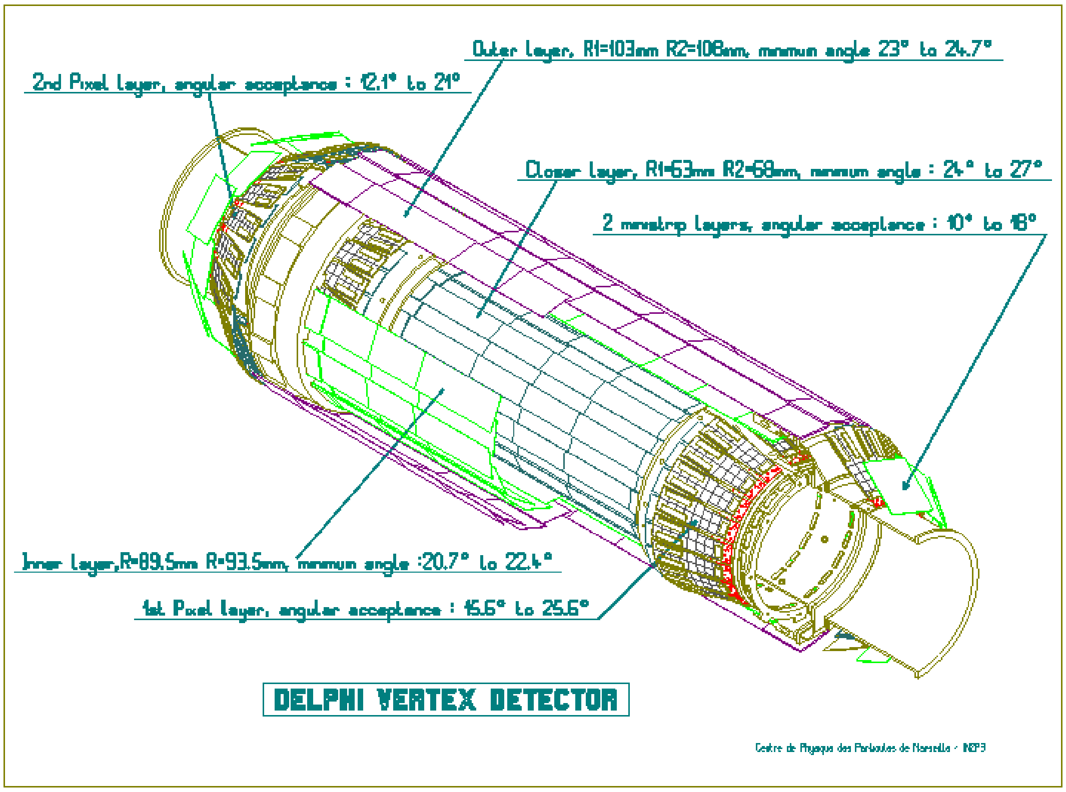

Figure 2.8: *Outline of DELPHI silicon tracker*

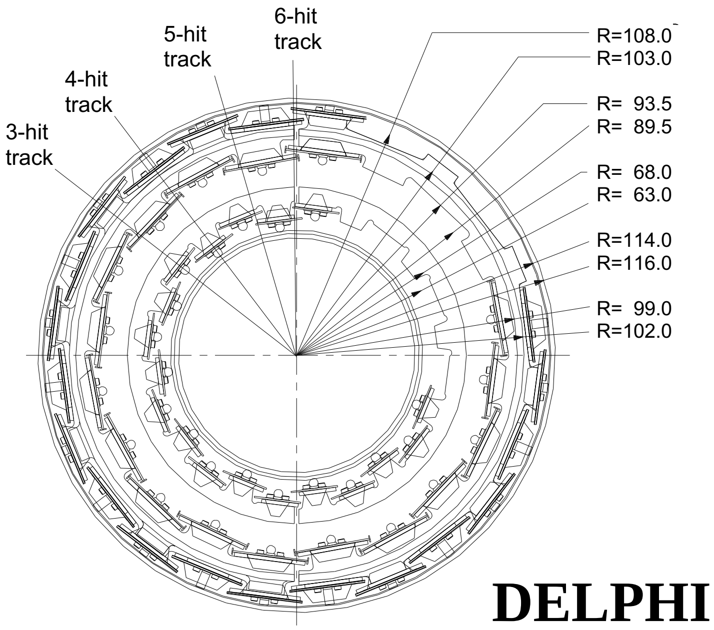

Figure 2.9: *$R\phi$ cross section of the three layer vertex detector.*

The intermediate “Inner” microstrip layer consists of 20 modules, the internal “Closer” and external “Outer” layers of 24 modules. Up to 8 silicon plaquettes are used per module. With the Outer layer where multiple scattering is less severe, a back-to-back solution with 16 single-sided plaquettes has been chosen.

The strip pitch is 25 μ and the readout pitch is 50 μ for the Rphi coordinates , but varies for the z coordinates in order to optimise the spatial resolution of enlarged clusters of hit strips for inclined tracks at low polar angles.

2.3.3.2 The Very Forward Tracker

The spatial resolution required from the VFT is of the order of 100 μm. This precision is sufficient taking into account Coulomb scattering in the material in front of the VFT. Furthermore, its track elements are extrapolated towards the Forward Chambers which are located further outside after several radiation lengths of additional material. Therefore, no extreme resolution as with the microstrip vertex detector is necessary and the task reduces to unambiguous and efficient pattern recognition. Ministrip and macro pixel detectors, characterized by rather large strip pitch or element size, meet this situation.

The detector modules are arranged in cones. The Ministrip detector layers are inclined by 50^o and the pixel detectors by 12^o and 35^o with respect the beam. Table 2.1 summarises important characteristics of the VFT.

DELPHI VFT	pixel detector	mini strip detector
layers/end cap	2	2
radii [cm]	6.9–8.4, 7.5–11.2	6.9–8.4
inclination [°]	12, 32	50
modules/layer	38	12
detectors/module	1	2
silicon size [cm^2]	6.9 $\times$ 1.7$\rightarrow$2.3	5.3 $\times$ 5.3
$\|cos\theta\|$	0.906-0.978	0.951-0.985
modules overlap [%]	12, 37	15
channels	1.2 million	24.500
readout pitch [μm]	330 (pixel size)	200 (1 intermediate strip)
sensitive area [m^2]	0.15	0.26

Table 2.1: *Characteristics of the DELPHI Very Forward Tracker*

2.3.3.3 Experience with the vertex detector

During 1997 I contributed to the insertion in DELPHI of the last version of the vertex detector. In particular I contributed to the measurements of its geometrical structure before the insertion, which consists in determining the positions of reference points in each module of the detector. This is an idea developed by the Milano microvertex group and the final aim is to have a zero order approximation of the relative position of modules. This is the indispensable starting point for the alignment realised with $Z^0 \to \mu^+\mu^-$ events (see chapter 3).

During 1999 I participated, as run coordinator of the vertex detector, to all phases of the VD operation during the data taking. This means taking care of the voltage and current settings for the correct working of the detector, and controlling the performances and the quality of recorded data.

2.3.4 Identification of photons, leptons and hadrons

In the construction of DELPHI one of the strong aims was to provide photon, lepton and hadron identification in nearly 90% of the solid angle. The tools are quite diverse and will now be summarized. Particle identification is performed using essentially two kinds of information:

- measurement of specific quantities giving direct information on the type of particle (namely dE/dx and Čerenkov angles),
- combined information from tracking devices, electromagnetic calorimeters and hadron calorimeters.

The particle identification capabilities of the DELPHI detector are based on the TPC dE/dx measurements and on the information of the Čerenkov detectors. These tools are rather powerful in the identification of charged particles of low momenta, both leptons and hadrons. They are essential in analyses requiring the separation of light hadrons of different types. The dE/dx information is heavily used for electron identification in particular in the barrel region of the detector.

The combined information of the tracking devices and calorimeters is the main tool for lepton, photon and hadron identification at higher momenta. For this, the separated measurement of the electromagnetic and hadronic energies is essential. Table 2.2 summarizes the signatures left by particles of different types in the central tracking devices, electromagnetic calorimeters, hadron calorimeters and muon chambers.

Particle	Tracking	e.m. calo.	had. calo.	μ chamb.
e	yes	$E/p \sim 1$	$E/p \sim 0$	no
μ	yes	$E/p \sim 0$	$E/p < 0.1$	yes
γ	no	$E \gg 0$	$E \sim 0$	no
hadrons	yes/no	$E/p \sim 0$	$E/p \sim 1$	no

Table 2.2: *Signature of different types of particles in the various subdetectors.*

Electron and photon identification and reconstruction is realized by REMCLU algorithm ([42]). Electrons produce tracks in the central region of the detector with an associated shower in the electromagnetic calorimeter and no associated hadronic shower. The comparison of the energy E in the electromagnetic calorimeter with the momentum p measured by the tracking system provides a powerful tool for charged lepton identification. This ratio is expected to be close to unity for electrons independently of their energy and close to zero (< 0.05) for muons. The identification of electrons is complicated by electromagnetic interactions of the particles before reaching the calorimeters. In the barrel region, the amount of material in front of the calorimeter corresponds to about $0.8X_0/sin\theta$. In the forward region it is larger ($\sim 2X_0$) and the material is on average further away from the calorimeter.

Photon showers in the electromagnetic calorimeters are reconstructed by associating neighboring clusters. A shower is assumed to be caused by a neutral particle if it cannot be associated to a track. Photons are electromagnetic clusters with no associated track and no associated hadronic shower. Photon identification is complicated by conversion into e^+e^- pairs, in particular if it occurs within the tracking system. About 40% of the photons convert before they reach the HPC. About 7% of the photons convert in front of the TPC, creating visible tracks. Another problem for photon identification are the photon pairs coming from the prompt decays of neutral pions. A π^0 can be reconstructed either by pairing resolved photons or by analyzing the energy depositions in the electromagnetic calorimeter, looking for internal structure compatible with two photons.

Both muons and charged hadrons are tracks in the central detectors with no (or very low) energy depositions in the electromagnetic calorimeter. While hadrons are expected to shower in the hadron calorimeters, muons will have also there a very low energy deposition. The iron of the hadron calorimeter provides a filter which gives a first level separation between muons and hadrons. Most hadrons are stopped by this material, while muons of momenta above 2 GeV/c are expected to penetrate to the muon chambers.

Specific investigations of heavy quark production require the measurement of small flight paths of long-lived particles and the reconstruction of secondary vertices. The VD has a crucial role in the identification of such particles.

2.3.5 Hermeticity

The importance of having a hermetic detector able to provide as much information as possible about the physical final state is particularly evident in the search for new physics. In fact, many new physics channels could involve the production of energetic, sometimes massive, invisible particles. The experimental signature of such processes would be the presence of missing energy and missing mass in the event. Only a detector covering the full solid angle can give reliable information on the missing quantities. Hermeticity can, on the other hand, mean different things. For example, hermeticity for charged particles obviously does not mean hermeticity for neutrals. Also, a detector can be able to count the produced particles without being able to measure their properties in the full solid angle.

The DELPHI detector covers about 90% of the solid angle. The only totally uncovered region is the one around the beam pipe: $\theta < 2^\circ$ and $\theta > 178^\circ$. However, the efficiency is not the same in all the solid angle. In particular, from the point of view

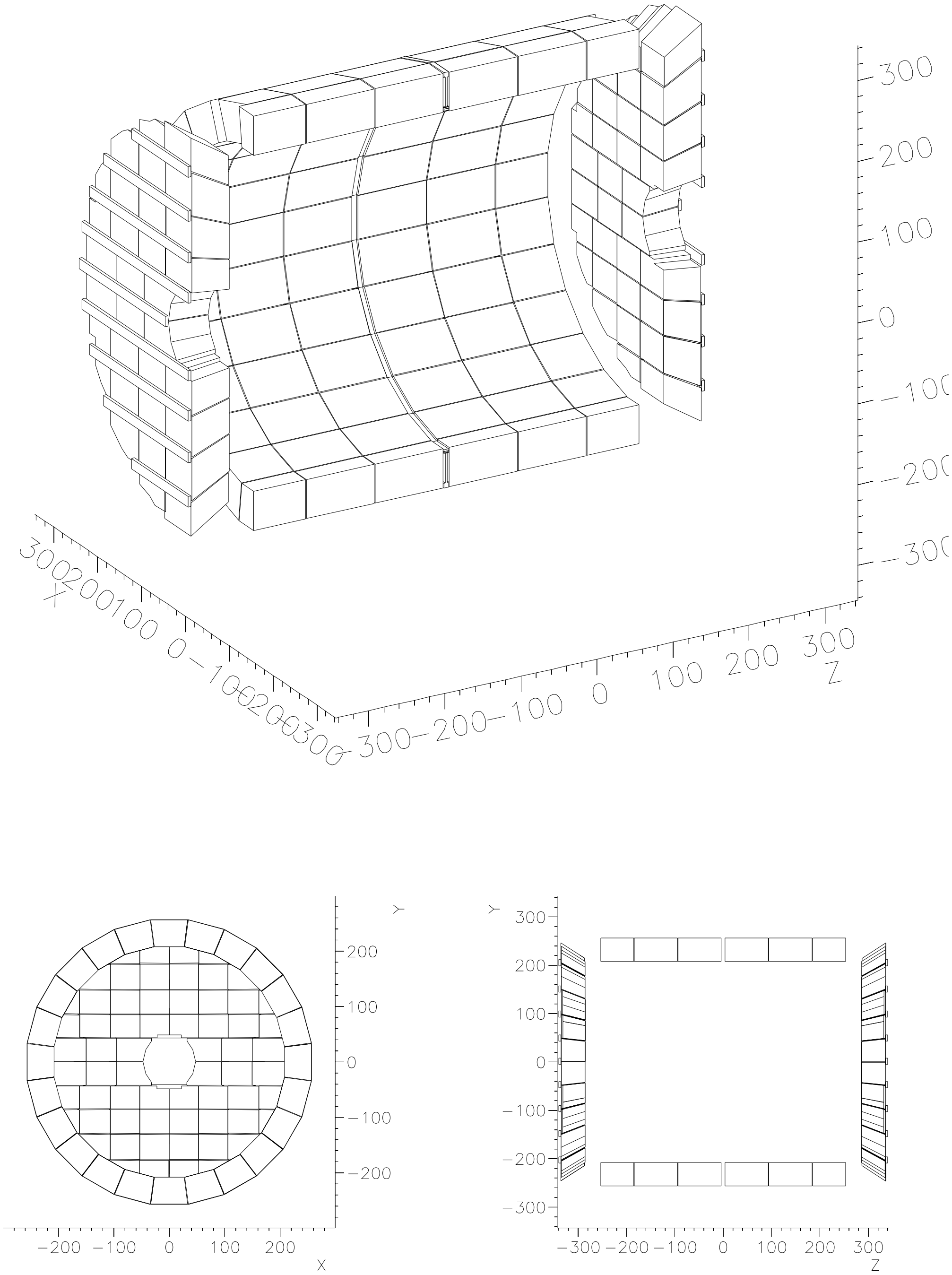

Figure 2.10: *Angular coverage of the electromagnetic calorimeters of DELPHI.*

of electromagnetic energy detection there are some weak regions. These can be seen in figure 2.10 and are listed below:

- $\theta \sim 40^\circ$
  uncovered region between the barrel and the forward electromagnetic calorimeters, with polar angles $\theta \simeq [35^\circ, 42^\circ]$ and $\theta \simeq [138^\circ, 145^\circ]$. This is the region through which the cables pass carrying the signals from the various internal detectors,
- $\theta \sim 90^\circ$
  uncovered region at $\theta \simeq 90^\circ \pm 1.5^\circ$. This is the region for passage of the supports of the superconducting solenoid,
- $\phi \sim 7.5^\circ + (n-1)15^\circ$, $n = 1, 24$,
  the borders between the 24 HPC ϕ modules. These regions are not really uncovered but have a lower detection efficiency due to an insufficient containment of the showers. As a result there will also be energy deposition in the hadron calorimeter.

The weak regions for electromagnetic energy detection have important effects in the search for new physics in channels involving invisible particles and also in all the analyses for which the photon detection efficiency is important. Since it is not possible, due to lack of space, to install a "surrounding electromagnetic calorimeter" in the uncovered regions, it would be useful to have at least the information of the passage of a particle, even without measuring its energy.

In the regions where there is hadron calorimeter coverage, the efficiency for the detection of photons can be recovered by associating to the electromagnetic showers the energy deposited in the hadron calorimeter. Photon/hadron separation can still be achieved by taking into account that in the case of photons nearly all the energy will be deposited in the first layer of the hadron calorimeter.

2.3.5.1 The 40° taggers

The weak region at $\theta \sim 40^\circ$ corresponds to about 6% of the total solid angle covered by DELPHI. Although the advantages of placing a detector able to measure the energy in this region are obvious, the main difficulties are the lack of space and the presence of many obstacles. The chosen solution was to cover this region with a set of scintillator counters able to record the passage of photons, but not to measure their energy. The counters are small and are distributed to cover as well as possible the existing space.

Each counter is formed by a 2 cm thick scintillator plane. The scintillation light is collected by WLS fibers and read by photomultiplier tubes able to operate under the intense DELPHI magnetic field. There are essentially 3 groups of counters, labeled A, B and C. The counters A form the outer ring and are connected to the support structures of the RICH. The B counters form an intermediate ring and have a curved side in order to increase to geometric coverage. The C counters constitute the inner ring. Both the B and the C counters are attached to the supports of the cables passing

type of counter	θ_{center}	ϕ_{center}	z_{center} (cm)	$\Delta\theta$	$\Delta\phi$
A 40°	40.6°	75.0°	217 cm	1.98°	12.6°
B 40°	38.6°	75.0°	188 cm	2.37°	21.8°
C 40°	38.3°	75.0°	180 cm	2.34°	30.6°

Table 2.3: *Positions and dimensions of the 40° counters.*

between the barrel and the endcaps of the detector. The shape and dimensions of each type of counter in shown in table 2.3.

The taggers were installed in DELPHI in 1994. Since the first year of operation, performance tests have shown that the efficiency of the taggers for the detection of electrons above 1 GeV/c is better than 90 % for the A counters and above 95 % for the B and C counters, while the contamination of false signals was found to be of the order of 0.1% and 0.04% for the A and the B/C counters respectively. For electrons of momentum above 20 GeV/c the efficiency is above 98%.

2.3.5.2 Other hermeticity detectors

The weak region around $\theta \sim 90°$ corresponds to about 2.3% of the solid angle covered by DELPHI. To improve the hermeticity in this region 24 counters each covering an angular range $\Delta\theta \times \Delta\phi = 1.53° \times 14.38°$ were installed 1.2 m away from the interaction point. The angular coverage is still not complete, due to lack of space. The information of the $\theta \sim 90°$ taggers can be combined with that from the OD, a detector not having a weak region around 90°. The OD can detect the particles in showers resulting from photon conversion.

The ϕ counters were conceived to cover the weak regions between the HPC modules, corresponding to 10.2% of the total solid angle. These regions are also covered by the TOF, except where the supports of the superconducting solenoid are placed ($\phi \sim 210°$ and 330°). A total of 36 counters were installed in the particularly weak regions. As for the 90° counters, the angular coverage is still not complete.

The FCB can also be used as an hermeticity detector for photons escaping in the $\theta \sim 40°$ region: if a photon passes in this region of the detector it is very likely to interact with the existing material, originating a shower. The charged particles of this shower have low momenta and are very likely to spiral, giving a signal in the FCB which is in general well isolated and not associated to any other track.

2.3.6 The trigger and the data acquisition systems

The goal of the trigger system is to choose, at each beam crossing, the potentially interesting events, reducing the flux of data and the dead time of the acquisition system. The DELPHI trigger system is divided into 4 levels, in order to provide a large redundancy. The first two levels (T1 and T2) are synchronized with the beam crossing signal. The other two (T3 and T4) are asynchronous and based on pattern recognition algorithms for specific detectors. T1 is based on simple correlations between detectors and gives a decision in about 3.5 μs. T2 uses detectors with a slower response, taking about 40 μs.

The selection criteria are implemented in tables read by the trigger processors. They are made out of several combinations of signals from the different subdetectors and give a positive answer whenever any of the combinations is positive. The main categories in which the combinations can be classified are:

- charged track,
- muon,
- electromagnetic energy deposition,
- luminosity.

For $q\overline{q}$ events the trigger efficiency is essentially 100%.

The data acquisition system (DAS) of DELPHI is responsible for the full chain of data taking, from the subdetectors to the storage in disk or magnetic tape. It is a modular system, respecting the subdetector structure of DELPHI. It has 17 partitions each corresponding to a subdetector or part of a subdetector. Only after an event passes the second level trigger, the local memories are passed to the central partition, together with the respective pointers and other information like the number of the trigger and the date and time of acquisition.

2.3.7 Event reconstruction and simulation

The raw data stored by the DAS are treated by a dedicated event reconstruction program [34] giving as an output a reduced amount of data. The output stream is the DST (Data Summary Tape). At the output level, the information from the different subdetectors is already associated, defining the final state particles whose kinematic characteristics are available to be used in the analysis codes. The DELPHI reconstruction program, DELANA [34], is divided in parts which are executed in sequence:

- reconstruction of the local information in each subdetector,
- search for tracks, trajectory fit and extrapolation,
- combination of the information of the calorimeters,
- global reconstruction, solving of ambiguities and information superpositions,
- particle identification,
- vertex reconstruction,
- classification of the event.

The DELANA code uses a data structure with several levels, TANAGRA (Track ANAlysis and GRAphics) [35] to store the information of the various reconstruction steps.

Very important for any physics analysis is the possibility of comparing the selected data with equivalent samples of simulated data. For this, after a sample of events has been generated for the interesting physics process(es), the detector effects must be included. The code performing the simulation of the DELPHI detector is DELSIM: DELphi SIMulation program [46].

The information about the specific conditions of the detector at a given moment (calibration constants, specific operation modes for some of the subdetectors) needed for the simulation and reconstruction programs are kept in a data base.

Chapter 3

Alignment

During my PhD activities I have taken over the responsibility for the software task of the alignment. To align Delphi means to find the position of each tracking detector with respect to the others. Among the duties of the alignment task, there is the checking of the distortions introduced by the wrong position of detectors in the database, and by the wrong calibrations of the drift detectors. During the year many alignment databases are produced in an iterative procedure, finally converging towards the optimal sub-detectors performances, and therefore on the precision of the different physics analyses.

3.1 How to proceed

The alignment of the tracking detectors is one of the most important calibrations needed for extracting physics results from the DELPHI data. In order to have systematic errors below the intrinsic resolution of the tracking detectors, the alignment is required to be better than 100 μm and often constraints are even more severe, like for the Vertex Detector (VD) where the point resolution is at the level of a few μm.

The reference frame definition is the starting point in the alignment procedure of the DELPHI tracking detectors. The best choice would be the centre of the solenoid due to the primary role that the magnetic field plays both in the particle momentum measurement, and in the signal distortion in the drift chambers. But, since it is not feasible to use the tracks to find the positions of each detector with respect to the magnet, another choice of the reference frame is needed. From an experimental point of view, a precise and stable detector is the best solution to define the reference frame. The Time Projetion Chamber (TPC) and Inner Detector (ID) depend on various effects that change rapidly with time (atmospheric pressure, gas composition, etc.). The Vertex Detector was upgraded continuously during the years until 1997, changing in size and performances, therefore it can not be used for an absolute frame definition. The Outer Detector (OD) turns out to be the best choice to define the Z axis and the Rϕ coordinates, while for the origin of the Z axis the TPC is used.

The OD has $\sim$ 120 microns resolution in the Rϕ plane. Systematic errors on the Z origin due to TPC drift velocity and timing imprecisions are strongly reduced by the cancellation of such effects between the positive and negative Z halves of the TPC where the drifts are in opposite directions.

The alignment procedure starts with finding the position of the Vertex Detector (VD) with respect to OD and applying a translation along the Z axis according to the TPC informations. In a second stage the $R\phi$ alignment of the TPC and the ID is performed. Finally the forward detectors are considered.

The main "instrument" in the alignment procedure are the residuals defined as the distance between a reconstructed track and the hit in a detector. Whenever residuals are computed "on a specific detector", this means that the track has been refitted without taking in consideration the information coming from that detector. As it will be shown later, the translations and rotations of a detector to bring it on its true position are deduced from the distributions of residuals.

The sample of tracks used in alignment procedure comes from $Z \rightarrow \mu^+\mu^-$ decays. In these decays, the muons are highly collinear and the imposition of the beam energy to the tracks improves the resolution.

3.2 VD-OD alignment

3.2.1 The Rϕ alignment

The Vertex Detector consists of 68 modules arranged in three layers (Closer, Inner, Outer) as described in section 2.3.3. It must be internally aligned [36] before its overall position, considering the VD as a rigid object, is found with respect to the other tracking detectors. The internal alignment is obtained assigning the status of *master* to a layer (until 1998 it was the Outer, in 1999 it was the Closer), and treating the others layers (Inner and Closer till 1998, Inner and Outer in 1999) as *slaves*. This means that the Closer layer is aligned as a full pseudo-cylindrical object using all $R\phi$ and Z overlap constraints between adjacent modules. Modules of slave layers are aligned individually with respect to the corresponding master modules. The overall quality of VD alignment is estimated comparing intrinsic hit precision (measured from residuals of tracks in the overlaps in the master layer) with the effective hit precision (measured from the residuals of tracks in the overlaps in the slave layers and which have not been used in the alignment procedure). This can be seen in figure 3.1.

Once the internal VD alignment is performed, the global one is examined. As explained in section 3.1 this is obtained finding the $R\phi$ position of the VD as rigid object with respect to the OD and the Z position with respect to the TPC.

Tracks of muons from $Z \rightarrow \mu^+\mu^-$ decays and with hits in the OD are considered. At this stage a complication arises. The track segments in OD do not have enough precision to be extrapolated to the VD due to the low lever arm in the OD. It is possible to improve the resolution treating the μ^+ and the μ^- as one track with bending radius:

$$\rho = \frac{\sqrt{E_{beam}^2 - m_\mu^2} * \sin\theta_{OD}}{0.003B} \tag{3.1}$$

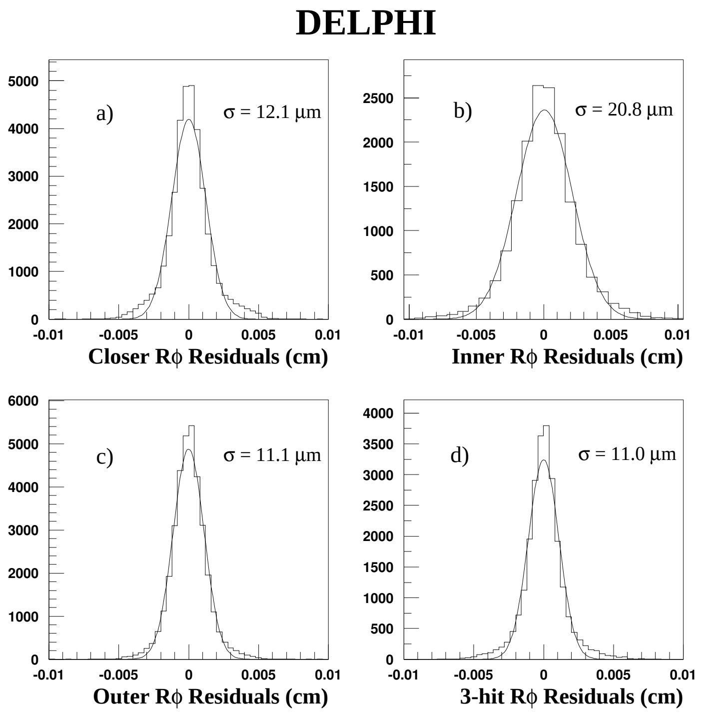

Figure 3.1: *Residuals distributions after internal alignment for 1999 data taking: a) tracks in Closer overlap, b) tracks in Inner overlaps and c) tracks in Outer overlaps. The residuals are computed between an hit in overlap and the track when it is forced through the other hit in the overlap. The width of each distribution has to be divided by* $\sqrt{2}$ *to obtain the single hit precision for that layer. Also shown are d) the Inner layer residuals for 3-hit tracks. The tracks are forced through hits associated in Closer and Outer and interpolated to Inner modules. What is plotted are the residuals between interpolated tracks and hits in Inner. For this plot, the width has to be divided by* $\sqrt{1.5}$ *to obtain the silicon precision, assuming that it is the same in each of the three layers.*

The θ_{OD} of this track is determined by averaging the two θ estimates from the two different TE's in TPC. The track is reconstructed simply as a circle with radius ρ passing through two OD hits.

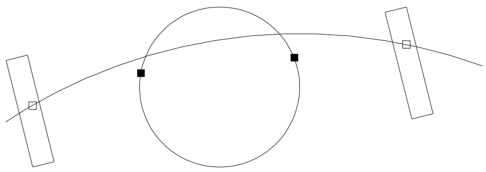

Figure 3.2: *Reconstructed track in OD can be extrapolated to VD.*

Finally this single $\mu^+\mu^-$ track is extrapolated to the VD (see fig. 3.2). The foreseen resolution (taking into account the resolution of the Outer Detector) is:

$$\sigma_{OD}/\sqrt{2} \simeq 120\ \mu m \quad \text{in } R\phi \tag{3.2}$$
$$\sigma_{OD}/\sqrt{2}R_{OD} \simeq 0.1\ mrad \quad \text{in } \phi \tag{3.3}$$

In figure 3.3 shows the distribution of the residuals between the track formed by the two $\mu^+\mu^-$ hits in opposite sides of OD and the hits in the VD. It can be noticed that the resolution ($300\mu m$) is considerably worse than the foreseen one. The main reason for this can be traced to the acollinearity of e^+e^- beams. In the Z^0 run at the beginning of 1999 data taking a first estimation of acollinearity was 98 ± 31 micro radians in both XY and XZ plane [37].

As a consequence, the single track formed by the muon pair can get an overall shift with respect to the two real muon tracks.

To demonstrate this, we can compute the kink angle between the trajectories of the two muons due to horizontal and vertical acollinearity [36]. Let us define:

- α_x = acoplanarity angle in horizontal plane
- α_y = acoplanarity angle in vertical plane
- ϕ, θ azimuthal and polar angle of the momentum vector of first muon

The kink angle is defined by:

$$\alpha = \frac{\alpha_x \sin\phi - \alpha_y \cos\phi}{\sin\theta} \tag{3.4}$$

In the geometrical acceptance of the VD this angle can assume values up to 0.4 $mrad$.

The tracks reconstructed as described above are extrapolated to the VD and the residuals between the track and the hit in VD are described in term of three translations (ΔX, ΔY, ΔZ) and three rotations (ϵ_x, ϵ_y, ϵ_z) of the nominal VD position with respect to the real one by:

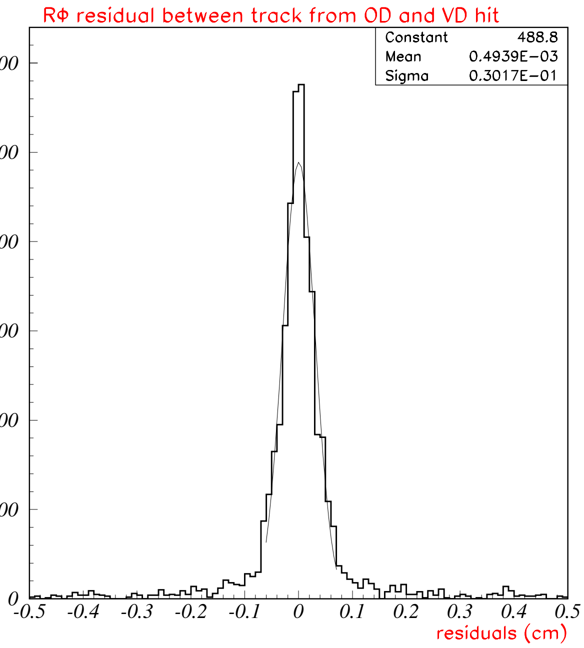

Figure 3.3: *Distribution of the residuals between a track computed using two $\mu^+\mu^-$ hits in opposite sides of the OD and the hit in the VD (from Z^0 run in 1999).*

$$\Delta R\phi = R\phi_{extr} - R\phi_{meas} \tag{3.5}$$
$$= \Delta X \sin\phi - \Delta Y \cos\phi - \epsilon_x Z \cos\phi - \epsilon_y Z \sin\phi + \epsilon_z R \tag{3.6}$$

The values of these parameters are computed by fitting the residuals distributions (fig. 3.4) and performing an iterative χ^2 minimisation.

The track extrapolation error contributes to the uncertainty in the alignment of the OD with respect to the VD. Although up to 12 points from the VD can be associated to the muon pair track, the errors are strongly correlated because of common contributions coming from extrapolation error.

To reduce the correlation in case of residuals computed in two points in opposite half shells of the VD one should proceed in the following way. For the residuals between the same OD track and two points in opposite half shells of the VD, the covariance matrix is approximately:

$$\begin{pmatrix} \sigma^2_{extr} + \sigma^2_{VD} & -\sigma^2_{extr} \\ -\sigma^2_{extr} & \sigma^2_{extr} + \sigma^2_{VD} \end{pmatrix} \tag{3.7}$$

The linear combinations (sum and difference) of the residuals diagonalizing the previous matrix are almost statistically independent and:

$$\sigma_{\Delta R\phi_1 + \Delta R\phi_2} \simeq \sqrt{2}\sigma_{VD} \tag{3.8}$$

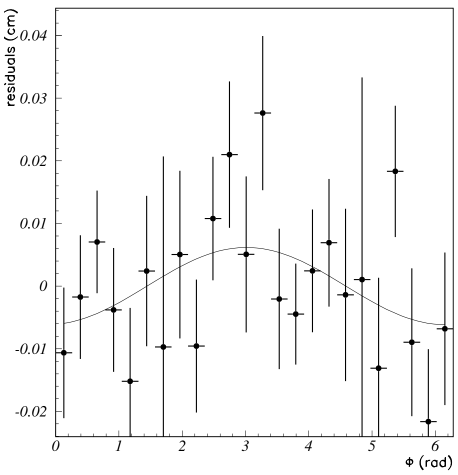

Figure 3.4: *$R\phi$ residuals between tracks reconstructed with OD TE's and VD hits, versus ϕ: the shape implies that that the VD detector is translated both along x and y with respect to the real position. The situation is the one on 1999 before alignment.*

$$\sigma_{\Delta R\phi_1 - \Delta R\phi_2} \simeq \sqrt{2}\sigma_{extr} \tag{3.9}$$

When taking into account the geometrical structure ($\phi_2 \simeq \phi_1 + \pi$ and $Z_2 \simeq -Z_1$) in eq. 3.6 the sum of residuals is sensitive to the rotation with respect to the nominal position, and the difference is sensitive to the translation.

Using the outer layer of the VD to extract the alignment parameters the following precisions are reached (see in figure 3.5):

$$\sigma_{\Delta X}, \sigma_{\Delta Y} = 700\ \mu m/\sqrt{N} \tag{3.10}$$
$$\sigma_{\epsilon_Z} = 0.4\ mrad/\sqrt{N} \tag{3.11}$$
$$\sigma_{\epsilon_X}, \sigma_{\epsilon_Y} = 1.6\ mrad/\sqrt{N} \tag{3.12}$$

During LEP2, at the beginning of data taking, a sample of Z^0 is collected to perform calibration tasks and the alignment of the detector. In 1999 2.5 pb^{-1} were collected; taking into account geometrical factors and efficiency, they correspond to about 2700 $\mu^+\mu^-$ usable in the alignment procedure.

When the request to have track hits in both the hemispheres in VD and OD detectors is added, the di-muon sample is reduced to $\simeq$1000 $\mu^+\mu^-$ and then:

$$\sigma_{\Delta X}, \sigma_{\Delta Y} \simeq 32\ \mu m \tag{3.13}$$
$$\sigma_{\epsilon_Z} \simeq 0.013\ mrad \tag{3.14}$$
$$\sigma_{\epsilon_X}, \sigma_{\epsilon_Y} \simeq 0.050\ mrad \tag{3.15}$$

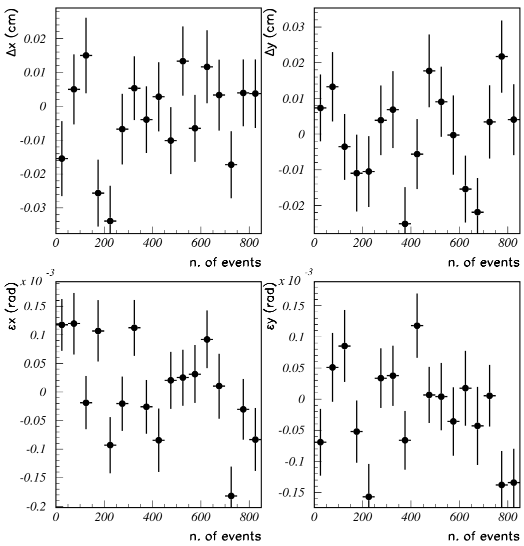

Figure 3.5: *Distribution of the alignment parameters for the VD after every 50 events.*

The use of more then one hit in VD does not improve the resolutions because of the correlation between the residuals. On the other hand the other VD hits are useful to control systematic errors on the internal VD alignment which can lead to different sets of alignment parameters depending on the VD layer used.

3.2.2 Z alignment

Once the VD position in the Rϕ plane is fixed, its position along the Z axis is determined looking at the residuals between TPC and VD. Tracks reconstructed using TPC-TE are extrapolated to the Outer layer of the VD and the residuals are computed. From the fit to the residuals distribution the VD translation along Z is extracted (fig. 3.6). All three layers are shifted according to the mean value of the residuals between the Outer VD layer and the TPC. There is no subdivision between the two half-shells of the VD because the relative position of them is fixed by the internal alignment.

It is important to notice that the Z alignment performed in such a way is not affected by eventual miscalibration of the drift velocity or timing in TPC. This is due to the fact that di-muons events have always hits in both the sides A and C of the TPC where the drift is in opposite directions, resulting in a cancellation of systematic effects with opposite sign in the two halves.

3.3 TPC and ID alignment

Once the VD is aligned, it represents a stable reference system within the full data taking period (it is affected by movements of the order of only 5 μm, see figure 3.22).

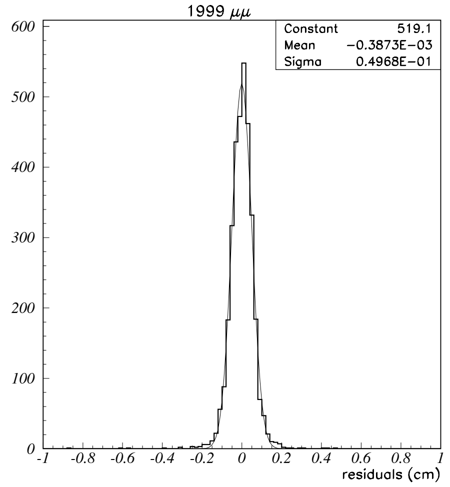

Figure 3.6: *z residuals between tracks computed with TPC TE and hits in Outer layer of the VD. The sample of track used is composed by muons from $Z^0 \rightarrow \mu^+\mu^-$ in 1999.*

To find the positions of the other barrel tracking devices of DELPHI, the TPC and the ID, a procedure based on both VD and OD is used. In this way one can take profit of the better resolution of VD the hypothesis of collinearity of muons is no more imposed and tracks are fitted using VD and OD hits only on the same side.

The OD hits are useful to decrease the extrapolation error with respect to the case in which only VD hits are used. This can be quantified by computing the error coming from the extrapolation of a track. Let R_1 and R_2 be the radius at which the track is measured, and σ_1 e σ_2 the corresponding errors on the measurement due to detector intrinsic resolution. Let R_{extr} be the radius at which the track is extrapolated. The error on the position of extrapolation is then:

$$\sigma_{extr.} = \sqrt{\left(\frac{R_2 - R_{extr.}}{R_2 - R_1}\right)^2 \sigma_1^2 + \left(\frac{R_{extr.} - R_1}{R_2 - R_1}\right)^2 \sigma_2^2} \tag{3.16}$$

When a hit in the OD is used, the term $R_2 - R_1$ (2 meters for VD+OD with respect to 5 cm for VD only) gives a significant improvement in the resolution with respect to the case when only VD is used (see table 3.1). In figure 3.7 residuals between tracks reconstructed with VD and OD and hits in TPC or ID are shown: the resolution is dominated by the detector intrinsic precision, and the extrapolation error is negligible.

Using (3.6) it is possible to fit the alignment parameters minimising the residuals.

The resolution obtained on the alignment parameters is now better (see figures 3.8 and 3.9) with respect to the one in VD–OD alignment due to the following reasons:

- the error on residuals ($\sqrt{\sigma_{point}^2 + \sigma_{extr.}^2}$) is lower than in VD–OD;
- the number of useful tracks is greater because now each event is used twice (once per track), and because it is possible to use events in which only one track has

	R_1 [cm]	R_2 [cm]	σ_1 [μm]	σ_2 [μm]	$R_{extr.}$ [cm]	$\sigma_{extr.}$ [μm]
VD only	6.3	10.9	9	9	R_{TPC} =71	150
VD + OD	6.3	201	9	120	R_{TPC} =71	40
VD only	6.3	10.9	9	9	R_{ID} =17.5	18
VD + OD	6.3	201	9	120	R_{ID} =17.5	10

Table 3.1: *Resolution in μm obtained extrapolating tracks with VD hits only or with VD and OD hits. The extrapolation has been computed in the middle of TPC ($R_{extr.}$=71 cm) and in the middle of ID ($R_{extr.}$=17.5 cm).*

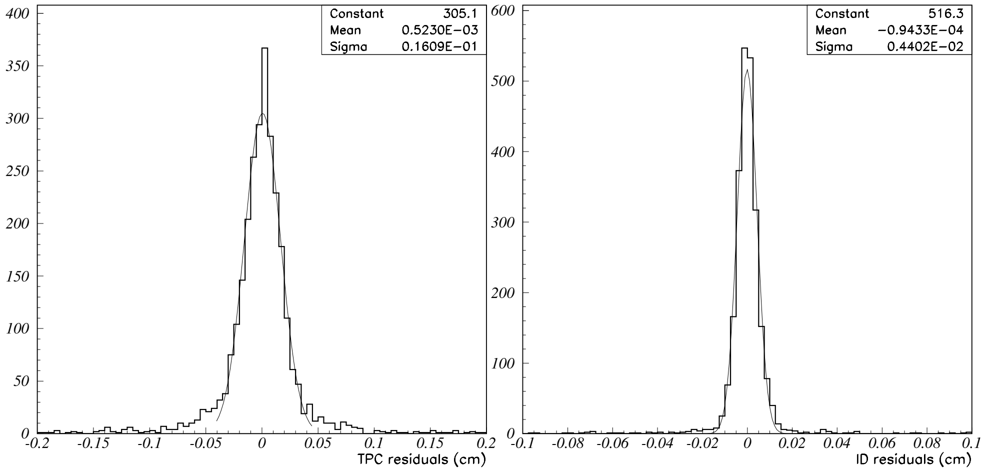

Figure 3.7: *$R\phi$ residuals between VD+OD tracks (dimuons from Z^0 run in 1999) and hits in TPC (left) and ID (right).*

hits in the OD;

- removing the collinearity hypothesis it is possible to reduce errors due to events with initial state radiation and to diverging beams.

3.4 Forward tracking detectors alignment

After having aligned the barrel detectors, the forward chambers (FC) are considered [38]. First of all the Forward Chamber B (FCB) is taken in consideration. A sample of forward muons is selected and muon tracks are reconstructed using VD, VFT (Very Forward Tracker) and ID. In this case the TPC is not used even if it partially covers the angular region of forward chambers, because of the distortions problem.

At the very early stage of data processing (when alignment is performed), the TPC is affected by calibration problems and distortions induced by the non homogeneity of the drifting field and the non perfect parallelism between the electric and magnetic

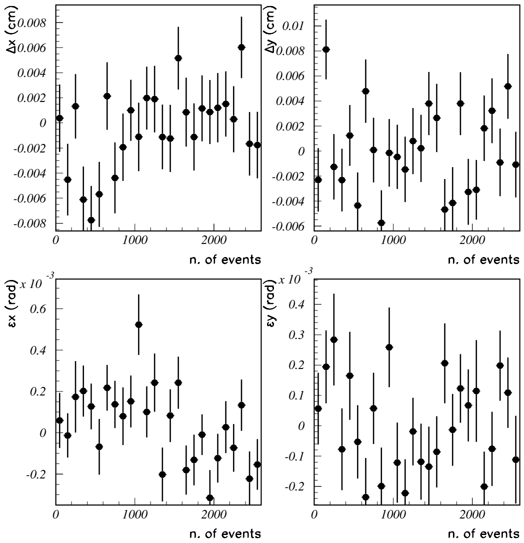

Figure 3.8: *Distribution of alignment parameters for the TPC every 100 events*

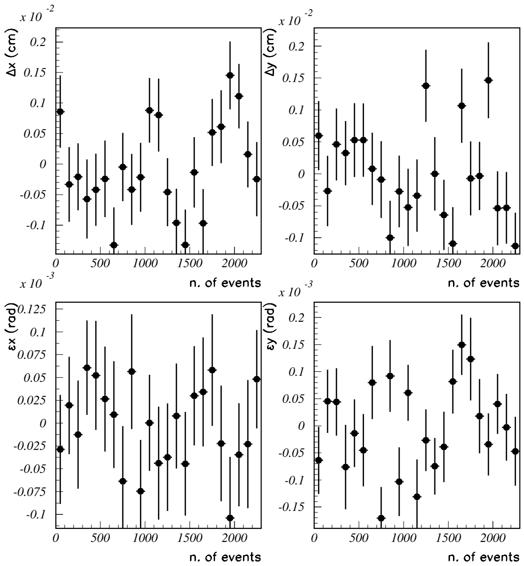

Figure 3.9: *Distribution of alignment parameters for the ID every 100 events*

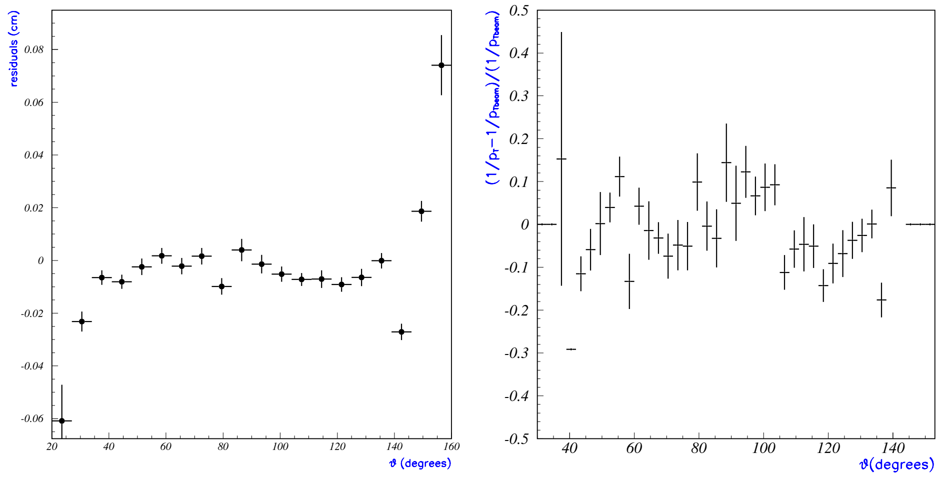

Figure 3.10: *Left: Z residuals versus θ of TPC track and corresponding VD hits. Right: $(1/p_T - 1/p_{Tbeam})/1/p_{Tbeam}$ versus θ_m: p_T is the momentum estimation in $R\phi$ plane coming from TPC TE only; p_{Tbeam} is the beam momentum multiplied by $sin\theta_m$; θ_m is the average between two θ from TEs of TPC (dimuons from Z^0 run in 1999).*

fields [39]. A check on the amount of distortions can be done taking the track element TE in the TPC and extrapolating it to the VD and computing the residual with the associated hits in the VD. As it is shown in figure 3.10, the residuals at low and high values of θ have a considerable shift which can affect the forward chambers alignment (see next paragraph). Another estimate comes by the momentum resolution when computing $1/p$ using the information from the TE of TPC only (figure 3.10).

For this reason it has been decided to not use TPC in the refit of the tracks in the forward alignment. For forward chambers, the computation of residuals is made in the local reference frame of each different module and in cartesian coordinates. The description of residuals in terms of translations and rotations is:

$$\begin{aligned} x_{fc} - x_{extr} &= -\Delta x + \Delta z \tan\theta \cos\phi && (3.17)\\ &+ y_{fc} \tan\theta \cos\phi \epsilon_x - x_{fc} \tan\theta \cos\phi \epsilon_y + y_{fc}\epsilon_z \\ y_{fc} - y_{extr} &= -\Delta y + \Delta z \tan\theta \sin\phi && (3.18)\\ &+ y_{fc} \tan\theta \sin\phi \epsilon_x - x_{fc} \tan\theta \sin\phi \epsilon_y + x_{fc}\epsilon_z \end{aligned}$$

where (x_{fc}, y_{fc}) and (x_{extr}, y_{extr}) are the cartesian coordinates in the local reference frame for the hit and the extrapolation respectively. Translations and rotations are derived minimizing the distributions of the residuals.

Modules AB, AD, CB, CDare treated independently in the alignment of FCB.

The next step is the alignment of Forward Chamber A (FCA). In this case in the fit of the tracks the information from just-aligned FCB is added to the one from VD, VFT and ID, reducing considerably the interpolation error to FCA. Sides A and C are treated independently.

The last step is the alignment of VFT [40]. Tracks fitted with VD, ID, FCA, FCB are used, and in this case also the information of beam spot is taken into consideration. All the degrees of freedom coming from considering the global position of VFT as a rigid object and the ones coming from the internal positions of all modules are fixed minimising residuals from refitted tracks.

One should note that also in this case the TPC is not used. To assure a consistent position of the VFT with respect to the other barrel detectors, the overlap between the first layer of pixels and the Outer layer of VD (in region $21^o \leq \theta \leq 25^o$) is used (see figure 3.11).

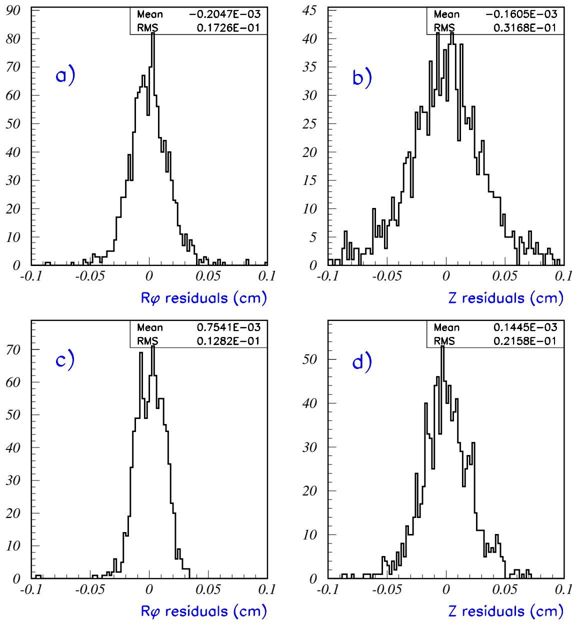

Figure 3.11: *Residuals in $R\phi$ and Z between hits in VFT and tracks fitted with VD, ID, FCA, FCB. The upper plots are made for tracks in the region $15^o \leq \theta \leq 21^o$ (no overlap with VD) and lower plots in region $21^o < \theta < 25^o$ (overlap with VD). In both cases the mean values are at zero showing an alignment position consistent both with the barrel and the forward detectors. The sample of tracks is composed by muons from Z^0 run in 1999.*

3.5 Alignment with cosmics

The flux of cosmic rays through the DELPHI detector is not negligible. The study of the potentiality of cosmic events in the alignment task is motivated by the lack of di-muons from Z^0 decays.

Some remarks are important when talking about cosmics:

- they are not synchronised with BCO (Beam Crossing Over);
- they do not have the same geometrical distributions as e^+e^- interactions;
- the tracks are not of fixed momentum.

Most of the DELPHI tracking detectors are gaseous detectors measuring the electrons drift time. The fact that cosmics are not synchronized with BCO implies that a determination of the crossing time T_0 of the cosmic muons in the detector is needed. That is the most important technical problem in analysing the data.

The second remark refers to the fact muons from cosmic rays are not pointing to the interaction region, but they are uniformly distributed in position and follow an angular distribution peaked toward the vertical direction. It means that the detector components of the tracks are quite different from the ones in collision events. Also few cosmics cross both barrel and forward detectors and have reduced utility for the alignment of the forward region.

The last remark is very important in defining the alignment procedure. For muon pairs the possibility to constrain the energy to be equal to that of the beam is extremely important to reduce extrapolation uncertainties and to partially correct for detector distortions. To provide an acceptable resolution, it is required that the In the case of a cosmic crossing the centre of the detector, it is reconstructed as two tracks in the TPC. Joining the two tracks to form one with longer lever arm (as is done for di-muon events in opposite hemispheres of OD) is the key point in providing an acceptable resolution and exploiting this sample of events, but strongly reduces the acceptance'

3.5.1 Alignment procedure

The uniform distribution of cosmic rays results in the need of using the TPC as the main alignment tool, because all the selected tracks contain TPC element, while only a small fraction has VD or ID in. The first thing to realize in such a case is that TPC distortions are important and translate into big systematics.

In muon pairs from Z decay, as it was shown in section 3.2, the errors in extrapolating from one detector to another are much reduced by imposing the beam energy constraint and the assumption of collinearity.

In cosmic events one can take full advantage of the fact there is really only one track and merge the two TPC segments to form only one with significantly improved resolution, as the lever arm for the measurement is improved by a factor three with respect to a standard TPC track.

In a perfectly aligned detector, when 'reflecting' one muon track to the other side of the detector it should perfectly match the second track. The perigee parameters $\vec{\varepsilon}$ and the covariance matrix $C_{\vec{\varepsilon},\vec{\varepsilon}}$ of one TPC TE of the cosmic ray are computed, and then are "reflected" into the other side of the detector to match with the second half of the

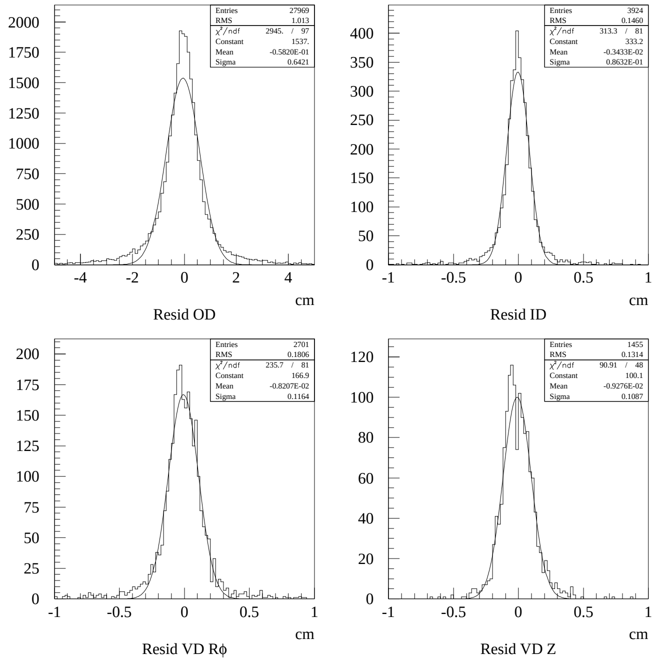

(a)

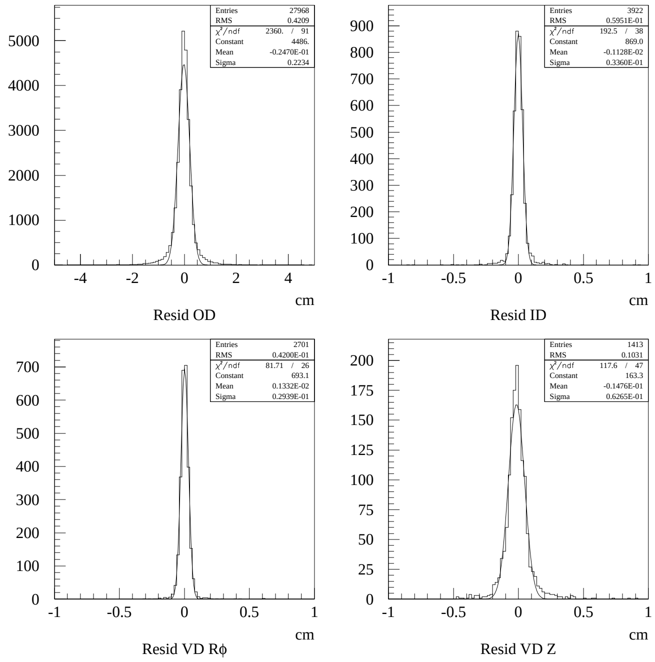

(b)

Figure 3.12: *Distribution of the difference between the measured points of OD, ID and VD with respect to the TPC extrapolation for cosmic rays: (a) with the single TPC TE and (b) joining the two TE's to form a single track.*

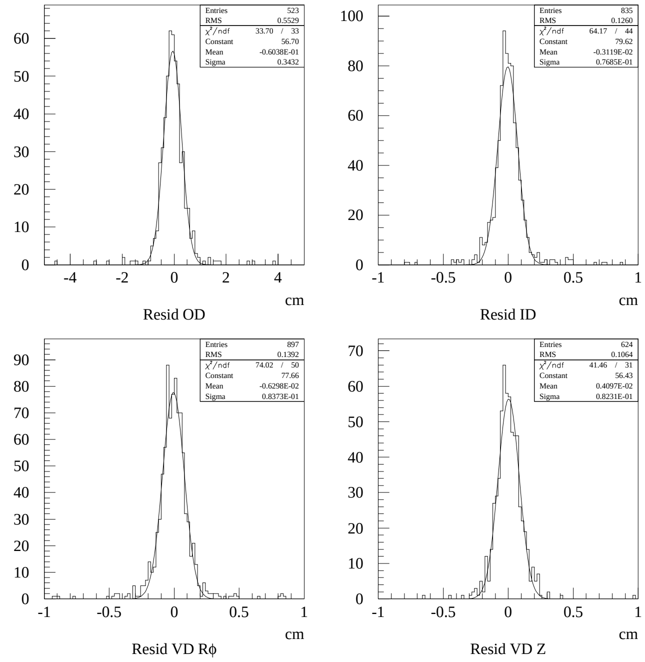

(a)

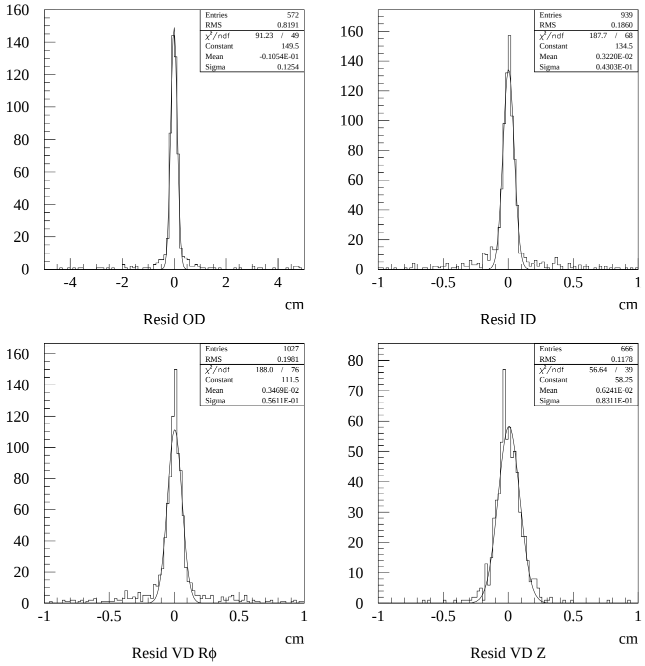

(b)

Figure 3.13: *Distribution of the difference between the measured points of OD, ID and VD with respect to the TPC extrapolation for muon pairs: (a) with the pure TPC TE and (b) imposing the momentum constraint.*

cosmic ray:

$$\begin{pmatrix} \varepsilon \\ z \\ \theta \\ \phi \\ 1/\rho \end{pmatrix} \longrightarrow \begin{pmatrix} -\varepsilon \\ z \\ \pi-\theta \\ \mathrm{mod}(\phi+\pi,2\pi) \\ -1/\rho \end{pmatrix} \tag{3.19}$$

$$\begin{pmatrix} C_{\varepsilon,\varepsilon} & & & & \\ C_{\varepsilon,z} & C_{z,z} & & & \\ C_{\varepsilon,\theta} & C_{z,\theta} & C_{\theta,\theta} & & \\ C_{\varepsilon,\phi} & C_{z,\phi} & C_{\theta,\phi} & C_{\phi,\phi} & \\ C_{\varepsilon,\frac{1}{\rho}} & C_{z,\frac{1}{\rho}} & C_{\theta,\frac{1}{\rho}} & C_{\phi,\frac{1}{\rho}} & C_{\frac{1}{\rho},\frac{1}{\rho}} \end{pmatrix} \longrightarrow \begin{pmatrix} C_{\varepsilon,\varepsilon} & & & & \\ -C_{\varepsilon,z} & C_{z,z} & & & \\ C_{\varepsilon,\theta} & -C_{z,\theta} & C_{\theta,\theta} & & \\ -C_{\varepsilon,\phi} & C_{z,\phi} & -C_{\theta,\phi} & C_{\phi,\phi} & \\ C_{\varepsilon,\frac{1}{\rho}} & -C_{z,\frac{1}{\rho}} & C_{\theta,\frac{1}{\rho}} & -C_{\phi,\frac{1}{\rho}} & C_{\frac{1}{\rho},\frac{1}{\rho}} \end{pmatrix}$$

After that a new set of parameters is obtained averaging the two measurements:

$$\vec{\varepsilon'} = \left(C^{-1}_{\vec{\varepsilon_1},\vec{\varepsilon_1}} + C^{-1}_{\vec{\varepsilon_2},\vec{\varepsilon_2}}\right)^{-1} \left(C^{-1}_{\vec{\varepsilon_1},\vec{\varepsilon_1}}\vec{\varepsilon_1} + C^{-1}_{\vec{\varepsilon_2},\vec{\varepsilon_2}}\vec{\varepsilon_2}\right), \tag{3.20}$$

$$C_{\vec{\varepsilon'},\vec{\varepsilon'}} = \left(C^{-1}_{\vec{\varepsilon_1},\vec{\varepsilon_1}} + C^{-1}_{\vec{\varepsilon_2},\vec{\varepsilon_2}}\right)^{-1}. \tag{3.21}$$

The new track is then used for extrapolation to all the other detectors. The improvement reachable with this approach is quite visible in figure 3.12, and should be compared with the effect of the momentum constraint for muon pairs in figure 3.13.

The relative position of the other detectors with respect to the TPC is determined extrapolating the new TPC track and performing an iterative χ^2 minimisation of the residuals between the track and associated hits in the detectors.

The functional dependence of the residuals on the alignment parameters (translations $\Delta_{x,y}$ in the $R\phi$ plane and rotation angles around the coordinate axes $\epsilon_{x,y,z}$) is very similar to the one used for the standard alignment (equation 3.6), with the difference that, as cosmics are not pointing tracks, one should take into account the effect of the angle $\beta = \phi_{\mathrm{direction}} - \phi_{\mathrm{position}}$ between the track direction and the normal to the extrapolation cylinder:

$$R\phi_{\mathrm{meas.}} - R\phi_{\mathrm{TPC\ extr.}} = \frac{\sin\phi}{\cos\beta}\Delta_x - \frac{\cos\phi}{\cos\beta}\Delta_y + \frac{z\cos\phi}{\cos\beta}\epsilon_x + \frac{z\sin\phi}{\cos\beta}\epsilon_y + R\epsilon_z. \tag{3.22}$$

In order to keep the convention according to which the DELPHI reference frame is given by the OD, first the TPC–OD relative position is determined, moving the TPC accordingly.

The subsequent step is to determine the relative position of VD, ID jet chamber and straw tubes with respect to the TPC. The TPC-OD fit involves a large number of tracks, but the single point resolution is of the order of 2 mm. The extrapolation toward the vertex region, instead, is quite accurate, since in reality it is an interpolation between two accurate TPC measurements.

In 1996, with a sample from two weeks of data taking, there was a total of 37k events with two tracks reconstructed in the TPC and with T0 determination. Of this sample about 2200 tracks had ID hits and 1300 had VD hits. With this set of tracks a statistical error of 10(15) μm in the $x(y)$ coordinate in the TPC-ID and TPC-VD alignment was obtained. The worse resolution in the y coordinate is due to the angular distribution of cosmics, which are mainly vertical.

However several systematic effects make difficult to reach this nominal resolution. The most important are:

- the additional errors induced by the T_0 uncertainty
- the fact that the detector point resolution is degraded for not pointing tracks.
- TPC distortions (which cannot be reduced imposing the momentum as in di-muons events)
- the fact that the non pointing distribution results in a very small probability to cross the overlap regions between VD modules.

To have an estimate on the better potentiality of di-muons events with respect to cosmics, one can make a comparison between the residuals used for alignment in the two different situations: figure 3.12 and figure 3.7.

In the forward region the statistics in cosmic events becomes more limited due to the low rate for low angle cosmics and the timing information is worse, therefore the use of cosmics data for the forward alignment is extremely difficult.

The cosmic events were particulary useful in 1996 and 1997, when during the winter shut down, the VD was extracted. They provided a preliminary alignment before the start of data taking. Since 1998 the DELPHI barrel detectors were not moved and the cosmics are used only for checks on the working of all modules of detectors and on preliminary estimation of possible movements of one detector with respect to another.

3.6 Alignment checks

The quality of the alignment can be checked by testing the tracks reconstruction. Systematic errors due to misalignment can be spotted by structures like the ones foreseen by formula 3.6 in the distribution of the residuals versus ϕ.

The overall precision can be estimated by looking at the sum of the impact parameters of the two muons (miss distance) in $Z \rightarrow \mu^+\mu^-$ events. Since both tracks are at high momentum, the smearing due to the multiple scattering can be neglected and effects due to misalignment can be detected. In figure 3.14 the improvement obtained after the alignment is evident both in the mean value and in the r.m.s. of the distributions.

Another interesting test is given by the momentum resolution (see figure 3.15). The distributions of $1/p_T - 1/p_{Tbeam}$ (where p_T is the momentum estimation in $R\phi$ plane and p_{Tbeam} is the beam momentum multiplied by $sin\theta_m$ with θ_m is the average between two θ from TEs of TPC) separated for positive and negative tracks is sensitive to possible rotations of detectors. As it is shown in figure 3.16, a rotation induces opposite variations on the value of the curvature for positive and negative tracks which can be seen separating the two samples.

After the alignment such rotations can be excluded (see figures 3.17 and 3.18).

It is interesting to see which would be the effect of uncorrected rotations on a physical analysis. During 1998 the forward chambers were aligned using also TPC in the refit of the tracks to be extrapolated. In a following processing of data the TPC corrections of distortions were updated without an update of forward detector alignment. The effect was an incompatible set of calibrations leading to an effective residual rotation of the forward chambers with respect to the TPC. The momentum for positive tracks was systematically decreased by $3 \div 4\%$ and the momentum for negative tracks was systematically increased by the same amount (see figure 3.19). As consequence, computing the W mass when the W decays to a muon detected in the forward regions, a shift between the two decays $W^+ \rightarrow \mu^+\nu$ and $W^- \rightarrow \mu^-\overline{\nu}$ channel was evident (see figure 3.20).

After a new alignment the rotation was corrected and the overall uncertainty on the W mass introduced by the muon momentum estimation was about 35 MeV/c^2 (see [41]) which is negligible with respect to the statistical error of 341 MeV/c^2 in the muon channel.

Another field in which the alignment directly influences physics performances of the DELPHI detector is the impact parameter resolution used in the b-tagging. In figure 3.21 the significance of impact parameters are shown in two different processings, with a preliminary alignment at the beginning of 1998 data taking and with the final alignment. The improvement after the detector calibration is clear and demonstrates the importance of the alignment task.

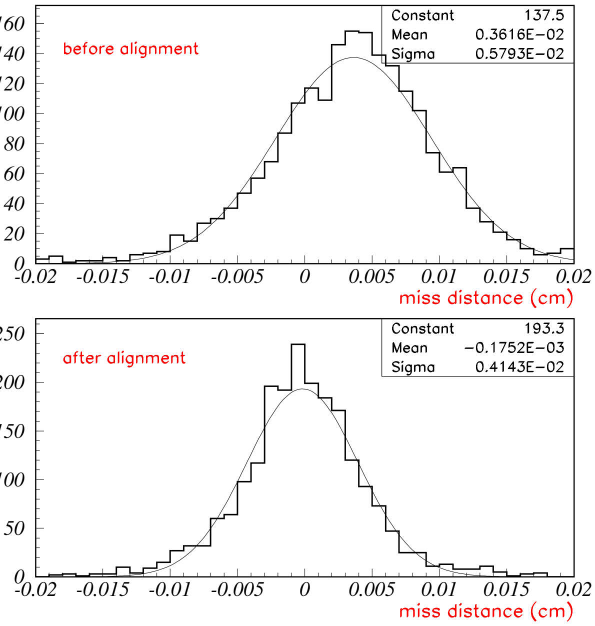

Figure 3.14: *Sum of impact parameter of muons in $Z^0 \to \mu^+\mu^-$ events, before and after the alignment for 1999 data taking.*

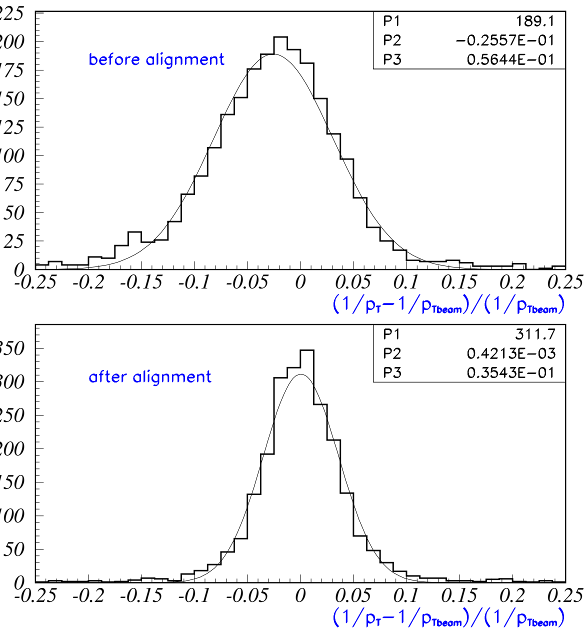

Figure 3.15: *Dimuons momentum resolution for barrel detectors before and after the alignment for 1999 data taking.*

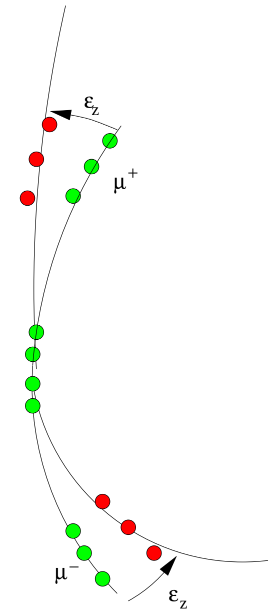

Figure 3.16: *A relative ϵ_z rotation between two sub-detectors causes a shift of opposite sign in the absolute value of the reconstructed curvature for positive (μ^+) and negative (μ^-) tracks, resulting in a difference in the momentum scale for opposite charges.*

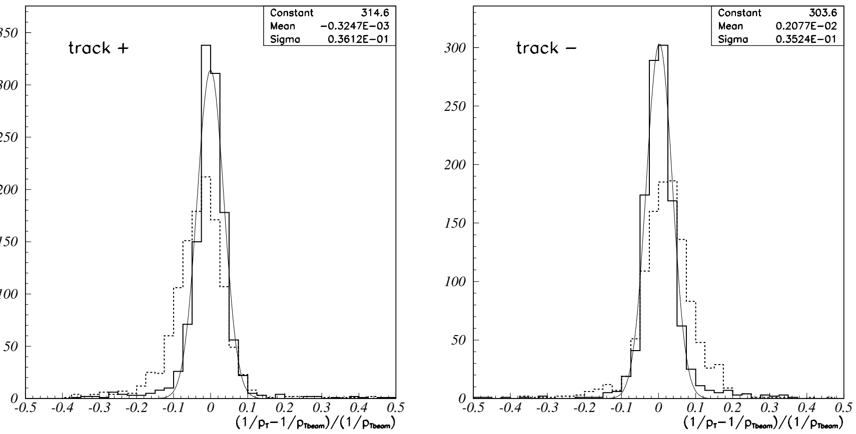

Figure 3.17: *Dimuons momentum resolution for barrel detectors before (dashed line) and after (full line) the alignment for positive and negative tracks. After the alignment the improvement in resolution is visible and there is no more a shift between positive and negative tracks.*

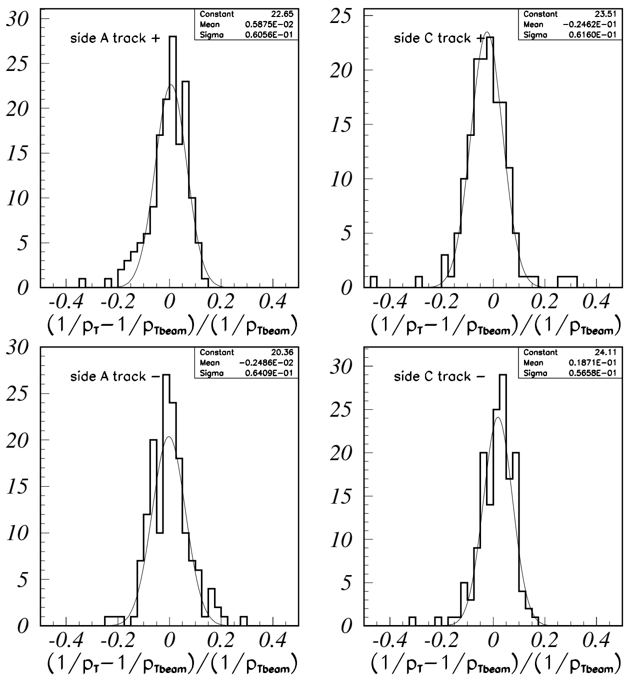

(a)

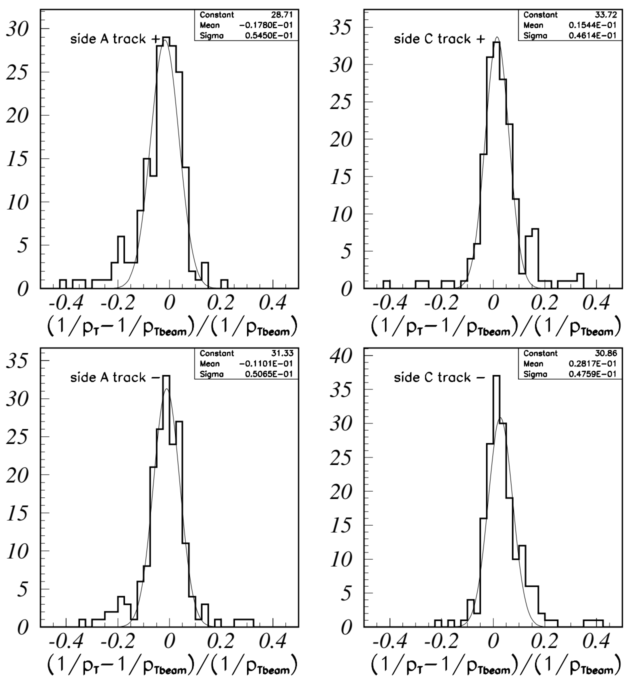

(b)

Figure 3.18: *Dimuons momentum resolution for forward chambers before (a) and after (b) the alignment for positive and negative tracks.*

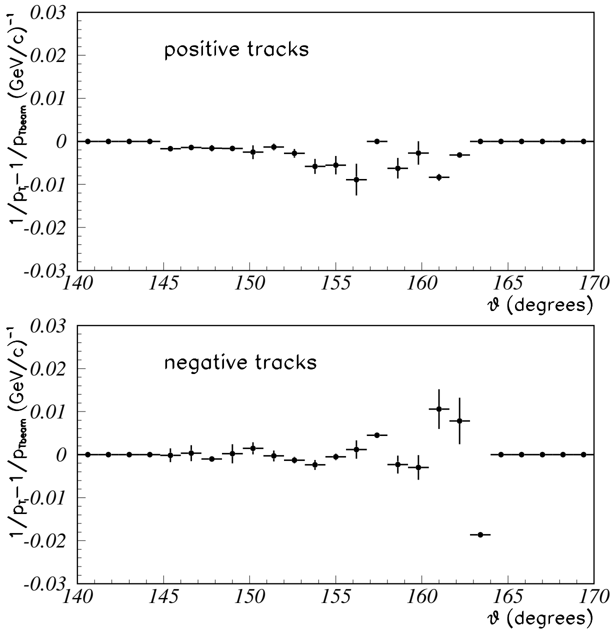

Figure 3.19: $1/p_T - 1/p_{Tbeam}$ *for positive and negative tracks in a module of FCB. A systematic overestimation (underestimation) is evident for negative (positive) tracks at high* θ.

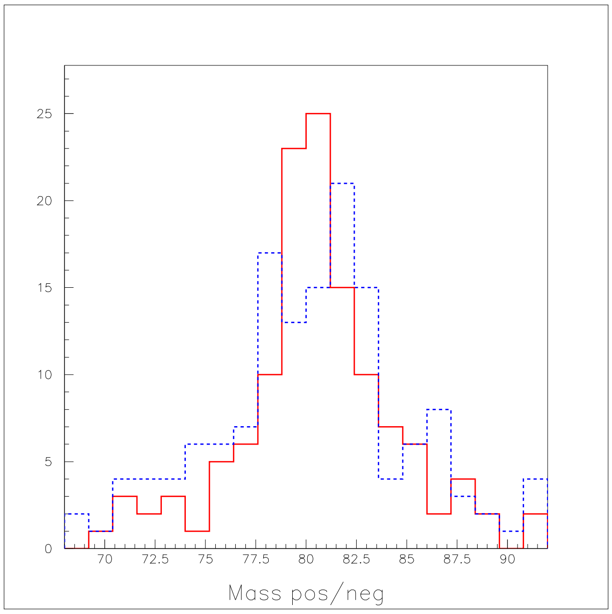

Figure 3.20: *W mass in [41]: full line for the decay* $W^+ \to \mu^+\nu$*, dotted line for the decay* $W^- \to \mu^-\overline{\nu}$*. The muons are detected in region of* $\theta > 140^o$*. There is a shift of 150 MeV.*

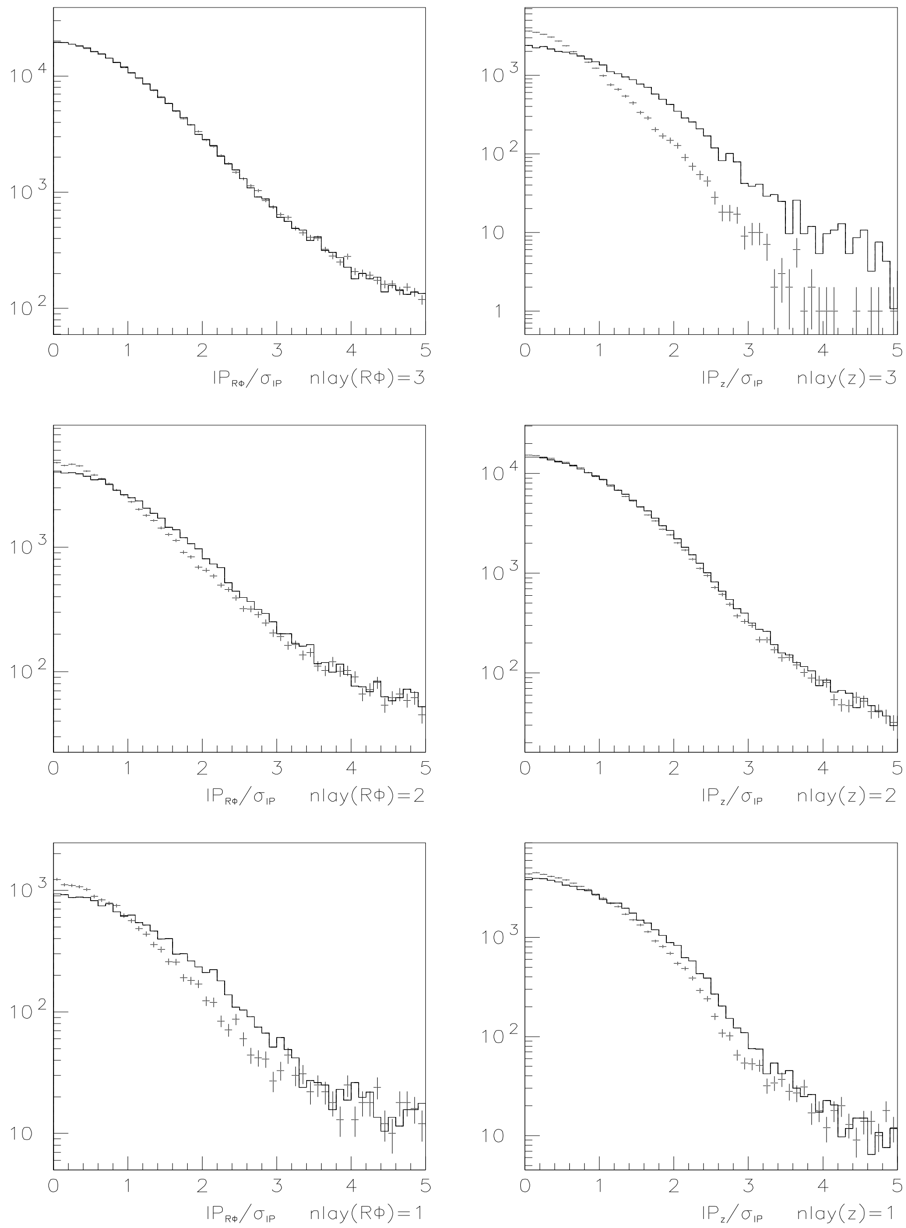

Figure 3.21: *Impact parameter significance in $R\phi$ and Z for tracks with hits in different number of VD layers. The full line is for the processing after the first alignment, the points refer to the processing after the last alignment. The resolution does not change significantly in the barrel part (three layers in $R\phi$ and two layers in Z), while it improves in the forward regions.*

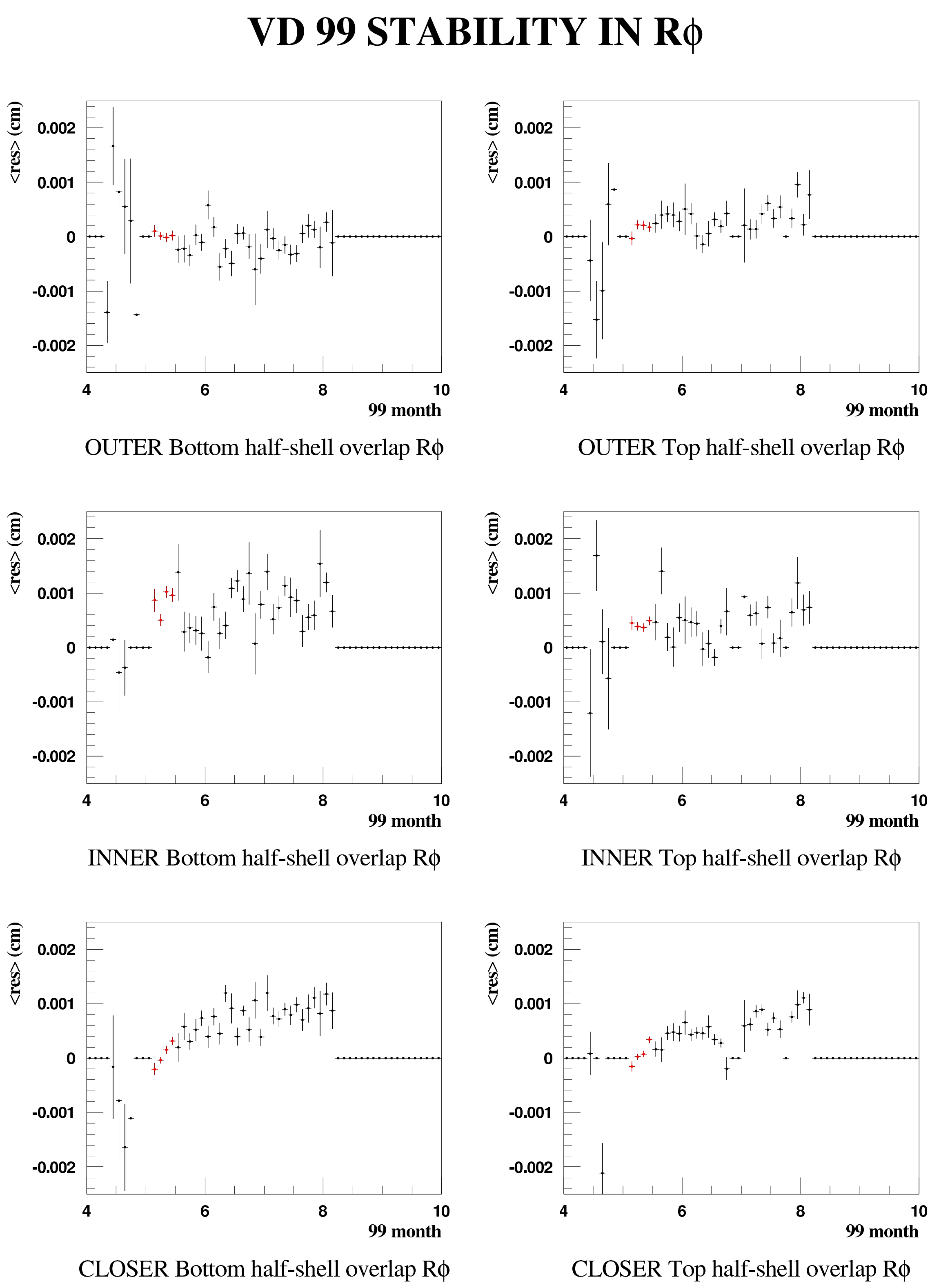

Figure 3.22: *Stability of $R\phi$ residuals for the overlapping regions (top: 90 degrees in ϕ and bottom: 270 degrees in ϕ) of two different half shellsof VD*

Chapter 4

Data selection to obtain a sample enriched in $e^+e^- \to H\nu\overline{\nu}$

In the analysis described in this thesis the Higgs bosons is searched in the final states with neutrinos: $e^+e^- \to H\nu\overline{\nu}$. They come from the Higgs-strahlung process: $e^+e^- \to Z^0H$ with $Z^0 \to \nu\overline{\nu}$; or from W^+W^- fusion process: $e^+e^- \to W^+W^-\nu_e\overline{\nu_e} \to H\nu\overline{\nu}$. All Higgs boson decays are considered. The branching ratio for these final states is of the order of 20% and they are the second most likely Higgs final states ag the LEP energies.

From now on, the process $e^+e^- \to H\nu\nu$ will be indicated as signal, while all the other LEP2 processes will be called background.

The first step for the Higgs hunting consists in applying a sequential series of cuts to select a sample of events with an increase in signal over background ratio. The main background processes are $e^+e^- \to e^+e^-$, $e^+e^- \to e^+e^-\gamma\gamma X$, $e^+e^- \to q\overline{q}\gamma$ and $e^+e^- \to W^+W^-$. The bulk of these events has a distribution in phase space with low overlap with the signal, and the sequential cuts can be used to remove them without affecting the signal efficiency. After the cuts, the remaining events have a distribution in phase space which has a not negligible overlap with Higgs signal. In such situation cuts on distributions are no more the most powerfull method to discriminate between signal and background.

4.1 Standard Model processes at LEP2

Since 1996 (LEP2 run) the centre of mass energy for LEP beams is increasing from 91.2 GeV to 200 GeV, and the integrated luminosities collected by the Delphi experiment are summarised in table 4.1(where at the time of writing this thesis, the 1999 data taking period was not yet finished) .

The SM cross-sections for some available processes at LEP2 energies as a function of the centre-of-mass energy are given in figure 4.1 [43]. Tree-level diagrams for the most relevant processes occurring at LEP2 are shown in figure 4.2. In next sections I will described some processes. I will give more details for the ones which constitute

Year	$\sqrt{\mathbf{s}}$(**GeV**)	$\mathcal{L}_{\text{DELPHI}}$ (pb^{-1})
1996	161.4	5.12
1996	161.6	1.23
1996	161.8	3.60
1996	170.4	0.74
1996	172.6	9.30
1997	183.2	53.7
1998	189.	158.
1999	192.	25.9
1999	196.	76.9
1999	200.	39.8

Table 4.1: *centre-of-mass energies and luminosities of the 1996-1999 LEP runs (last updates: september 1999).*

the relevant background in my Higgs search.

4.1.1 Two photons processes

The dominant process at LEP2 (whose cross section is not shown in figure 4.1) is $e^+e^- \to e^+e^-X$ (see figure 4.2(c)) where the system X is produced in the scattering of two quasi-real photons by $\gamma\gamma \to X$. It is necessary to use three different models to describe the process:

- VDM model (Vector Dominance Model): it is a non perturbative model where two photons interact creating vector mesons (ρ, ω, ϕ);
- QPM model (Quark Parton Model): the two photons interact exchanging a quark;
- QCD model: it is a model based on the partonic structure of photon which uses Quantum ChromoDinamics.

The cross section grows like $(\ln s/m^2_{electron})^2$ and reaches several thousands of picobarns (for example, at 184 GeV the cross section for $e^+e^- \to e^+e^-\gamma\gamma \to e^+e^-$ *hadrons* visible in the detector has been estimated to be $11.29nb$ summing the contributions from the three different models), but , as it will be shown later, the kinematics for this process is quite clear and it is easily removed in a selection of events for Higgs analysis.

4.1.2 Two fermion processes

The quark- and lepton-pair production $e^+e^- \to Z^0/\gamma(\gamma) \to f\overline{f}(\gamma)$ (see figure 4.2) is still a dominant process and can be used to extend the LEP1 precision measurements to this new energy range.

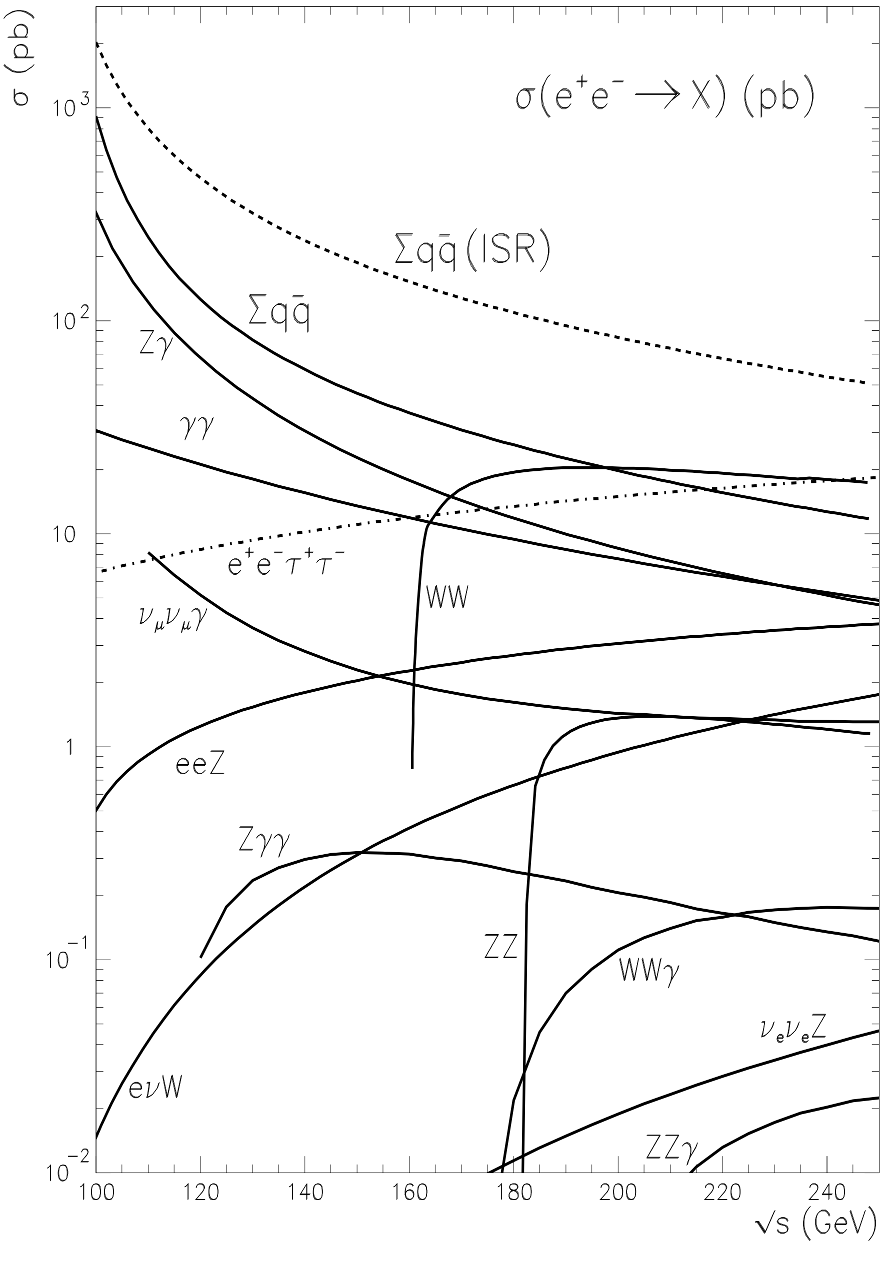

Figure 4.1: *Cross-section values for the most relevant SM processes as a function of the centre-of-mass energy.* $\sum q\overline{q}$*(ISR) refers to the hadronic final state of* $e^+e^- \to Z^*\gamma^*$ *with or without ISR photon.* $\sum q\overline{q}$ *refers to the hadronic final state of* $e^+e^- \to Z^*\gamma^*$ *without ISR photon.* $Z\gamma$ *refers to all final state of* $e^+e^- \to Z^*\gamma^*$ *with a ISR photon with polar angle satisfying* $|\cos\theta_\gamma| < 0.9$.

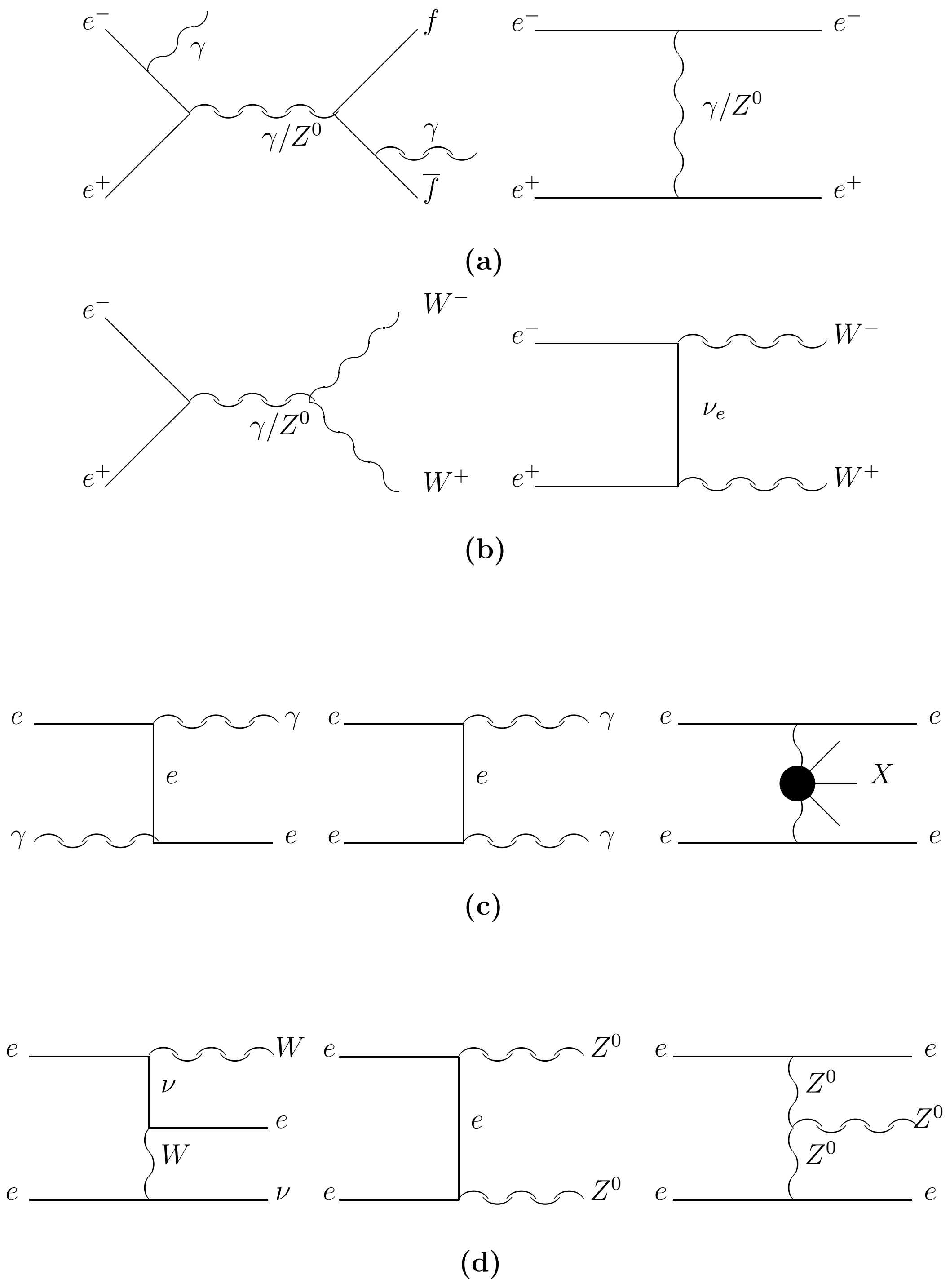

Figure 4.2: *Lowest order diagrams for the main processes occurring at LEP 2.* **(a)** $e^+e^- \to f\overline{f}$ *: s- and t-channel contributions,* **(b)** $e^+e^- \to W^+W^-$*: s- and t-channel contributions,* **(c)** *(from left to right) Compton,* $e^+e^- \to \gamma\gamma$ *and "$\gamma\gamma$" events,* **(d)** *other 4-fermion processes.*

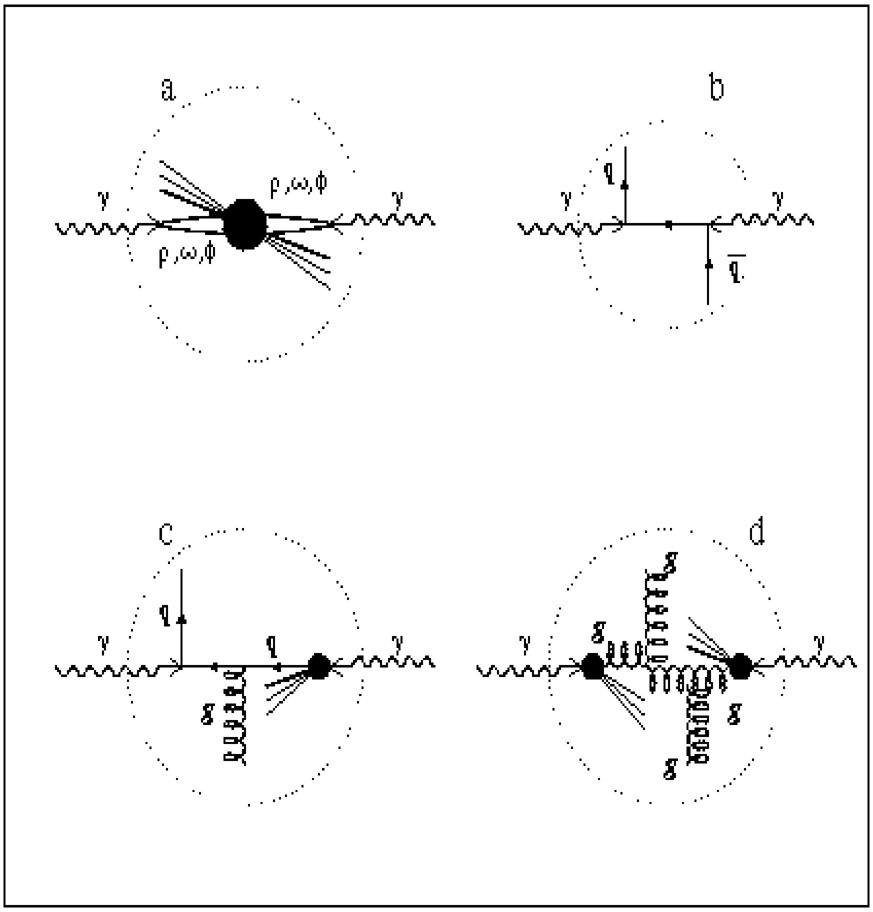

Figure 4.3: *Feynman diagrams in two photons process: a) non perturbative contribution (model VDM); b) direct contribution (model QPM); in c) and d) one or two photons interact directly through partonic structure (model QCD).*

For example the Bhabha cross section $e^+e^- \to Z/\gamma \to e^+e^-$ at 196 GeV with polar angle of the electron greater than 9 degrees has been estimated to be $1119 \pm 5pb$. The cross section is highly peaked at low polar angle, due to the contribution of the t-channel displayed in the second diagram in 4.2(a). Also in this case it is easy to remove Bhabha events in a Higgs analysis.

The cross-section $\sigma(e^+e^- \to Z^0/\gamma \to \ hadrons)$ measured by DELPHI from the Z^0 peak to $\sqrt{s}$ =172 GeV is shown in figure 4.4 [44], as well as the Standard Model predictions. It should be noted that now, away from the Z^0 peak, both the Z^0 and the γ exchange diagrams are relevant, as well as the interference term. One of the most remarkable features of this process at energies above the Z^0 peak is the radiative return to the $Z^0 : e^+e^- \to Z^0\gamma$ events (the emitted photon is called "Initial State Radiation" photon) in which the energy of the photon is such that the Z^0 is real. The ISR photon is preferentially emitted at low polar angles and often lost in the beam pipe.

From the convolution of the initial state radiation energy spectrum with the $e^+e^- \to$

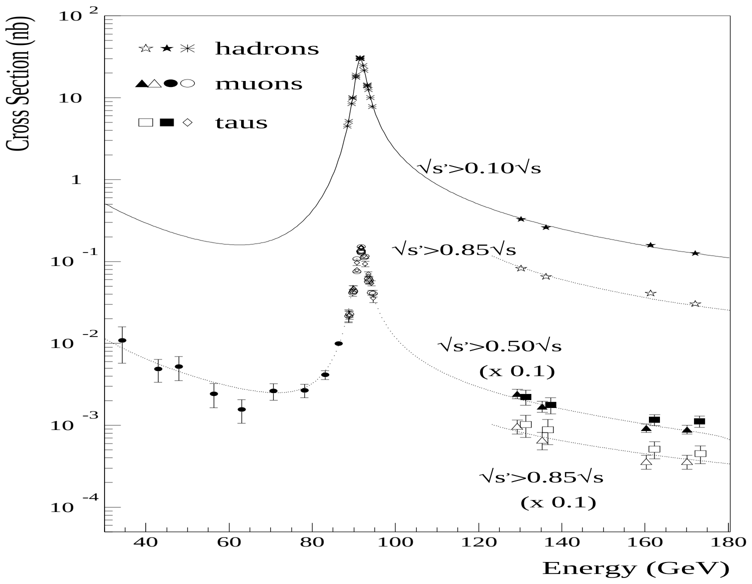

Figure 4.4: *Cross-sections of the process $e^+e^- \to f\overline{f}\gamma$ for hadron, electron, muon and tau final states as a function of the energy. The data correspond to DELPHI measurements at the Z^0 peak, at 130-136 GeV and at 161 and 172 GeV [44].*

$f\overline{f}(\gamma)$ cross-section, it results that the emission of an energetic photon such that the Z^0 is real is a highly favoured process.

This can be seen in figure 4.5, where the effective centre-of-mass energy is shown for $\sqrt{s}$ =189 GeV centre of mass energy data. As a consequence, the effective luminosity at centre of mass energy of 189 GeV will be lower. The energy of the radiative return photons can be computed as a function of the centre-of-mass energy and is given by:

$$E_\gamma = \frac{s - m_Z^2}{2\sqrt{s}}.$$

For $\sqrt{s}$ =189 GeV this gives $E_\gamma \simeq$72.5 GeV.

It will be shown later that these events are a non negligible background for the analysis done in this thesis.

4.1.3 Four fermion processes

As shown in figure 4.1, the threshold for the production of $W^\pm$ pairs is reached around $\sqrt{s}$ =161 GeV. Figure 4.2(b) shows the relevant diagrams. These t- and s-channel diagrams interfere negatively. At the threshold, the cross-section value is very sensitive to the $W^\pm$ mass. The cross-section values measured by DELPHI at different centre-of-mass energies and the corresponding SM prediction are shown in figure 4.6 [45]. W bosons decay $\sim$ 70% of the cases into quarks and $\sim$ 10% into each of the three lepton families . The possible final states are summarised in table 4.2.

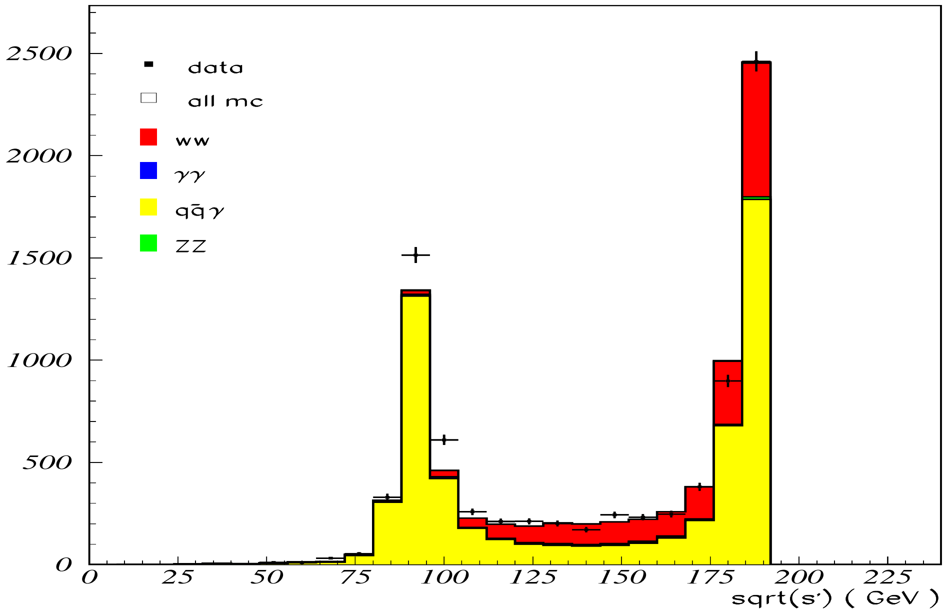

Figure 4.5: *Effective centre-of-mass energy at 189 GeV for hadronic final states. The crosses are the data and the histograms are the SM expectation.*

composition	br
$q_1\overline{q_2}q_3\overline{q_4}$	45.9
$q_1\overline{q_2}l\nu$	43.7
$l_1\overline{\nu_1}\overline{l_2}\nu_2$	10.4

Table 4.2: *Branching ratio of W^+W^- final states.*

At the centre-of-mass energy of $\sqrt{s}$ =183 GeV the threshold for the production of Z^0 pairs is reached. The relevant diagram is shown in figure 4.2(d) (central diagram). This t-channel diagram is present already below this energy but one of the Z^0's is virtual. When one Z^0 decays into neutrinos, such events are an irreducible background in the analysis done in this thesis.

Figure 4.2(d) shows also the diagrams of relevant 4-fermion processes not corresponding to the production of $W^\pm$ or Z^0 pairs. The main contributions (neglecting the $e^+e^- \to e^+e^-\gamma\gamma \to e^+e^-q\overline{q}$) come from single resonant processes such as: $e^+e^- \to e\nu W \to e\nu f f'$ and $e^+e^- \to e^+e^-Z \to e^+e^-ff$. The cross-sections are in general low, as seen in figure 4.1, but for some specific final states the contribution to background for the analysis done in this thesis is not negligible.

4.1.4 Other processes

In figure 4.2(c) are represented the diagrams corresponding to Compton-like events ($e\gamma \to e\gamma$), occurring by collision of one of the initial electrons with a photon emitted by the other one (with the other electron lost in the beam pipe), and the QED two-

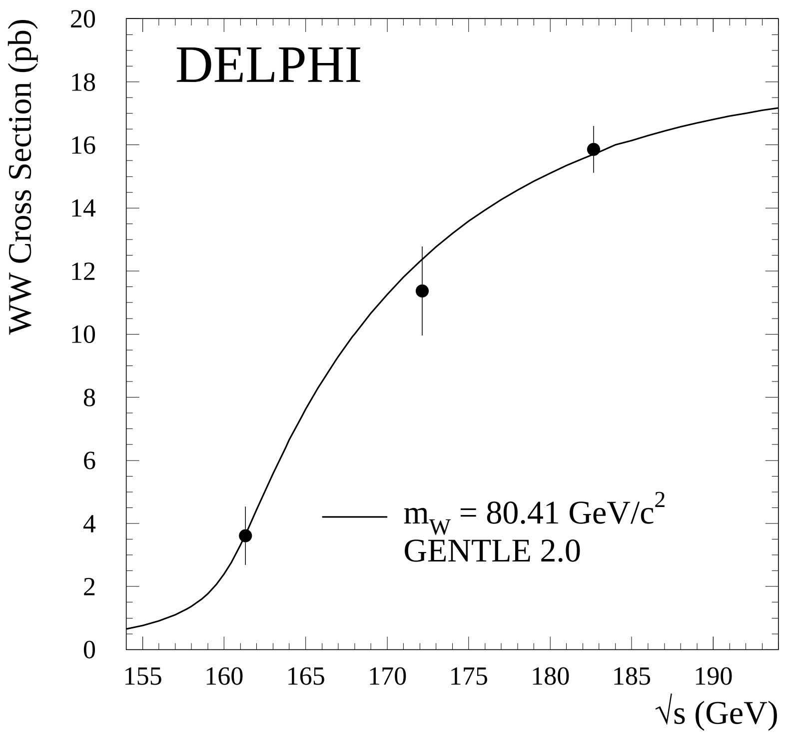

Figure 4.6: *$e^+e^- \to W^+W^-$ cross-section as a function of the centre-of-mass energy. The DELPHI measurements (dots) are shown together with the SM prediction using $m_W = 80.41$ GeV/c^2.*

photon production $e^+e^-\gamma\gamma$. Both of these classes of events are easily removed in Higgs analysis.

As figures 4.4 and 4.6 show, the measurements for energies above the Z^0 peak continue to show a good agreement between the model and the experimental results. The precision of the measurements is now much lower, due to the limited statistics, but the predicted values for the $e^+e^- \to q\bar{q}$ and $e^+e^- \to W^+W^-$ cross-sections agree with the measured ones and the branching fractions of the $W^\pm$ and Z^0 bosons are, for all the energies, within the expected values.

4.2 Study of the background

As has been shown in the first chapter, the cross section for Higgs production is of the order of some hundred femtobarns, while in the previous section we saw that other Standard Model processes have cross section of several hundred picobarn.

The first part of the analysis of this thesis consists in developing methods to select a sample of events where the background has been suppressed without dramatically affecting the signal efficiency. It results in an increase of the signal over noise ratio. The aim is achieved in two steps:

- a set of variables has been identified with spectra extending into regions of phase space without signal. A sequential series of cuts has been applied on these variables;

- another set of variables has been found with spectra that (even if covering more or less the same phase space as the signal) have different probability density functions with respect to the signal, and so have high discriminant power between background and signal.

To pursue the study, a set of all relevant LEP2 background processes and Higgs signal have been generated and the behaviour inside the detector must be simulated. The event simulation is made by generating the quadrimomentum $(E, \vec{p})$ of primary particles involved, and then generating the quadrimomentum of all particles following the decay of primary ones. When quarks are produced, the fragmentation and hadronisation has been performed using JETSET [47]. The interaction between particles and the DELPHI detectors must be reproduced. All the detector effects have been included. The code performing the simulation of DELPHI (DELSIM, DELphi SIMulation program) [46] contains a description of the detector from the point of view of the geometry, material composition and operation efficiency and follows the generated particles in their interaction with the material of the various subdetectors. Raw data structures similar to the ones obtained for real data are created and treated with the same reconstruction program.

4.2.1 Background simulation

Table 4.3 summarised the set of simulated processes, the generator used, the corresponding cross section and the number of generated events.

One should note that the number of generated events is several times the expected values considering the integrated luminosity of $158pb^{-1}$ during 1998 data taking. In this way statistical errors in simulated distributions can be strongly reduced.

Usually in the simulations some cuts are applied to avoid divergence of cross sections or simply to take into account detector acceptance. Here follows some of these cuts and some remarks:

- Bhabha: $\theta_{electron} > 9^o$ and energy of electron > 50 MeV;

- two fermions: in this case there are no cuts, but the final state with electrons has been excluded to avoid double counting with the previous generator. The ISR has been taken into account. Parameters for quark fragmentation have been derived from DELPHI data;

- two photons: all models described in section 4.1.1 have been taken into account;

- four fermions: concerning $e^+e^-e^+e^-$ final state, there are the following cuts:

  - $|\cos\theta_e| < .98$

process	final state	generator	cross section (pb)	n. of events
compton	$e^+e^-\gamma$	CMPT	55.97	29748
2 fermions:	e^+e^-	BHWIDE	1200	21000
	$Z^0\gamma \to \gamma\mu\overline{\mu}$	KORALZ	8.25	11481
	$Z^0\gamma \to \gamma\tau\overline{\tau}$	KORALZ	8.19	10866
	$Z^0\gamma \to \gamma q\overline{q}$	PYTHIA	99.0	140279
$\gamma\gamma$ unbiased:	$e^+e^-e^+e^-$	BDK	2165	377298
	$e^+e^-\mu\overline{\mu}$	BDK	1909	322058
	$e^+e^-\tau\overline{\tau}$	BDK	443.8	56214
	e^+e^-+ hadrons	VDM	7920	449035
	e^+e^-+ hadrons	TWOGAMMA	2395	350889
	e^+e^-+ hadrons	BDKRC	980.1	155651
4 fermions:	$e^+e^-e^+e^-$	EXCALIBUR	.42	2019
	$l\overline{l}l\overline{l}$	EXCALIBUR	0.0447	600
	$\mu\overline{\mu}q\overline{q}$	EXCALIBUR	0.262	752
	$\tau\overline{\tau}q\overline{q}$	EXCALIBUR	0.1057	723
	$\nu\overline{\nu}q\overline{q}$	EXCALIBUR	0.26	5811
	WW like	EXCALIBUR	17.73	41679
	$e\nu q\overline{q}$	GRC4F	0.35	1199
	$e\nu\mu\nu$	GRC4F	0.0539	900
	$e\nu\tau\nu$	GRC4F	0.0503	900
4 fermions:	$We\nu$	PYTHIA	.55	8997
	WW like	PYTHIA	16.51	12514
	ZZ	PYTHIA	1.59	13118
	Ze^+e^-	PYTHIA	8.16	13319

Table 4.3: *Simulated processes, used generator, corresponding cross section, number of generated events.*

- invariant mass for each e^+e^- combination > 50 MeV/c^2
- energy of electron > 1 GeV

Concerning $l\overline{l}l\overline{l}$ it contains final states with four μ or τ.
Concerning $q\overline{q}e\nu$, $\mu\nu e\nu$, $\tau\nu e\nu$ final states, the cut is $|\cos\theta_e > .9999|$. This cut has been required because the GRC4F generator has been used only to cover that particular region of phase space not covered by the WW EXCALIBUR generator. Concerning the WW: it contains also the final states WW like, but coming from ZZ;

- second sample of four fermions: as can be seen in table 4.3, there are two samples of four fermions: one realized using the EXCALIBUR and GRC4F generators , and the other using the PYTHIA generator. The two samples have been produced to cross check the results.

4.3 Study of the signal

During the studies to perform the analysis, a detail examination of signal generation has been done.

process	Higgs mass (GeV/c^2)	generator	n. of events
Higgs-strahlung	85	HZHA	5100
+ WW fusion	90	HZHA	5398
	95	HZHA	5400
	97.5	HZHA	2999
Higgs-strahlung	90	WPHACT	6000
+ WW fusion	95	WPHACT	6000
+ interference	97.5	WPHACT	5998

Table 4.4: *Simulated process, Higgs mass, used generator and number of generated events for signal.*

I considered two different generators (see table 4.4):

- HZHA [48].
  It allows eight different Higgs production processes to be simulated:
  - 1. $e^+e^- \to hZ \to hf\overline{f}$
  - 2. $e^+e^- \to HZ \to Hf\overline{f}$
  - 3. $e^+e^- \to hA$
  - 4. $e^+e^- \to HA$
  - 5. $e^+e^- \to \nu\overline{\nu}h$ via WW fusion
  - 6. $e^+e^- \to \nu\overline{\nu}H$ via WW fusion
  - 7. $e^+e^- \to e^+e^-h$ via ZZ fusion
  - 8. $e^+e^- \to e^+e^-H$ via ZZ fusion

  but no interference between these channels is included. The initial state radiation is implemented and the final state radiation is implemented for the leptonic Z decays in the processes 1 and 2.

  All SM and MSSM final states are considered. The coupling of the Higgs bosons to the quarks are computed using two-loop running quark masses evolved to the Higgs boson mass scale. The pole masses chosen for the c and b quarks are 1.64 and 4.87 GeV/c^2. The cross sections for all requested processes and decay width/branching ratios for Higgs bosons are computed with all QED and QCD corrections. The program is interfaced with JETSET for the hadronization of the final state quark.

- WPHACT [49].
  It computes all SM processes with four fermions in the final state at e^+e^- colliders. No stable Z or Higgs are allowed in the final state. They are always considered as virtual particles. The Higgs decay particles are always treated as massive, both in the matrix elements of signal and background and in the phase space. All four fermion final states can be massive or not. Initial state radiation is included. All amplitudes are evaluated with the helicity formalism which is based on the insertion in spinor lines of a complete set of states for every fermion propagator. These states are the eigenstates of $\not{p}$, where p is the momentum flowing in the fermion propagator. It is easy to obtain contributions from different set of diagrams and their interference, as each diagram is evaluated individually for each helicity configuration and then summed to the others before squaring and summing over helicity configurations.

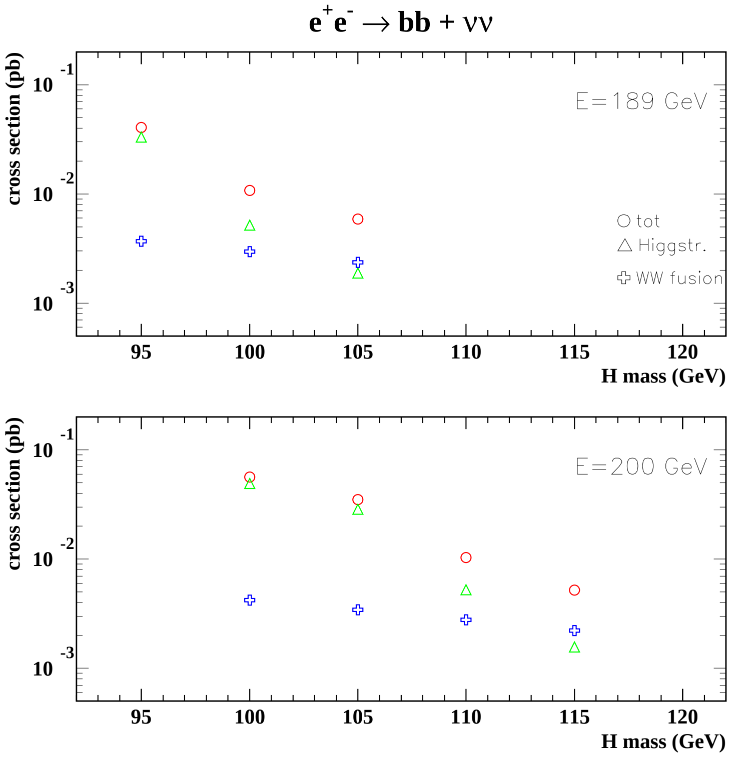

Figure 4.7: *Contributions to total cross section for $H\nu\overline{\nu}$ final state: Higgs-strahlung and WW fusion with interference included.*

Using WPHACT we have computed the cross sections for the final states $b\overline{b}\nu\overline{\nu}$ (4.7), mediated by Higgs particle. (Since Higgs decays $\sim 85\%$ of the cases in $b\overline{b}$ we produced only the b quark final state). From this plot a crucial point is immediately evident: the contribution to the cross section due to WW fusion becomes more and more important approaching the kinematical limit: at 200 GeV energy in the centre of mass and for a

Higgs of 110 GeV/c^2 mass, the total cross section with neutrinos in the final state is two times the one due to Higgs-strahlung and WW fusion.

The other crucial point is evident in figure 4.8. In this case using again WPHACT, we plotted the distributions for some interesting variables of the final states:

- acoplanarity of two final jets coming from b quarks. It is defined as 180^o minus the angle in $R\phi$ plane between the direction of the two jets;
- acollinearity of two final jets coming from b quarks. It is defined as 360^o minus the angle in space between the direction of two jets;
- energy of the most energetic jet (coming from hadronization of b quark);
- missing momentum along the beam pipe.

It is evident that the distributions for the variables are quite different (as one can expect) when Higgs-strahlung or WW fusion are the concerned process. The computation of signal efficiency after each cut is based on variables like those in figure 4.8. Moreover, the discrimination between signal and background is based on probability density functions of these (and other) variables as will be shown later.

So it is extremely important to have the right contributions from all processes to the total cross section to have the right distribution of variables in phase space to avoid systematic errors in signal estimation.

Since HZHA does not take into account the contribution from interference, and after the study I pursued, it has been decided to take WPHACT as the official DELPHI generator for the $H\nu\overline{\nu}$ final state.

4.4 Event reconstruction

In section 2.3.7 we explained how tracks have been reconstructed, and energy, momentum and charge of particles measured starting from the hits in detectors. Here follows a brief description of the particle selection, jet reconstruction and b-tagging used for this thesis.

4.4.1 Particle selection

Charged particles are selected if their momentum is greater than 100 MeV/c , if they originate from the interaction region (within 10 cm along the beam direction and within 4 cm in the transverse plane). An additional request is that the error on track momentum estimation is less than 100%. the track has a calorimeter cluster associated.

Neutral particles are defined either as energy clusters in the calorimeters not associated to charged particle tracks, or as reconstructed vertices of photon conversions, interactions of neutral hadrons or decays of neutral particles in the tracking volume. All neutral clusters of energy greater than 100 MeV are retained. The $\pi^{\pm}$ mass is used for all charged particles except identified leptons, while zero mass is used for electromagnetic clusters and the K^0 mass is assigned to neutral hadronic clusters.

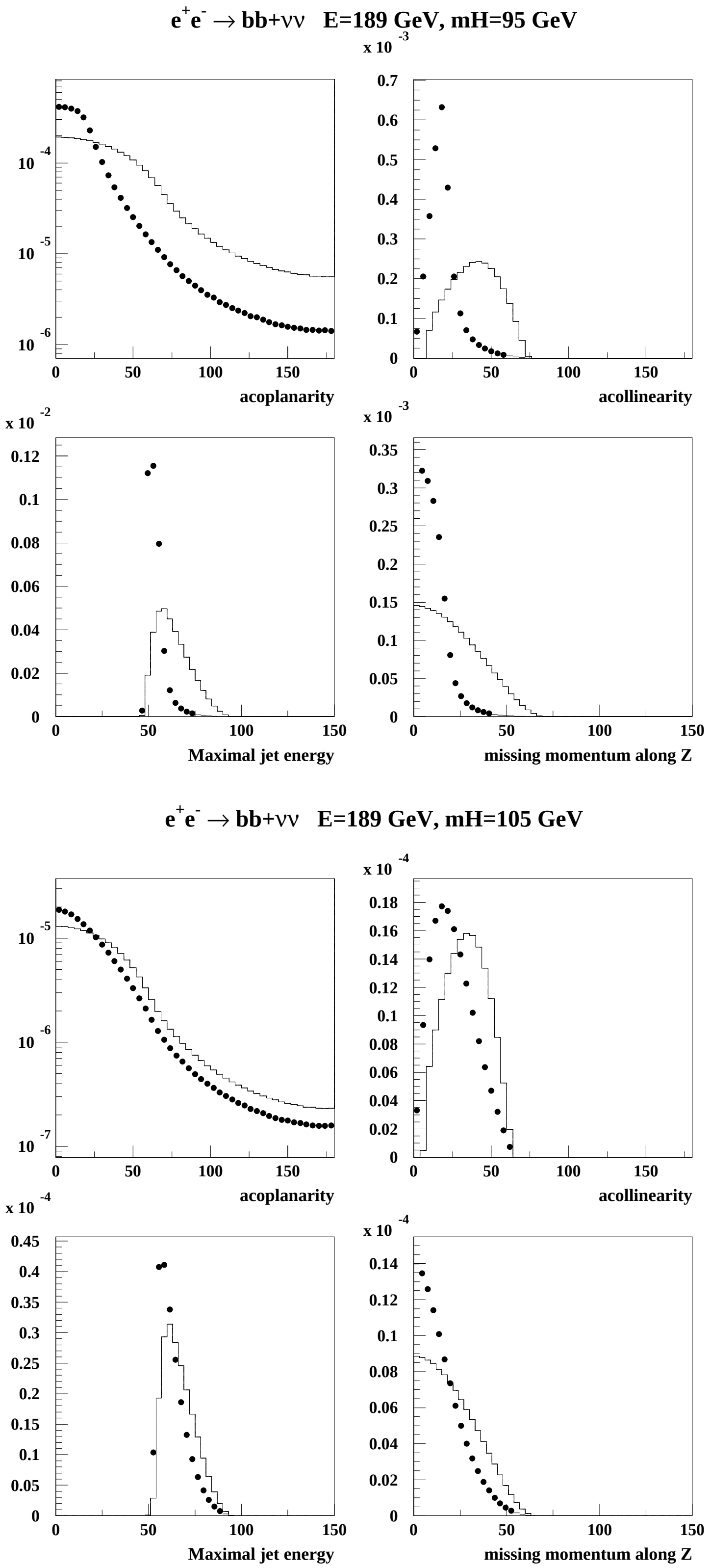

Figure 4.8: *Acoplanarity and acollinearity between two final jets, energy of most energetic jet, missing longitudinal momentum in the $bb\nu_e\nu_e$ final state where the two b quarks come from Higgs decay. The points correspond to events where Higgs has been produced by Higgs-strahlung and the line corresponds to events where Higgs has been produced by WW fusion.*

4.4.2 Jet reconstruction

When quarks and gluons hadronize they form aggregates of particles called jets. A jet clustering algorithm iteratively joins the two particles in the event with the smallest distance, the measure of distance depending on the specific algorithm. All the events were clustered into jets using the Durham jet algorithm [50]. In the Durham algorithm the distance

$$y_{ij} = 2min(E_i^2, E_j^2)/E_{vis}^2 .(1 - cos\alpha_{ij})$$

is computed for all pairs of particles (i, j). $E_{i,j}$ are the energies of the particles, α_{ij} is their opening angle and E_{vis} is the visible energy in the event. The pair for which y_{ij} is smallest (meaning that either the particles are close or at least one of the energies is low) is replaced by a *pseudo*-particle with four-momentum equal to the sum of the two four-momenta. A maximum allowed value y_{cut} for $y_{i,j}$ can be introduced. The procedure is iterated until all the particles are clustered into a certain fixed number of jets N_{jets}, the jets being the final state *pseudo*-particles.

In the analysis described in this thesis the greatest majority of signal events have a topology with two jets in final state, coming from the hadronization of the quark from Higgs decay. However it can happen that a quark emits a gluon and the event can have a three jet topology. And more, some background events may have a three ($Z\gamma$) or four (ZZ) jet topology. For this reason it has been decided to reconstruct each event in three different topologies going from two to four jets. The choice on topology can be done considering the distribution of the resulting y_{cut} for different number of jets (see figure 4.9).

Another jet algorithm (JADE) has been used to perform a study of systematics. In JADE the only difference with respect to DURHAM is the definition of the parameter $y_{i,j}$:

$$y_{ij} = 2E_iE_j/E_{vis}^2 .(1 - cos\alpha_{ij})$$

The choice of the algorithm is imposed by the analysis. In our case I am interested that:

- the kinematic of jets well reproduces the one of primary partons;
- number of jets per event is well reproduced by simulation. This means that the algorithm must not be sensitive to the details of the hadronization.

I choose the DURHAM algorithm since it better satisfies the previous conditions [57].

4.4.3 Tagging of b quark events

Events with weakly decaying b-hadrons are significantly different from those containing only lighter quarks, since b-hadrons have a large mass, a long lifetime, a high decay multiplicity and take more energy from the initial quark than do light hadrons, etc. In the analysis of this thesis, the b-tagging is a powerful variable to reduce background events. Here follows a description of the technique [58].

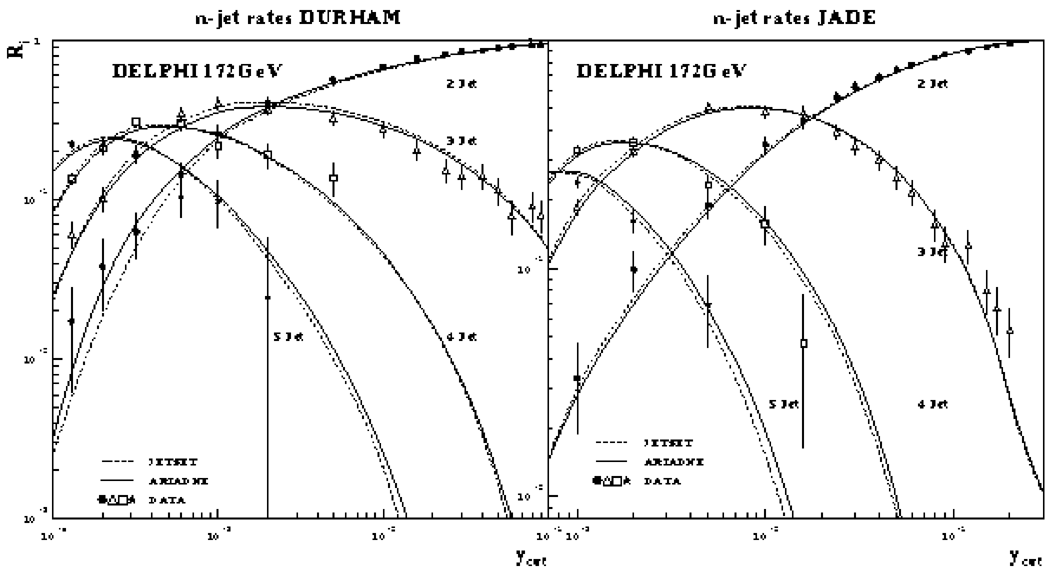

Figure 4.9: *Jet rate as a function of* y_{cut} *[51].*

First, the particles are clustered into jets and a tagging variable is calculated for each. For a hemisphere containing just one jet, the tagging variable is simply that for the single jet. If a hemisphere contains more than one jet, the jet with the highest probability of coming from a b-quark is used.

In this method all discriminating variables are defined for jets with reconstructed secondary vertices (by definition the secondary vertex is the one of hadron decay); jets without a reconstructed secondary vertex are not considered further. Such a condition allows properties specific to b-hadrons to be used for the tagging and allows the separation of their decay products from particles coming from b-quark hadronization. In addition, the requirement that jets have reconstructed secondary vertices is by itself a good b-quark selection as it removes a significant fraction of the background.

The description of the discriminating variables is as follows.

- The jet lifetime probability, P_j^+: it is constructed from the positively signed impact parameters of the tracks included in a jet and corresponds to the probability that a given group of tracks are compatible with origiating at the primary vertex. For jets with b-hadrons, this probability is usually very small due to the significant impact parameters of tracks from long-lived B decays. However, jets with c-quarks can also have low values of P_j^+ because of the non-zero lifetime of D-mesons, which limits the performance of the lifetime tag.

- The effective mass of particles included in the secondary vertex, M_s. The mass of the secondary vertex for c-jets is limited by the mass of D-mesons, and above M_s = 1.8 GeV/c^2 the number of c-jets decreases sharply, while for b-jets the mass distribution extends up to 5 GeV/c^2.

- The rapidity of particles included in the secondary vertex with respect to the jet direction, R_s^{tr}. Although a b-hadron has on average higher energy than a D-meson from a c-jet, the rapidities of particles from a B decay are usually less than those from a c-quark decay. This is explained by the higher mass of the b-hadron and the larger multiplicity of its decays. The secondary vertices in light quark jets are mainly the result of wrongly measured tracks. The wrong measurements occur due to multiple scattering in the detector, interaction in the material, etc so that particles included in the secondary vertices of light quark jets are usually soft and their rapidity distribution is shifted to lower values.

- The fraction of the energy of a jet carried by charged particles included in the secondary vertex, X_s^{ch}. In the case of b-hadrons, when almost all particles included in the secondary vertex come from the B decay, the distribution of X_s^{ch} is determined by the fragmentation function $f(\mathrm{b} \to B)$. The same is valid for c-quark jets where the distribution of X_s^{ch} is determined by $f(\mathrm{c} \to D)$, which is softer than $f(\mathrm{b} \to B)$. In light quark jets, the energy at the secondary vertex is much less than that in b-quark jets.

- The decay charged lepton transver momentum with respect the b jet. Since the b hadron mass is greater than the u, d, s, c quark, the transver momentum of lepton coming from b hadron decay is expected to be greater in b jets with respect u, d, s, c jets.

- the momentum of neutrino from b hadron decay: it is estimated from the missing energy and momenta. Also in this case it is expected to be greater in b with respect u, d, s, c events.

For the combination of the discriminating variables, the following quantity is defined:

$$y = n_{\mathrm{c}} \cdot \prod_i \frac{f_i^{\mathrm{c}}(x_i)}{f_i^{\mathrm{b}}(x_i)} + n_{\mathrm{q}} \cdot \prod_i \frac{f_i^{\mathrm{q}}(x_i)}{f_i^{\mathrm{b}}(x_i)} = n_{\mathrm{c}} \cdot \prod_i y_i^{\mathrm{c}} + n_{\mathrm{q}} \cdot \prod_i y_i^{\mathrm{q}}, \tag{4.1}$$

where n_{c} and n_{q} (q=uds) are the normalised numbers of jets with a reconstructed secondary vertex in $c\bar{c}$ and $q\bar{q}$ events respectively ($n_{\mathrm{c}} + n_{\mathrm{q}} = 1$) and $f_i^{\mathrm{q}}(x_i)$, $f_i^{\mathrm{c}}(x_i)$, $f_i^{\mathrm{b}}(x_i)$ are probability density functions of the variable x_i in uds-, c- and b-quark jets. All these quantities are taken from simulation.

Figure 4.10 shows the tagging efficiency versus purity.

The products in (4.1) run over all tagging variables of a given jet. The variable R_s^{tr} is defined for each particle included in the secondary vertex and so the corresponding ratio of probabilities for each particle enters in equation (4.1).

The jet is tagged as containing a b-quark if $y \leq y_0$, where the value y_0 can be varied to select the desired purity or efficiency of tagging.

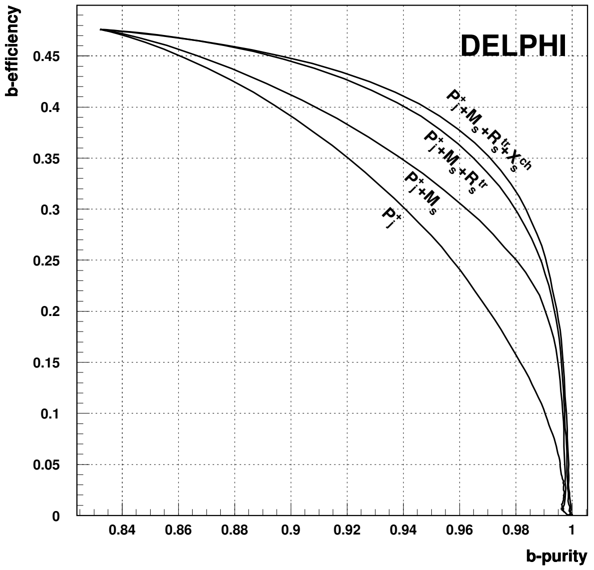

Figure 4.10: *b-tagging hemisphere efficiency versus purity for the enhanced impact parameter method, for different combinations of discriminating variables.*

4.5 Event selection

A series of sequential cuts has been performed to increase the signal over background ratio.

A starting sample of events has been selected requiring:

- total number of particles in event > 2;
- the transverse energy $E_{tr} = \sum_{particle} \sqrt{p_x^2 + p_y^2} > 4$ GeV;
- the absolute value of cosine of the polar angle of the missing momentum < 0.995.

Let us label this series of cuts as "I". As one can see in table 4.5 the selected sample contains $\sim 30\%$ more events in data than in simulation. The origin of this excess becomes evident from figure 4.11. The angle ϕ of the missing momentum in these events is peaked at 0 and 180 degrees, and also the angle θ of the most energetic electromagnetic cluster is peaked at 0 and 180 degrees. They are events in the horizontal plane (the plane of beams). This excess is clearly due to the so called "off momentum electrons". originated by bremsstrahlung by beam particles on residual gas molecules inside the beam pipe. This background can be simulated, but the simulation cannot be used for quantitative estimates since it needs as input the vacuum pressure in LEP, which is not known in detail. So we did not use this simulation in our background studies, and this explains the main bulk of the excess. The kinematics of these events explain the structures in figure 4.11: the off momentum electrons are peaked at theta near the beam pipe and they have high energy: they are peaked at 80 GeV in VSAT and at 50 GeV in STIC [59] . The probability to have an off momentum electron in a normal trigger event is 3%, and due to their high energy and their preferred orientation in the horizontal plane, they push the ϕ of missing momentum toward 0 and 180 degrees.

A simple way to get rid of these events is to cut on θ of the most energetic electromagnetic cluster. Let us call II the series of cuts I plus a rejection of events in which the most energetic electromagnetic cluster is below 5 degrees. In the second row of table 4.5 one can see that now the agreement in data and simulation is much better and in figure 4.12 the structure in ϕ of missing momentum has disappeared.

cut	$2f$(MC)	$4f$(MC)	$\gamma\gamma$(MC)	All MC	DATA	ϵ_{HIGGS}		
						$\epsilon_{m_h=85}$	$\epsilon_{m_h=90}$	$\epsilon_{m_h=95}$
I	68569.7	2915.14	66808.7	138293	192064	0.99	0.99	0.99
II	67168	2875.22	53712.7	123756	131067	0.98	0.98	0.98

Table 4.5: *Number of selected events in data and simulation after first preliminary cuts. The content of simulation has been detailed in three classes: two fermion, four fermions, two photons. The signal efficiency is also reported for three different Higgs masses.*

4.5.1 Rejection of two photon events

In the process $e^+e^- \rightarrow e^+e^-\gamma\gamma \rightarrow e^+e^-X$ electron and positron of the final state escape detection since they go down the beam pipe. The kinematics of these events is quite peculiar. As a consequence the total visible energy is low (especially in the plane perpendicular to the beam line, see E_{tr}) and actually it is contained in a cone along the beam pipe. Also the spectrum of visible invariant mass is concentrated at low values (figure 4.12).

To reject the bulk of these events one can take profit of these peculiarities which result in distributions quite different to the corresponding spectra for the signal. (figure 4.13).

Another interesting variable which has been found particularly efficient in rejecting two photon background is the total momentum along the thrust axis. The thrust axis $\mathcal{T}$ is defined as the direction which maximises the sum of momenta along it of all particles in the event.

$$\vec{\mathcal{T}} = \max_{\vec{n}} \frac{\sum_i |\vec{p_i} \cdot \vec{n}|}{\sum_i |\vec{p_i}|}$$

We defined the total momentum along thrust as:

$$p_{thr} = \sum_i |\vec{p_i} \cdot \vec{\mathcal{T}}| \tag{4.2}$$

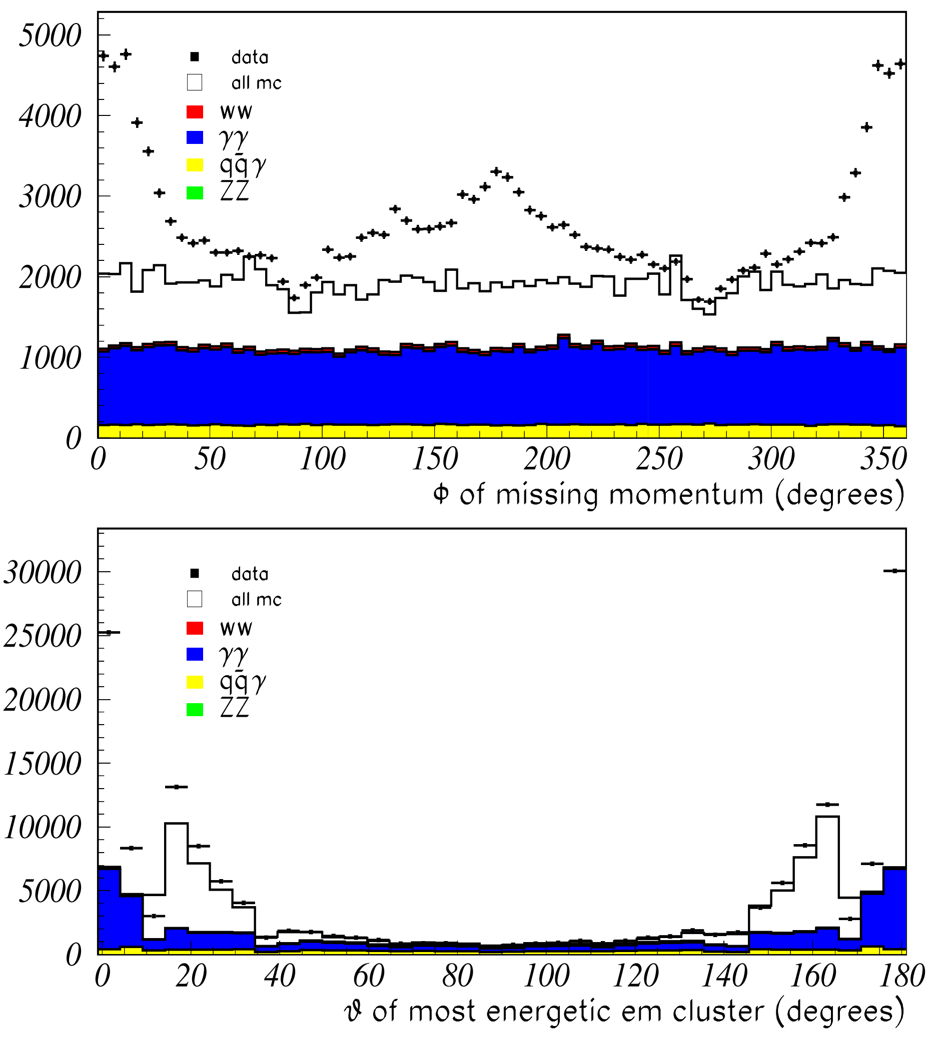

Figure 4.11: *ϕ of missing momentum and θ of most energetic electromagnetic cluster after cuts "I".*

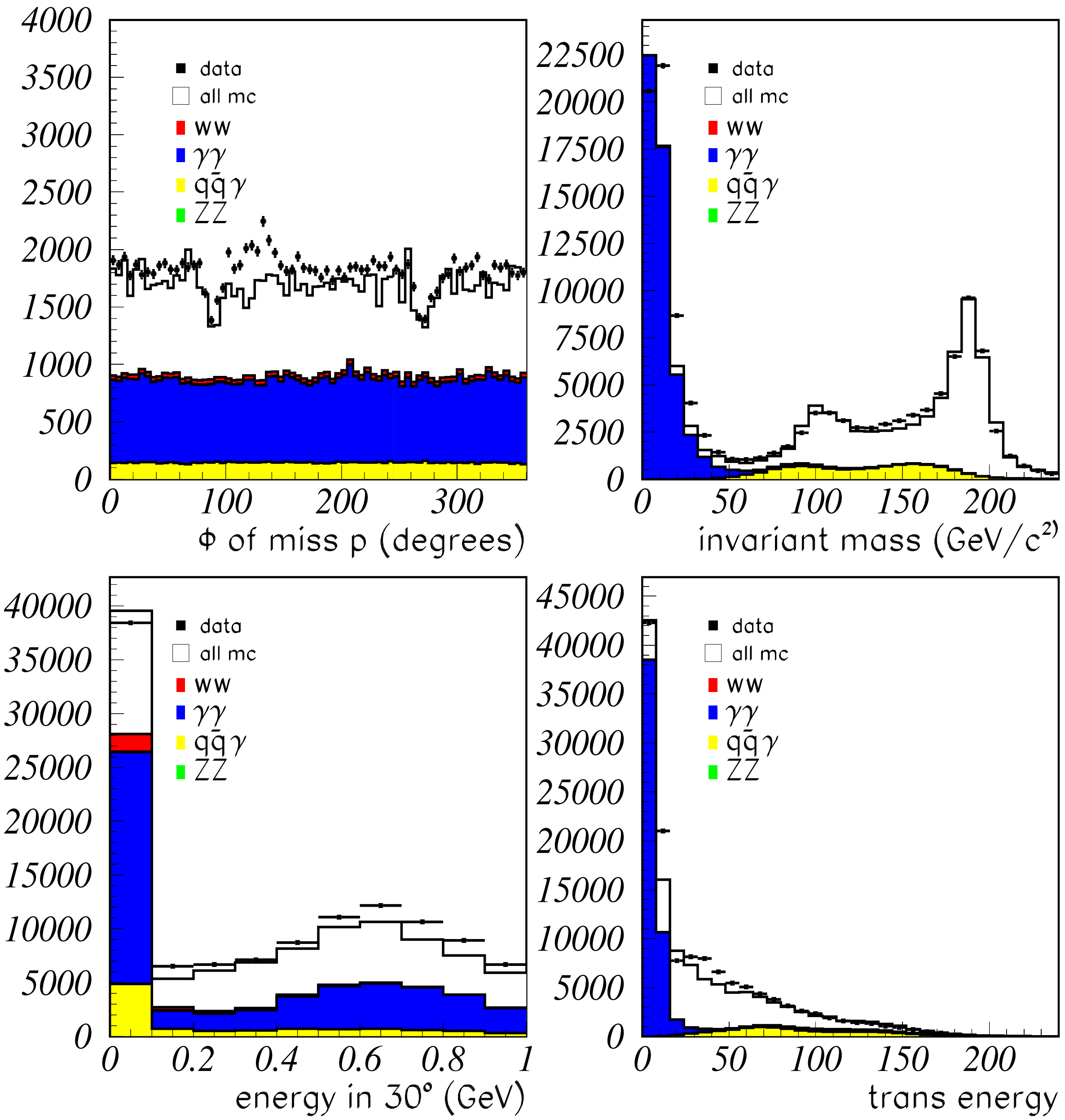

Figure 4.12: *ϕ of missing momentum, visible invariant mass, energy in a cone of 30 degrees around beam pipe, transverse energy after cuts "II".*

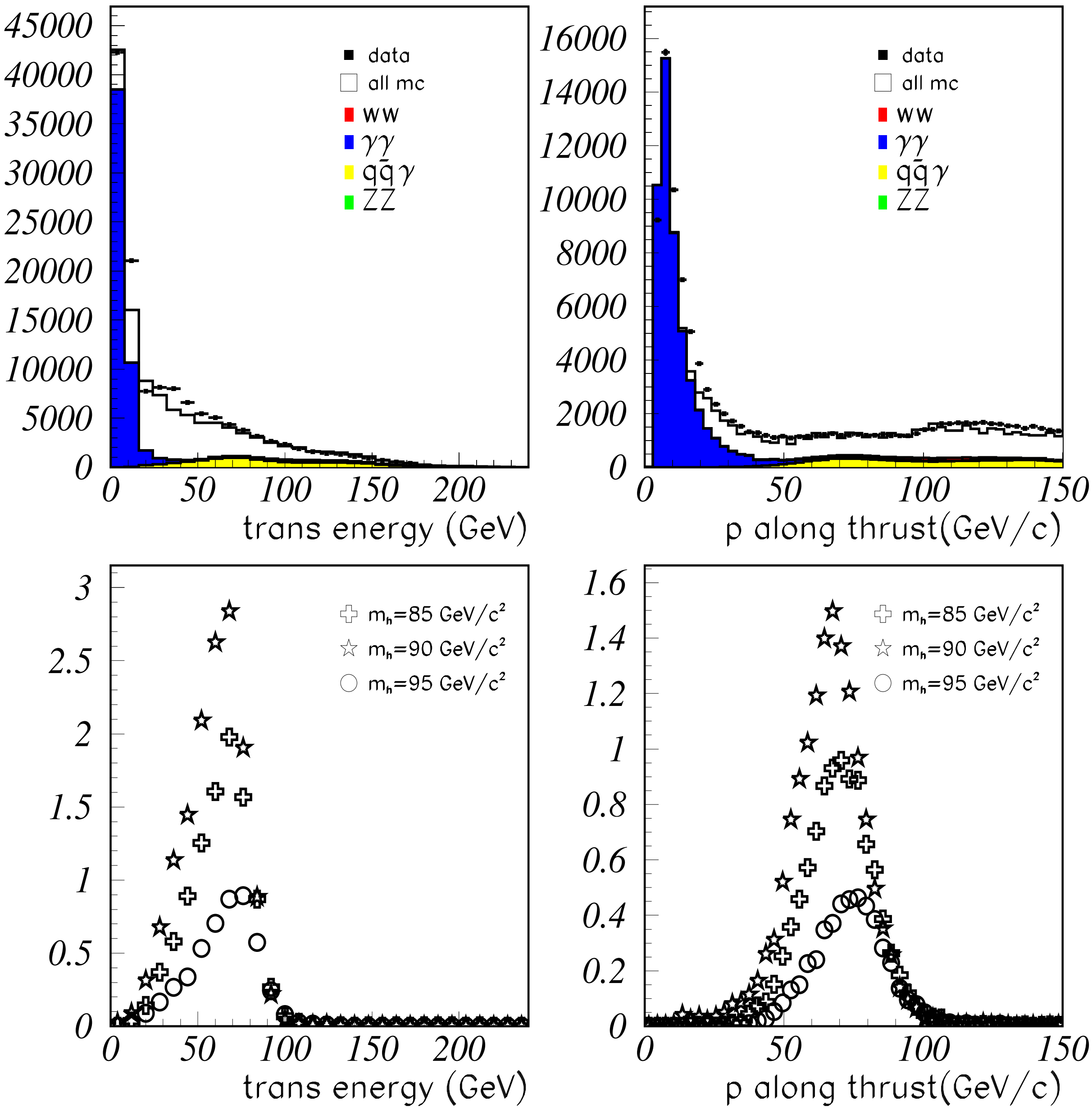

Figure 4.13: *Transverse energy and momentum along thrust axis for background events and for higgs, after cuts "II".*

The spectrum of this variable for two photon and for signal events are different (figure 4.13).

Summarising, adding to cut "II" the following (we call all cuts "III"):

- number of charged tracks > 5;
- total number of tracks > 10;
- $E_{tr} > 20$ GeV;
- E_{30} = energy in a cone of 30^o around Z- axis $< 0.7\sqrt{s}$;
- $|\cos\theta|$ of most forward jet < .95;
- $p_{thr} > 40$ GeV/c ;

we obtained a sample of 11946 events in data and 11031.1 in simulation (table 4.6). We have practically eliminated all two photon events (with some loss of signal efficiency) and the agreement between data and simulation is statistically good.

cut	$2f(MC)$	$4f(MC)$	$\gamma\gamma$(MC)	All MC	DATA	ϵ_{HIGGS}		
						$\epsilon_{m_h=85}$	$\epsilon_{m_h=90}$	$\epsilon_{m_h=95}$
III	8413.66	2452.66	164.761	11031.1	11946	.86	0.93	.91

Table 4.6: *Number of selected events in data and simulation after cuts "III". The content of simulation has been detailed in three classes: two fermion, four fermions, two photons. The signal efficiency is also given for three different Higgs masses.*

4.5.2 Rejection of Bhabha events

The remaining excess can be imputed to Bhabha events.

In fact (see figure 4.14 and 4.15) this excess is due to events with low multiplicity, with identified electrons and the θ of the electron is concentrated in the forward regions. In addition these events have a cluster in an electromagnetic calorimeter with energy of 90 GeV, which is exactly what one expects for one detected electron (or positron) in Bhabha events at energy of 189 GeV in the centre of mass.

The excess principally comes from a non perfect description of material in the DELPHI detectors. An underestimation of the material produces less showers in simulation with respect to real data which means that the mean multiplicity for Bhabha events is greater in data than in simulation. This is evident in the bulk of events at multiplicity around 10 not reproduced by simulation. Actually the majority of Bhabha events in simulation is rejected by the cut on 5 charged tracks and 10 total tracks (see figure 4.16).

Taking profit of the kinematics, Bhabha events, were removed adding to "III" the following requirements ("IV") to select the sample of events:

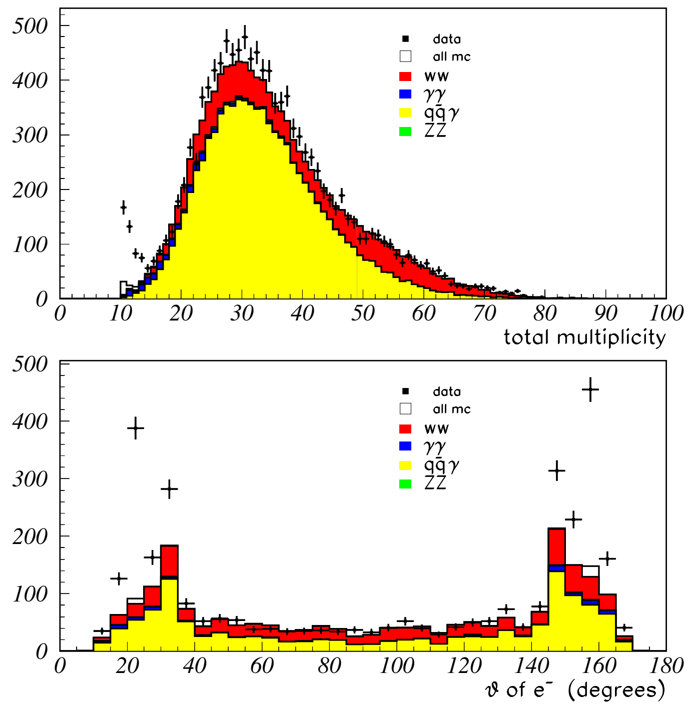

Figure 4.14: *Total number of tracks, θ of identified electron in background events after cuts "III".*

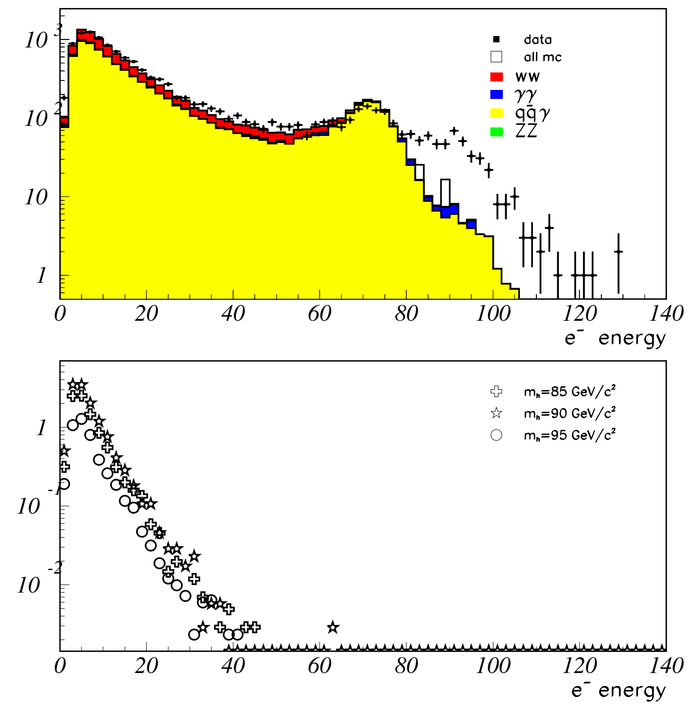

Figure 4.15: *Energy of electromagnetic clusters for background events and for Higgs, after cuts "III". The cluster at 72 GeV is due to photons in radiative returns to Z^0, the one at 90 GeV is due to Bhabha events.*

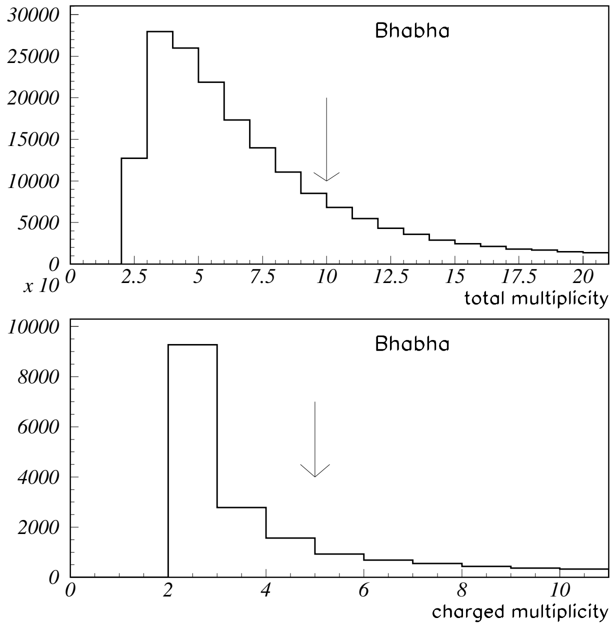

Figure 4.16: *Charged and total multiplicity for Bhabha events in simulation. The arrows indicate the value of cuts.*

- the electromagnetic energy $E_{em} < 90\%$ of total energy;
- the most energetic electromagnetic cluster < 50 GeV;
- I reject events where $E_{em} > \sqrt{s}/2$ and the angle between the two reconstructed jets > 175 degrees.

The selected samples contain 8082 events in data and 7772.2 in simulation.

cut	$2f$(MC)	$4f$(MC)	$\gamma\gamma$(MC)	All MC	DATA	ϵ_{HIGGS}		
						$\epsilon_{m_h=85}$	$\epsilon_{m_h=90}$	$\epsilon_{m_h=95}$
IV	5731.9	1965.18	75.1295	7772.2	8082	.80	.87	.87

Table 4.7: *Number of selected events in data and simulation after cuts "IV". The content of simulation has been detailed in three classes: two fermion, four fermions, two photons. The signal efficiency is also given for three different Higgs masses.*

4.5.3 Rejection of two and four fermion events

At this point the background is dominated by two fermion events (table 4.7). The two fermion sample in simulation is composed by 20 $\tau\overline{\tau}\gamma$ events and 5711.9 $q\overline{q}\gamma$ events. There are no more $\mu\overline{\mu}\gamma$ or Bhabha events.

The composition of four fermion events is summarised in table 4.8. In this case the dominant contribution comes from WW like events.

$e^+e^-e^+e^-$	$l\bar{l}l\bar{l}$	$\mu\overline{\mu}q\overline{q}$	$\tau\overline{\tau}q\overline{q}$	$\nu\overline{\nu}q\overline{q}$	WW	$e\nu q\overline{q}$
0.1	0.4	23.2302	10.88	28.90	1866.76	34.91

Table 4.8: *Composition of four fermion sample of simulation after cut "IV".*

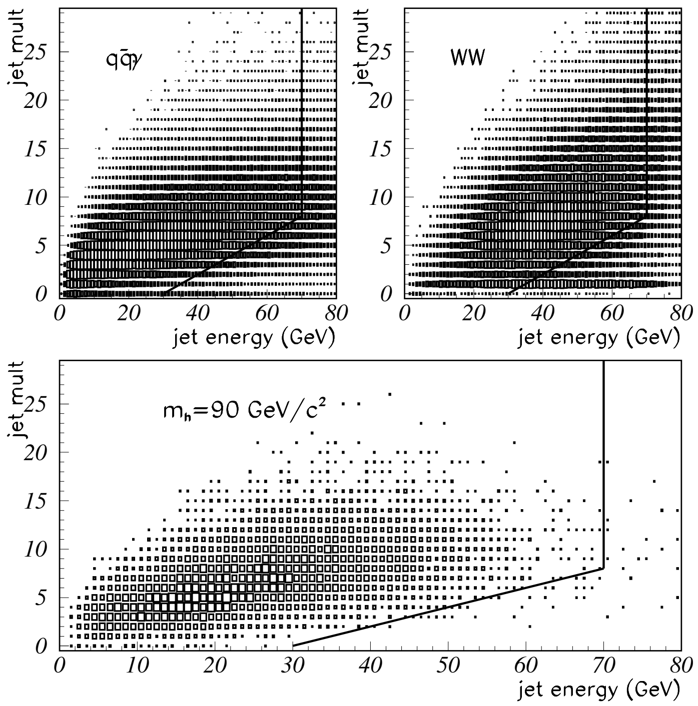

Figure 4.17: *Number of charged tracks in the lowest multiplicity jet versus the energy of jet, for $q\overline{q}\gamma$, WW, Higgs samples. Events on the right of the line are rejected.*

The method that I applied to get rid of the majority of WW is the following. The events have been reconstructed forcing a 3 jets topology. We found the jet with the lowest multiplicity and we looked at the distributions of jet multiplicity versus jet energy (figure 4.17).

A careful look shows that for the $q\overline{q}\gamma$ sample there are events with jets at zero charged multiplicity. These jets can be attributed to the ISR photon. On the other hand in the WW sample there is an accumulation of events with jets of charged multiplicity one and with high energy. They are events in which one of the W decays semileptonically $W \to l\nu$, and the jet algorithm makes a jet with the lepton only (or eventually some neutral tracks).

Another feature is the higher mean energy of the jets with lowest multiplicity in $q\overline{q}\gamma$ and WW samples with respect to the Higgs sample. This can be justified because forcing an event to the three jet topology may have a physical meaning in $q\overline{q}\gamma$ and WW where the hadronization can originate a number of jets varying from two to four. On the other hand the three jet topology is quite unlikely for $e^+e^- \to H\nu\overline{\nu} \to q\overline{q}$

events. Forcing the reconstruction of three jets produces a third jet which can come from hadronisation of a gluon emitted by the original quarks (but in this case it should have multiplicity higher then 1). The other possibility is that the third jet is physically meaningless and can only be a track (or few tracks) with relatively high transverse momentum with respect to the two main jets coming from the hadronization of the original $q\overline{q}$.

All above observations can be introduced in the analysis applying a two dimensional cut (as the one in figure 4.17) to remove WW and some $q\overline{q}\gamma$ events, without affecting the signal efficiency (table 4.9). The logical "and" of this request and the cuts "IV" is called "V")

The sample is still dominated by $q\overline{q}\gamma$ ($\sim 60\%$ of the events). At this stage we can use the fact that the photon radiation in the initial state lowers the energy available for e^+e^- collisions. It is possible to estimate the effective centre of mass energy ($\sqrt{s'}$) by measuring or estimating the energy and momentum of ISR photons [60]. The method is explained in the next section.

4.5.3.1 Estimation of centre of mass energy in ISR events

The first step consists in looking for the candidate ISR photons in the detector. Whenever the number of found ISR photons is less than two, the possibility of missing ISR photons is tested. All the particles in the event, except the ones considered as ISR photons, are forced to be clustered in two jets, using the DURHAM algorithm. The energy and momentum conservation is used to estimate $\sqrt{s'}$ and the energy of the ISR photons. The method uses different approaches according to the number of detected ISR photons.

Events with no detected ISR photons. When there are no detected ISR photons, a radiated photon along the beam direction (Z axis) is assumed. The directions of the two jets are used to constrain the photon energy.

For three particles to conserve energy and momentum, they must be in the same plane and obey the so called "triangle rule" (1,2 for jets):

$\alpha_{k,l} = (\widehat{k,l})$ = angle between particle (or jet) k and particle (or jet) l
$a = \mathrm{abs}(P_\gamma)$ $\quad\sin(A) = \sin(\alpha_{12})$
$b = \mathrm{abs}(P_1)$ $\quad\sin(B) = \sin(\alpha_{\gamma 2})$
$c = \mathrm{abs}(P_2)$ $\quad\sin(C) = \sin(\alpha_{1\gamma})$

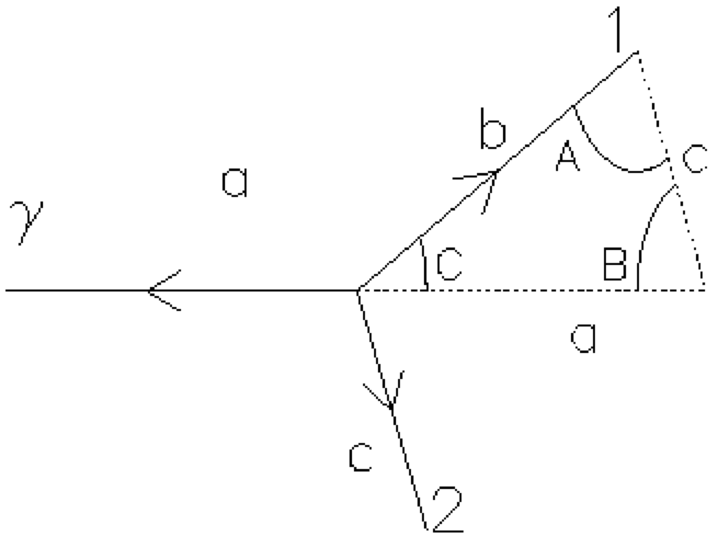

$$\alpha_{12} + \alpha_{\gamma 2} + \alpha_{1\gamma} = 360°$$
$$\sqrt{s} = P_1 + P_2 + P_\gamma$$
$$P_\gamma = \sqrt{s}\frac{\sin(A)}{\sin(A)+\sin(B)+\sin(C)}$$

An hypothetical photon is assumed to be along z, in the positive or negative direction, respectively if the sum of the jet polar angles is greater or less than 180 degrees. Its energy is then extracted from the above "triangle rule", which for the photon gives:

$$\begin{aligned} E_\gamma &= \sqrt{s}\cdot\frac{\sin(\alpha_{12})}{\sin(\theta_1)+\sin(\theta_2)+\sin(\alpha_{12})} & \\ P_\gamma &= E_\gamma & (z_\gamma > 0) \\ E_\gamma &= \sqrt{s}\cdot\frac{\sin(\alpha_{12})}{\sin(180°-\theta_1)+\sin(180°-\theta_2)+\sin(\alpha_{12})} & \\ P_\gamma &= -E_\gamma & (z_\gamma < 0) \end{aligned}$$

where α_{12} is the angle between the two jets, and θ_j are the jet polar angles.

The e^+e^- centre of mass effective energy, $\sqrt{s'}$, the boost factor (γ) and the boost vector (β_s), are obtained from

$$\begin{aligned} \sqrt{s'} &= \sqrt{(2E_b - E_\gamma)^2 - P_\gamma^2} \\ \gamma &= (2E_b - E_\gamma)/\sqrt{s'} \\ \beta_s &= -\vec{P}_\gamma/(2E_b - E_\gamma) \end{aligned}$$

One ISR photon. If only one ISR photon is measured in the detector, it is checked whether or not this photon alone can balance the two jets energy and momentum.

For the event energy to be distributed among three particles (two jets and the ISR photon), their directions must be in same plane, and not on the same side of the plane. Events are considered planar when

$$\alpha_{12} + \alpha_{2\gamma} + \alpha_{\gamma 1} > 345^\circ$$

where α_{ij} stands for the internal angle between particle(jet) i and j. Otherwise the events are considered aplanar.

- Planar event.

  For planar events the triangle rule explained in the previous subsection is used, with the measured photon directions. The ISR photon energy is then:

$$\begin{aligned} E_\gamma &= \sqrt{s} \cdot \frac{\sin(\alpha_{12})}{\sin(\alpha_{2\gamma})+\sin(\alpha_{\gamma 1})+\sin(\alpha_{12})} \quad \text{(planar event)} \\ \|P_\gamma\| &= E_\gamma \end{aligned}$$

  The e^+e^- centre of mass effective energy, $\sqrt{s'}$, the boost factor (γ) and the boost vector (β_s), are as previously obtained from

$$\begin{aligned} \sqrt{s'} &= \sqrt{(2E_b - E_\gamma)^2 - \vec{P}_\gamma^2} \\ \gamma &= (2E_b - E_\gamma)/\sqrt{s'} \\ \beta_s &= -\vec{P}_\gamma/(2E_b - E_\gamma) \end{aligned}$$

- Aplanar event.

  For aplanar events at least one particle must have been lost. The algorithm assumes then that one photon has been radiated inside the beam pipe. The energies and directions of the two jets and of the measured ISR photon are used to constrain this hypothetical photon direction. The hypothetical photon polar angle is 0 or 180 degrees, if there is no need to balance the transverse momentum of the event. Otherwise, as explained below, it is assumed to be 2 or 178 degrees.

  To determine the sign of the Z coordinate of the hypothetical photon along the beam pipe, the external product V of the two jets is constructed. The photon polar angle θ_{hip} is then

  $\theta_{\text{hip}} = 90^\circ + 90^\circ \text{sign}(\vec{V} \cdot \vec{P}_\gamma)\text{sign}(\vec{V} \cdot \vec{e_z})$

  where P_γ is the momentum of the measured ISR photon.

To determine if the two jets and the measured ISR photon could balance the transverse momentum, a set of tests on the azimuthal angles ϕ_i of the three particles (two jets and the photon) is performed. Let ϕ_H, ϕ_L and ϕ_3 be respectively the "greatest", the "smallest" and the "third" azimuthal angle of the three particles (all angles are in the range 0–360°).

If

- $\phi_H - \phi_L < 180°$, or
- $\phi_3 > \phi_L + 180°$, or
- $\phi_3 < \phi_H - 180°$,

the event cannot conserve the transverse momentum.

In this case, the hypothetical photon polar angle is assumed to be 2 or 178 degrees, according to the sign of its Z coordinate, previously determined. The azimuthal angle of the hypothetical photon is the azimuthal angle of the missing momentum.

Applying energy and momentum conservation to the four particles (the three measured and one hypothetical) to obtain the energies of each particle, the e^+e^- centre of mass effective energy, $\sqrt{s'}$, the boost factor (γ) and the boost vector (β_s), are computed as

$$\begin{aligned}
\sqrt{s'} &= \sqrt{(2E_b - E_\gamma - E_h)^2 - (\vec{P}_\gamma + \vec{P}_h)^2} \\
\gamma &= (2E_b - E_\gamma - E_h)/\sqrt{s'} \\
\beta_s &= -(\vec{P}_\gamma + \vec{P}_h)/(2E_b - E_\gamma - E_h)
\end{aligned}$$

where E_γ,E_h,$\vec{P}_\gamma$,$\vec{P}_h$ are respectively the energies and momenta of the measured ISR photon and of the hypothetical photon. This algorithm is explained in the following subsection.

Two ISR photons. If two ISR photons are found no hypothetical photons are assumed. The energy momentum conservation is applied, as a system of 4 equations and 4 unknowns:

$$\begin{aligned}
E_1 + E_2 + E_{\gamma1} + E_{\gamma2} &= 2E_b \\
E_1 cx_1 + E_2 cx_2 + E_{\gamma1} cx_{\gamma1} + E_{\gamma2} cx_{\gamma2} &= 0 \\
E_1 cy_1 + E_2 cy_2 + E_{\gamma1} cy_{\gamma1} + E_{\gamma2} cy_{\gamma2} &= 0 \\
E_1 cz_1 + E_2 cz_2 + E_{\gamma1} cz_{\gamma1} + E_{\gamma2} cz_{\gamma2} &= 0
\end{aligned}$$

where $E_1, E_2, E_{\gamma1}, E_{\gamma2}$ are the unknowns, and cx_i, cy_i and cz_i are the direction cosines for the particle i.

If this system has a physical solution, the e^+e^- centre of mass effective energy, $\sqrt{s'}$, the boost factor (γ) and the boost vector (β_s), are obtained from

$$\begin{aligned}\sqrt{s'} &= \sqrt{(2E_b - \Sigma_i E_{\gamma i})^2 - (\Sigma_i \vec{P_{\gamma i}})^2} \\ \gamma &= (2E_b - \Sigma_i E_{\gamma i})/\sqrt{s'} \\ \beta_s &= -\Sigma_i \vec{P_{\gamma i}}/(2E_b - \Sigma_i E_{\gamma i})\end{aligned}$$

where $E_{\gamma i}$ and $P_{\gamma i}$ are the energy and the momentum determined above for the ith ISR photon.

If there is no physical solution, the method fails.

The distribution for $\sqrt{s'}$ can be seen in figure 4.5.

4.5.4 Rejection of $q\bar{q}\gamma$

Once $\sqrt{s'}$ is computed, it is possible to profit from the kinematics of radiative events: in many of these events $\sqrt{s'}$ is at Z^0 peak, and the photon is emitted at low θ.

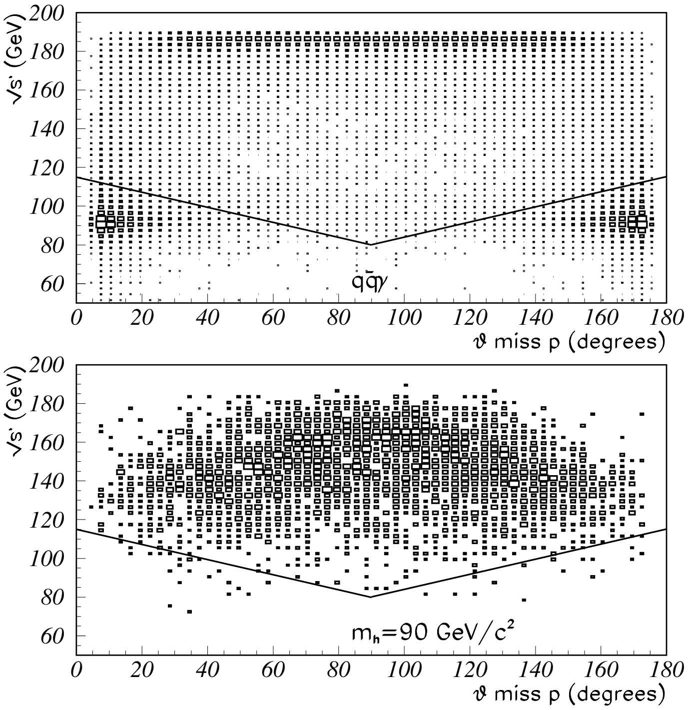

Figure 4.18: $\sqrt{s'}$ *versus* θ *of missing momentum for background and signal. The events below the lines are removed from the selected sample.*

In the case where the photon is lost in the beam pipe, the θ of the missing momentum has a low value. This configuration is unlikely in the signal sample and a two dimensional cut ("VII") on the plane of $\sqrt{s'}$ versus θ of missing momentum (see figure 4.18), reduces considerably the $q\bar{q}\gamma$ background (table 4.9).

Another request is applied in order to remove more $q\overline{q}\gamma$ events. It may happen that the ISR photon is undetected (because it is emitted in the beam pipe) and it carries a considerable amount of energy (the event is not a return to Z^0). In such a case, when reconstructing the event in the two jet topology, the momentum unbalance along the Z axis results in two jets not in the back to back configuration with the angle between two jets considerably less then 180^o. Moreover, due to the boost along Z, the jets are at low theta. As a consequence the amount of energy in a cone along Z can have high values. Also in this case this topology is unlikely for a signal event and a two dimensional cut on the plane of the angle between the two jets, and the energy along Z, reduces the background (figure 4.19).

The last cut (let us call all the cuts till this point "VIII") to further reduce the $q\overline{q}\gamma$ events profits from the hermeticy detectors (see section 2.3.5). At this level of selection $\simeq 50\%$ of radiative events with photons in the DELPHI acceptance have the photons in the 40^o taggers, and $\simeq 10\%$ of events have the photons in the 90^o taggers. An algorithm has been developped to remove the events with photons in the tagging detectors. The basic steps are:

- the signal over noise ratio for the fired tagger must be greater than 100;
- the fired tagger must be isolated: there must be no tracks in the angular intervals $\theta = 20^o$ and $\phi = 20^o$ around the tagger;
- the missing momentum must lie in the angular region of $\theta = 50^o$ and $\phi = 30^o$ around the tagger.

If these conditions are satisfied, the event is not considered to have a real missing momentum due to neutrinos in final state, but a missing momentum due to undetected particles escaping through the taggers. Such events are rejected (table 4.9).

cut	$2f$(MC)	$4f$(MC)	$\gamma\gamma$(MC)	All MC	DATA	ϵ_{HIGGS}		
						$\epsilon_{m_h=85}$	$\epsilon_{m_h=90}$	$\epsilon_{m_h=95}$
V	2513.85	692.839	55.638	3262.32	3599	.77	.84	.84
VI	1008.13	658.98	34.1604	1701.27	1753	.75	.83	.83
VII	428.113	227.905	34.1604	690.179	734	.74	.82	.80
VIII	334.724	190.043	25.12	549.89	561	.67	.73	.71

Table 4.9: *Number of selected events in data and simulation after cuts. The content of simulation has been detailed in three classes: two fermion, four fermions, two photons. The signal efficiency is also given for three different Higgs masses.*

After these last requests the remaining two fermion background is entirely composed by $q\overline{q}\gamma$ events, while the composition of four fermion events is shown in table 4.10.

There are principally four different background processes: $q\overline{q}\gamma$, WW, ZZ, $e\nu q\overline{q}$. The distribution of some interesting variables for data and simulation are shown in figure 4.20. The agreement between data and simulation is good.

$e^+e^-e^+e^-$	$l\bar{l}l\bar{l}$	$mu\overline{\mu}q\overline{q}$	$\tau\overline{\tau}q\overline{q}$	$\nu\overline{\nu}q\overline{q}$	WW	$e\nu q\overline{q}$
0.	0.	1.	1.45	18.56	153.12	15.91

Table 4.10: *Composition of four fermion sample in simulation after cut "VIII".*

At this stage it is possible to investigate more the kinematics of the different processes and to develop a new tool to decrease the background. It will be described in the next chapter.

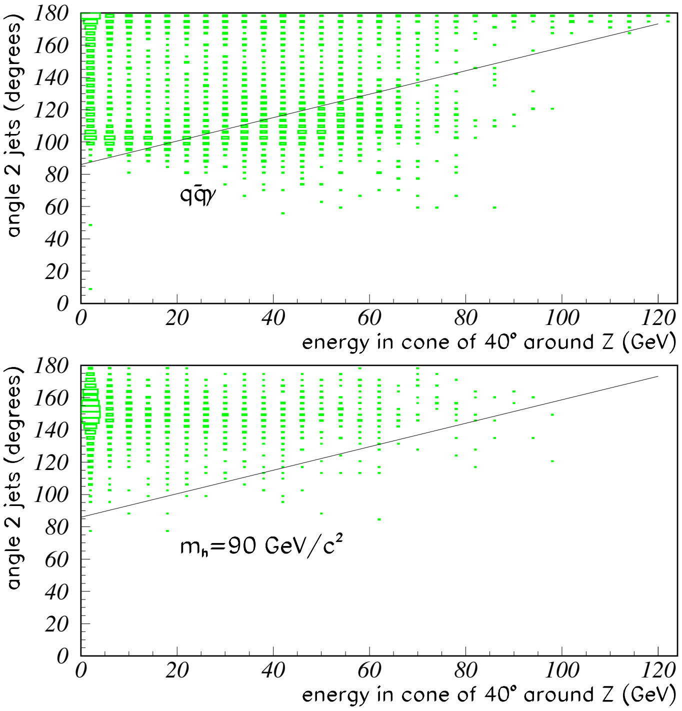

Figure 4.19: *Angle between the two jets versus energy in a cone of* 40^o *around Z, for background and signal. The events below the lines are removed from the selected sample.*

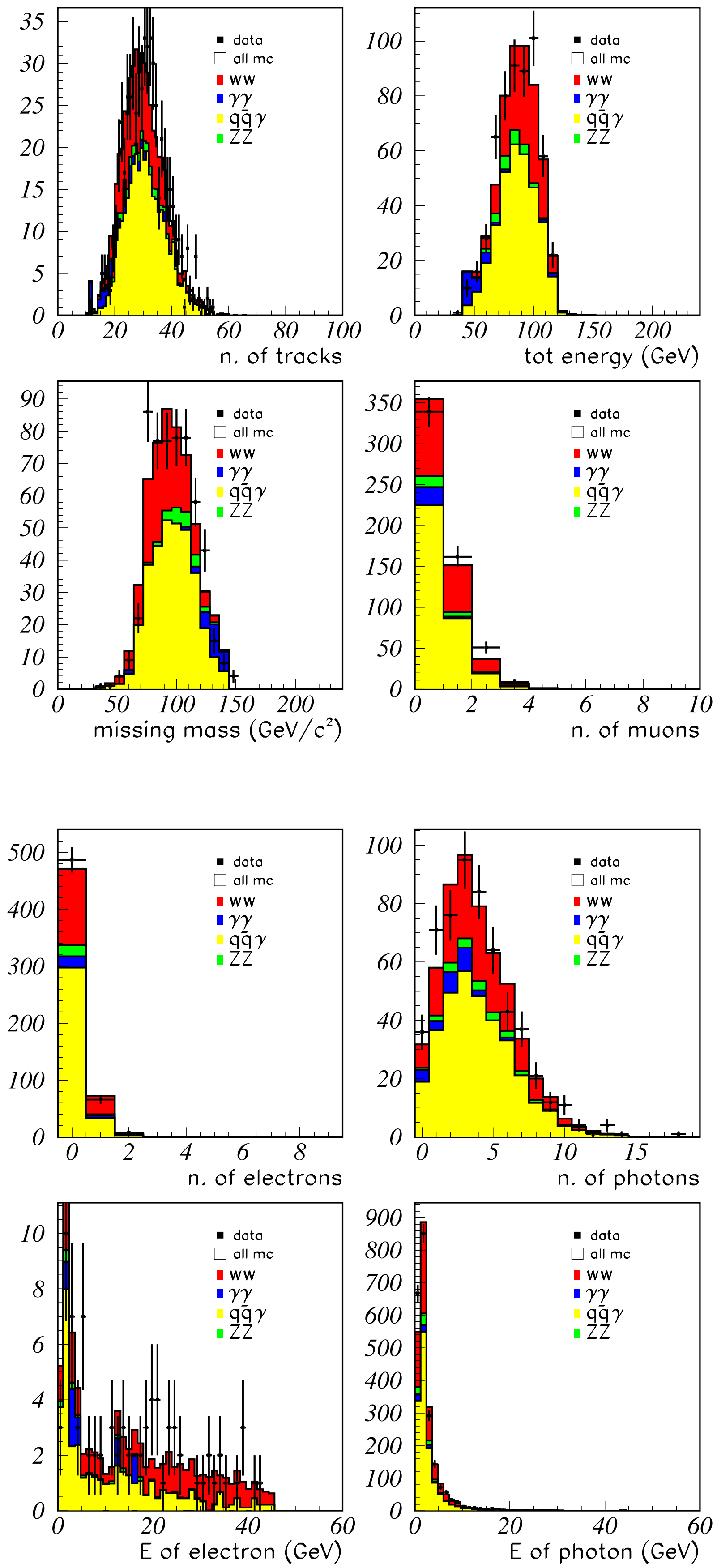

Figure 4.20: *Total number of tracks, total energy, missing mass, total number of muons, number of electrons, number of photons, energy of the electrons and of photons for data and simulation after cut "VIII".*

Chapter 5

Signal and background discrimination using the likelihood method

In the previous chapter I have shown how to select a sample of events with reduction of background, using sequential cuts. It is possible to exploit the different phase space distribution between signal and background, not only cutting sharply where spectra do not overlap, but also profiting from the different probability density functions of the kinematic variables for signal and background also in the region of overlap. The method is called "the likelihood ratio" and I applied it on the sample of events selected as described in previous chapter.

5.1 Description of the method

The selection of events based on successive cuts applied to a set of discriminating variables is efficient if the signal and the background are well separated so that the cuts remove most of the background but only a small part of the signal.

The main drawback of this method is that, when events are rejected from one part of the multidimensional space spanned by the discriminant variables, no use is made of the information in other parts of the variable space distributions. The second drawback, connected with the former, is that the method of cuts prevents the use of variables for which the signal and background have a large overlap.

For the Higgs boson search in the neutrino channel, such overlaps are expected in many variables. First, inefficiencies in the energy measurement (particle losses or bad reconstruction) tend to smear the distributions. Furthermore processes like:

- ZZ where one Z decays in neutrinos;
- $Z\gamma\gamma$ where the two γ are lost in the beam pipe;

are kinematically similar to the signal. For these reasons a new analysis method has been developed

It consists in constructing a discriminant variable $\mathcal{L}$ as the ratio between two likelihood functions:

$$\mathcal{L} = \frac{\mathcal{L}_H}{\mathcal{L}_{back}} \tag{5.1}$$

where $\mathcal{L}_H$ is the likelihood function for the signal and $\mathcal{L}_{back}$ is the one for background.

Let us consider N variables with different distributions in phase space for signal and background. Let $\mathcal{P}_i^H(x)$ ($\mathcal{P}_i^{back}(x)$) be the probability density function of variable i for the signal (background). Given a set of values for the N variables $x_1, ..., x_i, ...x_N$, then the likelihood function for the signal is defined as the probability that the N variables be in the hypercube N-dimensional centred at $x_1, ..., x_i, ...x_N$ and with sides $\delta_{x_1}, ..., \delta_{x_i}, ...\delta_{x_N}$, where δ_{x_i} is the detector resolution for variable i:

$$\mathcal{L}_H = \prod_{i=1}^{N} \mathcal{P}_i^H(x_i)\delta_{x_i} \tag{5.2}$$

In the same way the likelihood function for the background is:

$$\mathcal{L}_{back} = \prod_{i=1}^{N} \mathcal{P}_i^{back}(x_i)\delta_{x_i} \tag{5.3}$$

As explained in the previous chapter, after the preselection, the remaining sample consists principally of ZZ, WW, $e\nu q\overline{q}$ and $q\overline{q}\gamma$ events. Since the distribution for $e\nu q\overline{q}$ is similar to the other WW events it has been decided to consider the probability density function for ZZ, $q\overline{q}\gamma$ and for the sample of WW together with $e\nu q\overline{q}$ (called simply WW). In such a way, the discriminant variable (called likelihood $\mathcal{L}$) is defined by:

$$\mathcal{L} = \prod_{i=1}^{N} \frac{\mathcal{P}_i^H(x_i)}{[f_{ZZ}\mathcal{P}_i^{ZZ}(x_i) + f_{q\overline{q}\gamma}\mathcal{P}_i^{q\overline{q}\gamma}(x_i) + f_{WW}\mathcal{P}_i^{WW}(x_i)]} \tag{5.4}$$

For reason of representation, I then redefine $\mathcal{L} = \log \mathcal{L}$. In the following sections I describe which N variables I have chosen, and how I have computed the probability density functions.

5.2 Variable definition

For the analysis of 1998 data $N = 14$ variables have been chosen to construct $\mathcal{L}$. They are the following:

- $|\vec{T}|$: value of the thrust;
- ϑ_T: polar angle of thrust;
- E_{40^o}: energy in a cone of 40 degrees along the beam pipe;
- $\sqrt{s'}$;

- acoplanarity between two jets (in two jet topology);
- difference between acoplanarity and acollinearity;
- $\cos(\vartheta_{jet})$, where ϑ_{jet} is the polar angle of the most forward jet;
- $P_{R\phi}$: missing momentum in $R\phi$ plane;
- P_z: missing momentum along Z;
- ϑ_{miss}: polar angle of missing momentum;
- α_j angle between two jets (in two jet topology);
- p_{thr} sum of absolute values of momenta of all particles along the thrust axis;
- ϕ_{j-p} angle in $R\phi$ between the missing momentum and the nearest jet;
- b tag.

The distributions of these variables for signal and background are shown in figures 5.1, 5.2 5.3 5.4. For some of them the discriminant power is not evident in the overall distribution for the backgrounds, but only when looking at a single component of the background sample. This is the case for example for ϑ_T which is useful to discriminate $q\bar{q}\gamma$ events. It is flat for $q\bar{q}\gamma$ while it peaks at 90 degrees for the signal. In the case of E_{40}, it is peaked at zero for the signal while it has tails at higher values for $q\bar{q}\gamma$.

5.3 B tag

As will be shown later, one of the most powerful variables to discriminate between signal and background is the b tag variable (see section 4.4.3). For a $e^+e^- \to H\nu\bar{\nu}$ analysis, the b tag variable is defined in the following way:

- each event is reconstructed in the two jet topology;
- for each jet the variable y defined in 4.1 is computed ($y_{1,2}$ for jet 1,2);
- b tag variable $= \log y_1 + \log y_2$

In the analysis of 1998 data a problem appeared when comparing the data with the simulation. The number of events with b tag variable greater than a predefined value was higher in data with respect to simulation in the four jet topology, while it was less in the two jet topology (see figure 5.5.

A detailed examination of the problem was pursued by the DELPHI collaboration and, at the moment of writing this thesis, the conclusions were:

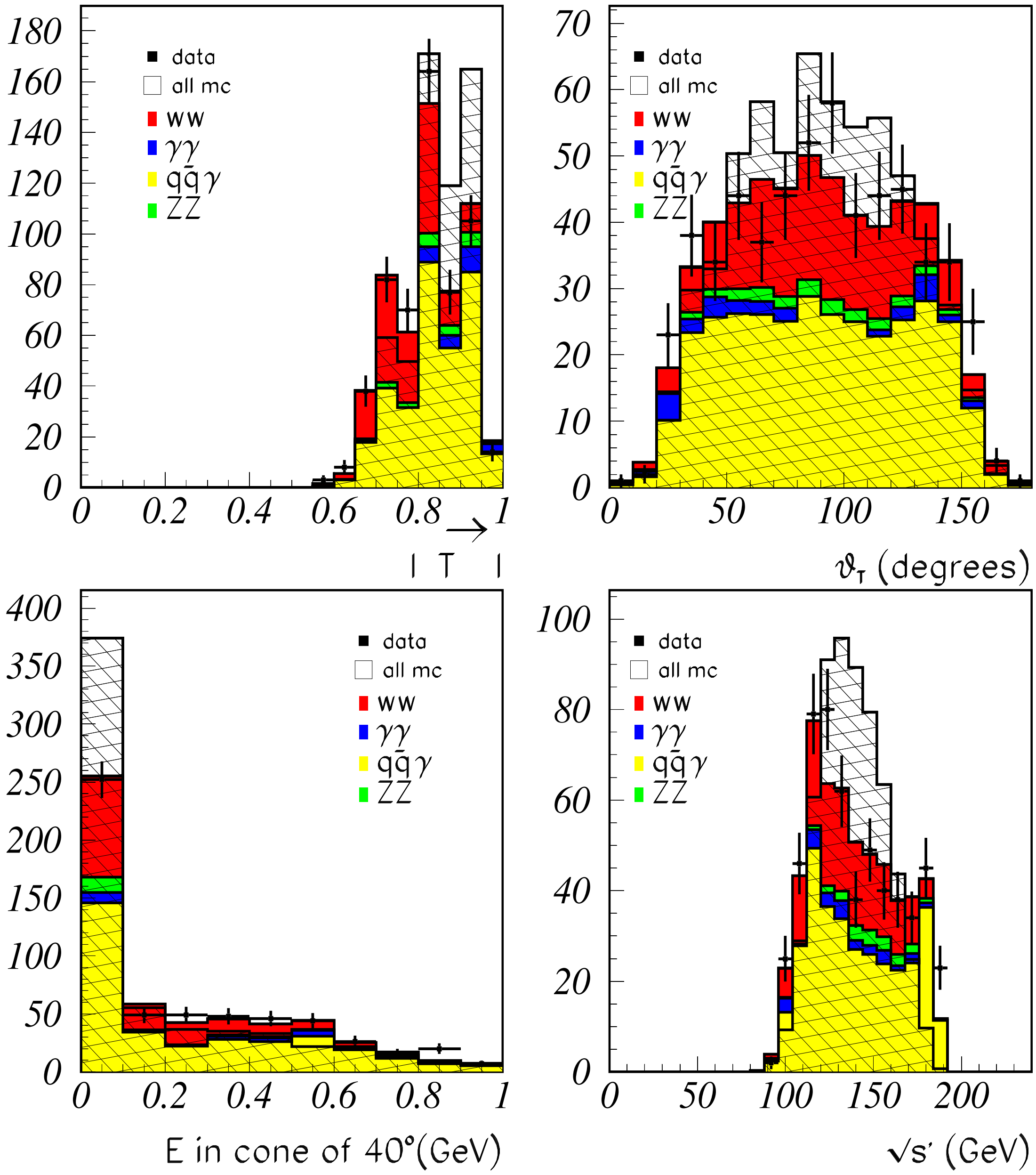

Figure 5.1: *Distribution of variables used in the likelihood. The superimposed hatched histogram corresponds to the distribution for signal ($m_H = 90$ GeV/c^2) with arbitrary normalisation.*

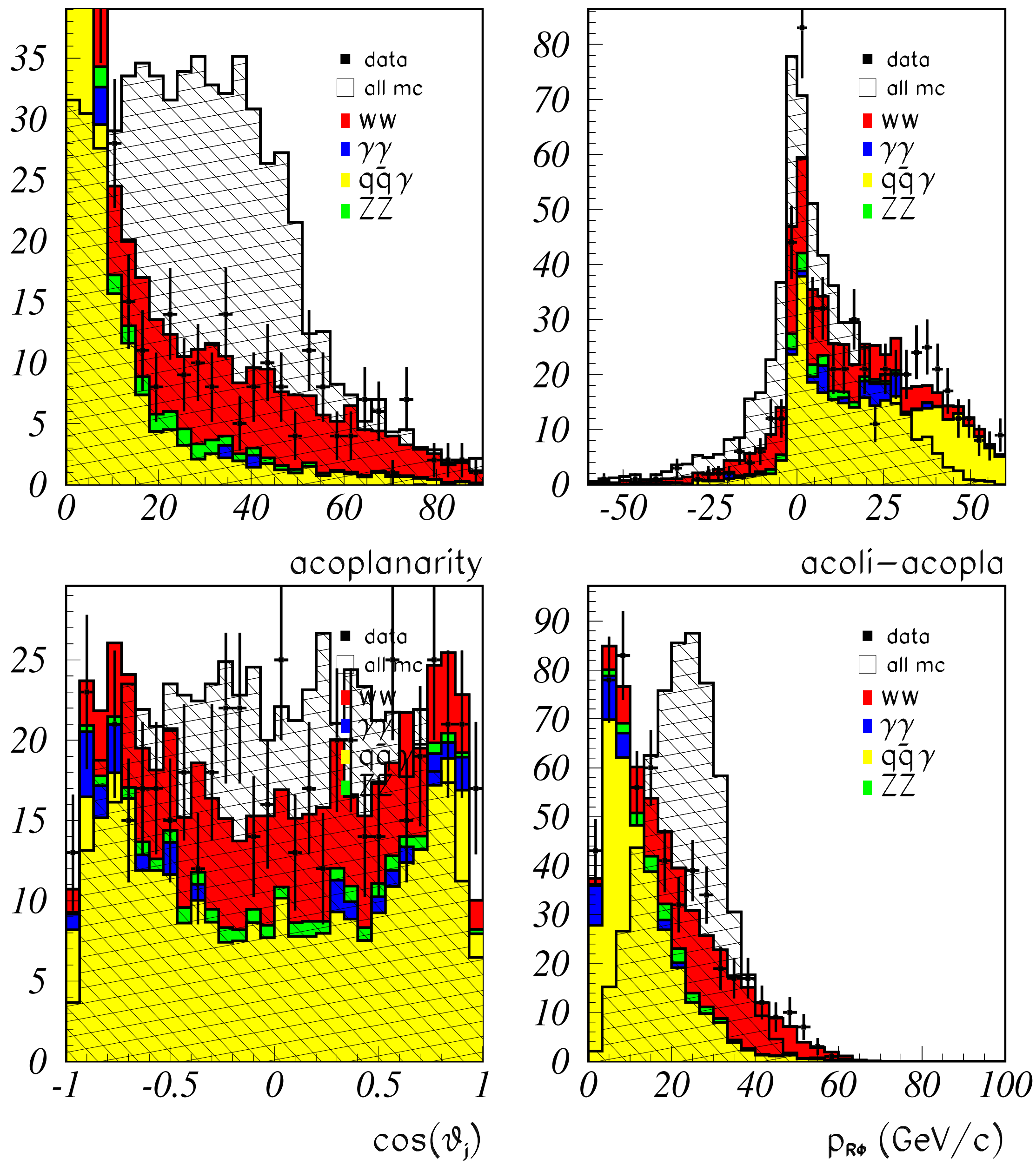

Figure 5.2: *Distribution of variables used in the likelihood. The superimposed hatched histogram corresponds to the distribution for signal ($m_H = 90$ GeV/c^2) with arbitrary normalisation.*

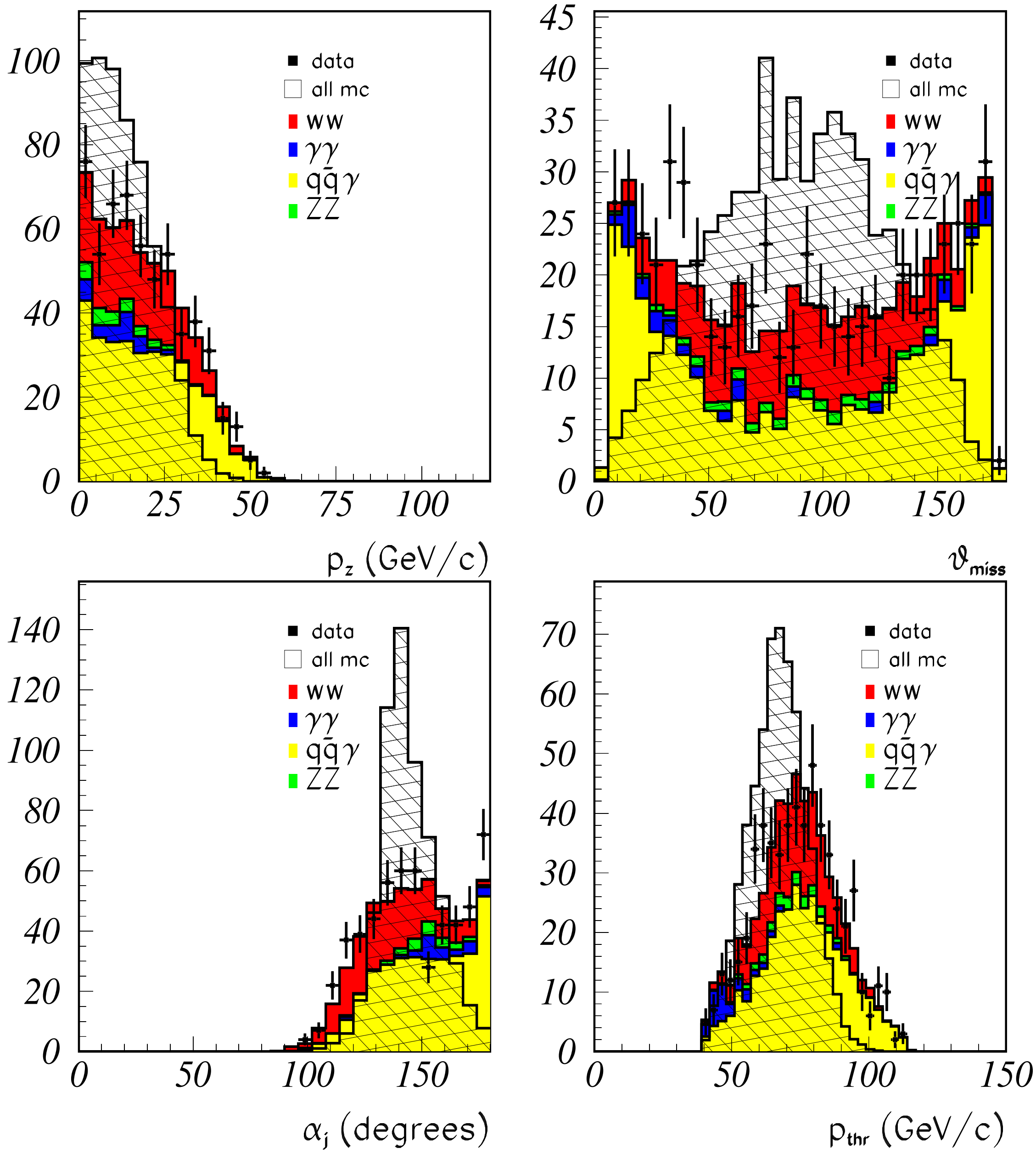

Figure 5.3: *Distribution of variables used in the likelihood. The superimposed hatched histogram corresponds to the distribution for signal ($m_H = 90$ GeV/c^2) with arbitrary normalisation.*

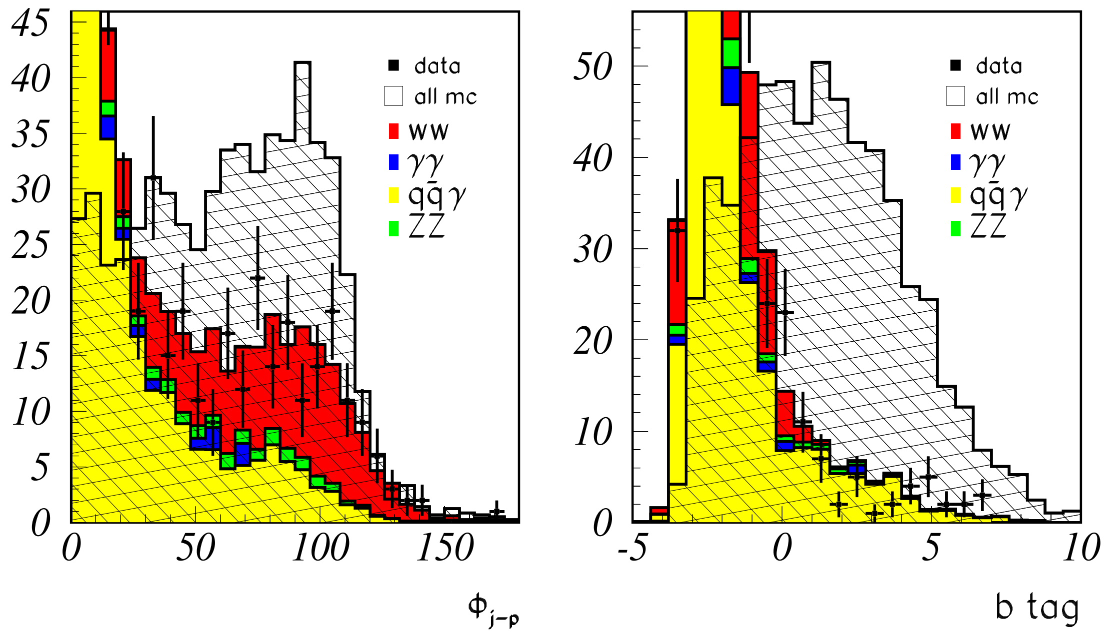

Figure 5.4: *Distribution of variables used in the likelihood. The superimposed hatched histogram corresponds to the distribution for signal ($m_H = 90$ GeV/c^2) with arbitrary normalisation.*

- using PYTHIA as the Monte Carlo for the generation of Z^0 (at $\sqrt{s} \approx 91$ GeV) and $Z^0\gamma$ events (where the ISR brings $\sqrt{s}$ again at ≈ 91 GeV), the rate of two b jet events was overestimated by 10% with respect to the data, while the rate of four b jet events was underestimated by 10%. The reason was due to a parameter (MSTJ(47)) set in a different way with respect to the value with which the Monte Carlo was tuned to the data.

- At $\sqrt{s} \approx 189$ GeV the same situation was present but the discrepancies were at 20 % level. Due to a $1/\sqrt{s}$ behavior, the setting of the parameter MSTJ(47) can explain only 3% of the effect. Other possible contributions come from:

  - value of the b quark mass in simulation. There has been a study on the predictions from the leading order massive matrix element expressions for two and four parton rates, using both a 5 GeV b quark pole mass (characteristic of hadronisation), and a 3 GeV running mass. It is natural to consider that because the rate of gluon radiation from b quarks depends on their mass (the higher the mass, the lower is the gluon radiation rate, which is known as the dead cone effect). Comparing the results obtained with the matrix element calculations to the predictions of the parton shower algorithm implemented in JETSET (the main program used at LEP), it has been found that consistently lower rates are produced with this program. At high energy the effect can be of the order of $5 \pm 3\%$.

  - gluon splitting rate into b quark pairs. At Z^0 peak energy the rate predicted

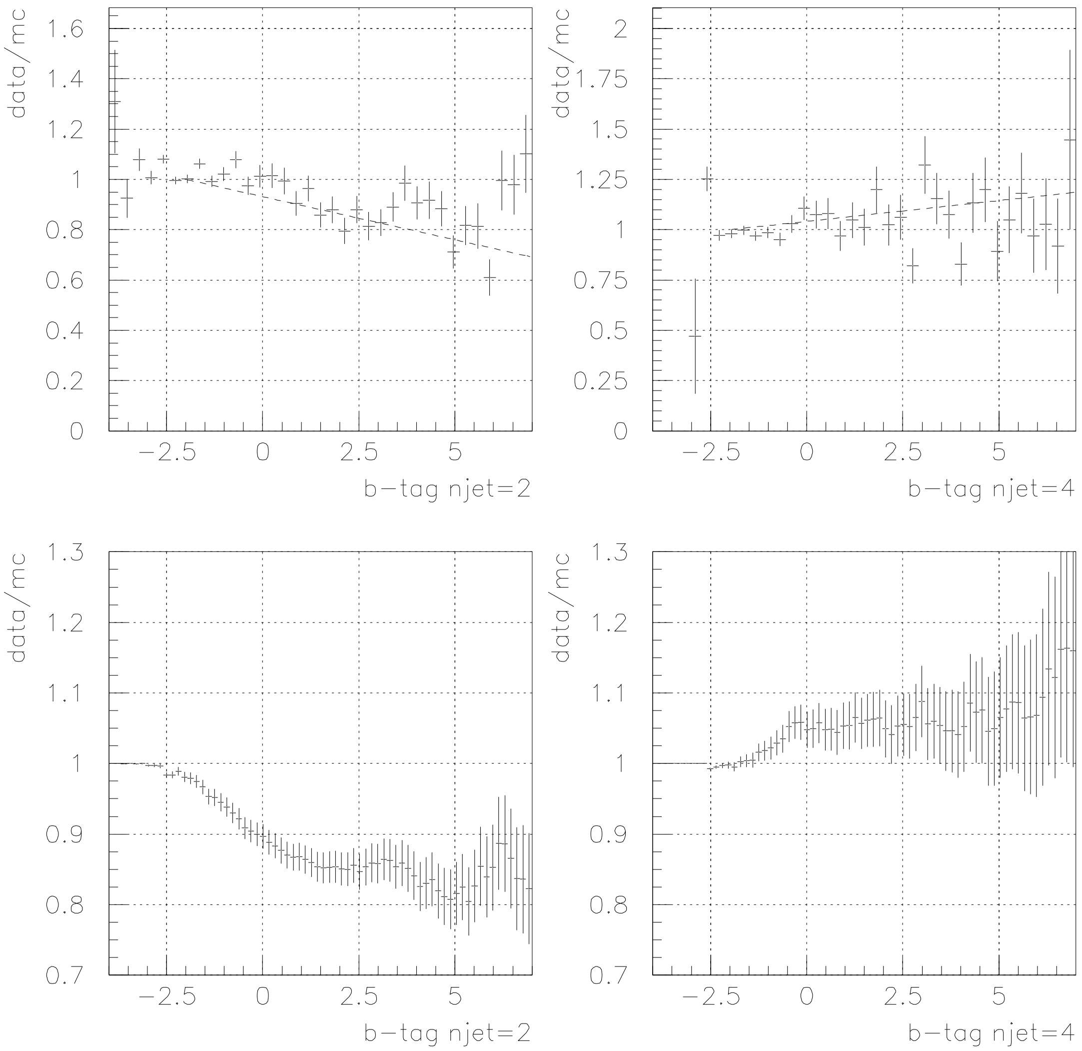

Figure 5.5: *The upper plots show the ratio between data and simulation of the number of jets with a predefined b tag value, in two and four jet topologies. The dotted lines are the fit described in the text. The lower plots show the ratio between data and simulation of the number of jets with b tag value greater then a predefined value, in two and four jet topologies.*

in the JETSET parton shower program needs to be increased by roughly a factor of 2 to agree with the known value. A similar, although smaller, factor exists also for the gluon splitting rate into c quark pairs. The extrapolation to high energy of these rates is a matter for discussion.

Since the main background in the $H\nu\overline{\nu}$ analysis is the $q\overline{q}\gamma$ with effective center of mass energy at the Z^0 peak, we are in the situation where the discrepancies between data and simulation are of the order of 10% which is mostly explained. To take into account the discrepancies, we fitted at Z^0 peak energy the ratio between data and simulation for the number of b tagged jets versus the value of the b tag variable, in the two and four jet topologies (figure 5.5). We apply the correction on the high energy $q\overline{q}\gamma$ simulation when in the generation chain a Z^0 on shell has been produced.

After this correction the data agree with the simulation also at high value of the b-tagging variable as shown in figure 5.6.

5.4 Derivation of probability density functions

The derivation of probability density functions for each variable and for each sample is based on the simulation.

For each process the spectrum for the considered variable has been derived , and plotted with a bin size compatible with the detector resolution.

Due to the limited statistics there can be some fluctuations in the distributions. To minimise them, an averaging procedure has been applied. This procedure consists in the following: if the bin i has a number of entries $n(i)$ less then 6, then the averaged $\overline{n(i)}$ is defined by:

$$\overline{n(i)} = \frac{n(i-2) + 2 * n(i-1) + 3 * n(i) + 2 * n(i+1) + n(i+2)}{9} \tag{5.5}$$

In other words the content of previuos two bins $(n(i-1),\ n(i-2))$ and the content of following two $(n(i+1),\ n(i+2))$ are taken into account. The probabilty density function is then defined by the interpolation of this averaged distribution (figure 5.7).

5.5 Performance

As mentioned before, the b tag is one of the most powerful variables to discriminate between signal and background. This can be understood taking into consideration the different branching ratios of background and signal into b quarks:

- $H \rightarrow b\overline{b} \sim 85\%$
- $Z \rightarrow b\overline{b} \sim 14\%$
- $W \rightarrow b\overline{c}$ proportional to $|V_{cb}|^2 \sim 0.039^2$

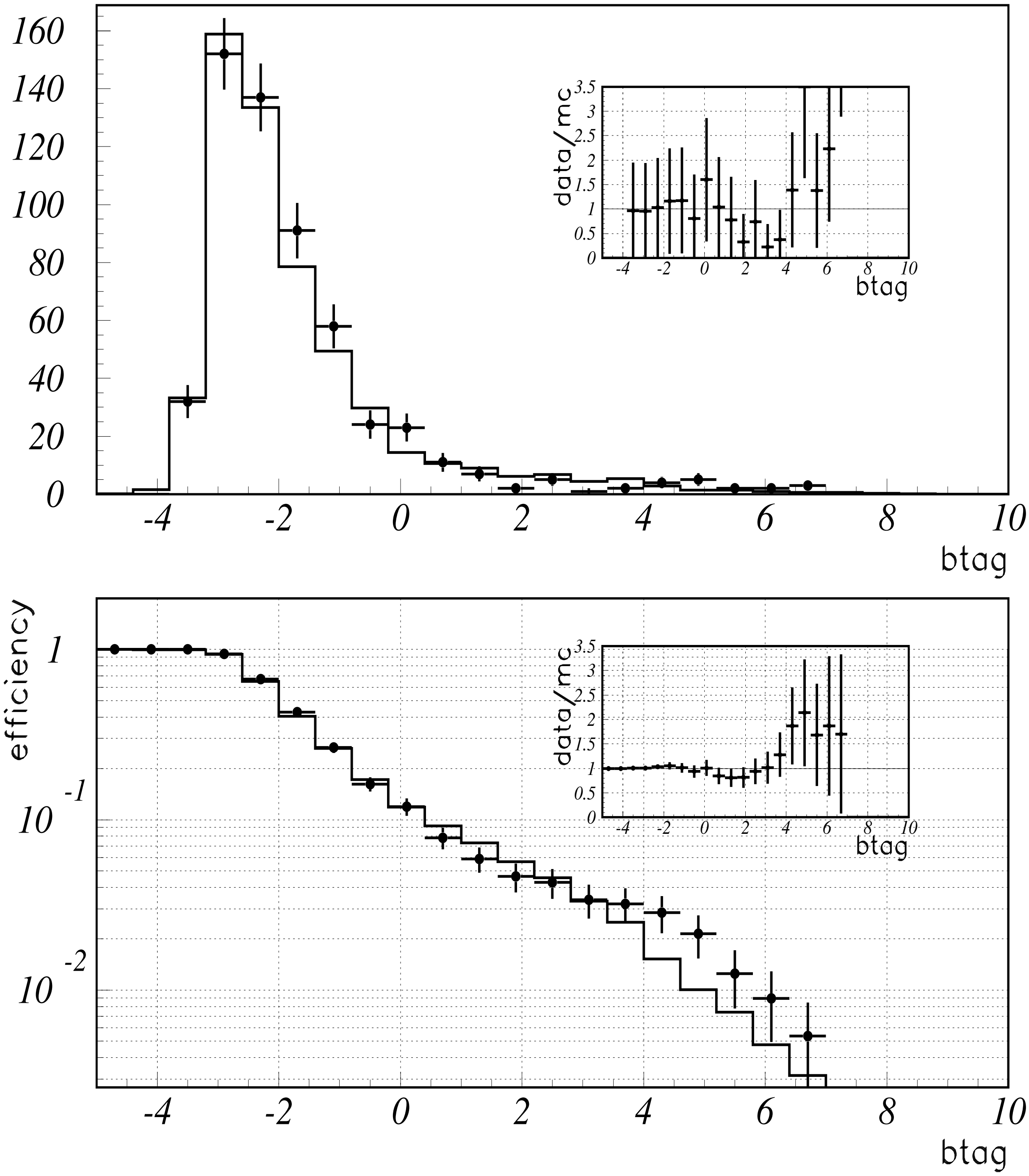

Figure 5.6: *The upper plot shows the distribution of b tag variable for data (points) and simulation (full line histogram). The lower plot shows the number of events with b tag value greater than the value in abscissa for data (points) and simulation (full line histogram). The inserts show the ratio between data and simulation for the corresponding distribution. The agreement is statistically good.*

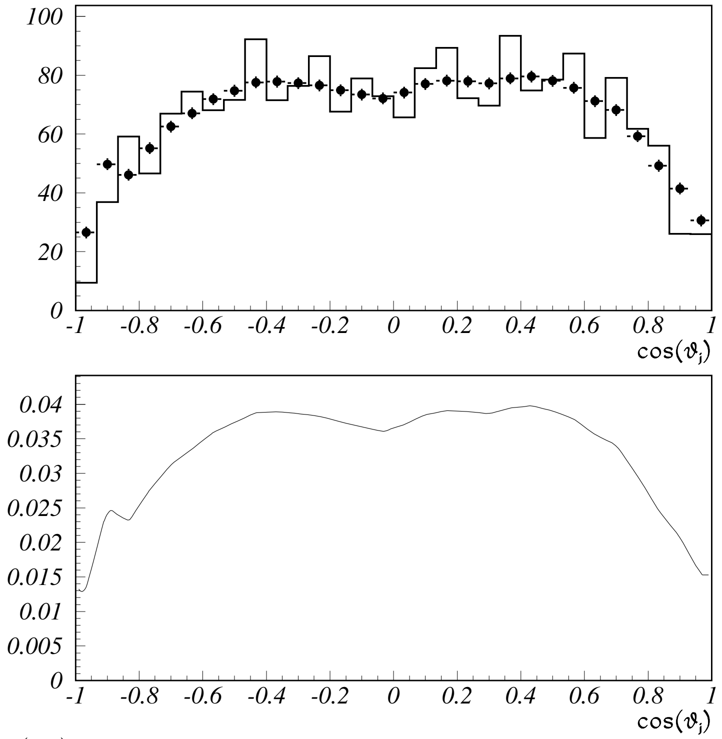

Figure 5.7: $\cos(\vartheta_j)$ *for ZZ events. This plot shows how the averaging procedure works: the full line histogram in the upper plot shows the original distribution, while the dots show the averaged one. The fluctuations are considerably decreased. The lower plot shows the fitted probability density function.*

Asking for a b quark in the WW sample immediately suppresses the contribution from these events. For the other samples, considering an equal efficiency of the b tag algorithm in the different backgrounds, one can expect a reduction of background with respect to signal approximately equal to a factor:

- 85/14 for $q\overline{q}\gamma$;
- 85/28 for ZZ.

This effect is visible in figure 5.10. For instance, when asking for a b tag variable greater than 2, the $q\overline{q}\gamma$ background is $\sim 7\%$ of the starting sample before asking for a b quark, the ZZ is 14% and Higgs is $\sim 50\%$.

The overall performance of the likelihood is shown in figure 5.11. One can see that, for example, in the region of $\sim 50\%$ for the signal efficiency, the efficiency for $q\overline{q}\gamma$ is $\sim 2\%$, considerably reduced compared to the case when only the b tag is used. On the contrary the efficiency for ZZ is still $\sim 12\%$, not so much reduced with respect the requirement of b tag only. The explanation is that if one of the Z decays into neutrinos this is an irreducible background, the topology of such ZZ events being very similar to the one for the signal.

Since the limit on the Standard Model Higgs boson mass from 1997 data is $m_h > 89.7$ GeV, we are in the critical region where the signal from Higgs is hardly distinguishible from ZZ events. If for instance the Higgs particle exists with mass near the mass of the Z, the only possibilities to detect evidence of a signal would be to measure the cross sections of ZZ to reveal an excess with respect to the prediction of the

Standard Model, or to measure the branching ratios into b quarks (taking advantage of the different branching ratios of Z and Higgs in b quarks). But this requires precise measurements, achievable only with high luminosity.

Another possibility should be the investigation of the distribution in θ of final decay products.

The angular distribution of the Z/H bosons in the Higgs-strahlung process is sensitive to the spin and parity of the Higgs particle. Since the production amplitude (for Higgs with quantum number 0^+) is given by $\mathcal{A}(0^+) \sim \vec{\epsilon}_{Z^*} \cdot \vec{\epsilon}_Z$ (where $\vec{\epsilon}_Z$ is the polarization vector of Z, and $\vec{\epsilon}_{Z^*}$ the one for the virtual intermediate Z), the Z boson is produced in a state of longitudinal polarization at high energies. As a result, the angular distribution

$$\frac{d\sigma}{d\cos\theta} \sim \sin^2\theta + \frac{8M_Z^2}{s\lambda} \tag{5.6}$$

(where $\lambda = [1-(M_H+M_Z)^2/s][1-(M_H-M_Z)^2/s]$) approaches the spin-zero $\sin^2\theta$ law asymptotically.

It is characteristically different from the distribution of the background process $e^+e^- \to ZZ$, which, as a result of t/u-channel e exchange (see figure 4.2.d), is strongly peaked in the forward/backward direction, as shown in figure 5.8.

Moreover the $\sin^2\theta$ distribution for a 0^+ Higgs boson contrasts with the distribution $\sim 1+\cos^2\theta$ for negative parity states, which follows from the transverse polarisation amplitude $\mathcal{A}(0^-) \sim \vec{\epsilon}_{Z^*} \times \vec{\epsilon}_Z \cdot \vec{k}_Z$. This can be a method to distinguish between two different Higgs bosons of MSSM.

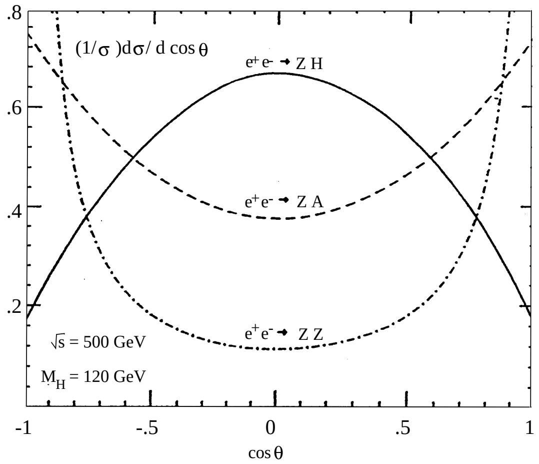

Figure 5.8: *Angular distribution of Z/H bosons in Higgs-strahlung, compared with the production of pseudoscalar particles and the ZZ background final states.*

The other background hard to remove is the double symmetric radiative return (it is included in the sample $q\overline{q}\gamma$) in which two photons are emitted by the e^- and e^+, and the resulting centre of mass energy is the one of Z^0 on shell production. The cross section is peaked when the emitted photons are near the beam line. Inspecting the simulation in the starting sample, before the preselection cuts described in a previous chapter, 8.3% of the events have both photons visible in the detectors, 37.4% of events have one photon visible and the other in the beam pipe, while in 54.3% of the cases both photons are in the beam pipe. After the preselection cuts for the $H\nu\overline{\nu}$ analysis, there are pratically no more double radiative returns with both photons in the detector, 7% with one photon in the detector, and 93% with two photons in the beam pipe. We were motivated by this situation to investigate in more details the double symmetric radiative return.

The next chapter is dedicated to this study, in which we measured for the first time at LEP the cross section for this process. As will be shown, these events are peaked at low acoplanarity and have high missing momentum along the beam pipe. For the Higgs signal coming from Higgs-strahlung process the acoplanarity increases approaching the kinematical limit (see figure 5.9). Using the WPHACT generator we produced the distributions for the invariant mass of $\nu\overline{\nu}$ and the boost of the Higgs particle to explain the increase of acoplanarity at the kinematical limit. As one can see in figure 5.9, approaching the kinematical limits, the Z is not produced on shell any longer, and then the probability to have an off-shell Z is almost flat as a function on the Z* mass thus favoring the situation of a boosted Higgs. For the WW fusion process this is of course no more true, and actually the acoplanarity does not increase approaching the kinematical limit.

To remove the double radiative return events, we decided to require acoplanarity greater than 1 degree (so they are reduced by 25%) and to require missing momentum along the beam pipe less then 30 GeV/c (when they are further reduced by 20%). These cuts have been applied after the likelihood computation, to avoid decreasing the statistics for the distributions fitted in order to determine the probability density functions.

An useful way to present the performance at this stage is to look at the number of selected events versus the efficiency for the signal (see figure 5.12). These are actually the inputs needed to compute the limit in case of absence of signal. Moreover, from this plot it is possible to deduce the signal over noise ratio for each value of the likelihood. In such a way one can choose which is the optimal working point to compute the limit on the Higgs mass. It is worthwhile to notice that at Higgs efficiency of 30% the signal over background ratio is of teh order of 0.3, while the starting signal over background was $\simeq 10^{-4}$.

5.5.1 Performance at different Higgs masses

One should note that the performances depend on the mass of the Higgs, and this is due to the fact that the "optimization of the likelihood" depends on the mass. To optimize the likelihood for a signal means to fit the probability density functions for that signal. In the Higgs analysis, the distribution of variables used in the likelihood depends on the Higgs mass and so also does the likelihood performance. To reduce

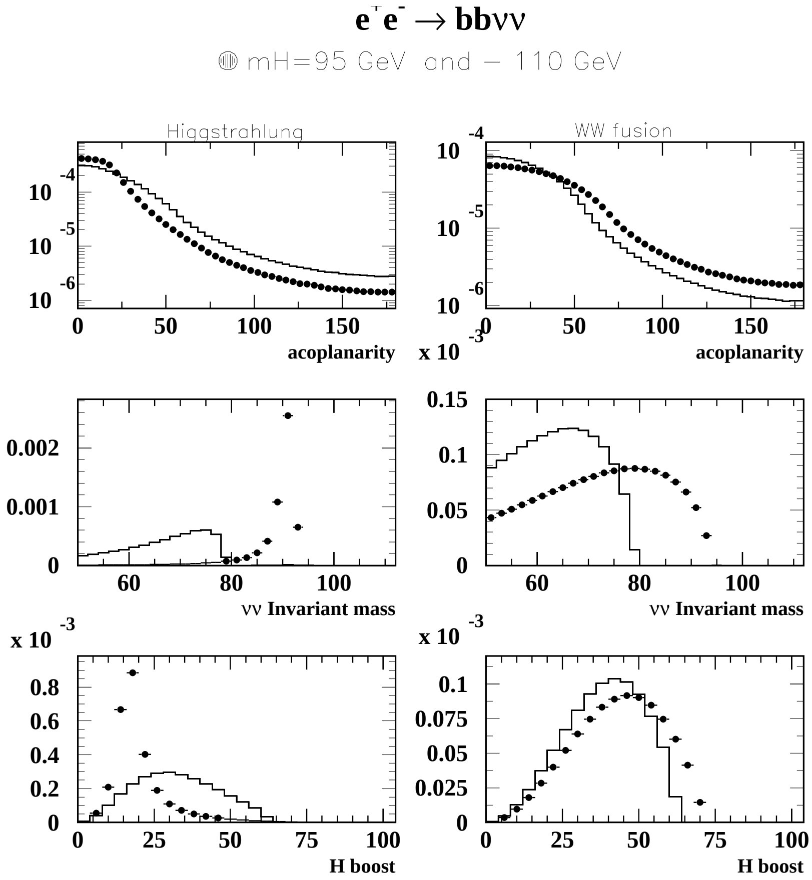

Figure 5.9: *The upper plots show the acoplanarity for Higgs masses of 95 and 110 GeV at 189 GeV center-of-mass energy. Approaching the kinematical limits, the Z is not produced on shell any longer, and then the probability to have an off-shell Z^0 is almost flat as a function on the Z^{0*} mass (see plots of invariant mass), thus favoring the situation of a boosted Higgs (see third line). The plots on the left are for the Higgs-strahlung process, the ones on the right for the WW fusion process.*

such dependence we decided to use as distribution for the signal a sum of distributions for different Higgs masses with equal weight. Since the limit on the Standard Model Higgs boson mass from 1997 data is $m_h > 89.7$ GeV we used signal simulations with Higgs mass of 85, 90, 95, 97.5 GeV. Figure 5.13 shows the efficiency for different Higgs masses when there are 10 events selected.

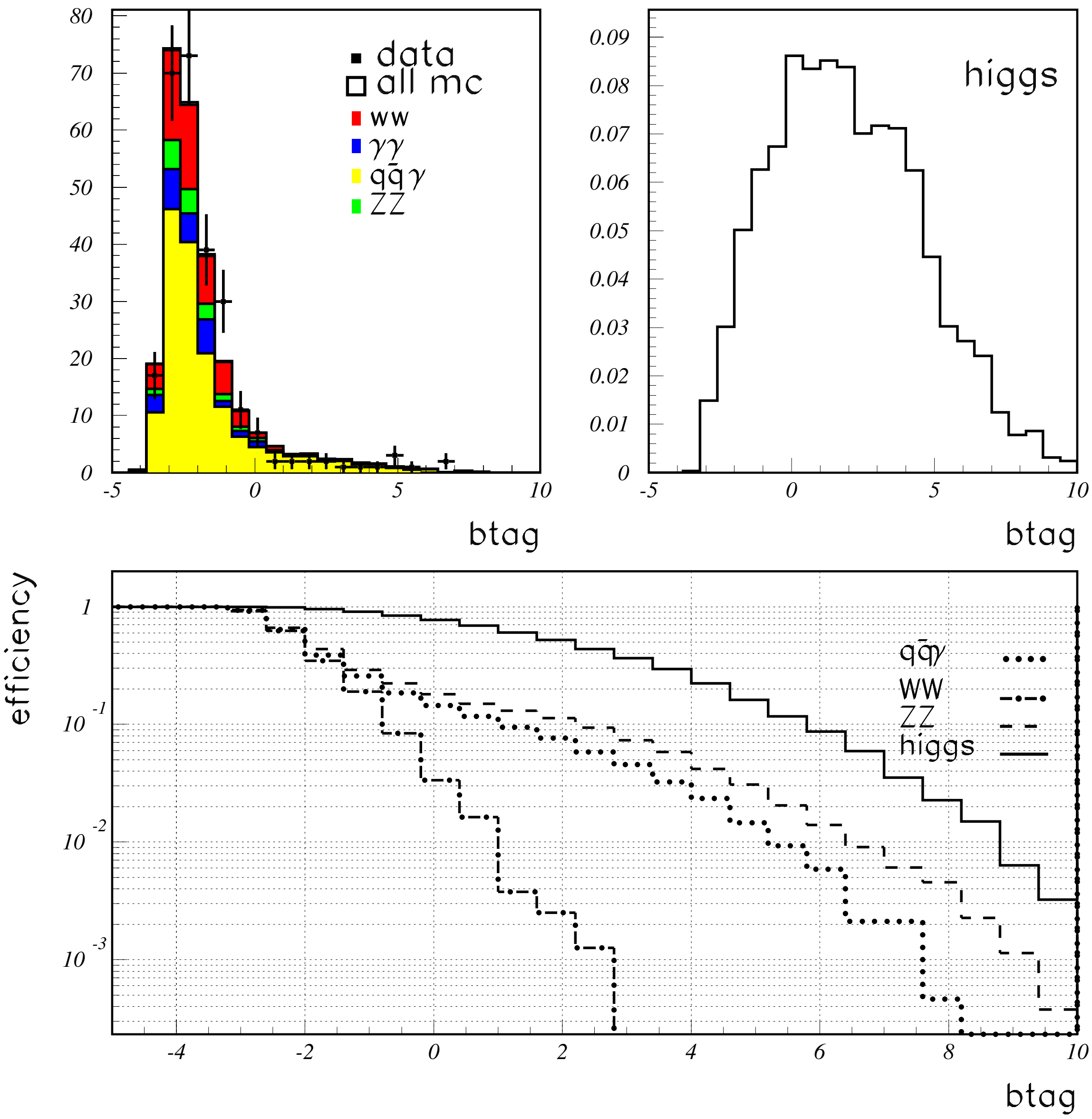

Figure 5.10: *The upper plots show the distribution of* $\log y_1 + \log y_2$ *for signal and background. The lower plot shows the efficiency for signal and background when asking for the b tag variable greater than the corresponding abscissa.*

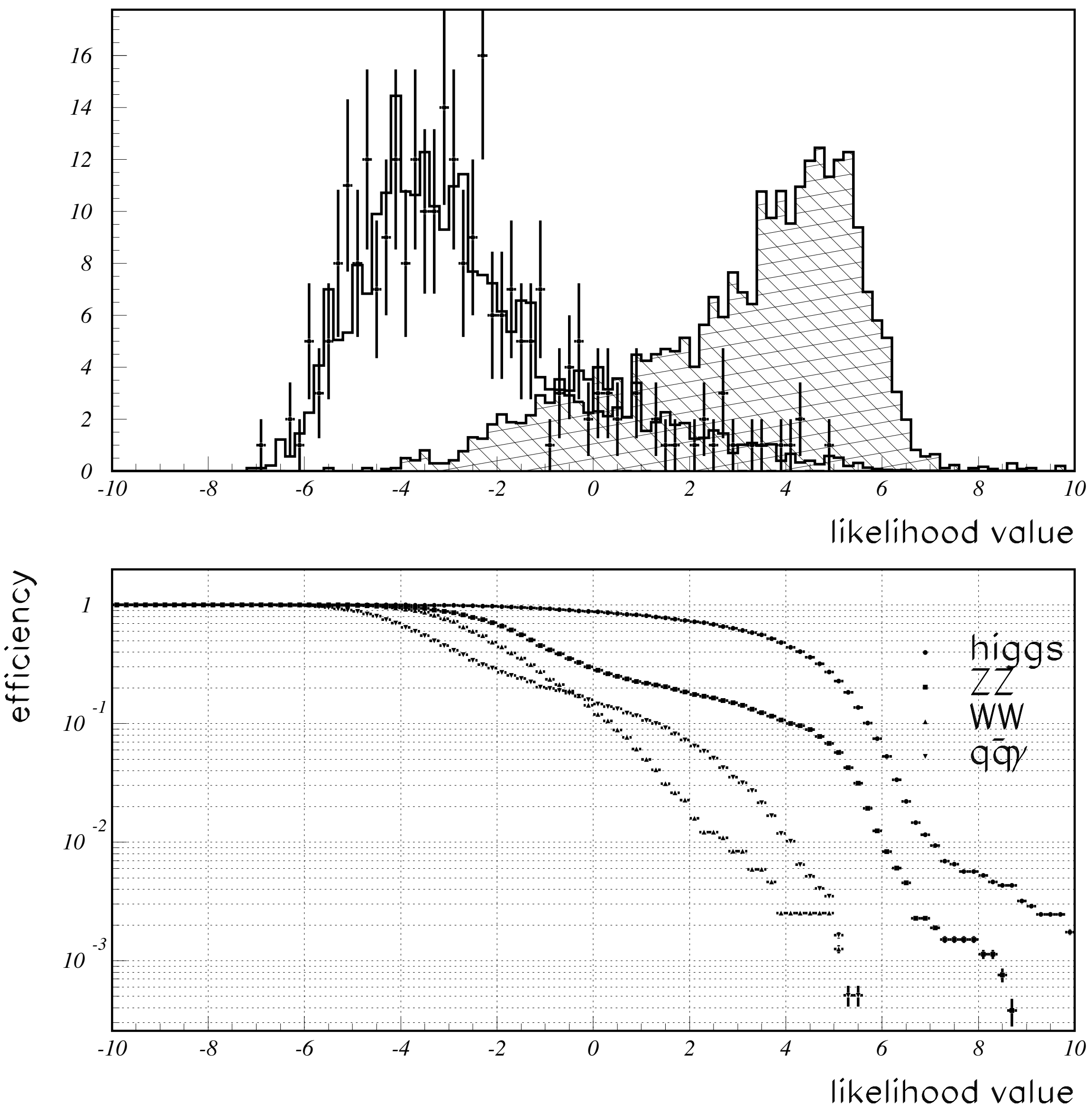

Figure 5.11: *Upper plot: distribution of the likelihood for data (points), simulation (full line) and Higgs signal of $m_h = 90$ GeV (hatched histogram). Lower plot: efficiency asking a likelihood value greater then the corresponding abscissa.*

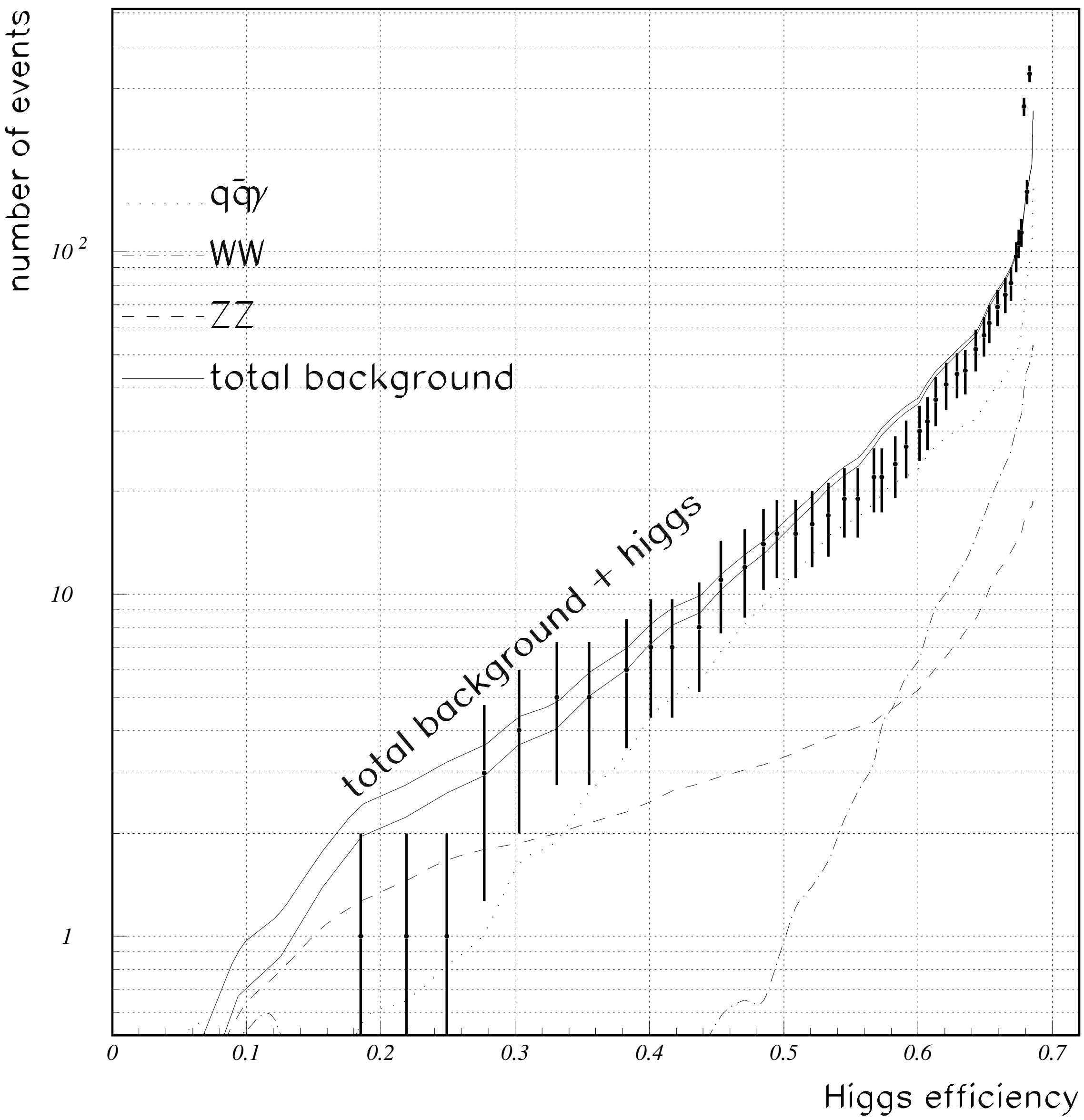

Figure 5.12: *Number of events (in data, total mc, WW, ZZ, $q\bar{q}\gamma$) versus efficiency for Higgs signal of $m_h = 90$ GeV.*

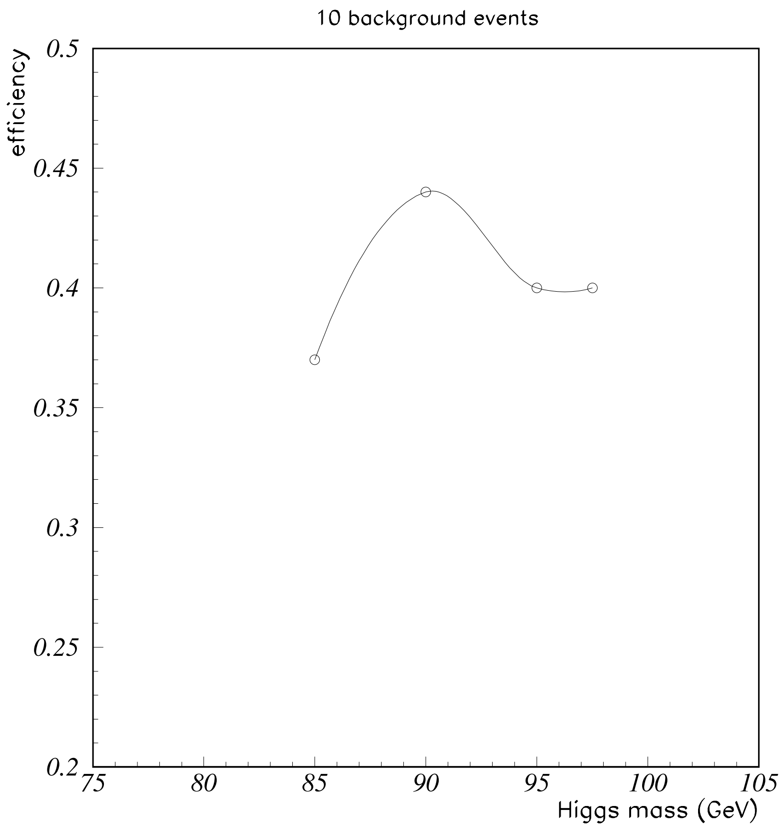

Figure 5.13: *Efficiency for different Higgs masses at fixed number of events (10 events).*

Chapter 6

The symmetric double radiative return to Z^0

At LEP2 energies the radiative return to the Z^0 boson is one of the dominant physics processes. More rare is the process in which two high energy photons are emitted and the Z^0 is produced at rest or with little boost. It is interesting to measure the cross section of this process because it has never been measured at LEP and because if the two photons escape detection it is one of the irreducible backgrounds for the Higgs search made in this thesis.

In this chapter the symmetric double radiative return events have been studied, i.e. the events in which two photons of similar energies are emitted and a Z^0 boson is produced almost at rest in the laboratory frame and decays into quarks. I considered three different final states: when both the photons are detected in the DELPHI apparatus, when only one is detected and the second is lost in the beam-pipe, and when both go undetected.

I estimated the efficiency using the PYTHIA simulation, and I extracted the cross section as a function of the centre-of-mass energy.

6.1 Data and Monte Carlo simulation

The analysis of the process has been done on the data collected in 1998 at a centre of mass energy of 189 GeV (158 pb^{-1}) and also on the data collected during 1999 at an energy of 196 GeV (76.9 pb^{-1}).

High statistics of background and signal events (in this chapter the signal is defined as the double radiative return to Z^0) have been produced by Monte Carlo simulation (see section 4.2.1). The signal events have been generated with `PYTHIA` [52] for ($e^+e^- \to q\bar{q}\gamma$, $e^+e^- \to q\bar{q}\gamma\gamma$)

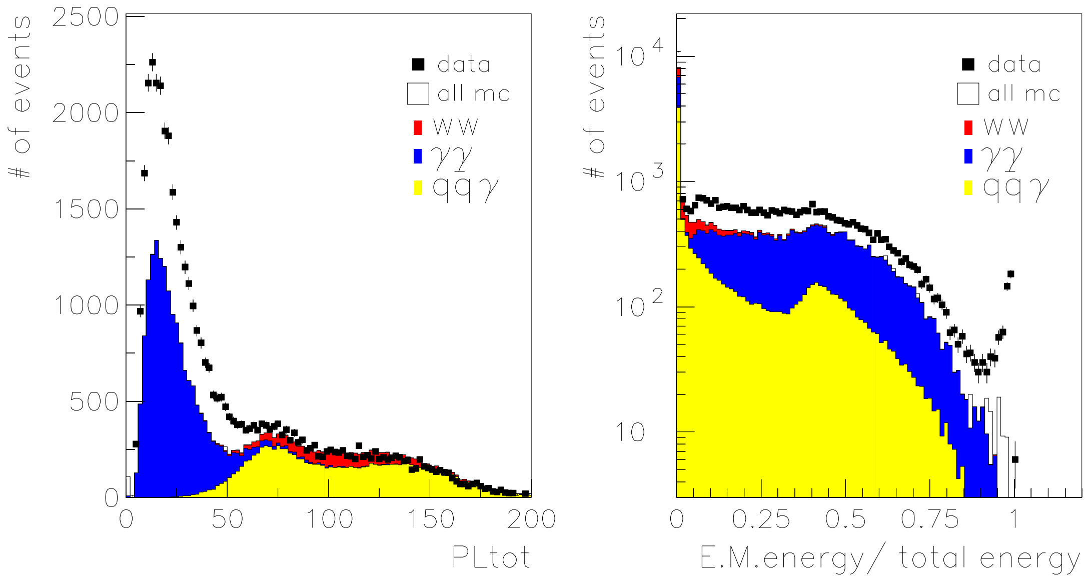

Figure 6.1: *The distribution for the selected events of two of the variables described in text that allows the $\gamma\gamma$ and Bhabha events identification*

6.2 Analysis and results

6.2.1 Event Selection

The particle selection is the same of the one applied for the Higgs analysis (see section 4.4.1). Sequential cuts are applied in order to reject the main background keeping the signal efficiency as high as possible.

Events are selected if:

- the total number of neutral particles is less than 60;
- the total number of charged tracks is more than 5;
- the total number of particles is more than 10.

6.2.1.1 Rejection of $\gamma\gamma$ and Bhabha events.

The following cuts were applied to suppress the $\gamma\gamma$ events and the Bhabha's:

- the transverse momentum should be greater than 20 GeV;
- the sum of the absolute values of the particle momenta along the thrust axis PL_{tot} should be more than 40 GeV;

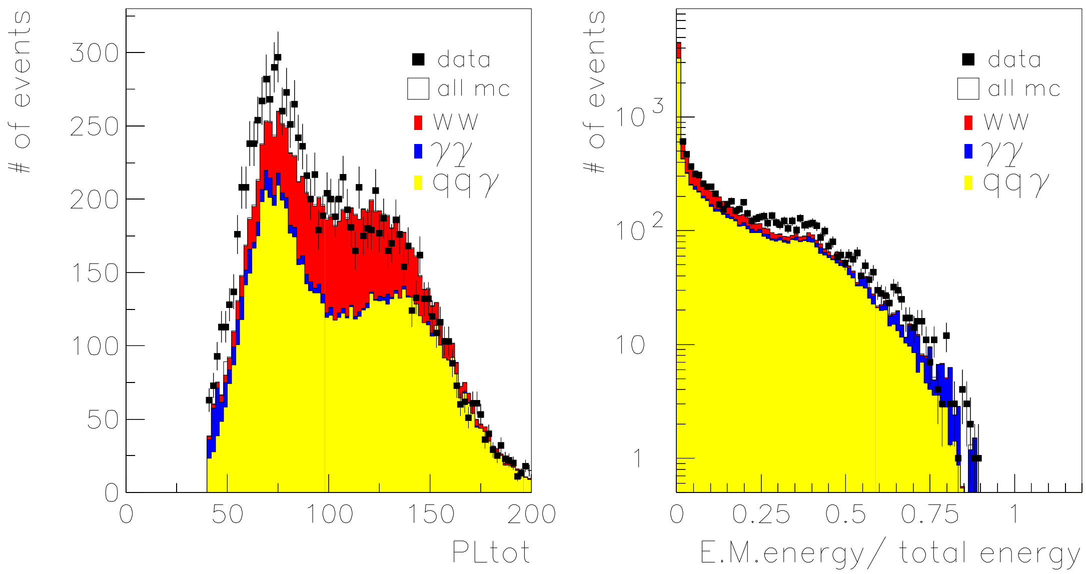

Figure 6.2: *Same as figure 6.1 after the $\gamma\gamma$ and Bhabha events suppression, at $\sqrt{s}$=189 GeV.*

- the electro-magnetic energy should be less than 90% of the total energy;
- no identified electron in the forward region;
- no electro-magnetic clusters of energy higher than 65 GeV

In fig.6.1 the distributions of the sum of the absolute values of the particle momenta along the thrust axis and the fraction of electro-magnetic energy are shown for data and simulation. After these cuts a relatively good agreement between data and simulation is obtained as shown in figure 6.2 for the same variables. The total number of events that survive at $\sqrt{s}$=189 GeV is 12029 in data and 11640.9 in simulation (i.e. 3.3% more events in data). The corresponding numbers at $\sqrt{s}$=196 GeV are 5111 in data and 5090.7 events in simulation.

6.2.2 The photon identification

Electro-magnetic clusters are identified by a dedicated software program REMCLU [42] in all the three electro-magnetic calorimeters: HPC, FEMC, STIC (see section 2.3.2.2). All the events with two identified photons (classified as tight or loose by REMCLU) are considered.

6.2.3 The kinematics of the double radiative events

An event is classified as a symmetric double radiative return when two photons of similar energies have been emitted (respectively by the e^+ and the e^-) and a Z^0 is produced almost at rest.

The biggest background to this process is the single radiative return to the Z^0, if the photon energy is not well measured and if there are other photons or mis-identified electrons in the events.

The distinctive kinematics of the symmetric double radiative return events can be exploited to obtain a very high signal purity with very simple cuts (especially when both the photons are seen in the detector). Ordering the photons according to their energy, and supposing them back to back, the following equation holds:

$$E_{\gamma 1} = \sqrt{s}/2. \; - \; m_{Z^0}^2/(2. \cdot \sqrt{s} - 4. \cdot E_{\gamma 2}) \tag{6.1}$$

and the second photon has maximal energy when:

$$E_{\gamma 2}^{max} = E_{\gamma 1} = (\sqrt{s} - m_{Z^0})/2 \tag{6.2}$$

The energy of the photon in the single radiative return event is a limiting case of equation 6.1:

$$E_{\gamma}^{single} = (s \; - \; m_{Z^0}^2) \; / \; 2\sqrt{s} \approx 72 \; GeV \;\; (at \; \sqrt{s} = 189 \; GeV) \tag{6.3}$$

In the “single” radiative return event there can be emission of more than one photon but mostly in the same direction. This means that the sum of the energy of the 2 most energetic photons in the event for a single radiative return decay will be peaked at $E = E_{\gamma}^{single}$ while for the symmetric double radiative decay at $E \; = \; (\sqrt{s} - m_{Z^0})GeV$.

In all these equations we neglected that the Z^0 has a finite width. In practice the energy of the photons will be in a range defined by the width of the Z^0 boson. In the following we consider that the Z^0 boson is defined by a mass range of ± 10 GeV around the central value of 91.187 GeV (i.e. in a 4 $\cdot \Gamma_{Z^0}$ interval). The full line in figure 6.3 shows the the energy of the first photon as a function of the energy of the second photon. The two dashed lines represent a 10 GeV range around the Z^0 mass. The aim of this analysis is to study events where the Z^0 is created with zero or small boost. To this extent the arrows shown in figure 6.3 separate the “single radiative return” from the “double radiative return” events. In practice the signal is selected by requiring that the most energetic photon of the event has energy lower than

$$E_{\gamma 1}^{max} = (s \; - \; (m_{Z^0} + 10)^2) \; / \; 2\sqrt{s} \quad (67 \; GeV \; at \; \sqrt{s} = 189 \; GeV). \tag{6.4}$$

and the second one has energy larger than $E_{\gamma 2}^{min}$, defined by equation 6.1 when $E_{\gamma 1} = E_{\gamma 1}^{max}$.

In figure 6.4.a the correlation between the sum of the two photon energies and the absolute difference of their θ angles is shown, when requiring that the second photon has energy larger than $E_{\gamma 2}^{min}$ GeV following equation 6.1. Figure 6.4.b shows the same

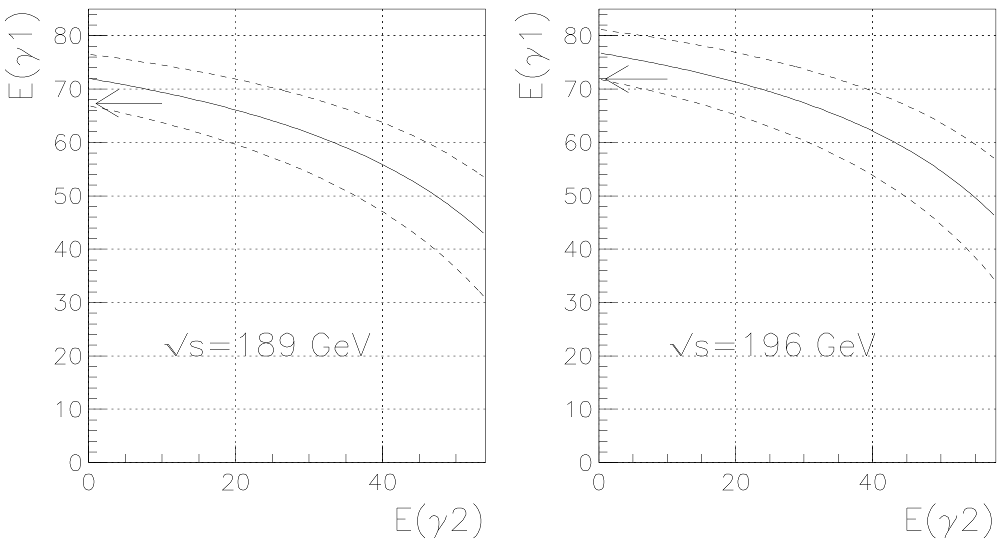

Figure 6.3: *The full line is the relation between the two photon energies (described by equation 6.1), and the two dashed lines are obtained allowing a $\pm$ 10 GeV range around the Z^0 mass, at the two different centre-of-mass energies. The arrow defines the cut used to separate the "single radiative return" from the "double radiative return" to the Z^0.*

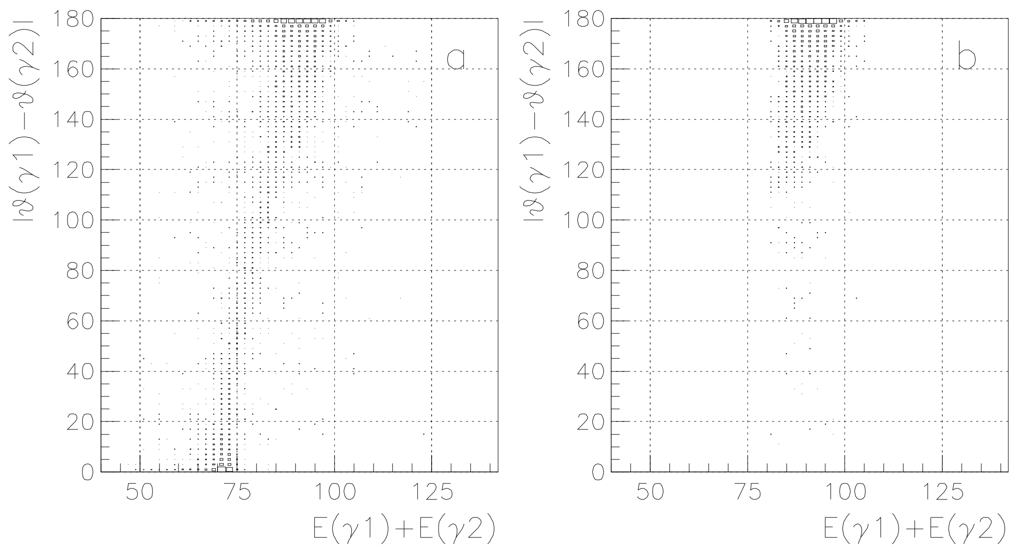

Figure 6.4: *The distribution of the absolute difference of the two photon polar angles versus the sum of the two photon energies for simulated events. In a) asking $E_{\gamma 2} \geq E_{\gamma 2}^{min}$ and in b) cutting also on the energy of the first photon as described in the text.*

when requiring in addition that the most energetic photon has energy lower than $E_{\gamma 1}^{max}$. The figure shows that the signal is mostly concentrated at values of angular difference larger than 90°. In figure 6.5 the boost of the Z^0 is shown as a full line for all the events, and as the dashed line for the selected "double radiative return" events.

Figure 6.6.a shows the sum of the energies of the two most energetic photons from PYTHIA simulated events; one can see the peak of the radiative return events and, at higher energy, a smaller shoulder which is our signal. Asking that the second photon has energy larger than E_{γ}^{min}, the radiative return peak is considerably reduced as is shown in figure 6.6.b . Finally in figure 6.6.c the relation between the two photon energies of equation 6.1 is applied demanding $E \leq E_{\gamma 1}^{max}$ and cutting on the sum of the photon polar angles. In fig. 6.6.c the dashed line is the same plot as fig. 6.6.a, proving that the signal can be efficiently identified by kinematic constraints.

6.2.4 The 1998 data results

6.2.4.1 Both photons in the detector

The percentage of the events in which both the photons are seen in the DELPHI detector, i.e. lie in the polar angle region $3° \leq \theta \leq 177°$, is only 8% (estimated using the PYTHIA simulation).

In figure 6.7 the energy spectra of the two most energetic photons and the polar

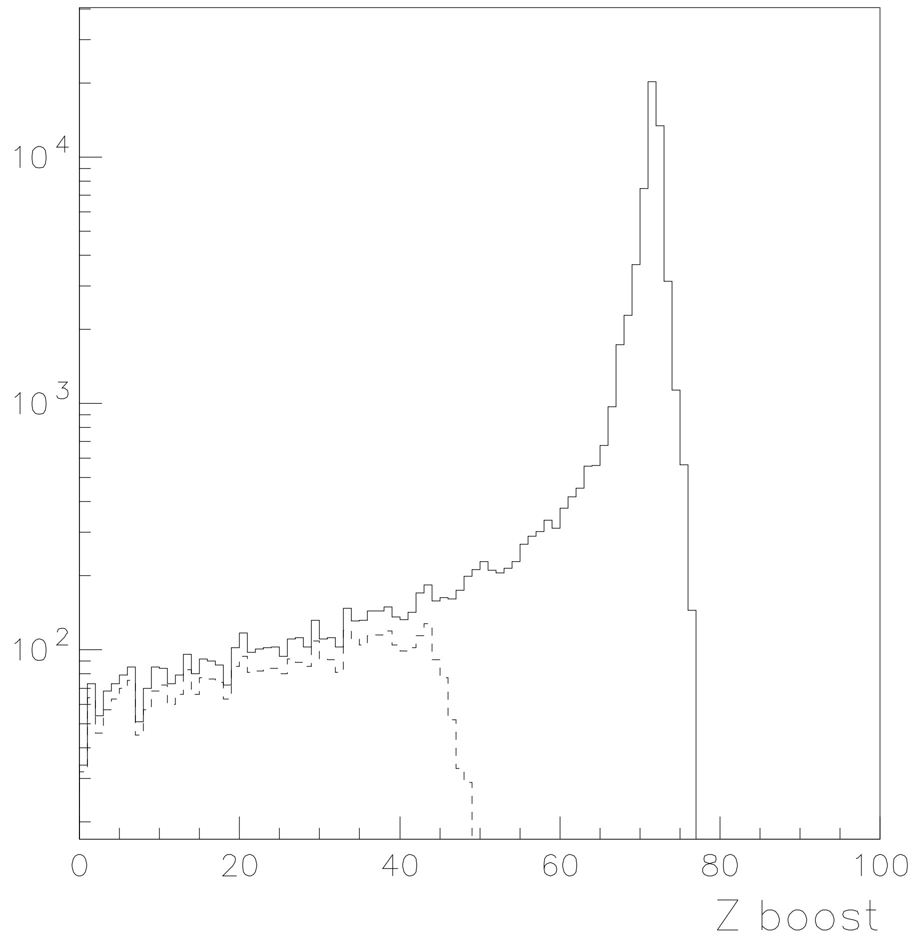

Figure 6.5: *The boost of the Z^0 for all the simulated $q\bar{q}(\gamma)$ events (full line) and for the selected "double radiative return events" (dashed line) for simulated events.*

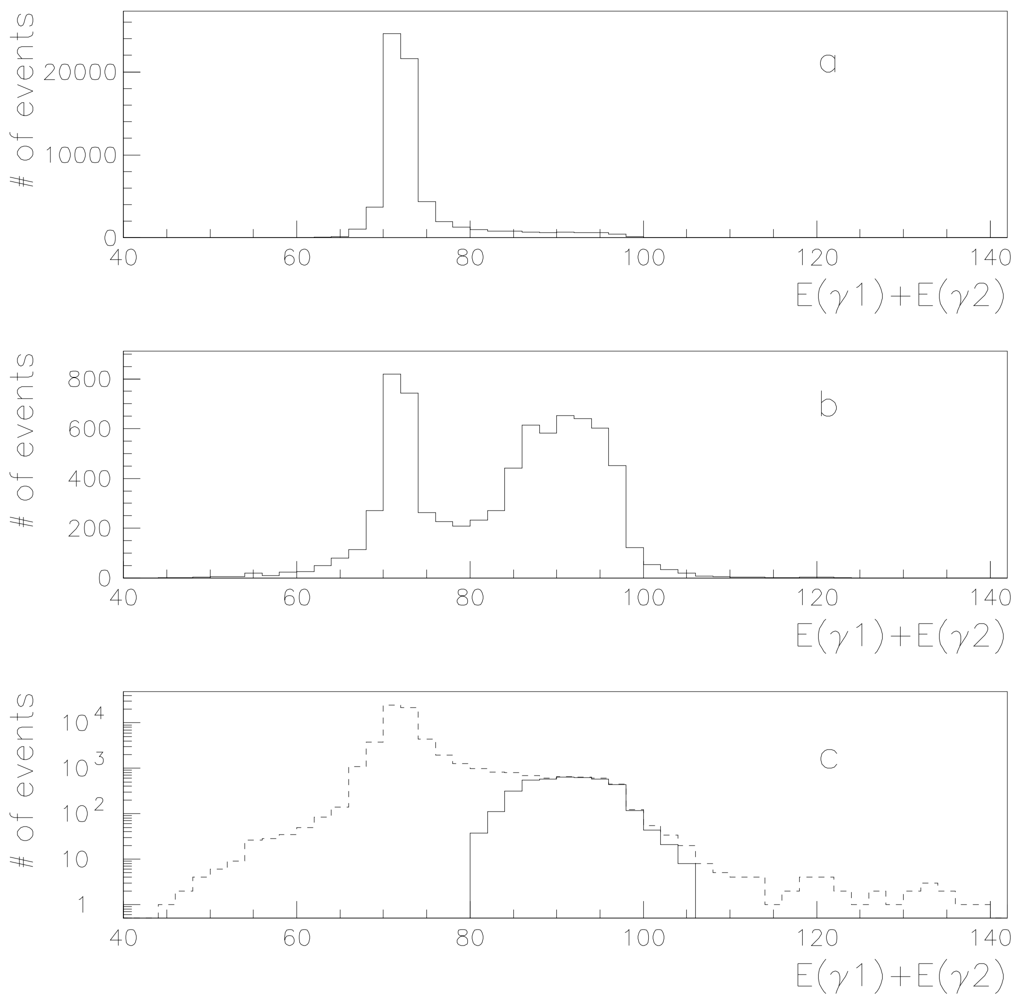

Figure 6.6: *The sum of the energies of the two most energetic photons for simulated events with a Z^0 at rest, at $\sqrt{s} = 189GeV$. a) all the events; b) demanding the energy of the second photon to be $E \geq E_\gamma^{min}$; c) applying in addition the upper cuts on the energy of the photons and the cut on the difference of the two photon polar angles (full line). Superimposed in the last plot as a dashed line is the plot of figure a).*

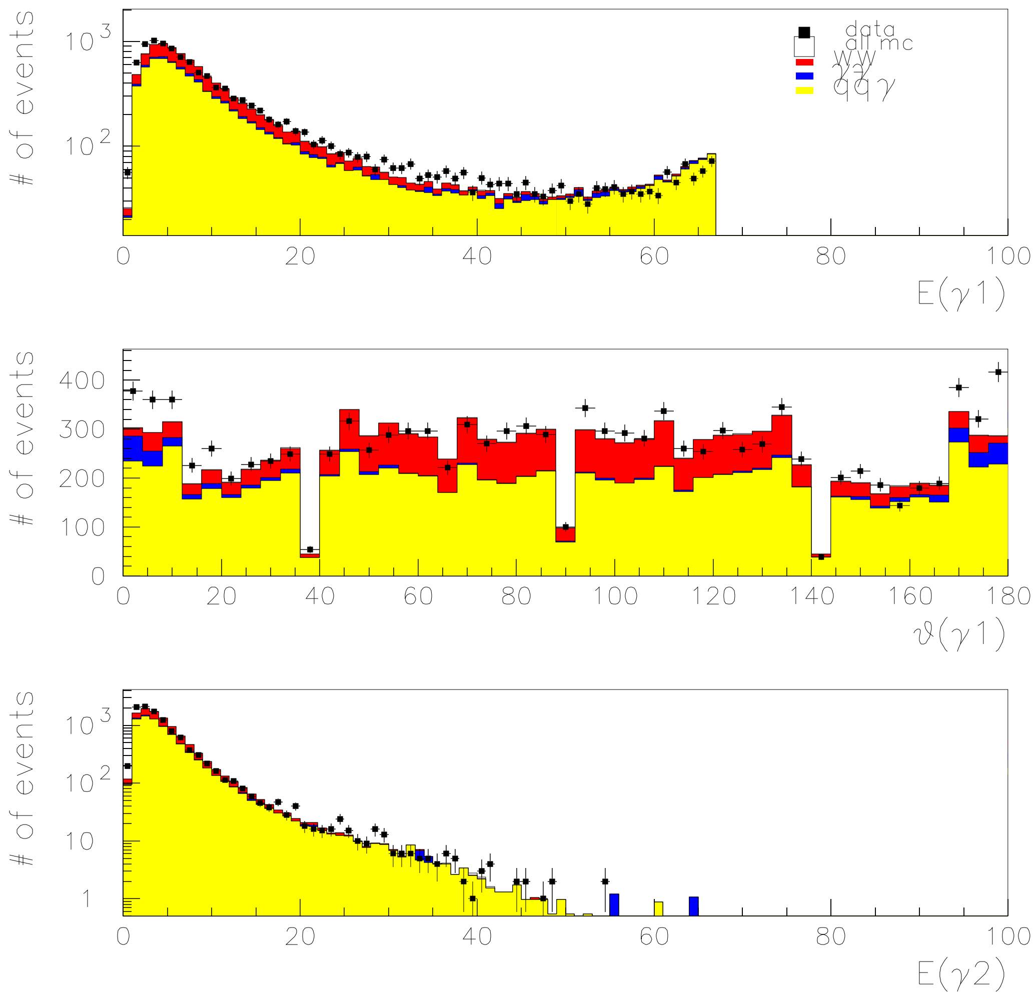

Figure 6.7: *The distribution of the energy and of the polar angle of the most energetic photon, and at the bottom the energy of the second most energetic photon, at $\sqrt{s}$=189 GeV.*

angle of the most energetic one are shown. There is a good agreement between data and simulation in the photon spectra [42].

When the two photons have been identified, the cuts defined above are applied, and the remaining tracks are clusterized into 2 jets (using the Durham algorithm and forcing to 2 jets). Subsequently, energy and momentum conservation is imposed (keeping fixed the directions of jets and photons) to correct for bad energy and momentum reconstruction, and finally the invariant mass of the 2 jets is computed. In figure 6.8 the invariant mass of the 2 jets is shown for data and simulation. The total number of events is 26 in the data and 22.3 in Monte-Carlo where 14.5 are signal.

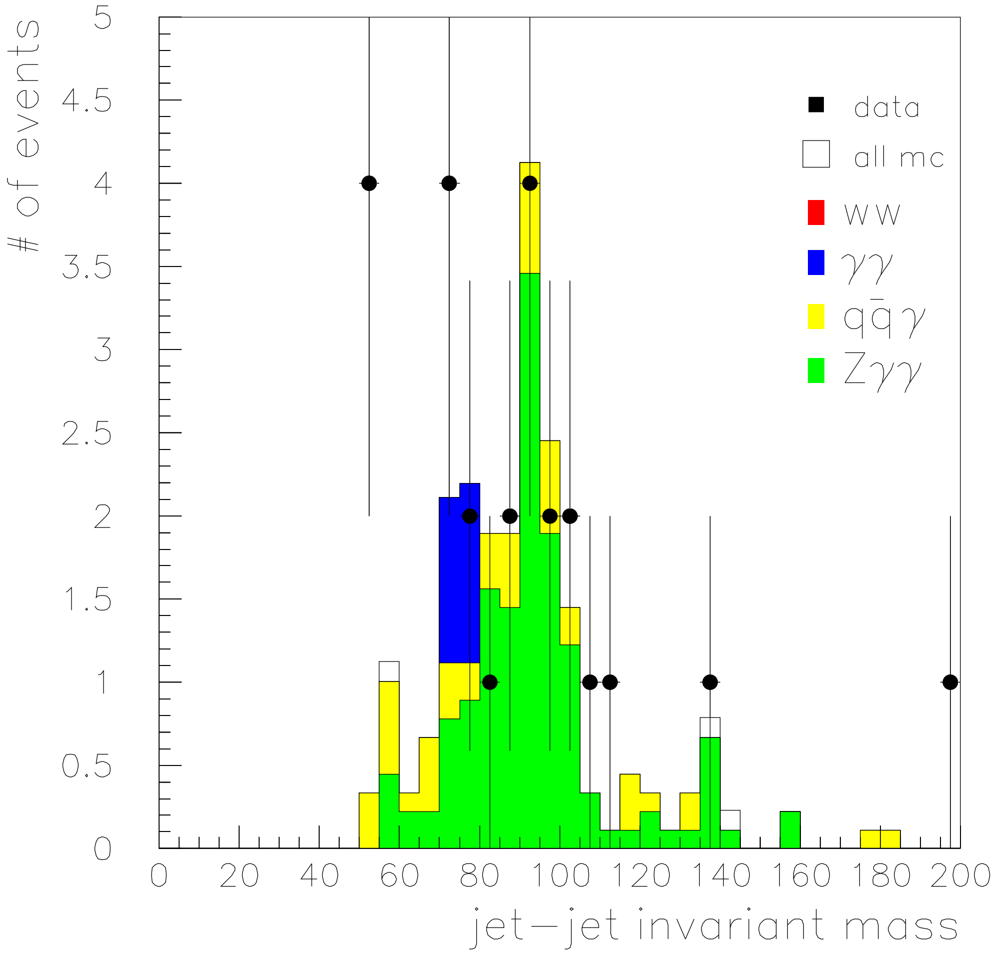

Figure 6.8: *The two jet invariant mass, at $\sqrt{s}$=189 GeV.*

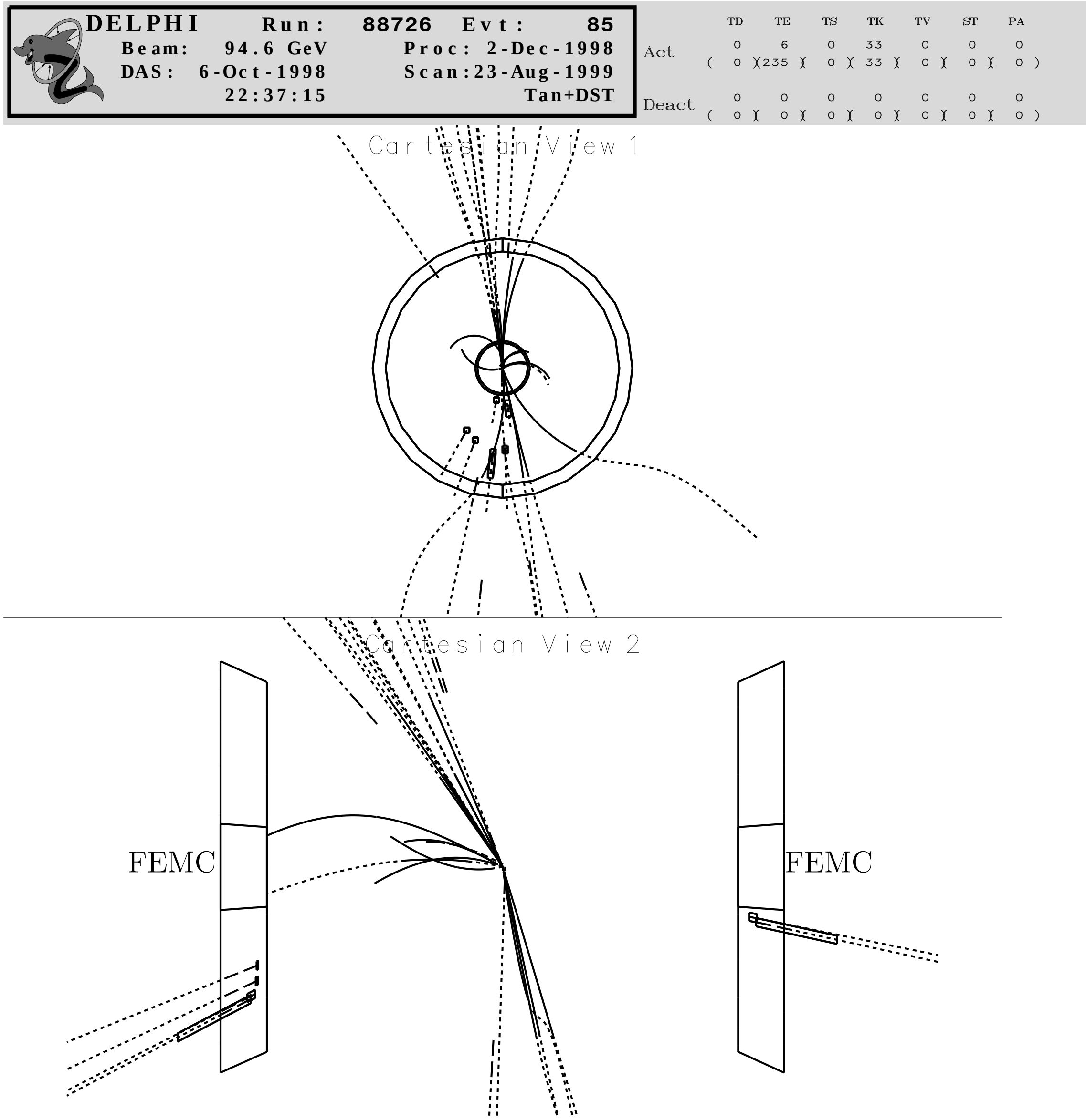

Figure 6.9: *One selected event with two photons in the FEMC of 56.5 and 36.8 GeV and a 2 jet invariant mass of 92. GeV/c^2, at $\sqrt{s}$=189 GeV.*

The efficiency to select this process is estimated using the PYTHIA Monte-Carlo to be 41.7% when both photons are in the acceptance of the detector, i.e. above 3° in θ (this cut is chosen to minimise background from off-momentum electrons, see ref.[59]).

One of the selected events is shown if fig.6.9.

6.2.4.2 Only one visible photon

When only one of the photons enters the detector (36% of the cases) the kinematics can be constrained using the θ of the missing momentum as seen in figure 6.10 for simulated events. In this case the detected photon is required to have energy between

$E_{\gamma 2}^{min}$ and $E_{\gamma 1}^{max}$ and the sum of its polar angle θ and the θ of the missing momentum vector must be larger than 90°. The remaining tracks are clusterized into two jets and energy and momentum conservation is imposed, identifying the second lost photon with the missing momentum vector. To try to further reduce the background, a cut on the acoplanarity of the event can be applied, since simulated events show that 60% of them have an acoplanarity [1] of less than 10°. In figure 6.11 the invariant mass of the 2 jets is shown for data and simulation. A total of 102 events in data and 110.1 in simulation (of which 21 are signal) remain. The efficiency for this selection is 18.6%.

One of the selected events is shown if fig.6.12.

6.2.4.3 No visible photons

The highest contribution to the total cross section is from events where both the photons are lost in the beam pipe. In this case only the 2 jets are detected and they are coplanar and collinear, with an invariant mass close to that of the Z^0, and there is about 100 GeV missing energy. Figure 6.13 shows the acoplanarity, the visible energy, the missing momentum and the component along the Z axis of the missing momentum for simulated symmetric double radiative return events where both photons are lost in the beam pipe.

This process is one of the important backgrounds to the Higgs search in the missing energy channel, described in this thesis. In a perfect detector a cut on acoplanarity greater than 1.5 degrees could kill it completely, without reducing the Higgs efficiency considerably (see section 4.5.4).

In the following additional cuts are used to further suppress the background. The cuts are the ones used in the $H\nu\bar{\nu}$ analysis (see chapter 4) to suppress the W^+W^-, $Z^0\gamma$ ("single" radiative return) background and , in addition , cuts on acoplanarity and on visible energy are applied following the distributions shown in fig.6.13. Finally the invariant mass spectrum is shown in fig.6.14 for an acoplanarity cut of 2° and demanding a visible energy of more than 60 GeV.

The total selected events are 102 in the data sample and 98.9 in the simulated one of which 47.9 are signal.

The efficiency of this selection is estimated to be 19.%.

6.2.5 The 1999 data results

The same analysis has been repeated on 1999 data at $\sqrt{s} = 196$ GeV where a luminosity of 76.9 pb^{-1} has been collected so far. When both photons are detected the efficiency is 52.4% and the total number of events is 13 and 11.7 for data and simulation respectively where 7.9 are expected from the signal sample. Figure 6.15 shows the mass plot of the hadronic system, recoiling against the two visible photons and in figure 6.17 one of the selected events is shown. When one of the photons is lost in the beam-pipe the efficiency

[1] The acoplanarity is defined as the complement to 180° of the scalar product of two jets directions in the $R\phi$ plane.

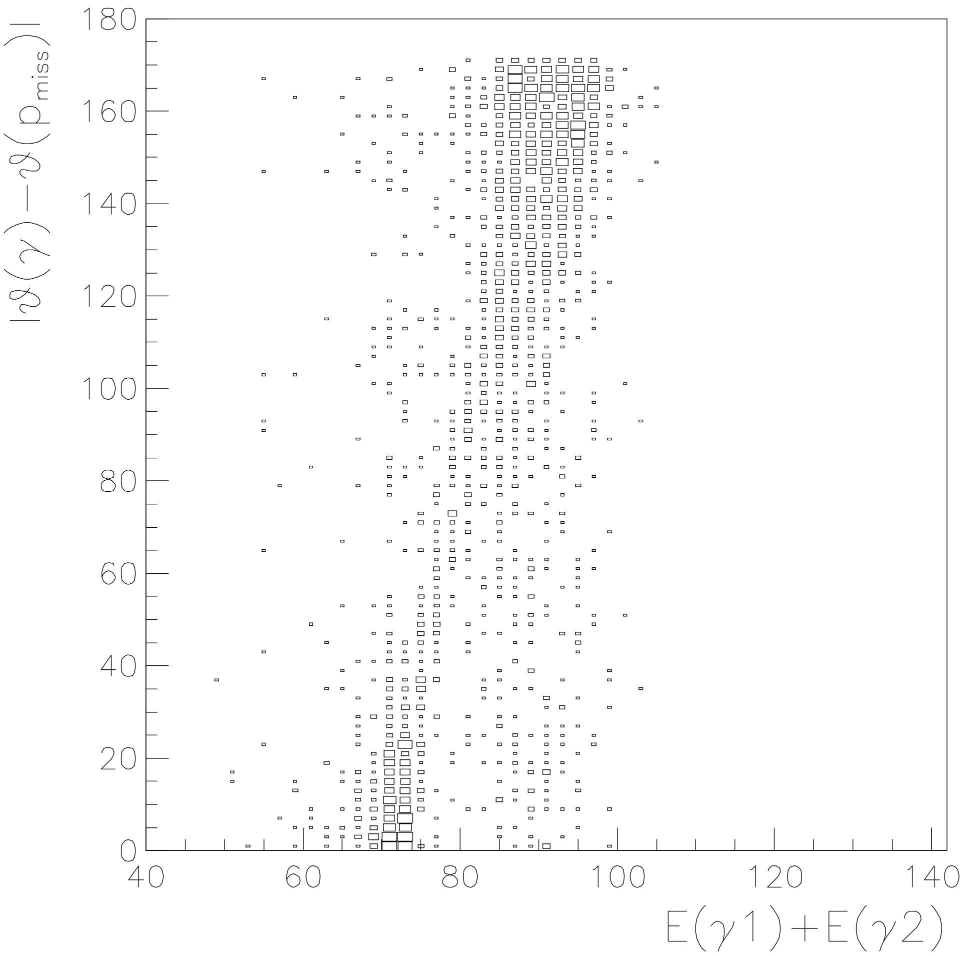

Figure 6.10: *The distribution of the sum of the polar angle of the photon and the polar angle of the missing momentum direction versus the sum of the two photon energies for simulated events.*

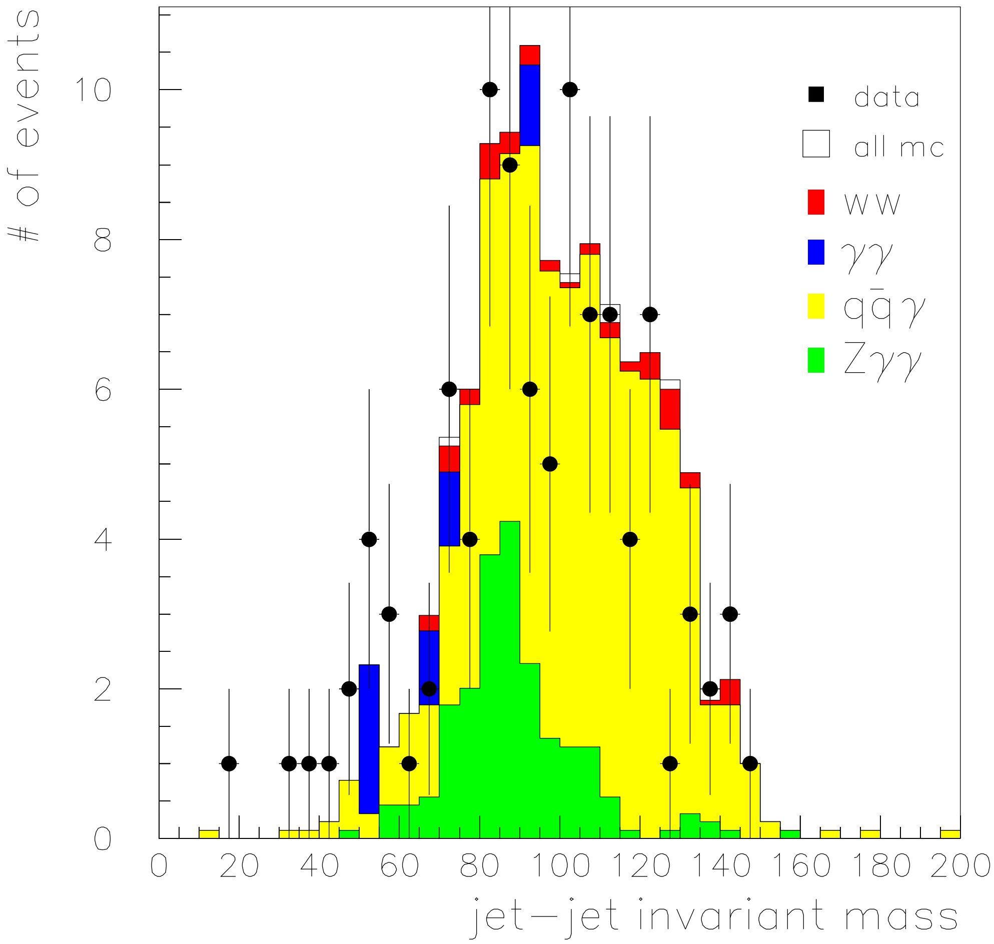

Figure 6.11: *The two jet invariant mass when only one photon is detected, at $\sqrt{s}$=189 GeV.*

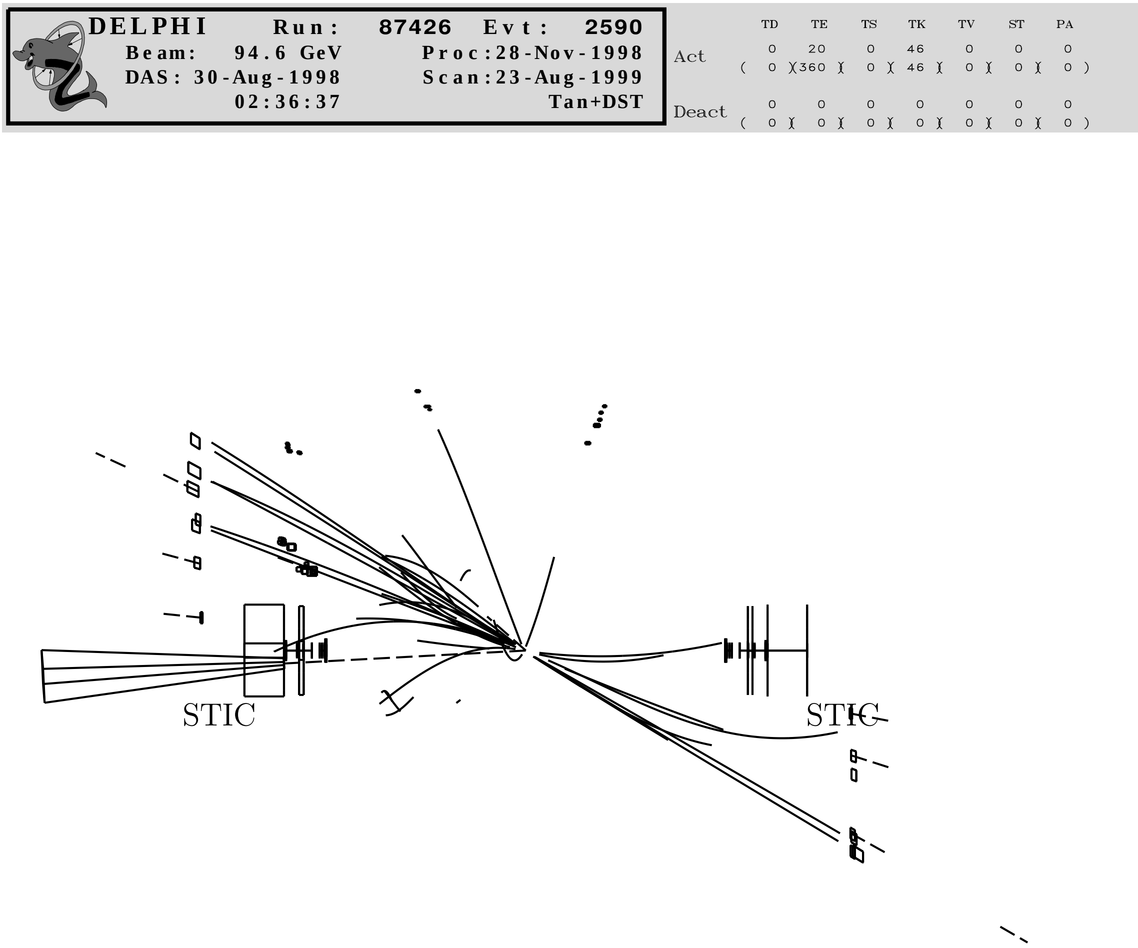

Figure 6.12: *One selected event with one photon in the STIC of 41.9 GeV and a 2 jet invariant mass of 91.2 GeV/c^2, at $\sqrt{s}$=189 GeV.*

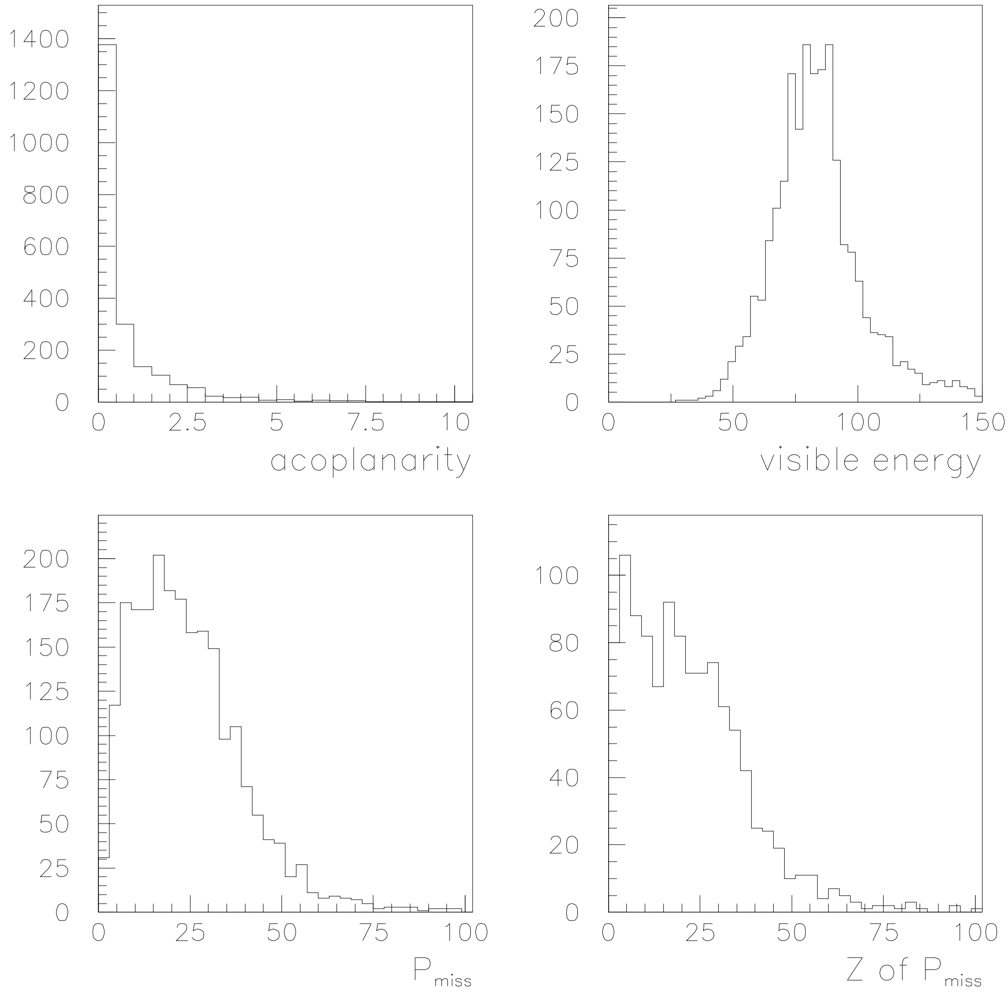

Figure 6.13: *Variables for the simulated events where both the photons are lost in the beam-pipe*

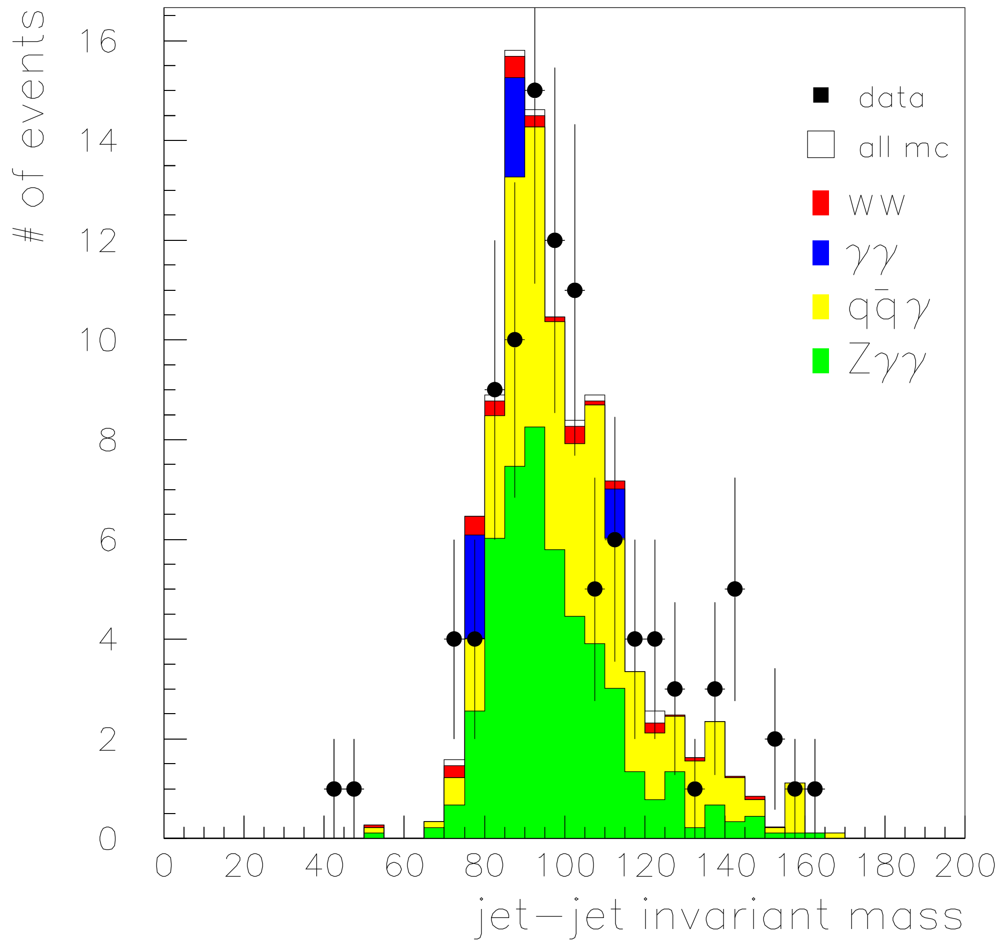

Figure 6.14: *Invariant mass of the hadronic system when both the photons are lost in the beam pipe, at $\sqrt{s}$=189 GeV.*

is estimated to be 16% and the total number of events is 55 and 57.2 respectively for data and simulation where 9.2 events are expected from signal. When both photons are lost in the beam-pipe the efficiency is 17.4% and the total number of events is 48 and 47.7 respectively for data and simulation where 19.6 events are expected from signal. Figure 6.16 shows the mass plot of the hadronic system when both photons are lost in the beam-pipe.

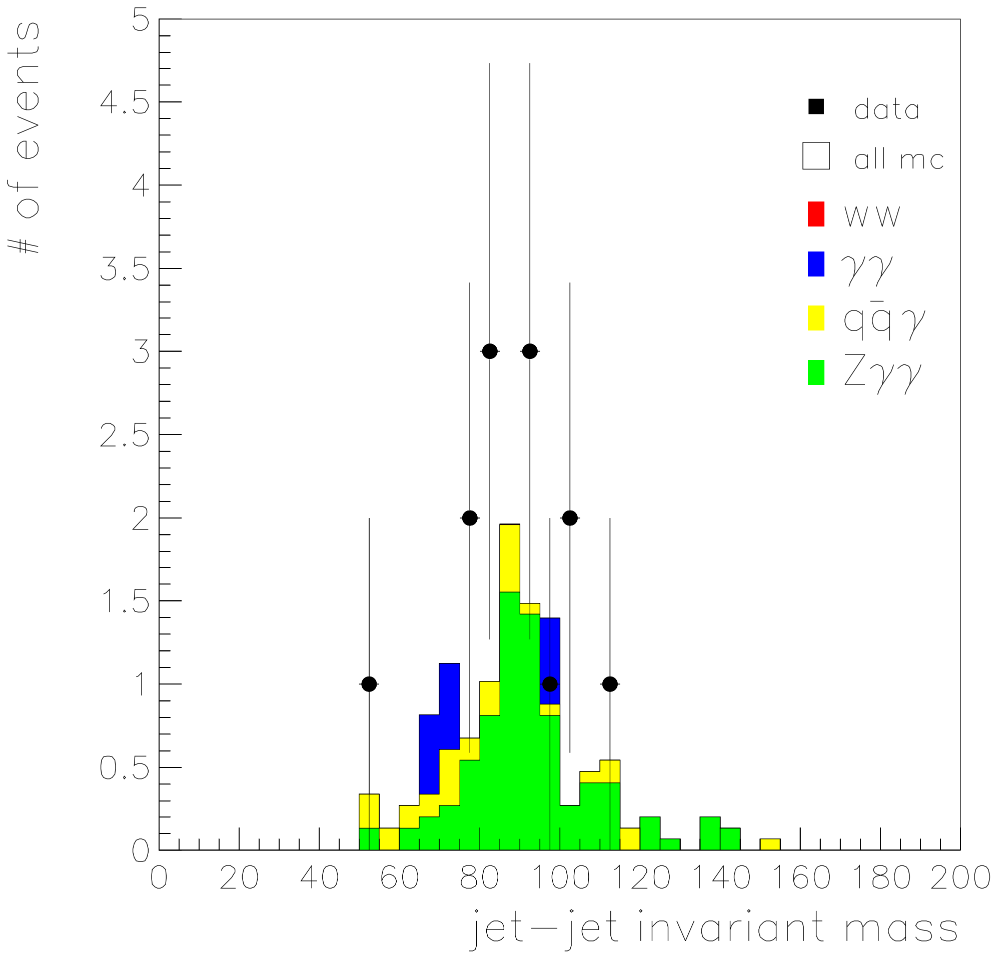

Figure 6.15: *Invariant mass of the hadronic system when both photons are seen in the detector, at $\sqrt{s}$= 196 GeV*

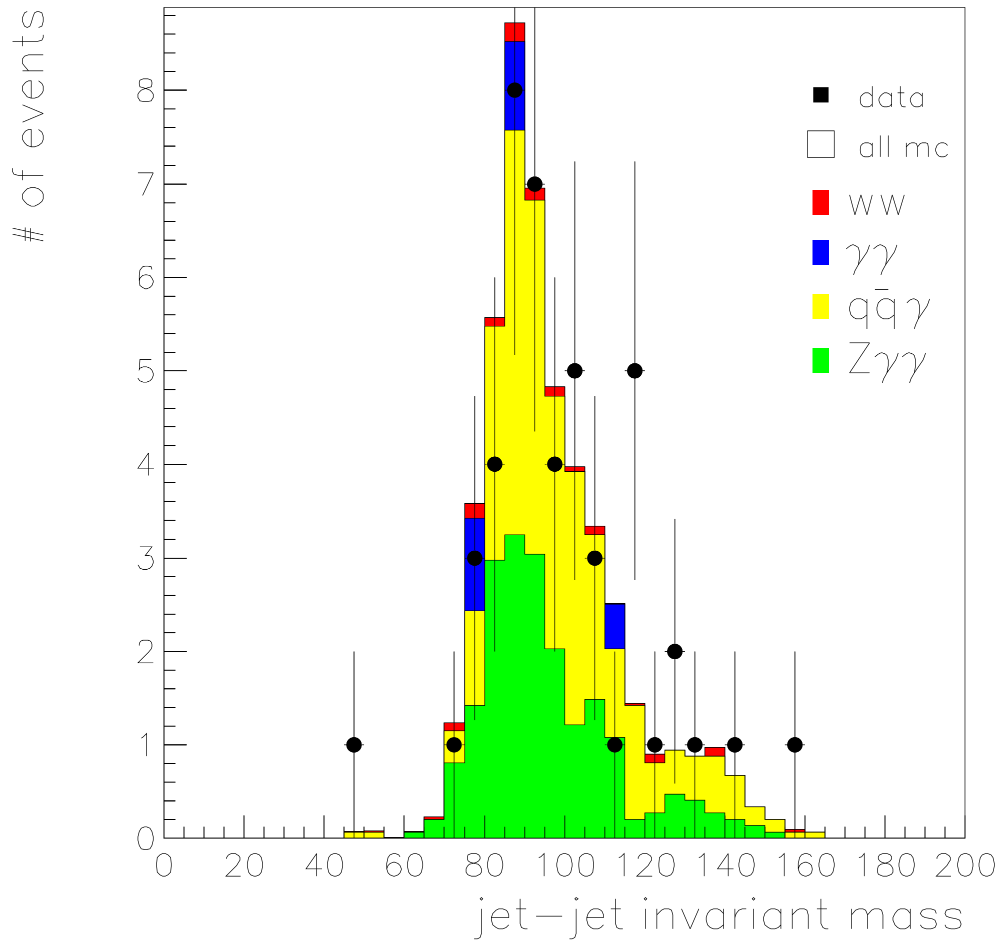

Figure 6.16: *Invariant mass of the hadronic system when both photons are lost in the beam pipe, at $\sqrt{s}$= 196 GeV*

6.2.6 $Z^0\gamma\gamma$ ($Z^0 \to q\bar{q}$) Cross Section

From the number of selected events and the efficiency estimated using the simulation, the cross section for the symmetric double radiative return is computed as a function of the centre-of-mass energy, for $Z^0 \to q\overline{q}$ decays. The most precise estimation is for the events where both photons are seen in the detector since, as has been described above, it is possible to reach a very high purity of the signal. The systematic errors on these values have been estimated by varying the energy range of the accepted photon (i.e. by varying the range around the Z^0 boson mass) from 10 GeV to 8 GeV, by changing the value of $E_{\gamma 2}^{min}$ by 2 GeV and by accepting as photons only those identified by the tight selection criteria of REMCLU ([42]). The variations were always much smaller

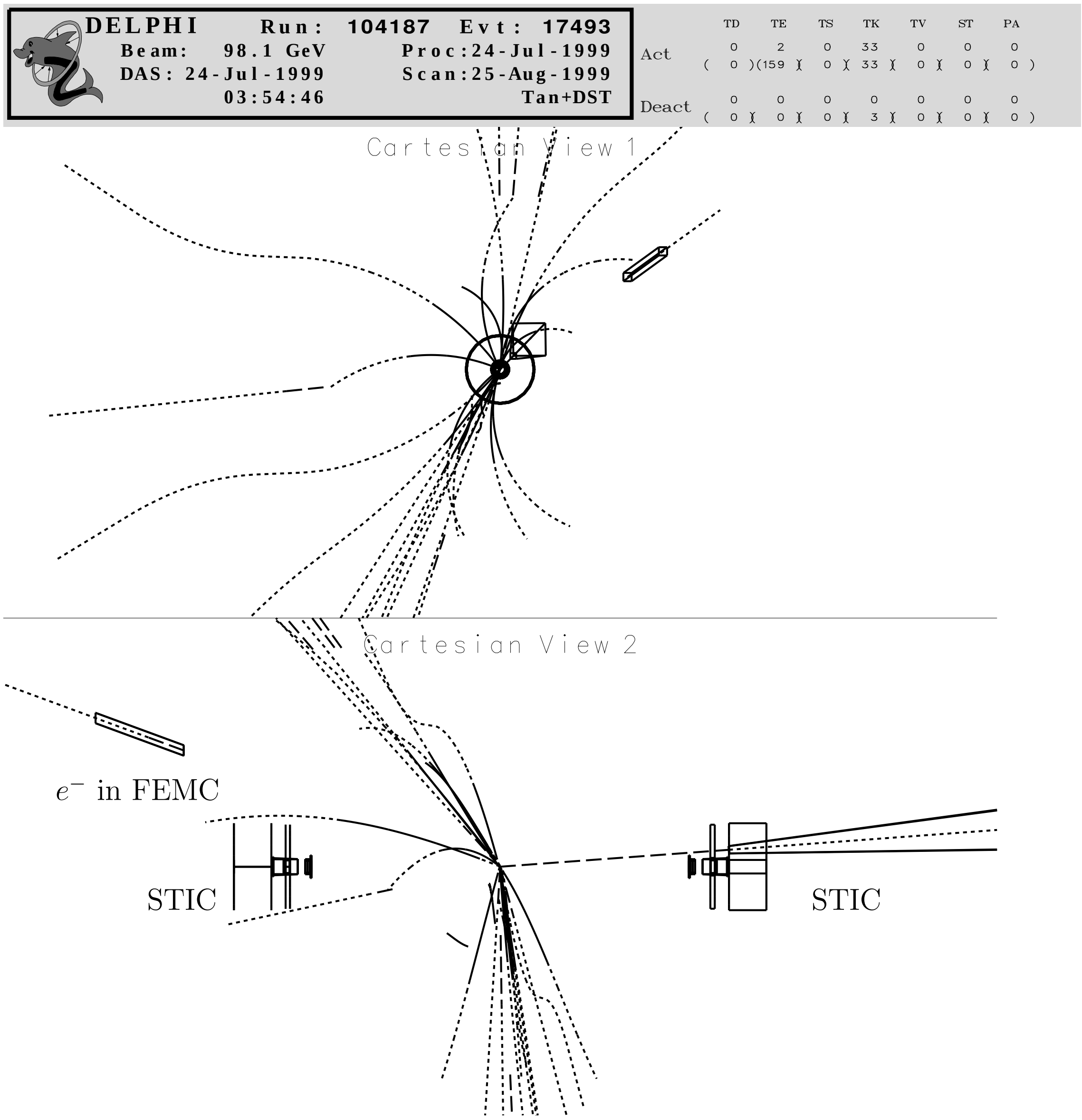

Figure 6.17: *One selected event at $\sqrt{s}$=196 GeV with one photon in the STIC of 54.7 GeV, one in the FEMC of 43.0 GeV and a 2 jet invariant mass of 92.5 GeV/c^2*

Energy	cross section [pb]		
	2 γ visible	1 γ lost	2 γ lost
	$3° \leq \theta_\gamma \leq 177°$		$\theta_\gamma \leq 3°, \geq 177°$
189 GeV	0.298$\pm$ 0.066	0.599 $\pm$ 0.158	0.683 $\pm$ 0.155
196 GeV	0.229$\pm$ 0.050	0.702 $\pm$ 0.192	0.725 $\pm$ 0.165

Table 6.1: *Cross-section (in pb) for the process $Z^0\gamma\gamma$, $Z^0 \to q\bar{q}$*

than the statistical error.

The results are summarised in table 6.1 where the error is statistical only.

6.3 Summary

For the first time, the symmetric double radiative return has been studied at LEP. The cross-section of this process has been measured at two different centre-of-mass energies (189 GeV and 196 GeV) and in three different experimental topologies: when both the photons are detected, where one of the photons is lost in the beam-pipe and finally when both photons are lost.

Chapter 7

Extraction of limit on Higgs mass

In this chapter the statistical significance required to establish the Higgs discovery has been defined. In the 1998 data no Higgs evidence has been reached. In this situation is it possible to determine a lower limit on the mass of the Higgs particle.

I will describe in details the statistical procedure to derive the limit, and how I applied it on my analysis. I will show the limit I obtained in the framework of the Standard Model and of Minimal Supersymmetric Standard Model.

Several systematic surces can influence the input for the limit derivation. I will examinate them and I will show the effect on the limit of the total systematic error.

7.1 Hypothesis testing in a search analysis

The goal of a search is to either exclude as strongly as possible the existence of a signal in its absence or to confirm as strongly as possible the discovery of a true signal. This can be formulated in terms of a hypothesis test:

- the null hypothesis is that the signal is absent;
- the alternate hypothesis is that the signal exists.

One should then quantify the degree to which one of the hypotheses is favoured or excluded by the experimental observations.

The process can be described in basically three steps [61]:

1. identification of the variables in the experiment that comprise the search result. The simplest observable is the number of candidates satisfying a certain set of criteria. More advanced observables may be some feature of the candidates such as the mass, b tag or the value of a discriminant variable (such as the likelihood of the analysis done in this thesis).
2. definition of a *test-statistic* (X), which is a function of these observables and of some model parameters (for example particle mass or production rates) of the signal and of the background which allows to rank experiments from the most background-like to the most signal-like,

3. define the rules for exclusion and discovery. This means to specify the ranges of values of the test statistic leading to one conclusion or the other. The significance of the exclusion or discovery, must be computed. In other words a confidence level for the exclusion (or discovery) must be cited. A confidence limit is the value of a population parameter (such as particle mass or production cross section) which is excluded at a specified confidence limit. A confidence limit is a lower (upper) limit if the excluded confidence is greater (less) than the specified confidence level, for all values of exclusion population parameter below the confidence limit.

In the simplest case possible, let us consider as the only observable comprising the result the number of candidates found, and we suppose no background expected. Assuming that the observed number of events has a Poisson probability distribution, the confidence level to which a signal distribution with a given mean value μ is excluded, for N_{obs} observed events, is given by the probability that the number of events found is less than or equal to N_{obs} [62]:

$$CL_s = P_s(N \leq N_{obs}),$$

where

$$P_s(N \leq N_{obs}) = \sum_{k=0}^{N_{obs}} \frac{\mu^k e^{-\mu}}{k!}.$$

This situation can become more complicated in three different ways ([63]):

1. there might be background expected from standard processes; a way of correcting for known backgrounds is then needed,

2. several channels, often having very different efficiencies and/or branching ratios and/or collected luminosities, may contribute to a certain search,

3. the search result may not be simply a number of candidates, and additional information can be present. In particular, there can be information on the mass range of each candidate.

All these points are relevant for the Higgs analyses.

A standard technique [62, 61] to deal with the first problem is to normalise the confidence level for the signal + background hypothesis, CL_{s+b}, to the confidence level for the background-only hypothesis CL_b. This also makes it possible to obtain sensible exclusion limits on the signal even when the observed rate is so low that the background hypothesis is called into question.

The test statistic is constructed to increase monotonically for increasingly signal like (decreasingly background like) experiments so that the confidence in the signal + background hypothesis is given by the probability that the test-statistic is less or equal to the value observed in the experiment, X_{obs}:

$$CL_{s+b} = P_{s+b}(X < X_{obs}) \tag{7.1}$$

where

$$P_{s+b}(X < X_{obs}) = \int_0^{X_{obs}} \frac{dP_{s+b}}{dX} dX \tag{7.2}$$

and where $\frac{dP_{s+b}}{dX}$ is the probability density function of the test-statistic for signal + background experiments. Similarly, the confidence in the background hypothesis is given by the probability that the test-statistic is less than or equal to the value observed in the experiment X_{obs}:

$$CL_b = P_b(X < X_{obs}) \tag{7.3}$$

where

$$P_b(X < X_{obs}) = \int_0^{X_{obs}} \frac{dP_b}{dX} dX \tag{7.4}$$

and where $\frac{dP_b}{dX}$ is the probability density function of the test-statistic for background only experiments.

Then the normalisation described above is simply:

$$CL_s \equiv CL_{s+b}/CL_b. \tag{7.5}$$

The signal hypothesis will be excluded at the confidence level CL when

$$1 - CL_s \leq CL \tag{7.6}$$

For example, considering that the search result is given by a number of events with a Poisson distribution, the CL_s is given by:

$$CL_s = \frac{e^{-s} \sum_{k=0}^{N_{obs}} (s+b)^k/k!}{\sum_{k=0}^{N_{obs}} b^k/k!}, \tag{7.7}$$

where N_{obs} is the number of events observed, b is the average background value (known) and s is the desired upper limit for the signal. This expression is commonly used to obtain conservative limits on the signal hypothesis [62].

Coming to the other two problems, in the case several channels are present, the *naïve* approach within this method is to add the backgrounds, the expected signal rates and the observed number of events for all the channels, taking into account the efficiencies (ϵ_i), cross-sections(σ_i) and luminosities $\mathcal{L}_i$:

$$b = \sum b_i \qquad s = \sum s_i = \sum \epsilon_i \sigma_i \mathcal{L}_i \qquad N_{obs} = \sum N_{obs_i}. \tag{7.8}$$

The drawback of this procedure becomes clear when channels with very different characteristics are combined. Namely, the presence of candidates in a channel with a very low value of s_i (very low efficiency, cross-section or luminosity), and hence with a small contribution to the total number of expected signal events, can deteriorate considerably the obtained limit. This is true even if there is expected background, given the characteristics of the Poisson distribution and of this ratio of Poisson distributions.

Another clear drawback of this procedure is that it does not take into account the mass information of the candidates. Clearly, an event of reconstructed mass m_i such that $|m_0 - m_i| \gg \sigma_m$, where σ_m is the mass resolution, should not be considered as a candidate for the mass m_0. In practice, an arbitrary and common convention is to take the events as candidates for the mass region defined by $m_i \pm 2\sigma_m$.

In fact there is no real consensus about how to compute limits and how to overcome the above problems. Different methods giving at least partial solutions are available, but none of them is universally accepted. In particular, the problem of the combination of different channels became a crucial point at the moment of combining the search results of the different LEP experiments. Methods used by the different experiments can be found in references [61]. They will not be extensively discussed here, only two methods used and developed within the DELPHI experiment will be briefly described.

The second of these methods, the Modified Frequentist Likelihood Ratio (MFLR) method discussed in reference [61] , will be used below to compute limits on Higgs mass for the analysis done in this thesis. It is the official method used in DELPHI, and both the combination of channels and the inclusion of the candidates mass and discriminant variable information are performed in a natural way.

7.1.1 Bayesian approach for a process with subchannels

A way of making better use of the information about the different search channels [64] is to give to each channel a weight, defined as $w_i = s_i/s_{tot}$ (the branching ratio of the signal in channel i) and to combine all the channels by assuming a probability function that is simply the product of the independent distributions for each channel. This is done in the framework of the Bayesian approach.

In the Bayesian approach the upper limit s on the parameter σ for the process with a probability function $W(n, \sigma)$ is given by:

$$1 - CL = \frac{\int_s^\infty W(n,\sigma)d\sigma}{\int_0^\infty W(n,\sigma)d\sigma}. \tag{7.9}$$

If we assume:

- Poisson distribution in the total number of signal events;
- k channel;
- an average background b_i and a branching ratio w_i in each subchannel;
- the joint probability function for the total number of events $n_i = n_i^s + n_i^b$ in each subchannel is the product of independent Poisson distributions: $W(n_1, ..., n_k; s; w_1, b_1 ..., w_k, b_k) = P(n_1; sw_1 + b_1) \times .... \times P(n_k; sw_k + b_k)$ where $P(n; s) = e^{-(s+b)}(s + b)^n/n!$ is the Poisson distribution;

then using 7.9 we obtain:

$$1 - CL = \frac{e^{-s_{tot}} \prod_{i=1}^k \sum_{j=0}^{n_i} (s_{tot} + b_i/w_i)^j/j!}{\prod_{i=1}^k \sum_{j=0}^{n_i} (b_i/w_i)^j/j!)} \tag{7.10}$$

which can be written as

$$1 - CL = \frac{e^{-s_{tot}} \sum_{i=0}^{N} (N-i)! \sum_{\nu_1+...\nu_k=i} C_{\nu_1}^{n_1} ... C_{\nu_k}^{n_k} (s_{tot} + b_1/w_1)^{\nu_1} ... (s_{tot} + b_k/w_k)^{\nu_k}}{\sum_{i=0}^{N} (N-i)! \sum_{\nu_1+...\nu_k=i} C_{\nu_1}^{n_1} ... C_{\nu_k}^{n_k} (b_1/w_1)^{\nu_1} ... (b_k/w_k)^{\nu_k}} \tag{7.11}$$

where $N = \sum_{i=1}^{k} n_i$ and $C_\nu^n = \frac{n!}{\nu!(n-\nu)!}$ are binomial coefficients.

Up to now this method accounts for the combination of different channels but not for the problem if including the mass information. More generally, the problem of search results given by continuous variables is not treated in a natural way by this method. A way of introducing the mass information is described in [64], which basically consists in "plugging" into the obtained expression the mass resolution function.

7.1.2 The Modified Frequentist Likelihood Ratio method

In the MFLR method the choice of the test statistic is based on the likelihood ratio, $X = L(s+b)/L(b)$, which is the ratio of probability densities for the signal + background hypothesis to the signal free or background hypothesis. It can be demonstrated (Neyman Pearson theorem) that the likelihood ratio used as test statistic maximises the probability of rejecting a false hypothesis at a given confidence level, and conversely minimises the probability of making a false discovery at a given discovery confidence level.

Moreover, the likelihood ratio solves the problem of combining different channels, since the likelihood ratio for an experiment with independent channels is simply a product of the likelihood ratios of the individual channels. Hence the combination of additional histogram bins, independent search channels, experiments or centre of mass energies is straightforward and automatically optimal for both discovery and exclusion.

In the context of searching for small signals in the presence of small backgrounds in several distinct channels, and when more information than simply the number of candidates (in our case the mass and the likelihood) will enter in the likelihood ratio, it is in general not possible to obtain analytic expressions for the likelihood ratio probability density functions (p.d.f.'s). The p.d.f.'s may instead be obtained by the Monte Carlo generation of experiments according to the relevant hypothesis (signal plus background or background only) and confidence levels may be computed as the fraction of experiments satisfying $X \leq X_{obs}$.

The likelihood ratio X for experiments with N_{ch} independent search channels and measurements of a single discriminant variable x for each candidate, and where the absolute signal and background rates are known, can be written as:

$$X = \frac{\prod_{i=1}^{N_{ch}} \frac{e^{-(s_i+b_i)}(s_i+b_i)^{n_i}}{n_i!}}{\prod_{i=1}^{N_{ch}} \frac{e^{-b_i} b_i^{n_i}}{n_i!}} \frac{\prod_{j=1}^{n_i} \frac{(s_i S_i(x_{ij}) + b_i B_i(x_{ij}))}{s_i+b_i})}{\prod_{j=1}^{n_i} B_i(x_{ij})} \tag{7.12}$$

where:

- n_i is the number of observed candidates in each channel; item x_{ij} is the value of the discriminant variable measured for each of the candidates;

- s_i and b_i are the integrated signal and background rates per channel;
- s_{tot} is the total signal rate for all channels;
- $S_i(x)$ and $B_i(x)$ are the probability distribution functions of the discriminating variable for the signal and the background respectively.

The above expression can be simplified to

$$X = e^{-s_{tot}} \prod_{i=1}^{N_{ch}} \prod_{j=1}^{n_i} \left(1 + \frac{s_i S_i(x_{ij})}{b_i B_i(x_{ij})}\right). \tag{7.13}$$

It can be proved that the likelihood ratio method is effectively based on counting weighted events. Since $P(X \leq X_{obs}) = P(\ln(X) \leq \ln(X_{obs}))$ we can write

$$\ln(X) = -s_{tot} + \sum_{k=1}^{n} n_k w_k \tag{7.14}$$

where n is the total number of events observed in all channels and the weight for each candidate k is given by

$$w_k = \ln(1 + \frac{s_k}{b_k} \frac{S_k(M_h, m_k)}{B_k(m_k)}) \tag{7.15}$$

where the k index also assigns the candidate to the search channel in which it was observed. Since the constant s_{tot} appears on both sides of $\ln(X) \leq \ln(X_{obs})$ the method consists of comparing the observed number of weighted events with the distributions expected for the signal + background and the background hypotheses.

For a counting experiment with a single channel all the candidate events have the same weight, $\ln(1 + s/b)$ so that equation 7.5 becomes:

$$\frac{P(X \leq X_{obs})}{P_b(X \leq X_{obs})} = \frac{P(n \leq n_{obs})}{P(n_b \leq n_{obs})} = CL_s \tag{7.16}$$

where n_b and n come from the Poisson distributions of the number of events for the background and signal + background hypothesis respectively, and n_{obs} is the number of candidates observed in the experiment. Thus the Modified Frequentist signal exclusion becomes the one in equation 7.7, the Particle Data Group formula. An identical result is obtained by computing the Bayesian confidence interval (with uniform probability for signal).

7.1.2.1 Exclusion and discovery potential

The exclusion potential ([65]) is defined as the probability to exclude a signal hypothesis if it is false, in other words, the fraction of gedanken background experiments which satisfy $1 - CL_s \geq 95\%$. The discovery potential is defined as the probability to confirm the signal hypothesis if it is true and exclude the background experiments with $1 - CL_b \leq 5.7 \times 10^{-7}$.

The exclusion potential for a hypothetical experiment is illustrated in figure 7.1, where the probability distribution and their integrals, the confidences, are shown. The shaded areas correspond to the confidences observed for an imaginary experiment with $2 \ln X_{obs} = 3$; the signal hypothesis for this experiment is excluded at 95 % CL. In addition, the shaded area of the background distribution is the exclusion potential of the experiment.

7.1.2.2 Exclusion and discovery limit

To establish the sensitivity of LEP collaborations in Higgs searches, it is necessary to define the exclusion and the discovery limits. By definition (since the LEP200 workshop), the exclusion limit of the Higgs mass is the value of m_H at which 50% of background experiments (with the same properties as a typical LEP experiment) are expected to lead to a 95% or better CL exclusion of the signal hypothesis. In a similar manner, the discovery limit of the Higgs boson mass is the value of m_H for which 50% of signal experiments are expected to have a significance of 5σ or better ($1 - CL_b \leq 5.7 \times 10^{-7}$).

From figure 7.2 it should be clear that there is no guarantee of 5σ discovery even if the true mass is below the discovery limit and that it is possible to make a 5σ discovery even if the true mass is above the discovery limit.

7.2 How to extract the limit

The different steps in the application of the method on the present analysis will now be detailed:

- the search result is, in our case, given by the number of candidates in each channel, by their mass distribution and their likelihood $\mathcal{L}$ value;
- the Higgs boson cross sections are functions of its mass, so the test-statistic X for N_{ch} distinct search channels with measurements of number of events, mass and likelihood, can be written as:

$$X = \frac{\prod_{i=1}^{N_{ch}} \frac{e^{-(s_i(m_H)+b_i)}(s_i(m_H)+b_i)^{n_i}}{n_i!}}{\prod_{i=1}^{N_{ch}} \frac{e^{-b_i} b_i^{n_i}}{n_i!}} \frac{\prod_{j=1}^{n_i} \frac{s_i(m_H)S_i(m_H,m_{ij},\mathcal{L}_{ij})+b_i B_i(m_{ij},\mathcal{L}_{ij})}{s_i(m_H)+b_i}}{\prod_{j=1}^{n_i} B_i(m_{ij},\mathcal{L}_{ij})} \tag{7.17}$$

which can be simplified to:

$$X = e^{-s_{tot}(m_H)} \prod_{i=1}^{N_{ch}} \prod_{j=1}^{n_i} \left(1 + \frac{s_i(m_H)S_i(m_H, m_{ij}, \mathcal{L}_{ij})}{b_i B_i(m_{ij})}\right) \tag{7.18}$$

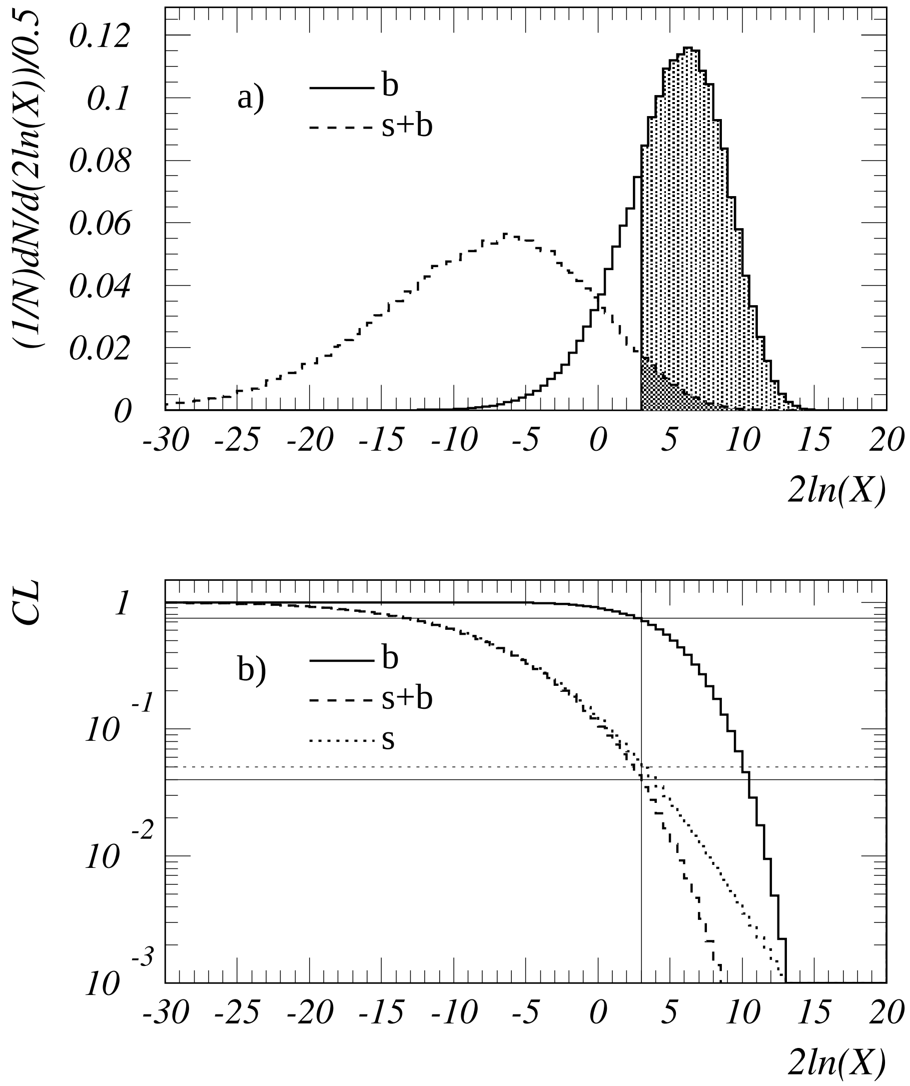

Figure 7.1: *The probability distribution of* $\ln X_{obs}$ *for background "b" and signal "s+b" gedanken experiments (a) and the confidences* CL_b, CL_{s+b} *and* CL_s *(b) which are the integrals (from right to left) of the distribution in the upper plot. The shaded areas in the upper plot can be read off from the intersection of* $2\ln X = 3$ *with the confidence curves in the lower plot. The horizontal dotted line at 0.05 shows that the signal hypothesis for this fictitious experiment is excluded at 95% CL.*

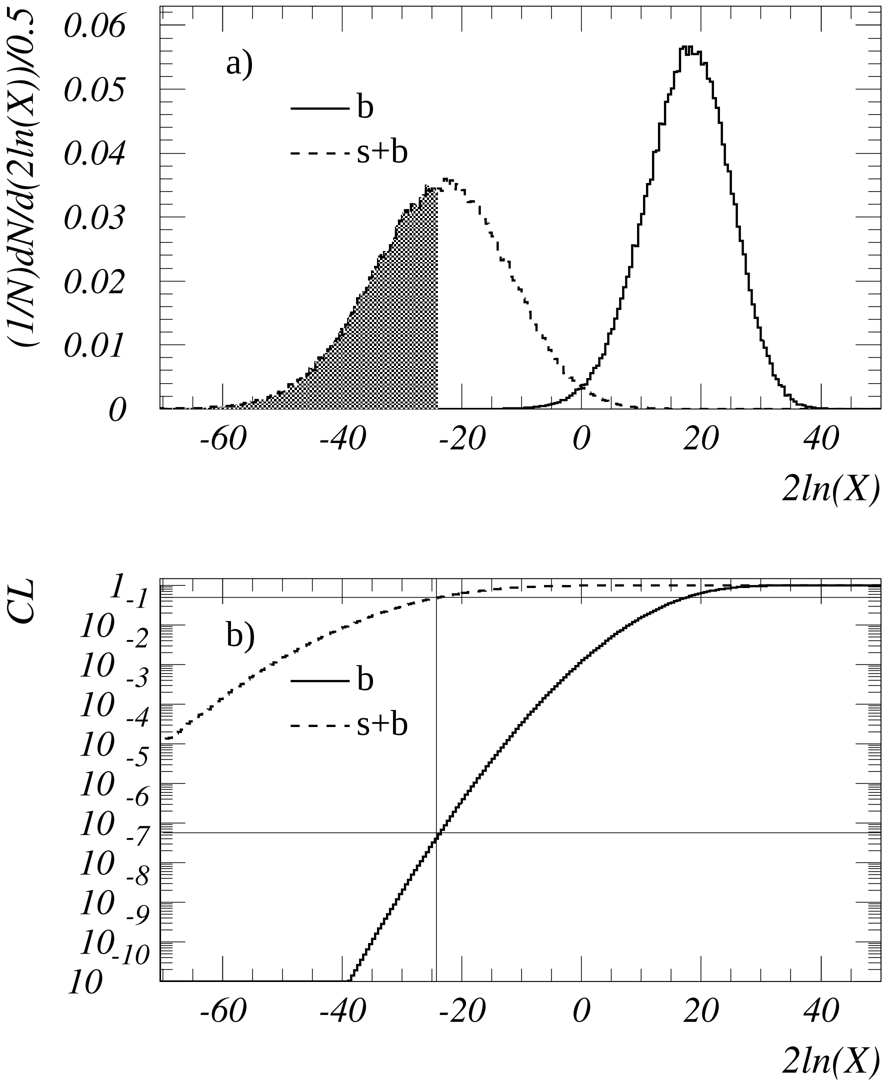

Figure 7.2: *An example of the probability distributions of $2\ln X$ for background "b" and signal "s+b" gedanken experiments (a) and the complements of the confidences $1-CL_b$ and $1-CL_{s+b}$ (b) which are the integrals (from left to right) of the distributions in the upper plot.*

where n_i is the number of observed candidates in each channel, m_{ij} is the invariant mass of the candidates, $s_i(m_{i,j})$ are the integrated signal and background rates per channel, s_{tot} is the total signal rate for all channels, and $S_i(m_H, m_{i,j}, \mathcal{L}_{ij})$ and $B_i(m_{ij}, \mathcal{L}_{ij})$ are the two dimensional probability density functions of invariant mass and likelihood for the signal and background respectively, evaluated at the observed masses and likelihood value.

- this test statistic is evaluated for the observed number of events, giving X_{obs},
- the test statistic probability density function is obtained for the signal + background hypothesis by generating signal + background Monte Carlo experiments: the number of events found in each Monte Carlo experiment is randomly generated for each channel according to a Poisson distribution of mean value $s_i + b_i$ and the mass and likelihood distributions are obtained by distributing the events according to the respective $(s_i(m_H)S_i(m_H, m_{ij}, \mathcal{L}_{ij}) + b_i B_i(m_{ij}, \mathcal{L}_{ij}))$ function.
- in exactly the same way, but considering a Poisson with mean value b_i, a test statistics probability distribution for the background-like experiments is obtained.
- the background and signal + background test statistics probability distributions are integrated up to X_{obs}, giving, respectively, CL_{s+b} and CL_b. The signal confidence level is taken as the ratio $CL_s \equiv CL_{s+b}/CL_b$.

When the signal rates are functions of one population parameter, such as the mass of the particle, we can obtain in this way the signal confidence level as a function of the mass. The mass region excluded at a given CL is then obtained. This is the case for the Higgs analysis and lower limits on the mass will be derived in this way.

7.3 Two Jets mass

As has been shown above, one of the ingredients for the CL computation is the mass of the selected events. In the analysis discussed in this thesis two different methods have been developed to estimate the mass:

- the constraint fit with the Z^0 recoiling mass imposed;
- the reweighting of the jet energy.

Constraint fit with the Z^0 recoiling mass imposed.

In a ideal detector, in the process $e^+e^- \rightarrow H\nu\overline{\nu}$ the energy E_H and momentum $\vec{p_H}$ of Higgs particle are given by the collected energy E_{vis} and detected momenta $\vec{p_{vis}}$. Due to detector effects, such as inefficiencies, non-ideal hermeticity and calibration uncertainties, one should allow for corrections on E_{vis} and $\vec{p_{vis}}$ to obtain the Higgs energy and momentum. At first approximation such corrections can be assumed linear:

$$\begin{aligned} E_H &= \alpha_1 E_{vis} \\ \vec{p_H} &= \alpha_2 \vec{p_{vis}} \end{aligned} \tag{7.19}$$

The next approximation is to take $\alpha_1 = \alpha_2 = \alpha$. Since

$$\begin{aligned} m_Z^2 &= (\sqrt{s} - E_H)^2 - |\vec{p_H}|^2 \\ &= s - 2\sqrt{s}\alpha E_{vis} + \alpha^2 (E_{vis}^2 - |\vec{p_{vis}}|^2) \end{aligned} \tag{7.20}$$

it is possible to find the value of α and then:

$$\begin{aligned} m_H &= \sqrt{E_H^2 - |\vec{p_H}|^2} \\ &= \frac{\sqrt{s}E_{vis} \pm \sqrt{sE_{vis}^2 - (E_{vis}^2 - |\vec{p_{vis}}|^2)(s - m_z^2)}}{\sqrt{E_{vis} - |\vec{p_{vis}}|^2}} \end{aligned} \tag{7.21}$$

Reweighting of jet energy

Instead of computing event by event the coefficient α on a kinematical basis, it is possible to use the simulated events to deduce the correction to be applied to the reconstructed energy [66] by comparing the generated energy with the detected one. In this way it is possible to make a detailed study of the response of the detectors, dividing the events in different classes following the jet energies and the polar angle of the jets. The coefficients are then computed for different bins of jet energy and different bins of θ (see figure 7.3) as the ratio: reconstructed/generated energy.

Figure 7.4 shows the improvement in mass reconstruction using the reweighting.

The reconstructed invariant mass of two jets applying both methods (imposing Z^0 recoiling mass and the reweighting) in the selected sample after the cuts described in previous chapters is shown in figure 7.5. Since imposing the recoiling mass gives a better resolution we decided to derive the mass probability density functions to compute the limit, using this method. However one should note that the Z^0 recoiling mass constraint is no more valid in the WW fusion production of Higgs bosons, and the reweighting should be applied whenever the Higgs mass approaches the kinematical limit and the WW fusion process dominates.

7.4 Limit on Standard Model Higgs mass from $e^+e^- \to ZH \to H\nu\overline{\nu}$ channel

In previous sections all the ingredients to derive the limit on Higgs boson masses have been described. From what has been shown in equation 1.148, the MSSM h boson

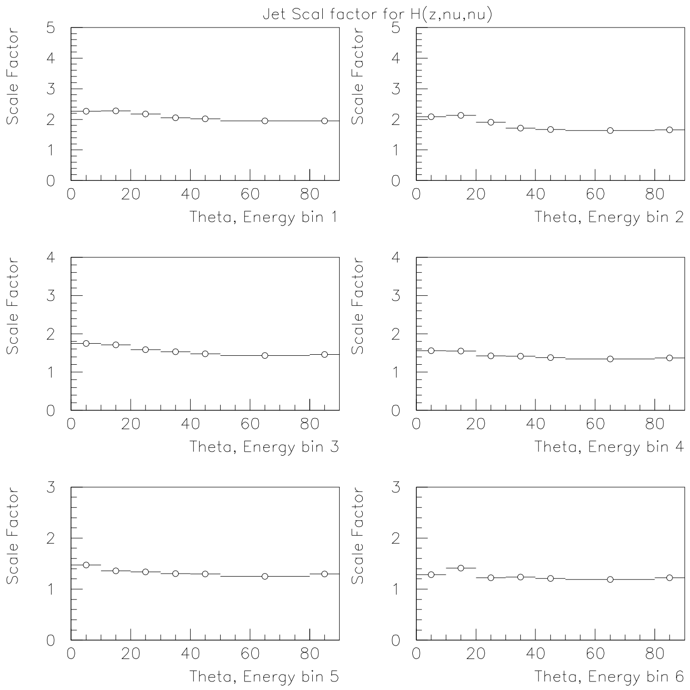

Figure 7.3: *Correction coefficients for different values of jets energy and of polar angle.*

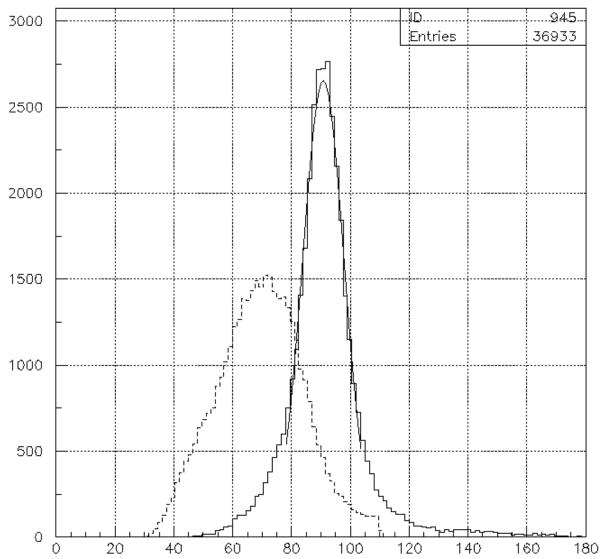

Figure 7.4: *Invariant mass of two jets in $Z^0\gamma$ events with (full line) and without rescaling (dashed line).*

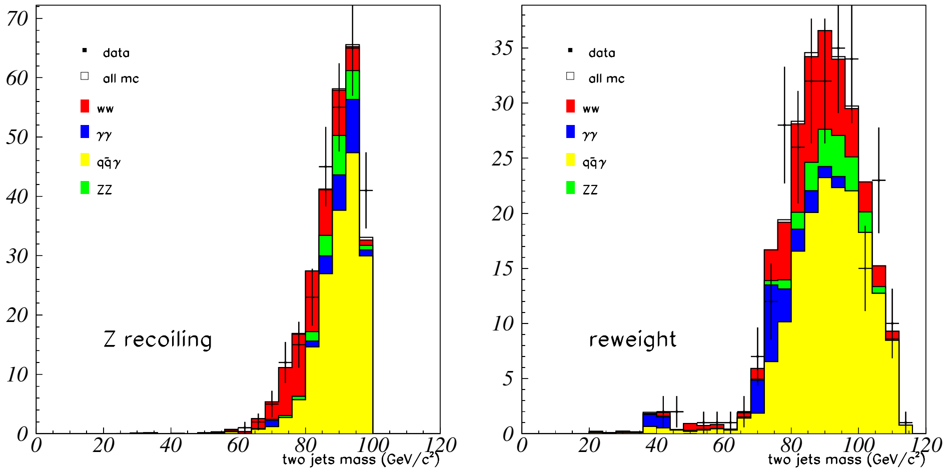

Figure 7.5: *Two jets mass reconstructed requiring the Z^0 mass recoiling (left), or reweighting the energy of jets (right).*

production in the channel $e^+e^- \to Zh \to h\nu\overline{\nu}$ scales with $\sin^2(\beta-\alpha)$ with respect to the standard model Higgs boson H production. Because of this, the information from the channel $e^+e^- \to Zh \to h\nu\overline{\nu}$ can improve the limit on MSSM h boson only at high value of $\tan\beta$. Thus the MSSM Higgs mass limit has been extracted by combining this analysis and the others developed by the DELPHI collaboration, and will be discussed later. In this section I extract the limit only in the framework of the Standard Model, and using only the information coming from the analysis described in this thesis.

We have set different working points, with different signal efficiencies and different number of selected events and its p.d.f. for signal and backgrounds (see figure 7.6).

For each of them, using the statistical method described above, we computed CL_s, CL_{s+b} and CL_b. The different CLs have been computed for signal hypotheses of the following masses: $m_H = 75, 80, 85, 90, 92.5, 95, 97.5$ GeV/c^2. For each different mass hypothesis we found the optimal working point defined as the one where the CL_s is minimum (see for example the evolution of CL_s, CL_{s+b} and CL_b with signal efficiency in figure 7.7.)

In deriving the minimum of CL_s, attention must be payed to avoid "overoptimisation". As has been shown in section 7.2, the CLs are computed generating gedanken experiments with number of events distributed with Poisson probability with weight given by the two dimensional p.d.f. of likelihood and mass. When using a one or two dimensional histogram to describe the background and the signal distribution, the CL will be forced by the bin with the most significant difference between signal and background. Decreasing the bin size of the p.d.f. will increase the statistical fluctuation. Since the algorithm looks specifically for bins with a high ratio of signal over background, this will create a bias in the CL (overoptimisation). On the other hand the bin size of the p.d.f. can not be made as large as possible otherwise there will be a loss in experimental resolution. The overoptimisation has been carefully studied for

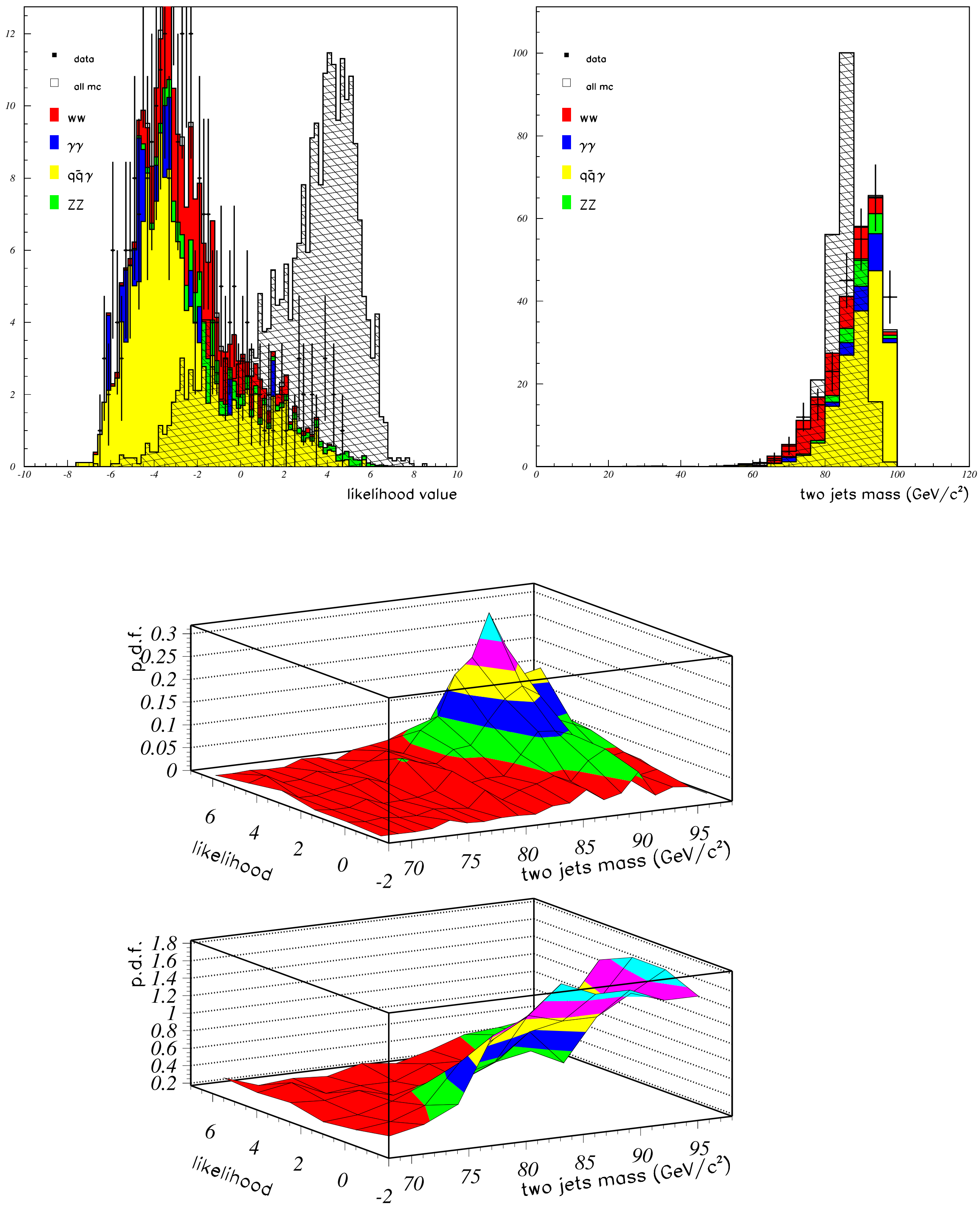

Figure 7.6: *Input for the limit derivation: two jets invariant mass and likelihood; the hatched histogram corresponds to distribution for Higgs of 90 GeV/c^2 mass. The two lower plots show the two dimensional (mass and likelihood) probability density functions for Higgs of 90 GeV/c^2 mass and for background.*

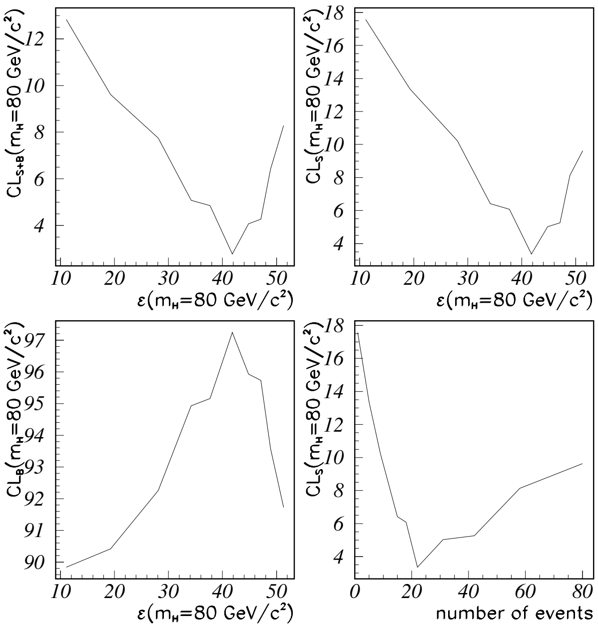

Figure 7.7: *CL_s, CL_{s+b} and CL_b for Higgs mass of 80 GeV/c^2 for different working points defined by the signal efficiency and the number of selected events.*

the limit derivation in this thesis. Three sets of distribution were used: one derived from the full sample of selected events and two derived from two subsamples of equal size (and equal to half of the original population) with events randomly chosen from the original population. One would expect the result from the full sample to be better than those from the two half samples. When overoptimisation starts to take place, both half sample give better result (lower CL_s) than the full sample.

Figure 7.8 shows that for the limit derivation made in this thesis the overoptimisation has been avoided since the two half subsamples give higher CL_s than the full sample.

The expected (derived using the simulation sample of backgrounds) and observed (derived using the data sample of events) limits have been computed from the intersection of the 5% CL_s line with the curve of CL_s versus Higgs mass (see figure 7.9):

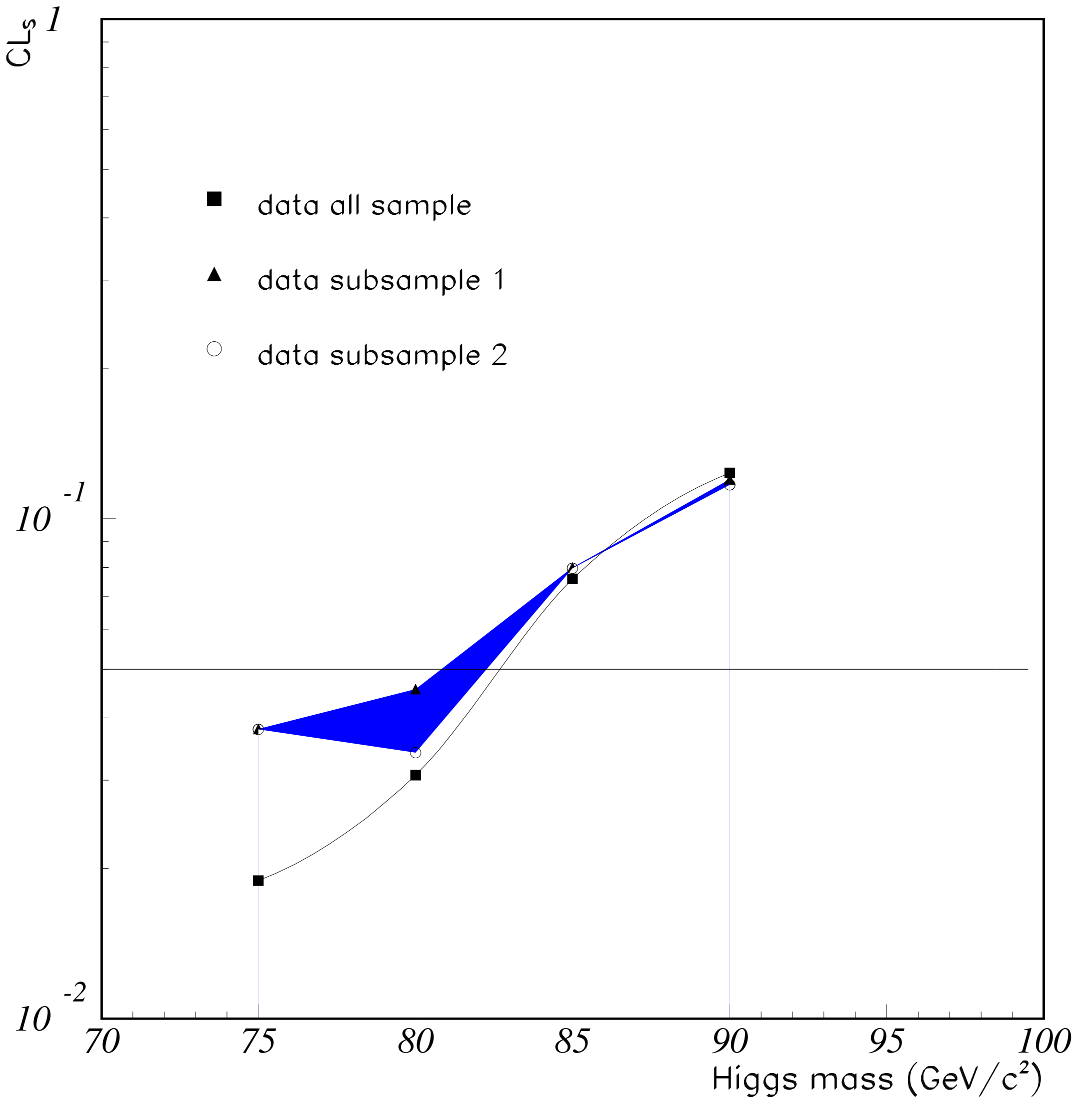

Figure 7.8: *CL_s, for different Higgs masses, for the full sample of selected events and two half subsample. In the interesting region for the limit derivation, the overoptimisation has been avoid: the two sub samples give higher CL_s with respect the full sample. The gray area shows the CL_s region between the two half subsamples.*

- **expected limit at $\sqrt{s}$=189 GeV/c^2** :

$$m_H \geq 82.7GeV/c^2 \tag{7.22}$$

- **observed limit at $\sqrt{s}$=189 GeV/c^2** :

$$m_H \geq 82.7GeV/c^2 \tag{7.23}$$

One should note that, with only the channel explored in this thesis, it is possible to set a limit which is near to the limit obtained combining all the DELPHI analyses of the previous years data:

- **observed limit at $\sqrt{s}$=183 GeV/c^2** combining all analyses:

$$m_h \geq 85.7GeV/c^2 \tag{7.24}$$

Figure 7.10 shows a selected event.

7.5 Evaluation of systematic uncertainties

In section 7.2 it has been shown that the number of background events, the Higgs efficiency, the two dimensional probability density function for mass and likelihood ratio are the input to extract the limit on the Higgs mass. Several systematic effects can influence these quantities.

The strategy that I adopted to compute the systematic errors can be summarised as follows:

- identify the source of error and change its value by the corresponding uncertainty;
- repeat the event selection, recompute the mass and the value of the likelihood ratio for all the selected events;
- compute the difference in the number of events at fixed signal efficiency by introducing the systematic, and compute the difference with the "central number" defined as the one without the systematic change.

Finally, all the differences are added in quadrature.

In principle the probability density functions should also change, but the effect on the limit derivation is minor and it has not been taken into account.

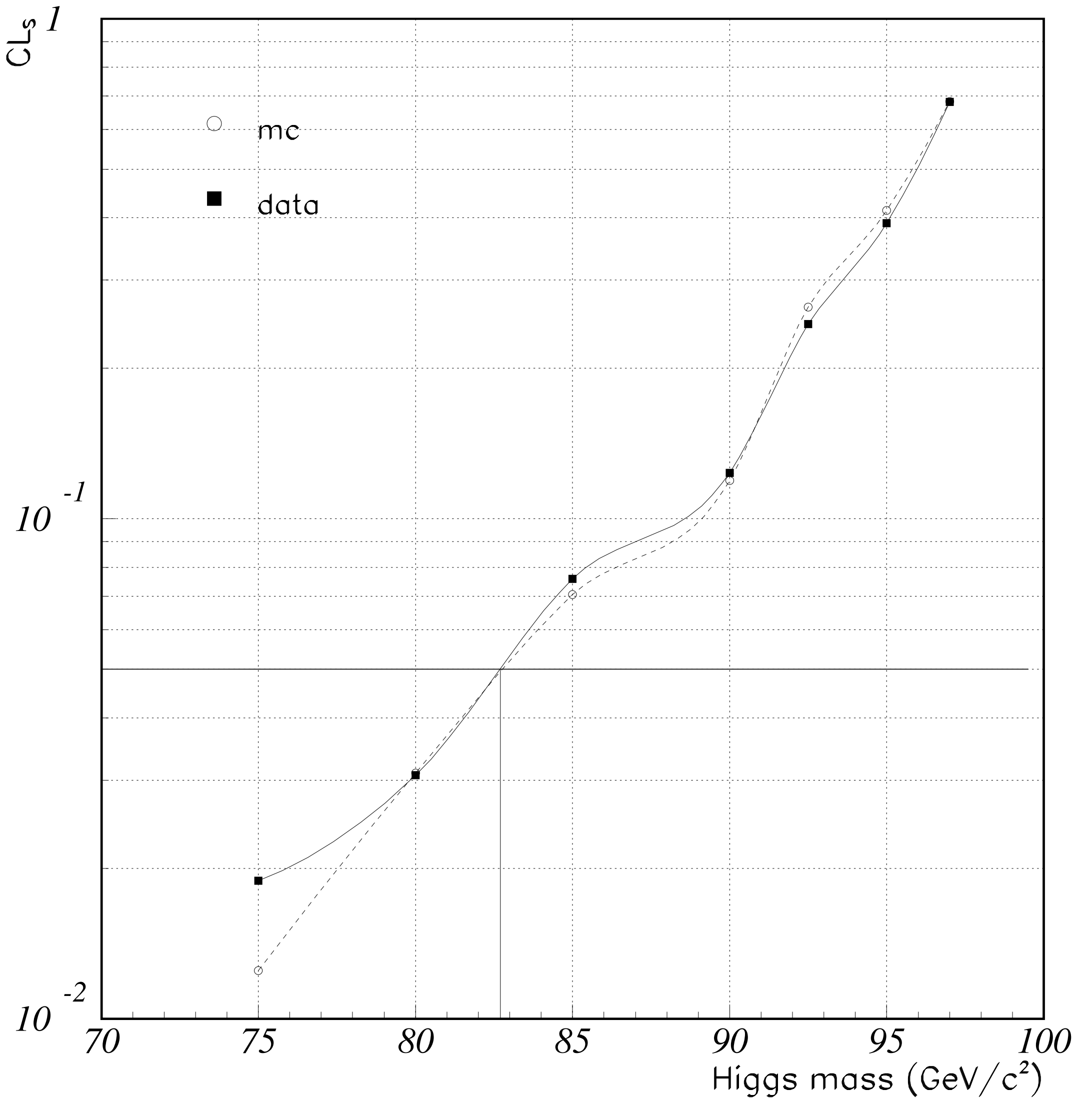

Figure 7.9: *CL_s versus Higgs masses. The intersection with the 5% CL line gives the limit on Higgs mass. The full squares are the CL_s obtained in data and the open circles are the ones from simulation*

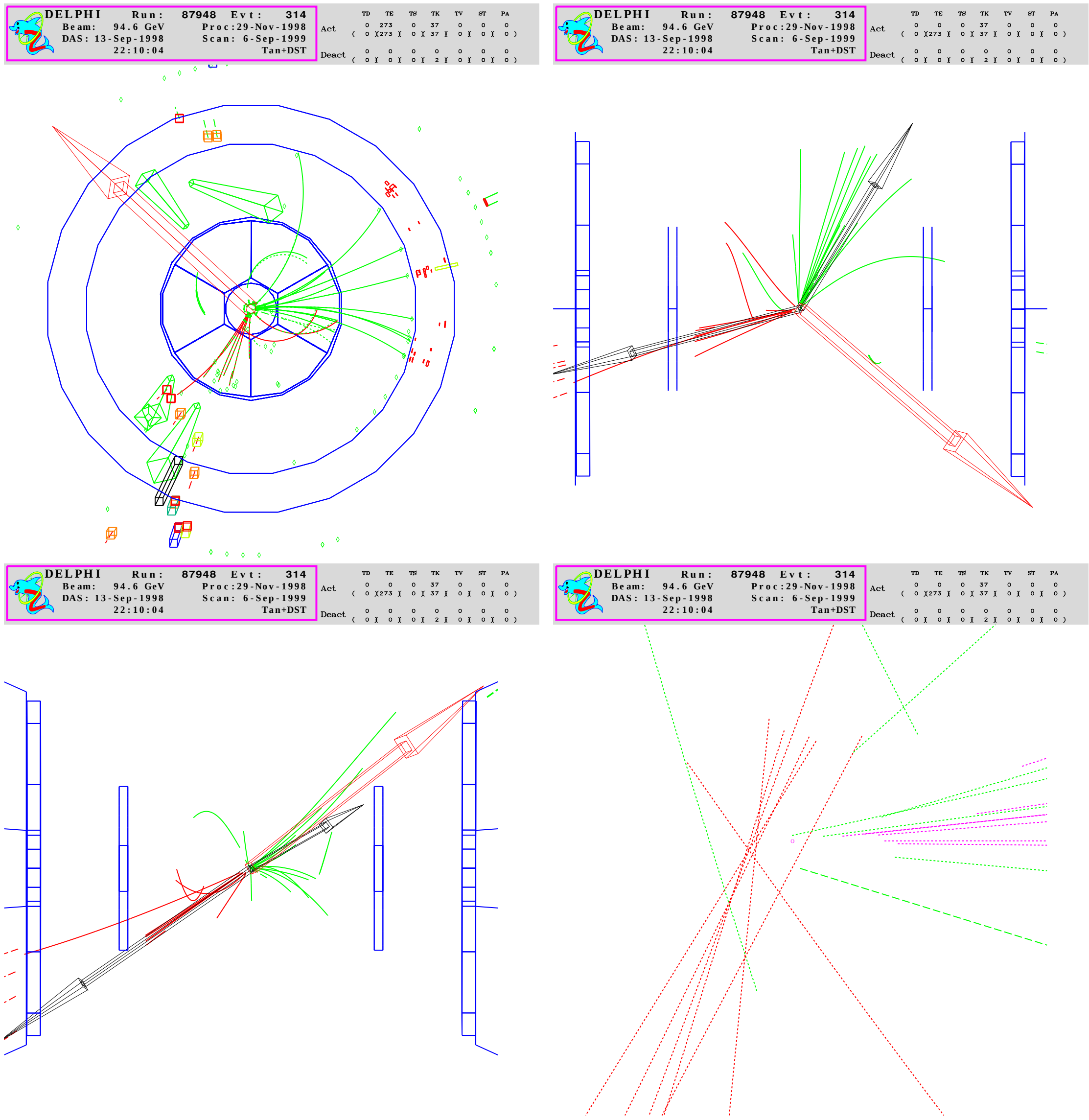

Figure 7.10: *A selected event. Upper left: $R\phi$ view, upper right: XZ view; lower left: YZ view, lower right:zoom in XZ view: the tracks are converging towards two nice secondary vertices. The big arrow in these plots shows the missing momentum. The btag variable for this event is 3.2 and the mass of the two jets is 86.1 GeV/c^2.*

7.6 Systematic sources

The following sources of systematic errors have been considered:

- btag;
- jet reconstruction algorithm;
- hermeticity algorithm;
- signal simulation;
- jet energy reconstruction.

Each source is described in the following sections.

7.6.1 b tag

In section 5.3 it has been shown that in order to account for the discrepancy between data and simulation at the Z^0 in the number of b tagged jets in 2 and 4 jet topologies , a weight has been applied on the $q\overline{q}\gamma$ simulated events. The natural way to take into account the systematic error introduced by this effect is to remove the weight.

A further check has been made. In section 4.4.3 it has been shown that one of the most powerful variables to compute the btag is based on the impact parameter significance (i.e. impact parameter divided by its error) of the particles in the event. A disagreement between data and simulation in the description of this variable results in a large discrepancy in the fraction of b tagged events. It is then essential to have an understanding of the effect of detector resolution on impact parameter. This can be achieved using tracks with negative impact parameter. Successively a fine tuning of the $R\phi$ and Rz impact parameter distributions in the simulation was developed and applied [75]. To evaluate the effect of the detector, the resolution of the detector as estimated from the data was used in the definition of the tagging probability of simulated events. Figure 7.11 shows how the number of events at fixed Higgs efficiency changes when both the checks on btag are applied.

7.6.2 Jet reconstruction algorithm

As explained in section 4.4.2 the DURHAM jet algorithm has been chosen to reconstruct the jets. To estimate the systematic connected with the clusterization the analysis has been repeated using the JADE algorithm. The number of events at fixed Higgs efficiency changes as shown in figure 7.11.

7.6.3 Hermeticity

In section 4.5.4 it has been shown how it is possible to remove $q\overline{q}\gamma$ events using the taggers. The applied algorithm is based on the agreement between data and simulation on the number of background and signal events with fired taggers. A pessimistic way to take into account any possible disagreement is to compare the results of the analyses in which the cut on fired taggers is and is not applied (see figure 7.11).

7.6.4 Higgs generator

As explained in section 4.3 a detailed comparison between two signal generators has been done. The main difference comes from the interference between Higgs-strahlung and WW fusion which is taken into account in the WPHACT generator and not in HZHA. At present WPHACT is the only available generator which takes into account the interference between the two processes. The only possibility to compute the systematics coming from the Higgs generator is to repeat the analysis using HZHA and WPHACT; this gives a pessimistic estimate since the main contribution comes from the interference mechanism (see figure 7.11).

7.6.5 Energy reconstruction

One of the crucial variables in the limit computation is the two jet invariant mass. To compute it, the basic ingredients are the jet quadri-momenta. It is therefore important to have an estimation of the systematic error coming from energy reconstruction. The reweighting of quadri-momenta described in section 7.3 is based on the simulation: the coefficients to rescale the jet momenta are computed as the ratio between the generated and the reconstructed momenta in different bins of the jet polar angle. The comparison between the jet quadri-momenta in data and simulation after the reweighting is therefore a test on how the simulation reproduced the real data.

A sample of $q\overline{q}\gamma$ events has been selected. In data 1504 candidate $q\overline{q}\gamma$ events have been found. Applying the same cuts on simulation, a contamination of 3% coming from four fermions events has been estimated in the $q\overline{q}\gamma$ sample. The study on energy reconstruction has been done on this sample. Figure 7.12 shows that the agreement between data and simulation is good before and after applying the reweighting (less the 1% difference in mean values of data and simulation). Finally to take into account any possible systematics coming from energy reconstruction it has been decided to introduce a smearing of 3% in the jet quadri-momenta of simulation (see figure 7.11).

7.7 Limit derivation taking into account systematic uncertainties

All error contributions have been added in quadrature and the total systematic error and the statistical one have been plotted in figure 7.13. In the interesting region where the confidence levels for signal are optimized (at Higgs efficiency between 20 and 60%) the total systematic error is of the order of $20 \div 30\%$).

The problem of incorporating the systematic uncertainty into the calculation of an upper confidence limit on a branching ratio is exstensively discussed in [76]. Let us

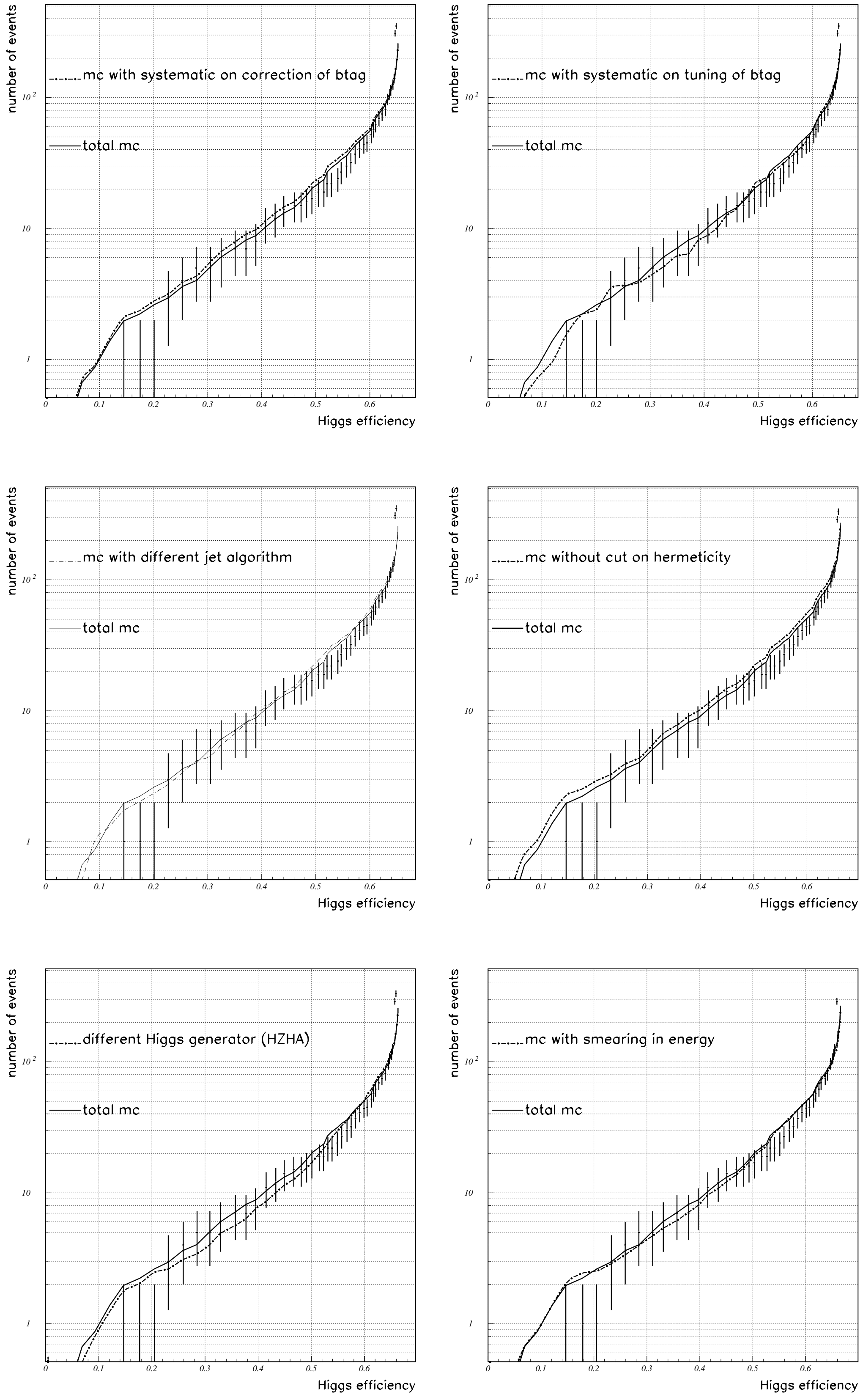

Figure 7.11: *Number of events versus Higgs efficiency (for $m_H = 95$ GeV/c^2). The dot-dashed line refers to the computation with specified systematic included.*

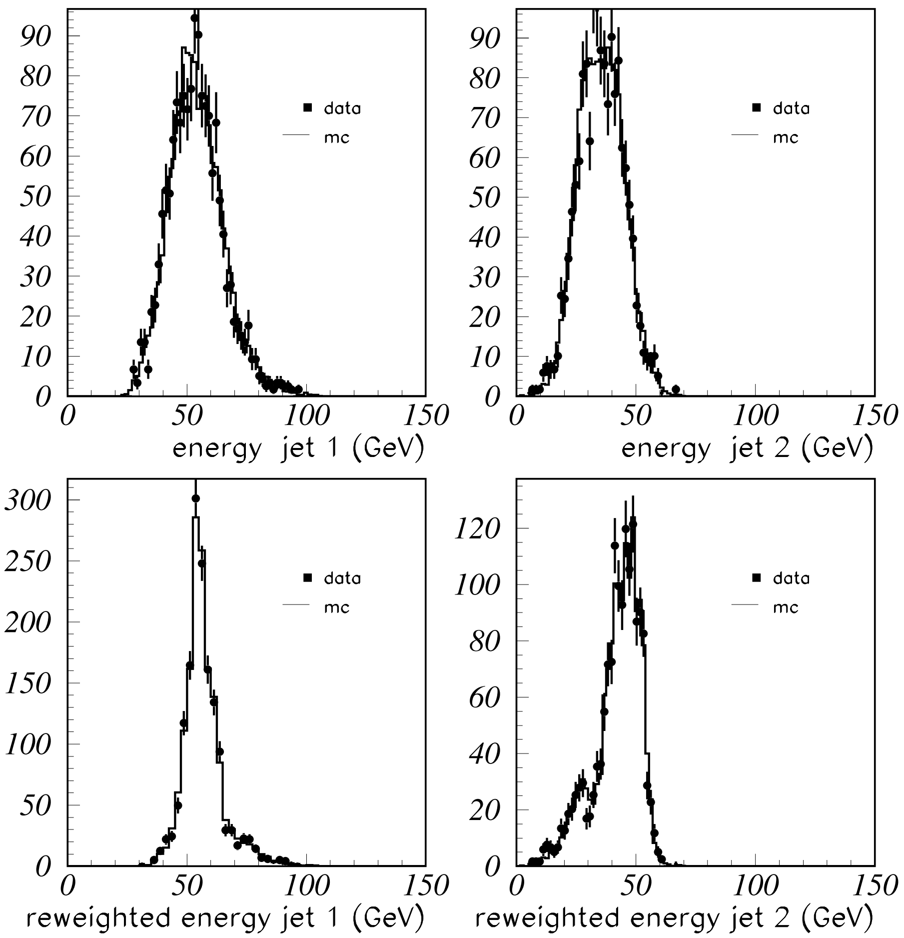

Figure 7.12: *Energy of the most and less energetic jet before (upper plot) and after (lower plot) reweighting the jet energy.*

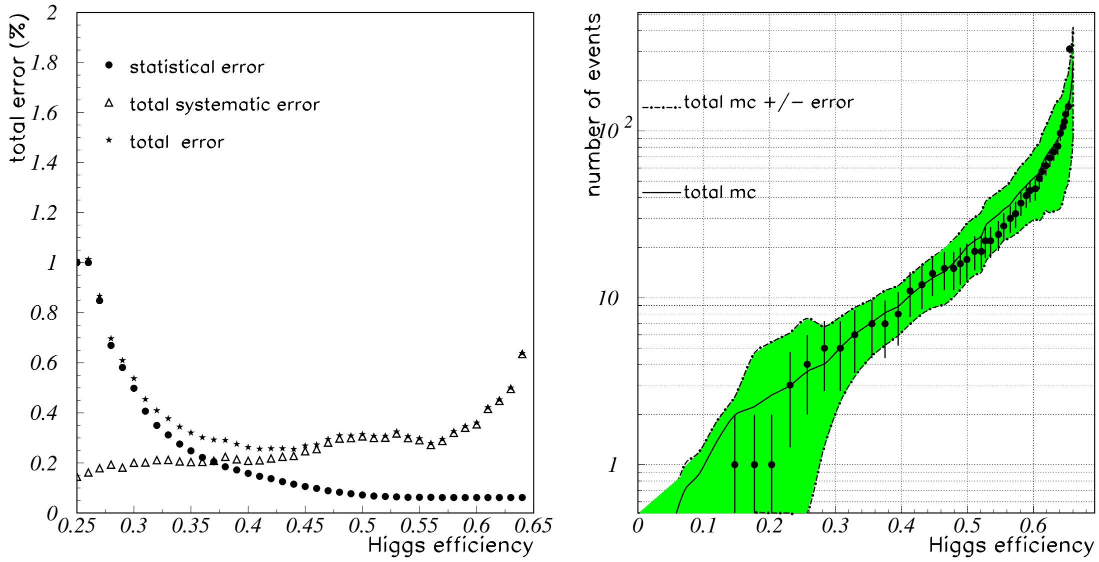

Figure 7.13: *Left: relative statistical and systematic errors on number of events and their quadratic sum versus the Higgs efficiency. Right: number of expected and observed events versus Higgs efficiency: the shaded band shows one standard deviation uncertainties taking into account statistical and systematic errors.*

define:

- R: the branching ratio to be measured;
- R_t: the true value of the branching ratio;
- S_t: the value of true detector sensitivity (such that the number of expected events is $\mu_t = R_t S_t$);
- $\hat{S}$, σ: the mean value and the error on evaluation of S_t.

In the case in which no events are observed and the error on S_t is not taken into account, the probability $p(R)$ to measure a value R or less for R_t is given by:

$$p(R) = e^{-RS} \tag{7.25}$$

where S is the measured value of S_t, and the Poisson distribution has been considered for the distribution of events. In this case the 90% CL upper limit for R is given by (solving the equation $p(R) = 0.1$):

$$R = \frac{2.30}{\hat{S}} \tag{7.26}$$

Let us now take into account the error on S. Suppose that the probability density function to find S_t around the mean $\hat{S}$ be $W(S; \hat{S}, \sigma)$. In this case the probability $p(R)$

to measure a value R or less for R_t is given by:

$$p(R) = \int_0^\infty e^{-RS} W(S; \hat{S}, \sigma) dS \tag{7.27}$$

In the simple case when W can be considered Gaussian:

$$p(R) = \int_0^\infty e^{-RS} \frac{1}{\sqrt{2\pi\sigma^2}} e^{-(S-\hat{S})^2/2\sigma^2} dS \tag{7.28}$$

The 90% CL upper limit is:

$$R = \frac{2.30(1 + 2.30\sigma^2/2S^2)}{\hat{S}} \tag{7.29}$$

In the more general case when n candidate events have been found [76]:

$$R = R_0(1 + (R_0 - n))\sigma^2/2S) \tag{7.30}$$

where R_0 is the usual upper limit quoted for a Poisson parameter when n events are observed. One should note that the introduction of systematic error can only increase the upper limit on the branching ratio.

When the expression for W is not trivial, Monte Carlo techniques must be used. This is the case of the method used in this thesis: to take into account the systematic error, a smearing (according to the estimated systematic effects) has been introduced in the number of events in the generation of Monte Carlo experiments (see section 7.2).

The limit has been recomputed and the results are:

- **expected limit** :
$$m_H \geq 81.9 GeV/c^2 \tag{7.31}$$
- **observed limit** :
$$m_H \geq 81.7 GeV/c^2 \tag{7.32}$$

A variation of 1 (0.8) GeV/c^2 has been found in data (simulation) with respect to the limit derivation without taking into account the systematic error.

7.8 Combination of $e^+e^- \to ZH \to H\nu\overline{\nu}$ channel with others channels

7.8.1 Standard Model Higgs

In the framework of the Standard Model, the DELPHI collaboration examined the following channels:

- $e^+e^- \to Z^0H \to He^+e^- \to q\overline{q}e^+e^-$

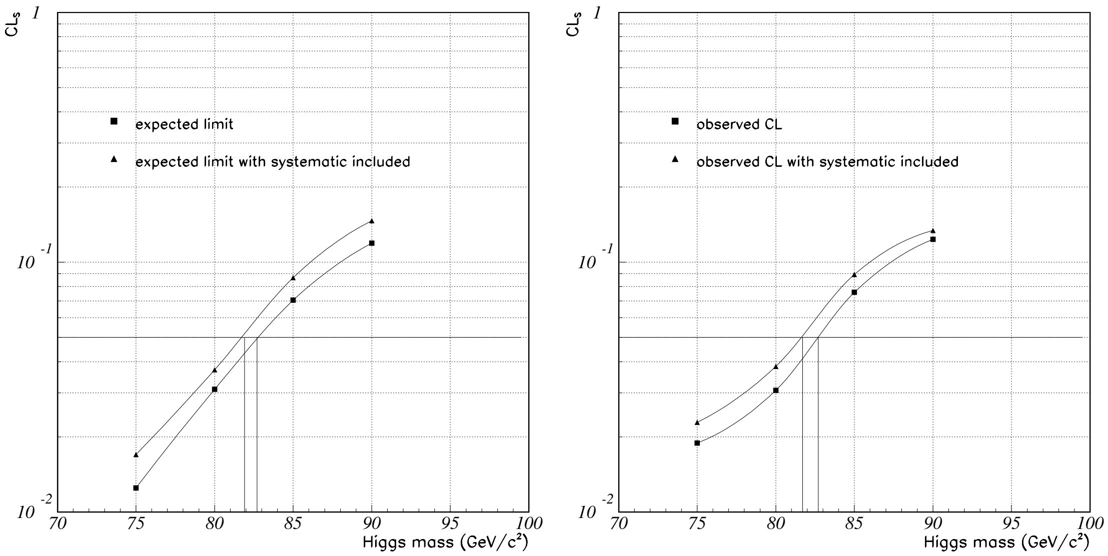

Figure 7.14: *Variation of expected (left) and observed (right) limit when the systematic error is taken into account.*

- $e^+e^- \rightarrow Z^0H \rightarrow H\mu^+\mu^- \rightarrow q\overline{q}\mu^+\mu^-$
- $e^+e^- \rightarrow Z^0H \rightarrow H\tau^+\tau^- \rightarrow q\overline{q}\tau^+\tau^-$ and $e^+e^- \rightarrow Z^0H \rightarrow Z\tau^+\tau^- \rightarrow q\overline{q}\tau^+\tau^-$
- $e^+e^- \rightarrow Z^0H \rightarrow Hq\overline{q} \rightarrow q\overline{q}q\overline{q}$

and the channel developed in this thesis:

- $e^+e^- \rightarrow H\nu\overline{\nu}$

Table 7.1 summarises the integrated luminosity, the efficiencies, the expected backgrounds and their errors, and number of observed events at various levels of the analyses.

Figure 7.15 shows the distribution of the reconstructed Higgs boson mass found in the previous channels after all selection criteria for data, simulated background and signal events. The last cut in each channel has been chosen such that the signal-over-background ratio (for the reference mass) is almost equal for all channels (between .2 and .35). Within the 189 GeV data, the total number of events observed in all channels is 31, which is consistent with the 33.2 expected background. Since the two hypotheses (background only and background plus signal at 95 GeV/c^2) are almost indistinguishable, a possible signal at 90 GeV/c^2 has been superimposed in order to visualise the resolution in the mass of such a signal.

The confidence levels CL_b, CL_{sb} and CL_s are computed as described above. In the presence of a sizeable Higgs signal the value of the observed CL_b (top of Figure 7.16) would approach one, because it measures the fraction of background-only experiments

Selection	Data	Total background	$q\overline{q}\gamma$	4 fermion	Efficiency
Electron channel 155.4 pb^{-1}					
Preselection	1290	1227.4± 6.1	924	267	78.5
tight lepton id.	28	27.9± 0.9	13	12.4	61.0
final selection	5	6.63±0.26	1.29	5.34	58.1
b-tagging	1	2.58±0.17	0.59	1.99	50.4
Muon channel 158.0 pb^{-1}					
Preselection	6441	6177 ± 22	4871	1239	84.8
tight lepton id.	15	15.5 ± 0.7	1.96	13.6	75.0
final selection	5	5.09 ± 0.19	0.09	5.00	70.8
b-tagging	2	1.69±0.12	0.02	1.67	60.6
Tau channel 158.0 pb^{-1}					
Preselection	7128	7091± 6.6	4810	2281	95.8
$l^+l^-q\bar{q}$	21	20.4± 0.5	3.8	16.6	31.4
final selection	11	11.25±0.39	1.70	9.55	29.6
mass plot	0	0.76±0.03	0.03	0.73	18.0
Missing energy channel 158. pb^{-1}					
Anti $\gamma\gamma$	11946	11030.11	8413.66	2452.66	91.
Preselection	561	549.89	334.72	190.	71.
final selection	28	27.8± 1.0	17.1	10.1	54.3
mass plot	4	6.0±0.22	3.1	2.9	33.9
Four-jet channel 158.0 pb^{-1}					
Preselection	1730	1706.2± 9.1	583	1123	87.1
final selection	138	121.9± 1.1	26.8	95.1	63.3
mass plot	24	22.2± 0.2	6.5	15.7	43.9

Table 7.1: *Effect of the selection cuts (summarised on first column) on data, simulated background and simulated signal events at $\sqrt{s}$ = 189 GeV. Efficiencies (in %) are given for the signal, ie. m_H = 95 GeV/c^2. Within each channel, the last line gives the entries for the mass-plot, while the preceding line represent the inputs for the limit derivation. The quoted errors are statistical only.*

which are less signal-like than the observation. On the contrary in the 1998 data the observation agrees well with the expectation (background only).

To set a limit on the SM Higgs boson mass, all the channels must be combined and also results from data taken at lower energies must be taken into account. The improvement on the limit from adding 1997 data is very weak indeed. The combined CL_s is shown in Fig. 7.16. The 95% CL lower limit on the mass are

- **expected limit** :
$$m_H \geq 94.1 GeV/c^2 \tag{7.33}$$

- **observed limit** :
$$m_H \geq 94.6 GeV/c^2 \tag{7.34}$$

7.8.2 MSSM Higgs

The results of the analysis done in this thesis and of the other analyses in the DELPHI collaboration are combined in the framework of MSSM using the same statistical method as for the SM. Earlier results at $\sqrt{s}$ = 130-136 GeV, 161-172 GeV and 183 GeV are also included. With respect to the Standard Model processes (see at the beginning of section 7.8.1), another channel is added for the MSSM:

- $e^+e^- \rightarrow hA \rightarrow q\bar{q}q\bar{q}$

A realistic analysis of the phenomenology of the MSSM Higgs sector has to include radiative corrections [67, 68, 69, 70, 71, 72, 73]. In the first chapter it has been shown that, at tree level, the Higgs sector of the MSSM can be effectively parametrised in terms of two free variables, for example $\tan\beta$ and m_A. After including the 1-loop corrections, Higgs boson masses and couplings depend also on the top quark mass and the additional unknown parameters of the MSSM. Several approaches have been developed to compute radiative corrections to the tree-level approximation, the Effective Potential Approach (EPA) [68], the Renormalisation Group Equations (RGE) approach [69, 70], and the Full 1-loop Diagrammatic Calculations (FDC) in the on-shell renormalisation scheme [71, 72]. Full analytic 1-loop corrections are calculated in the EPA and good agreement with the FDC of neutral Higgs boson masses are found [74]. A simple approximation scheme for radiative corrections to the neutral Higgs boson masses gives good precision [31]. A detailed description of the FDC is given in [71].

Using numerical simulation, the important parameters (and assumptions) for the Higgs boson phenomenology are the following:

- m_A and $\tan\beta$: the allowed limits of variation are usually ([43], page 399):
  - 20Gev$\leq m_A \leq$ 300 GeV;
  - $0.5 \leq \tan\beta \leq 60$.

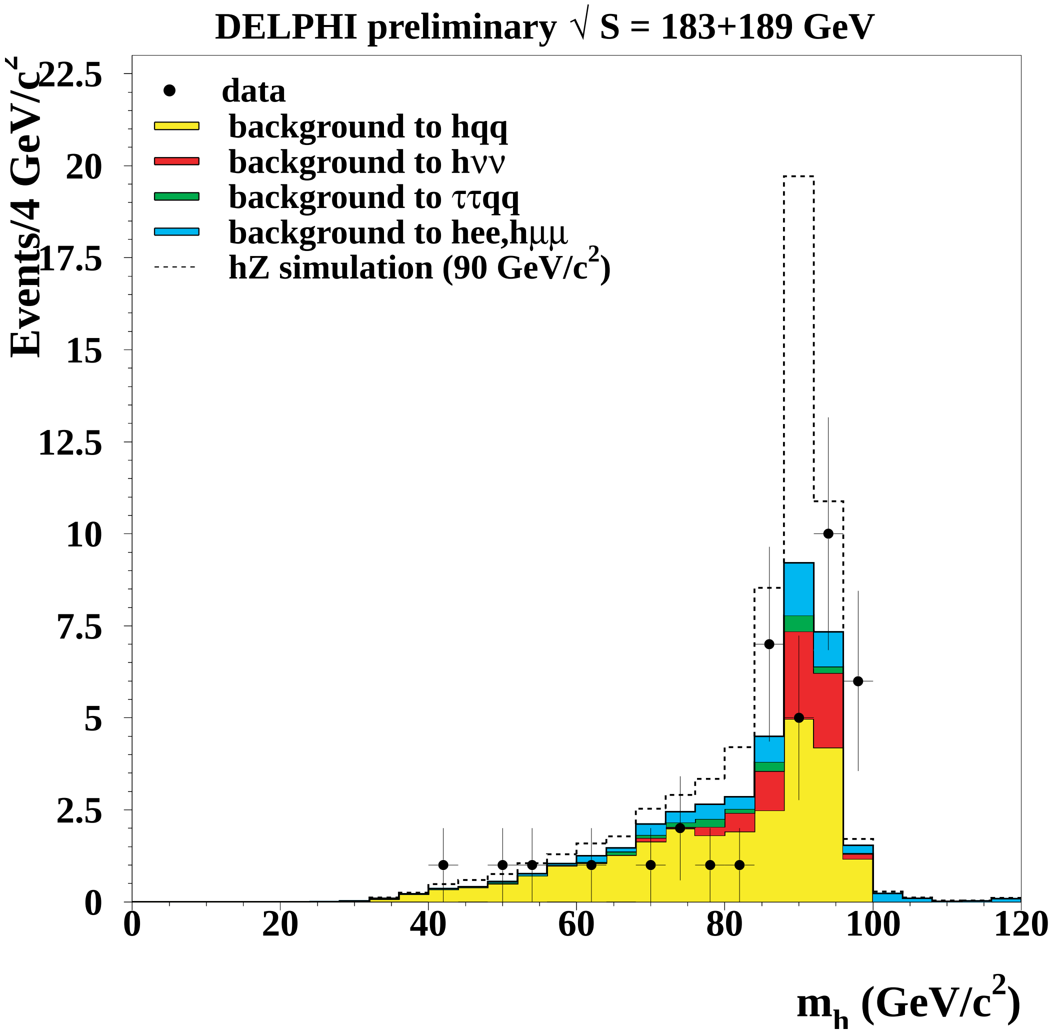

Figure 7.15: *Final distribution of the reconstructed Higgs boson mass when combining all analyses at 183 and 189 GeV. Data are compared with background expectations. The expected spectrum, with the correct rate, from a signal at 90 GeV/c^2 is also shown added to the background contributions.*

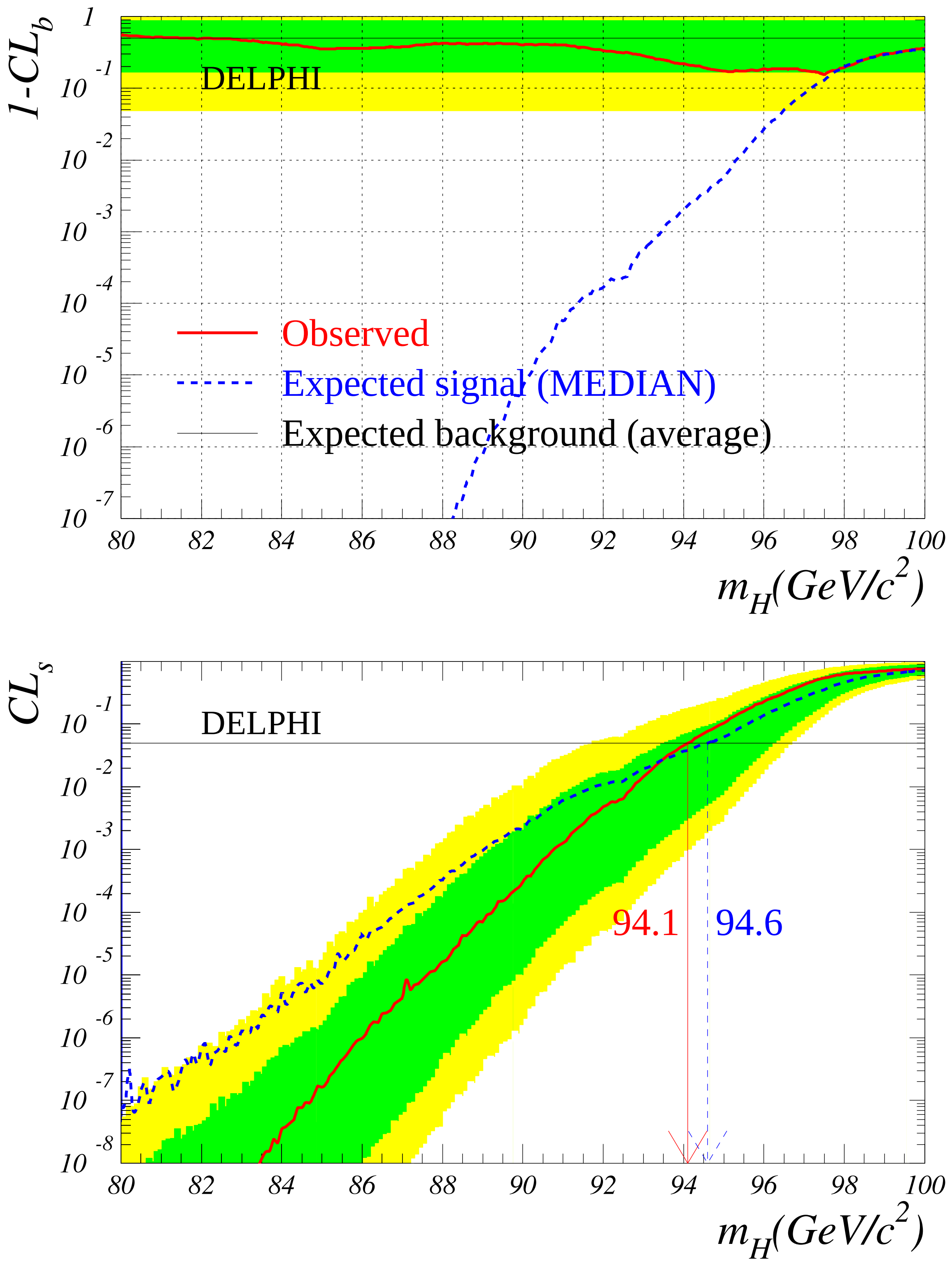

Figure 7.16: *Confidence levels as a function of the* SM *Higgs boson mass. Curves are shown for the expected (dashed) and observed (solid) confidences and the bands correspond to the 68.3% and 91% confidence intervals. Top : Confidence level in the background hypothesis. Bottom : Confidence level in the signal hypothesis. The intersections of the horizontal line at 5% with the curves define the expected and observed 95%* CL *lower limits on the Higgs boson mass.*

The upper limit on m_A is introduced since the variation of m_h with m_A becomes negligible for $m_A \geq 200 - 250$ GeV/c^2. The upper value of $\tan\beta$ is chosen such that the bottom Yukawa coupling remains in the perturbative regime for scales below the Grand Unification (GUT). A given value of $\tan\beta$ implies an upper limit on the top mass for which the theory can be extended perturbatively up to the GUT scale. For $\tan\beta = 0.5$ this upper limit is already close to 150 GeV, so that lower values of $\tan\beta$ would be inconsistent with the experimental value of the top quark mass.

- universality assumption: all sfermion masses (and gaugino masses) are assumed to be unified either at the ElectroWeak scale or at the GUT scale;

- M_S – the universal mass parameter for all squarks. The assumption of the same mass parameters (universality) for the three squark generations has a small effect. Results depend mostly on the stop mass parameter and only weakly on the masses of other sfermions.

- M_2 – the universal gaugino mass. Also in this case the assumption of universality has little impact on the results.

- μ – the mixing parameter of the Higgs doublets in the SUSY superpotential.

- A – the mixing parameter in the sfermion sector. As for M_S only one universal mixing parameter is considered for all squark generations. The mixing term is defined as $AM_S + \mu/\tan\beta$. Note that μ and A are real parameters, i.e. no phases are assumed.

To obtain the results described hereafter, the parameters beyond tree level have been set to the following values [43]: 175 GeV/c^2 for the top mass, 1 TeV/c^2 for M_S at the EW scale, 1.6 TeV/c^2 for M_2 at the EW scale and $\mu = -100 << M_S$ GeV. In addition, two benchmark hypotheses [43] have been made for the parameters A which together with μ determines the mixing in the stop sector:

- no mixing ($A = 0$)

- maximal mixing ($A = \sqrt{6}M_S$).

The no mixing hypothesis leads to minimal radiative corrections to m_h while the maximal mixing induces the largest corrections. In the two cases, the scale at which the squark tri-linear couplings are assumed to be equal is the EW scale, as for M_S and M_2.

Then, the MSSM parameter space is scanned in the ($\tan\beta$, m_{A}) plane. At each point of the parameter space, the hZ and hA cross-sections and the Higgs branching fractions are computed.

The signal expectations in each channel are derived from the cross-sections, the experimental luminosity and the efficiencies. The signal expectations, expected backgrounds and numbers of candidates enter in the computation of the observed confidence level in the signal hypothesis at the input point, CL_s. The expected confidence level in the signal hypothesis is also derived at each point. As there is a large overlap in the background selected by different analyses at 189 GeV (e.g. between the two four-jet channels or between the three tau channels), only one channel among each set of overlapping channels is selected at each input point, on the basis of the best signal over background ratio. This ensures that the channels which are combined in the confidence level computations are independent.

The confidence level computations make use of the probability density functions of the reconstructed mass in each channel for the data sets at 161-172 GeV and 183 GeV, while the results at 189 GeV are derived with the two-dimensional p.d.f of the reconstructed mass vs. a second channel-dependent discriminant variable (b-tagging variable in the He^+e^- and $H\mu^+\mu^-$ channels, likelihood variable in all others). As far as mass information is concerned, the reconstructed Higgs boson mass is used in the hZ channels and the sum of the reconstructed h and A masses in the hA channels.

The results translate into regions of the MSSM parameter space excluded at least at 95% CL. Except for m_{A} at low $\tan\beta$, they are not strongly dependent on the assumption about the mixing in the stop sector. The results are presented in the (m_{h}, $\tan\beta$) plane in Fig. 7.17, in the (m_{A}, $\tan\beta$) plane in Fig. 7.18 and in the (m_{A}, m_{h}) plane in Fig. 7.19.

The results shown in Figs. 7.17, 7.18 and 7.19 establish 95% CL lower limits on m_{h} and m_{A}, whatever the assumption on the mixing in the stop sector and for all values of $\tan\beta$ greater than or equal to 0.5:

$$\begin{aligned} m_{\mathrm{h}} &> 82.1\ GeV/c^2 \\ m_{\mathrm{A}} &> 83.2\ GeV/c^2 \end{aligned} \tag{7.35}$$

These limits arise from the performance of the searches at large $\tan\beta$, i.e. in the hA channel. The expected limits are 81.1 GeV/c^2 in m_{h} and 82.2 GeV/c^2 in m_{A}. In addition, in the low $\tan\beta$ region, all values of m_{A} are excluded, providing an excluded range in $\tan\beta$ between 0.6 and 2.4 in the no mixing case and between 1. and 1.4 in the maximal mixing case (see Fig. 7.18).

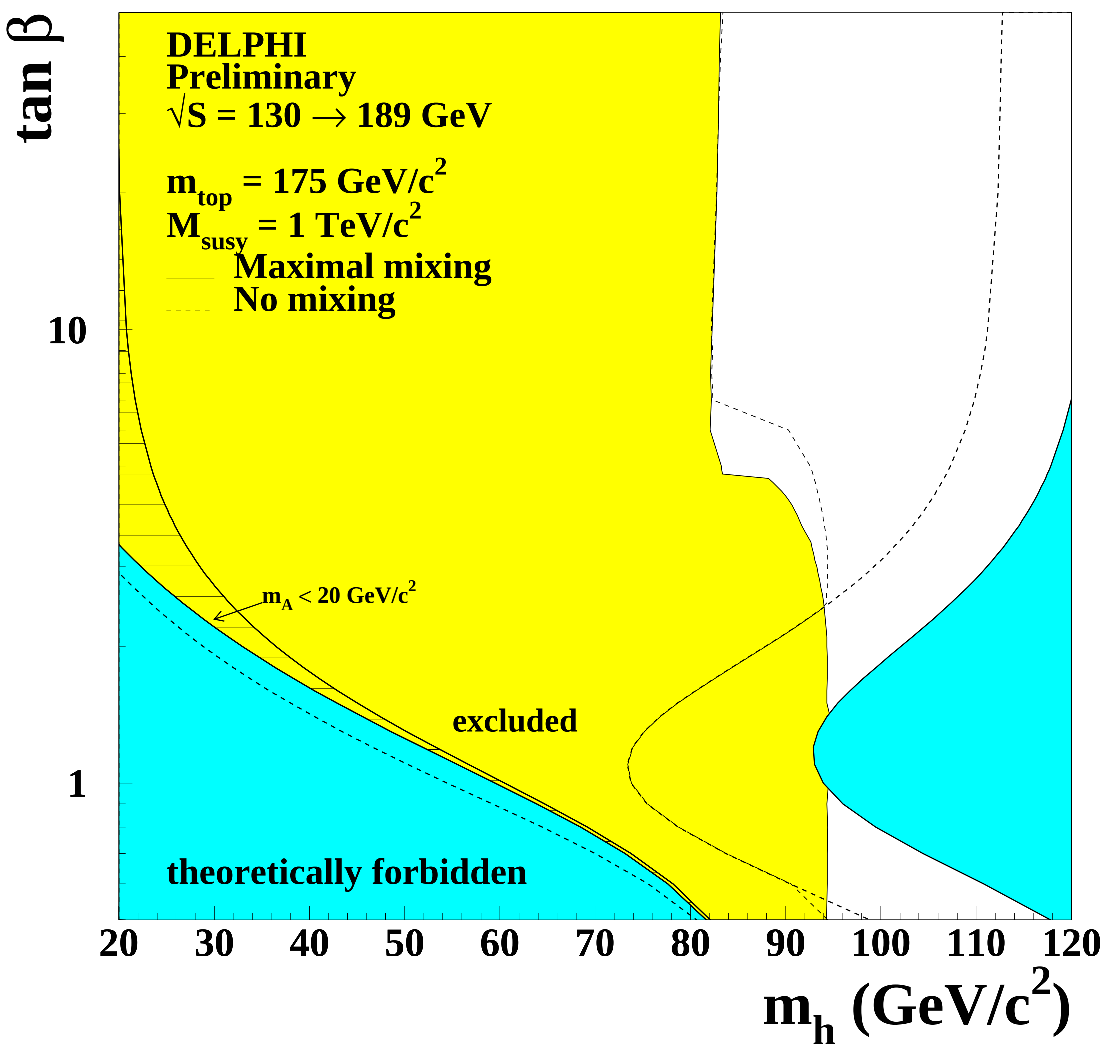

Figure 7.17: *Regions in the (m_{h}, $\tan\beta$) plane excluded at 95% CL by the searches in the hZ and hA production modes at $\sqrt{s} = 130 \div 189$ GeV . Two hypotheses for the mixing in the stop sector have been considered. The region of m_{A} below 20 GeV, not covered by these results, is shown for the maximal mixing in the hatched area. The regions not allowed by the MSSM model for a top mass of 175 GeV/c^2 and a SUSY scale of 1 TeV/c^2 are also indicated (shaded for the maximal mixing).*

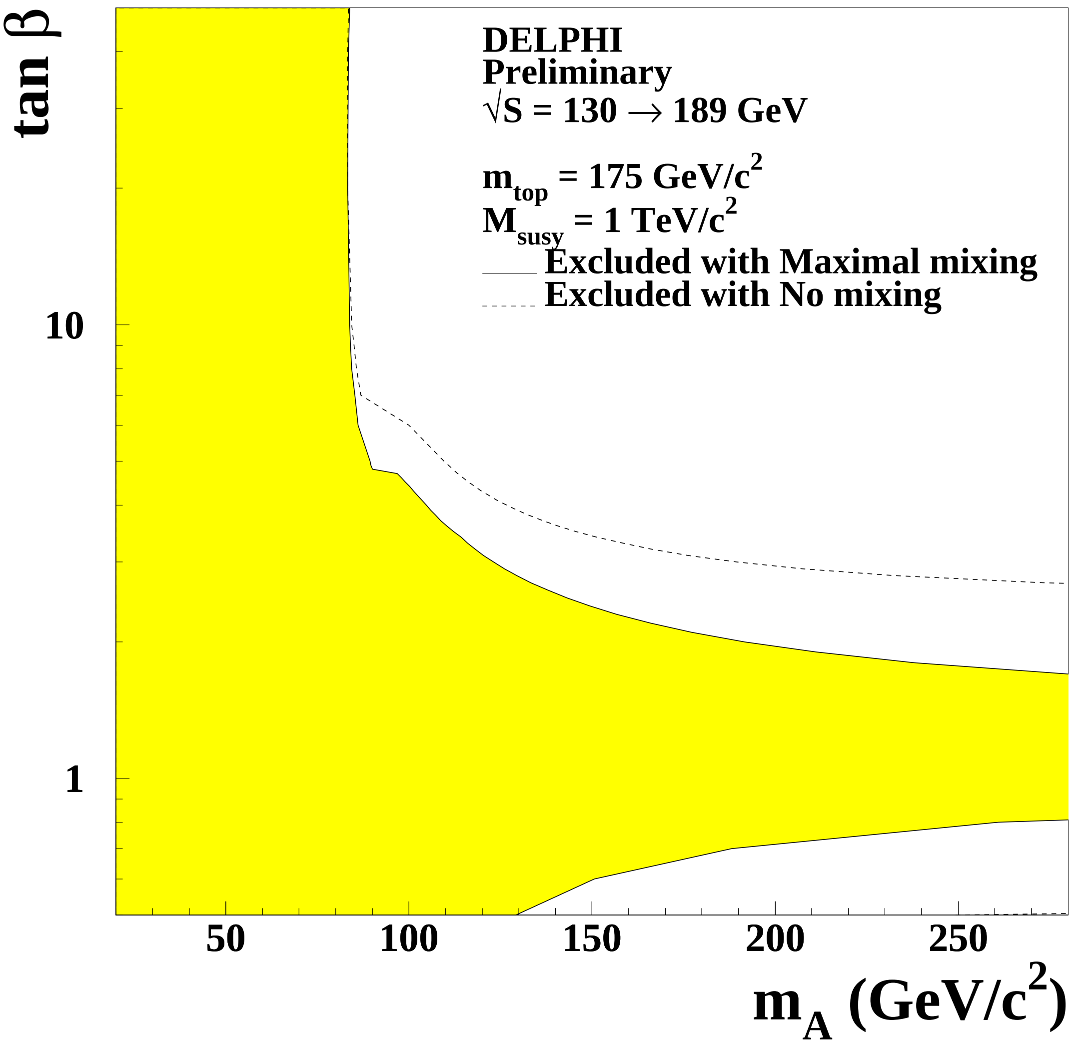

Figure 7.18: *Region in the* $(m_{\mathrm{A}}\,, \tan\beta)$ *plane excluded at 95% CL by the result of the searches in the hZ and hA channels at* $\sqrt{s} = 130 \div 189$ *GeV. Two different hypotheses for the mixing in the stop sector are presented.*

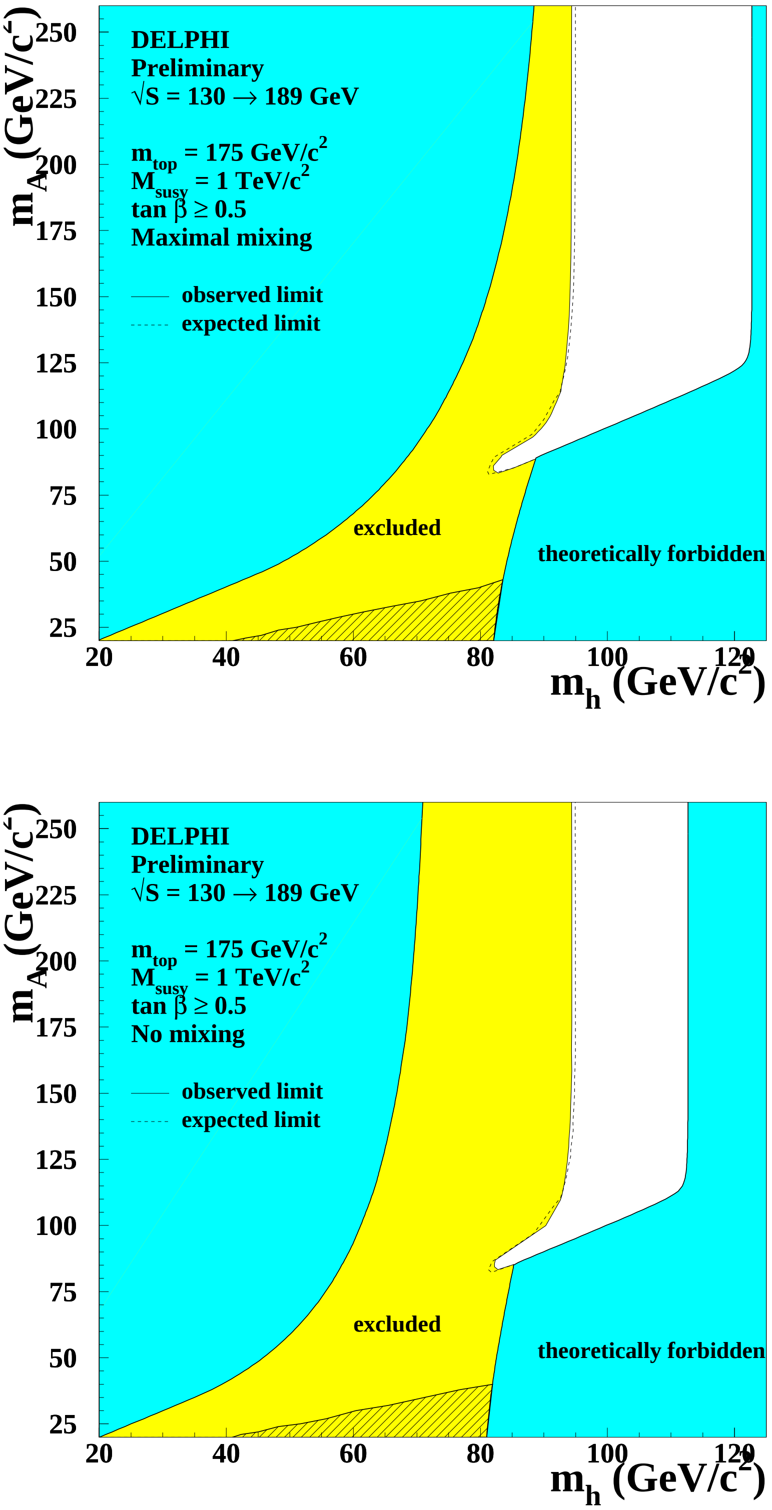

Figure 7.19: *Region in the (m_A , m_h) plane excluded at 95% CL by the result of the searches in the hZ and hA channels at $\sqrt{s}$ = 130 ÷ 189 GeV (in light grey). Two different hypotheses for the mixing in the stop sector are presented. The regions not allowed by the MSSM model for a top mass of 175 GeV/c^2 and a SUSY scale of 1 TeV/c^2 are shaded. The hatched area shows the region where the h→AA decay may occur.*

Chapter 8

Preliminary analysis on 1999 data

During 1999, data have been collected at centre of mass energies of 192, 196 and 200 GeV with integrated luminosities given in table 8.1. A preliminary analysis of these data has been made and will be described in the following sections. I will review how the exclusion limit and discovery sensitivity change as a function of centre of mass energy and collected luminosity.

8.1 Selection of events

During 1999 data taking (which is still on-going at the moment of writing this thesis) the centre of mass energy increased from 189 to 200 GeV (see table 8.1). In this range no new threshold for known processes has been reached, and the cross sections and kinematics of different processes changed smoothly (see table 8.2).

Year	$\sqrt{s}$(GeV)	$\mathcal{L}_{\text{DELPHI}}$ (pb^{-1})
1999	192.	25.9
1999	196.	76.9
1999	200.	39.8

Table 8.1: *centre-of-mass energies and luminosities of the 1999 LEP runs (last update: september 1999.*

Nevertheless, to study the backgrounds and the signal efficiency it was necessary to simulate three set of samples like the one described in table 4.3 at the three energies.

The detector performances are nearly the same for 1998 and 1999 data taking. Infact, there were nor interventions neither upgradets for the detectors during the shut down 1998-1999. On the other hand there has been an improuvement on the tracking algorithm, and in the overall alignment. As an example in figure 8.1 the resolution in $1/p$ and the sum in impact parameters in the $R\phi$ plane are plotted for $Z^0 \to \mu^+\mu^-$ events for 1998 and 1999.

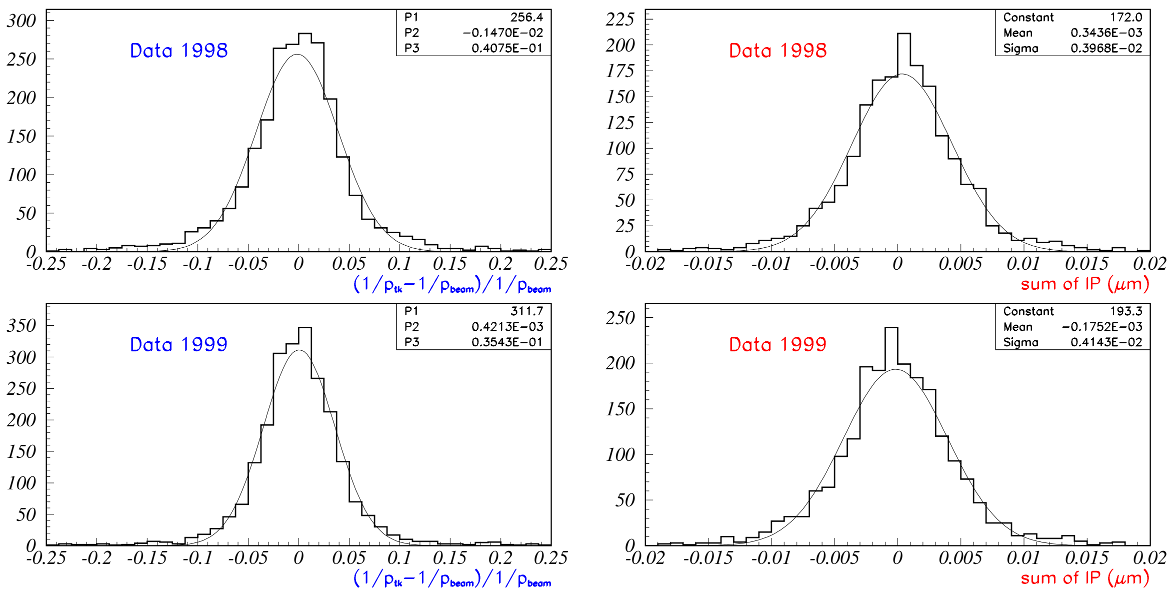

Figure 8.1: *Left:* $(1/p_{tk} - 1/p_{beam})/1/p_{beam}$ *where* p_{tk} *is the momentum estimation from the tracking detectors for muons from* $Z^0 \rightarrow \mu^+\mu^-$. *Right: sum of impact parameters in* $R\phi$ *plane for the two muon tracks. The sample of events was collected during the calibration runs at the* Z^0 *in 1998 and 1999. The performances of the detectors are nearly the same. A improvement can be seen in momentum resolution in 1999 coming from a better alignment of forward chambers.*

process	cross sections (pb) @			
	189 GeV	192 GeV	196 GeV	200 GeV
$q\bar{q}\gamma$	99.0	96.04	90.38	85.6
WW	17.733	18.127	18.482	18.720
ZZ	1.46	1.67	1.761	1.81

Table 8.2: *Cross sections for dominant background processes at different centre of mass energies.*

One of the greatest time dependent effects is surely the machine background. Clearly, increasing the energy results in an increase of the synchrotron radiation. More photons, electrons and positrons from converted photons in the quadrupoles arrive in the detectors. Also the vacuum condition inside beam pipe is a time dependent factor. It has a direct impact on the rate of off momentum electrons (section 4.5): see for example figure 8.2. During 1998 data taking, a leak in the beam pipe increased considerably the rate. We checked carefully this background to determine if some differences could be seen moving from 1998 to 1999 data taking (see for example the probability that an off momentum electron will be found in STIC in figure 8.2 for 1998 and 1999). The cut that we applied, rejecting the event when the polar angle of the most energetic electromagnetic cluster is below 5^o or greater than 175^o assures, an almost complete rejection of off momentum electrons (see figure 8.3 and table 8.3).

E_{min} [GeV]	$\mathcal{P}$[%]	$\mathcal{P}_{\theta>3^\circ}$[%]
0.1	3.65±0.15	0.39±0.05
0.5	2.89±0.14	0.16±0.03
2.5	1.52±0.10	0.05±0.02
5	1.03±0.08	0.03±0.01
10	0.53±0.05	0.01±0.01
15	0.38±0.05	–
20	0.35±0.05	–
25	0.33±0.05	–
30	0.31±0.05	–
40	0.23±0.04	–
50	0.16±0.03	–
60	0.05±0.02	–

Table 8.3: *The probability to have a shower with energy larger than E_{min} in STIC. The measurement was done with random triggered events recorded in 1999.*

The experience I acquired in the analysis of 1998 data gave me a deep understanding of 1999 data. Furthermore, the work on alignment and the analysis of $Z^0 \rightarrow \mu^+\mu^-$ was useful for understanding the detector performances, and gave me the possibility to disentangle those problems and data/simulation disagreements coming from detector effects and those coming from the simulations. Consequently a statistically good de-

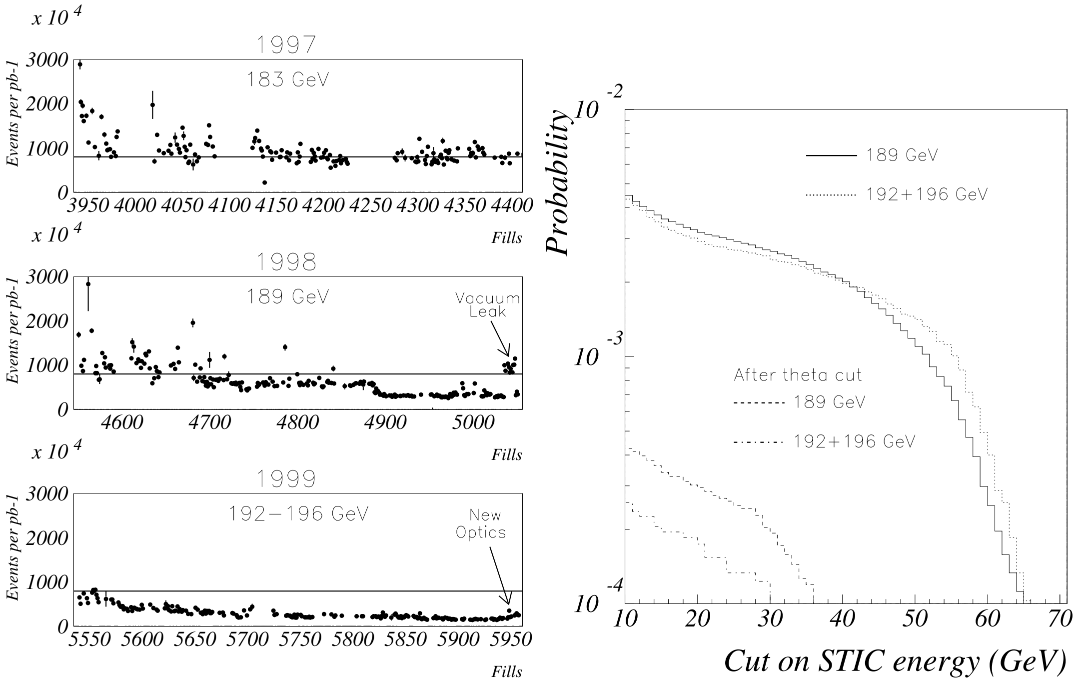

Figure 8.2: *Left: the number of off-energy electrons in STIC per* pb^{-1}*. Only the first 400-500 high energy fills during each year are shown. Right: the probability that an off energy shower will be found in STIC as a function of the energy cut [59].*

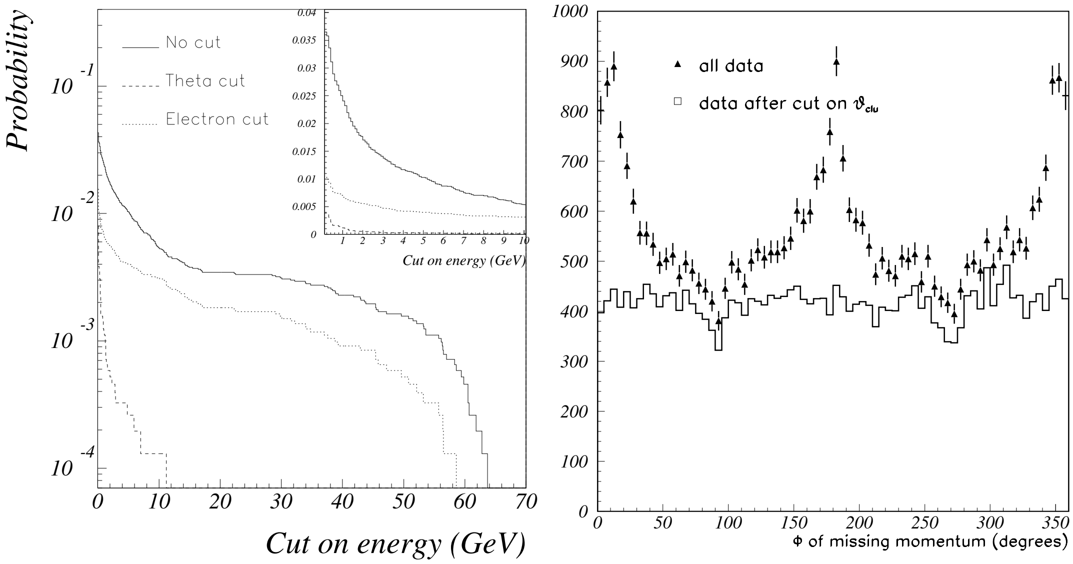

Figure 8.3: *Left: the probability to have a STIC shower in a random triggered event as a function of a cut on the STIC energy. The probability has been calculated for all events with a shower in STIC and for the subsamples when the incoming particle is identified as an electron and when the shower has a polar angle larger than 3 degrees Right: selected data before and after applying the cut in the polar angle of the most energetic electromagnetic cluster. After the cut all the off momentum background events are removed.*

scription of 1999 data has been achieved using the simulation for all the three energies. The agreement between data and simulation has been quantified in table 8.4 and can be seen in figures 8.4, 8.5, 8.6 and 8.7.

The preselection requirements are almost equal those one of the previous year, proving that the different applied criteria are based on understanding of underlying physics processes and detector effects and there is no tuning on applied cuts. The preselection requirements at different selection levels can be summarised as follow:

- rejection of $\gamma\gamma$:
  - total number of charged tracks in event > 5;
  - total number of tracks in event > 10;
  - the transverse energy $E_{tr} = \sum_{particle} \sqrt{p_x^2 + p_y^2} > 25$ GeV;
  - $|\cos(\theta_{pmiss})| < 0.995$ (where θ_{pmiss} is polar angle of missing momentum);
  - all electromagnetic clusters must have polar angle between 5^o and 175^o.
  - E_{30} = energy in a cone of 30^o around Z $< 0.7\sqrt{s}$;
  - $|\cos\theta|$ of most forward jet $< .95$;
  - $p_{thr} > 40$ GeV/c ;
- rejection of Bhabha:
  - the electromagnetic energy $E_{em} < 90\%$ of the total energy;
  - the most energetic electromagnetic cluster < 50 GeV;
  - we reject events where $E_{em} > \sqrt{s}/2$ and the angle between the two reconstructed jets is $> 175^o$.
- rejection of $q\bar{q}\gamma$:
  - $\cos\theta_{jet} < .95$ where θ_{jet} is the polar angle of the most forward jet;
  - cut on $\sqrt{s'}$ and polar angle of missing momentum as explained in section 4.5.4
  - energy of most energetic jet between 30 and 90 GeV;
  - energy of less energetic jet between 10 and 60 GeV;

The results are shown in table 8.4 and in figures 8.5 and 8.7.

Whenever a discrepancy between data and simulation is noticed, it may arise from a problem in simulation (some process may be not well described) or from a detector behavior which is not taken into consideration by the simulation, or from a new process. The most powerful instrument to disentangle the effects coming from the above sources

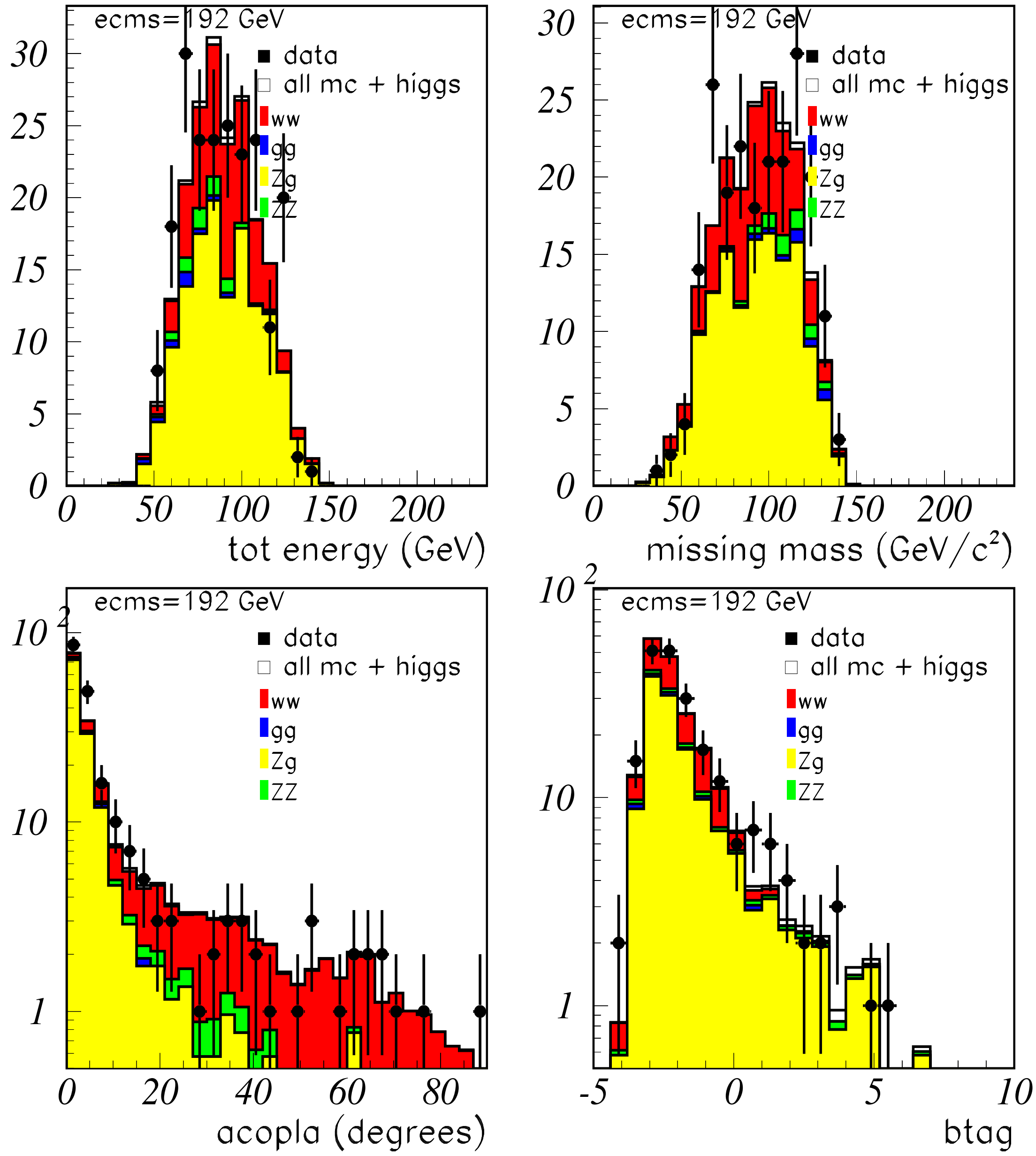

Figure 8.4: *Distributions of total energy, invariant missing mass, acoplanarity between two jets, btag variable for the selected events at centre of mass energies of 192 GeV.*

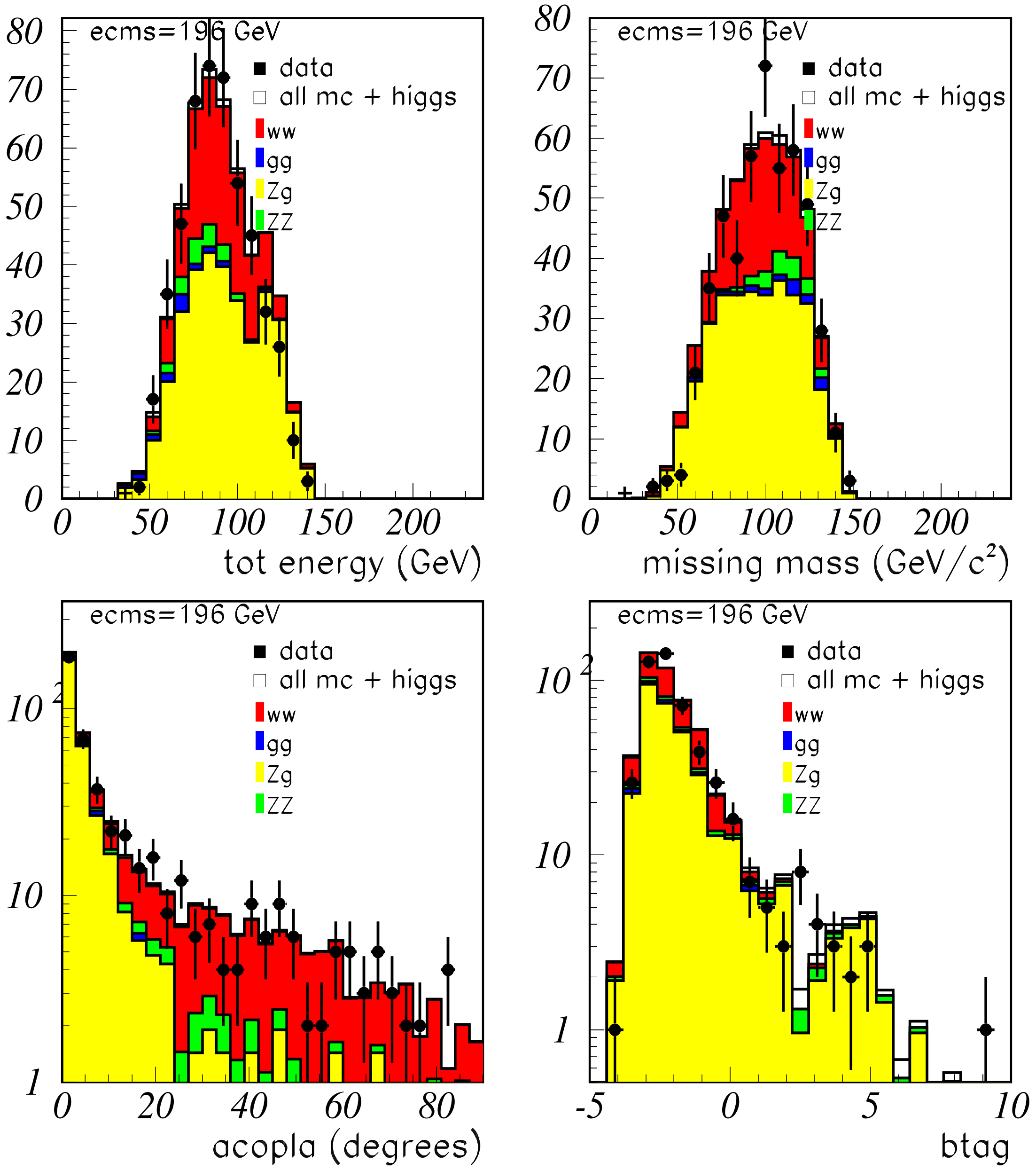

Figure 8.5: *Distributions of total energy, invariant missing mass, acoplanarity between two jets, btag variable for the selected events at centre of mass energies of 196 GeV.*

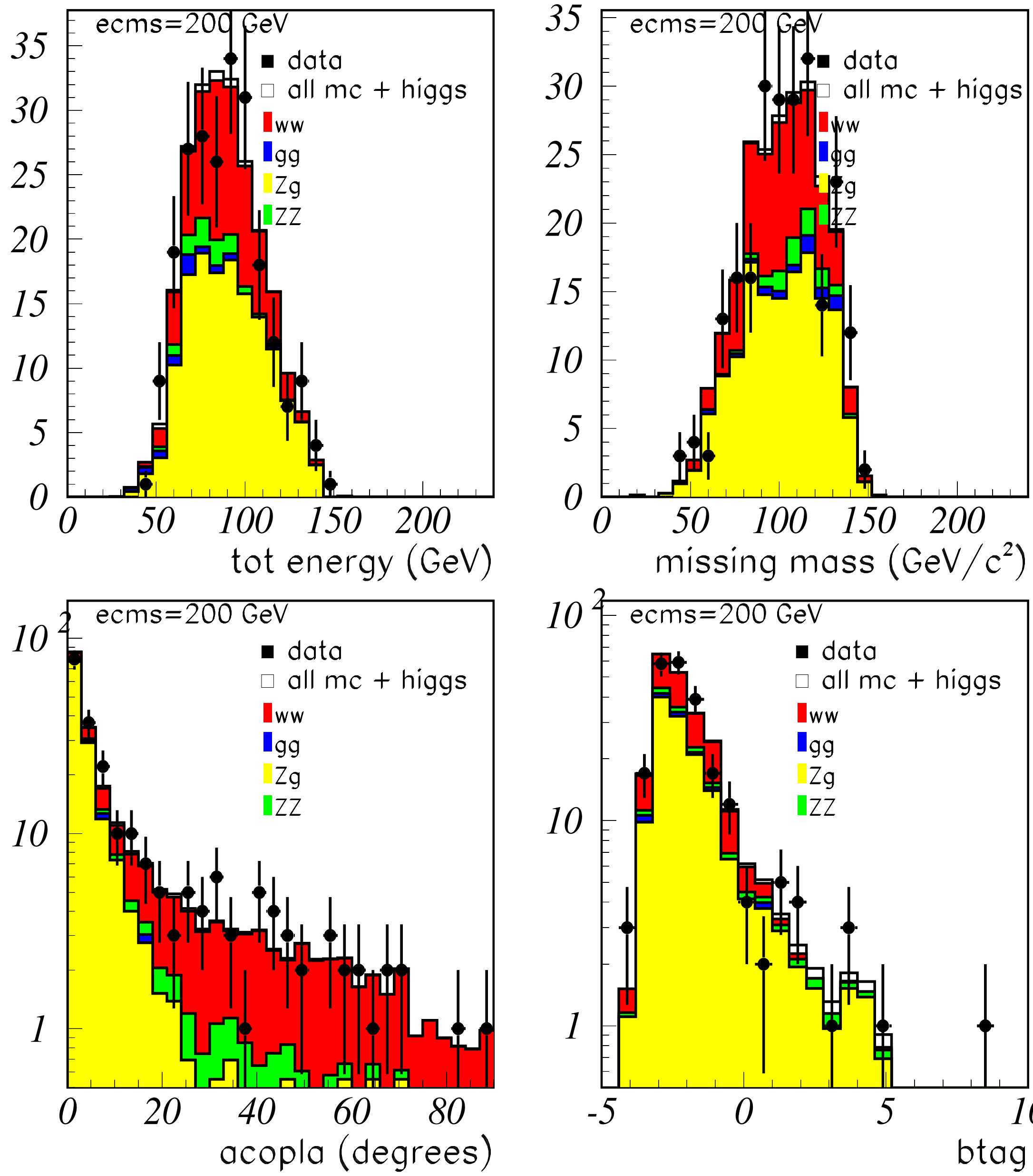

Figure 8.6: *Distributions of total energy, invariant missing mass, acoplanarity between two jets, btag variable for the selected events at centre of mass energy of 200 GeV.*

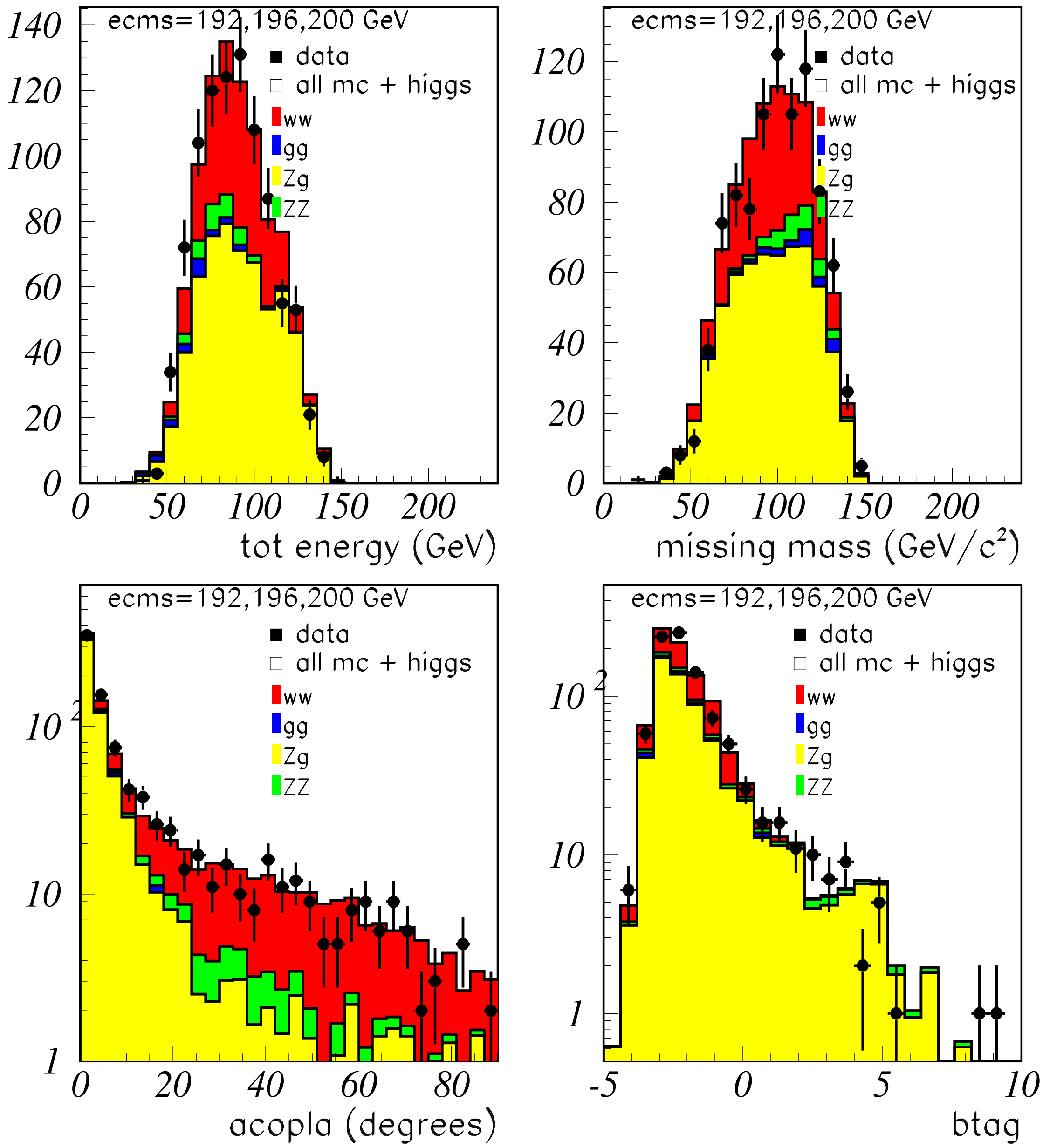

Figure 8.7: *Distributions of total energy, invariant missing mass, acoplanarity between two jets, btag variable for the selected events at centre of mass energy of for all the three sets of events at different energies together.*

selection	$2f$(MC)	$4f$(MC)	$\gamma\gamma$(MC)	All MC	DATA	ϵ_{HIGGS}		
						$\epsilon_{m_h=95}$	$\epsilon_{m_h=100}$	$\epsilon_{m_h=105}$
$28.5pb^{-1}$@$192GeV$								
after $\gamma\gamma$	1650.11	444.53	47.05	2141.69	2297	0.88	0.88	0.88
after Bhabha	1145.62	389.47	23.19	1558.28	1602	0.88	0.88	0.88
after $q\bar{q}\gamma$	135.45	59.96	3.517	198.93	210	0.79	0.79	0.74
$76.9pb^{-1}$@$196GeV$								
after $\gamma\gamma$	4539.82	1327.64	139.804	6007.27	6496	0.88	0.88	0.88
after Bhabha	3079.48	1153.59	68.90	4301.98	4497	0.88	0.88	0.88
after $q\bar{q}\gamma$	335.67	161.94	10.45	508.07	486	0.79	0.79	0.74
$39.8pb^{-1}$@$200GeV$								
after $\gamma\gamma$	2252.82	681.501	72.75	3007.07	3223	0.88	0.88	0.88
after Bhabha	1513.28	593.79	35.69	2142.77	2253	0.88	0.88	0.88
after $q\bar{q}\gamma$	144.67	78.62	5.41	228.70	226	0.79	0.79	0.74

Table 8.4: *Number of events in data and simulation at different levels of selection and for different centre of mass energies. The content of simulation has been detailed in three classes: two fermion, four fermions, two photons. The signal efficiency (in %) is also given for three different Higgs masses.*

is the comparision of two different sets of data at different centre of mass energies and one should identify variables in which the increase of energy is a second order effect with respect to a new signal or a detector problem. This is what I have done for preliminary analysis of the 1999 data.

Since no evidence of a signal has been found in 1998 data (as has been shown in previous chapters) they constitute the best background sample to use in the analysis in view of understanding the 1999 sample.

In figures 8.8 and 8.9 distributions for data at 196 GeV have been superimposed on distributions of 189 GeV data.

Some variables are sensitive to the increase of centre of mass energy (see for example, in figure 8.9, the total visible energy and the sum of absolute momenta along the thrust axis). In addition there are distributions sensitive to detector effects: for example in figure 8.8 it can be seen that the distribution of the polar angle of tracks for 1999 has an excess in the forward regions with respect to the distribution of 1998. This reflects an increase of efficiency of the new forward tracking algorithm which has been developped for this year's data. Acoplanarity, the angle between jets and missing momentum, the btag...are some of the variables sensitive to the presence of a signal. Some of them (btag) should not be sensitive to the increase in centre of mass energy of a few GeV, unless new processes (like the Higgs production) reach their threshold. and these are the best variable on which to base a detailed understanding of the underlying effects.

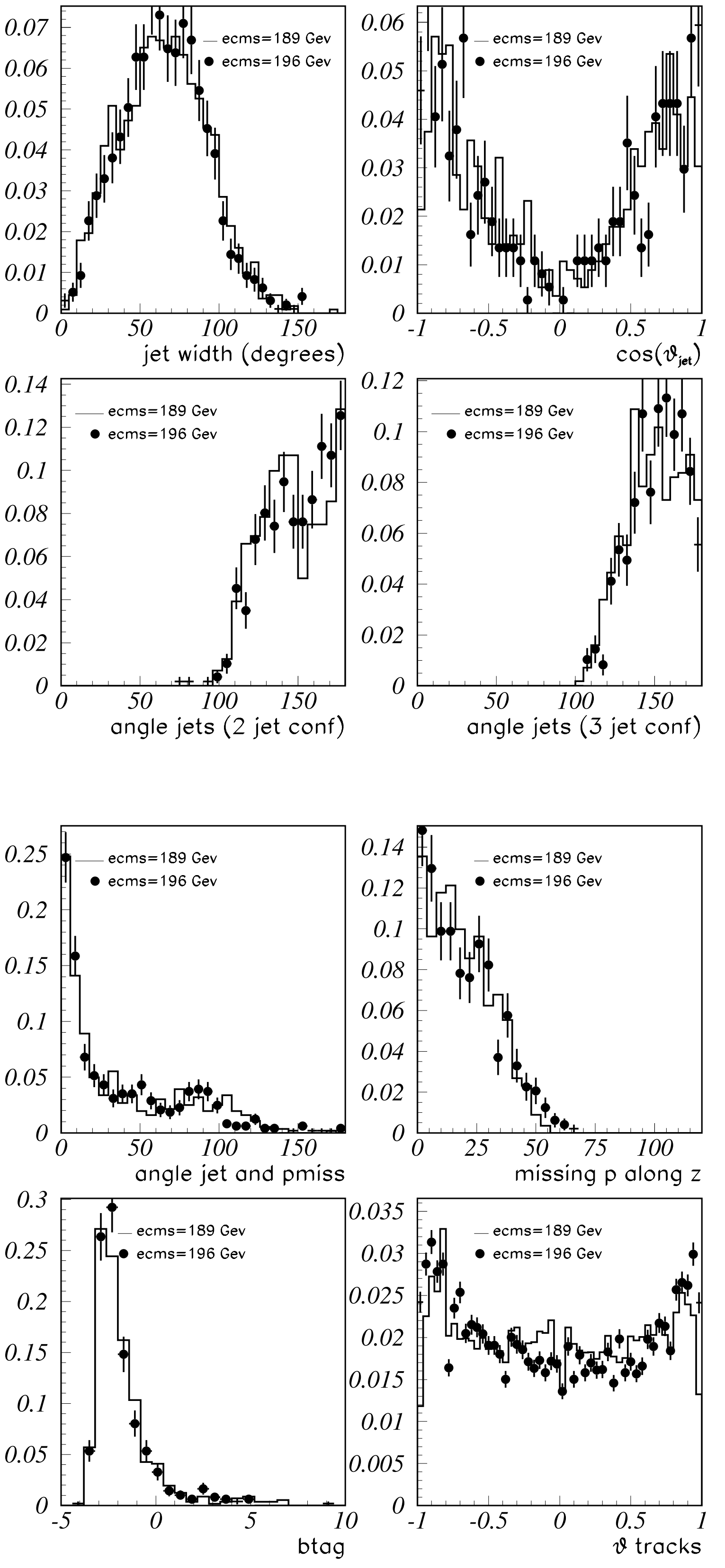

Figure 8.8: *Comparison between distributions for data at 189 and 196 GeV centre of mass energies.*

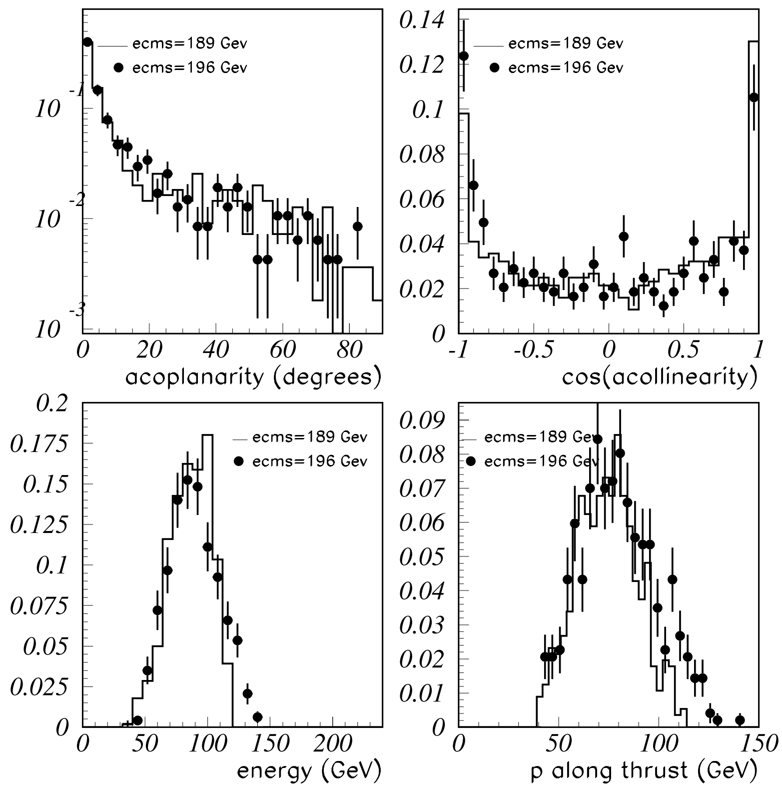

Figure 8.9: *Comparison between distributions for data at 189 and 196 GeV centre of mass energies.*

8.2 Likelihood computation and mass distribution

Since no major problem has been found, it was worthwhile to go a step further in the analysis, and the likelihood has been computed in the three samples at different centre of mass energies. The likelihood computation is based on the simulated samples (as described in section 5.4) and the agreement between data and simulation is the starting condition to trust in the results.

A new variable has been added with respect to the likelihood used for 1998 data: reconstructing the events in the four jet configuration, the new variable is given by the number of jets with charged multiplicity less then 3 (see figure 8.10). One can note that for WW events there are many events with jets with multiplicity less then 3. These are events in which one or both of the W's decay leptonically.

Inspecting the number of events versus Higgs efficiency (for m_H = 105 GeV/c^2) a good agreement has been found with the simulated curve of background plus signal (the signal is coming from a Higgs boson with m_H = 105 GeV/c^2). Due to the low integrated luminosity collected so far the agreement is not statistically significative.

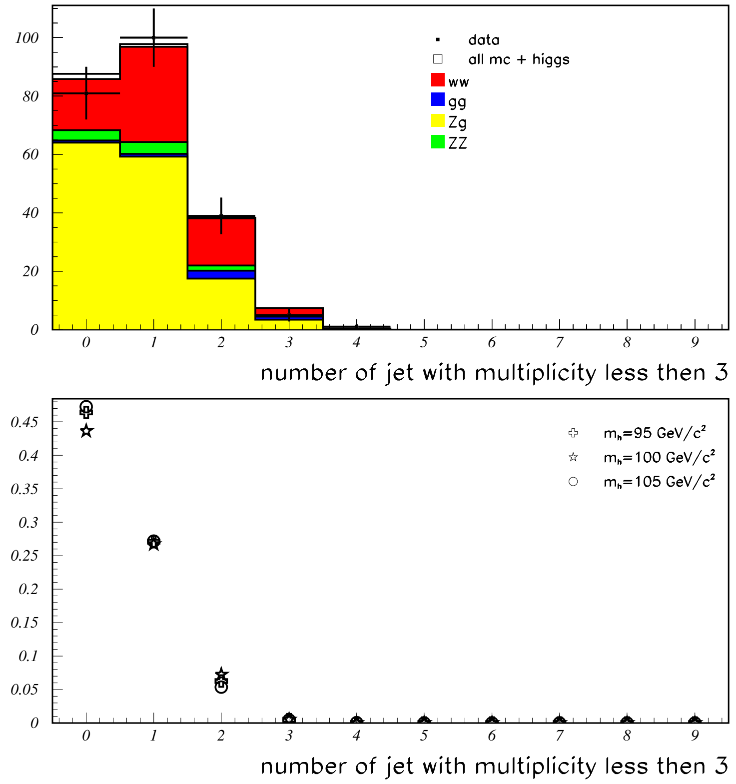

Figure 8.10: *Number of jets in an event with charged multiplicity less then 3.*

The other crucial variable in the Higgs search (the one that enters in the discovery/limit Confidence Level computation) is the two jet invariant mass. In figures 8.12

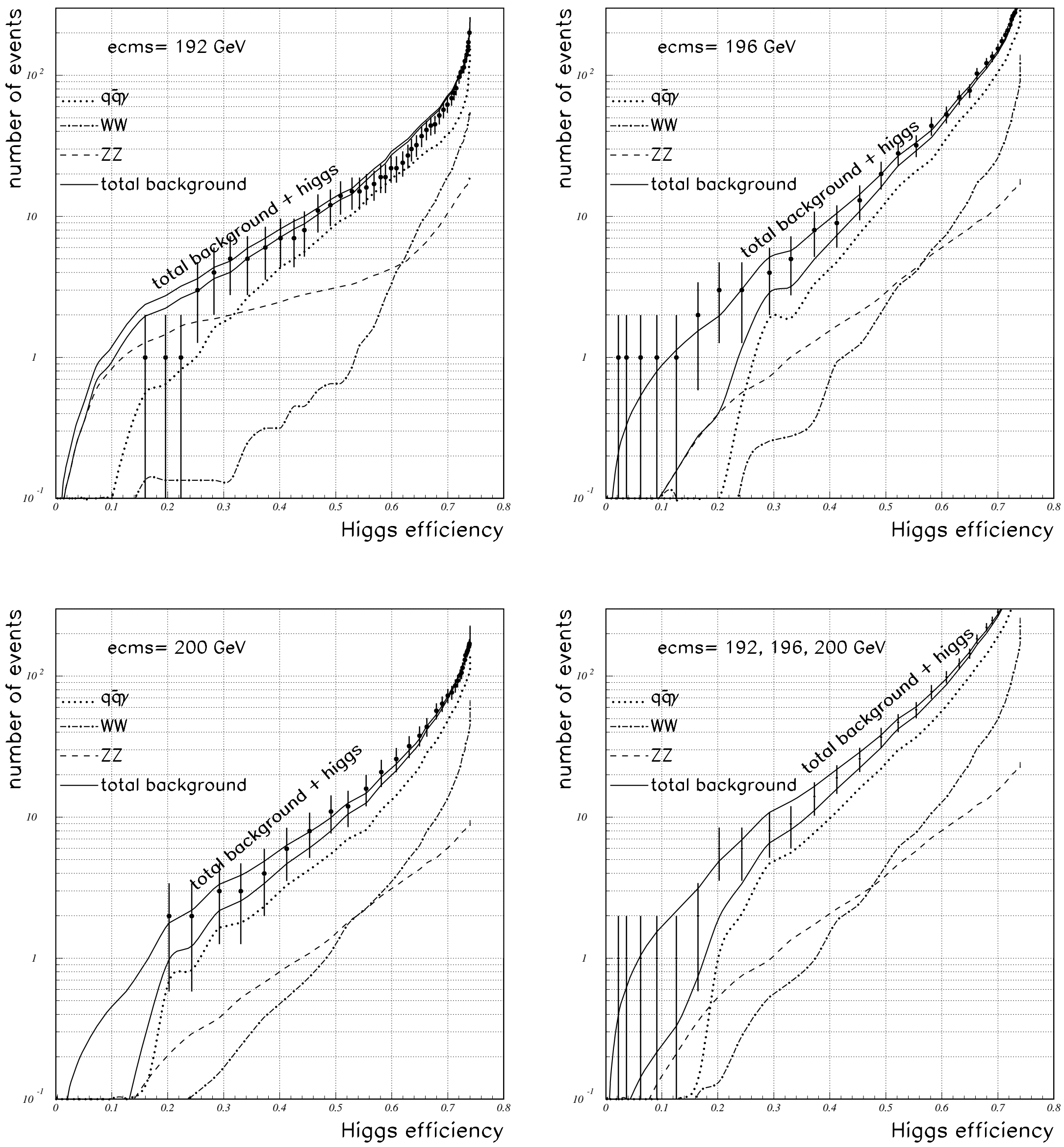

Figure 8.11: *Number of events versus Higgs efficiency (for $m_H = 105$ GeV/c^2) in the three samples of data at 192, 196, 200 GeV, and for the 3 sets together.*

and 8.13 the invariant mass is shown at different levels of Higgs efficiency. It can be noticed that the distributions are sensitive to the Higgs contribution clearly only at high value of signal over background ratio. A slight excess of data (not statistically significant) is evident at Higgs efficiency of 46% for the set of data at 200 GeV centre of mass energy. The ongoing collection of data may throw more light on this.

8.3 Greatest expectations

To conclude it is worthwhile to see what are the prospects from the running of LEP. The upper part of figure 8.14 shows the luminosity needed to exclude the signal hypothesis in 50% of background experiments at 95% or greater CL. One can see from the plot that ,from the SM Higgs point of view, there is not much to gain by increasing the integrated luminosity above 50 pb^{-1}, and that the combination of lower centre of mass energy data with higher centre of mass energy data does not improve the sensitivity for an integrated luminosity above 50 pb^{-1}. It is also seen that the exclusion sensitivity when collecting 200 pb^{-1} at $\sqrt{s} = 198$ GeV ($m_H = 107.0$ GeV/c^2) is comparable to that obtained if one trades the last 100 pb^{-1} collected at $\sqrt{s} = 198$ GeV with 50 pb^{-1} collected at $\sqrt{s} = 200$ GeV ($m_H = 107.6$ GeV/c^2). However if one can provide higher luminosity at $\sqrt{s} = 200$ GeV, the search sensitivity is improved. For example, if the additional luminosity collected at $\sqrt{s} = 200$ GeV is 100 pb^{-1} rather than 50 pb^{-1}, the exclusion sensitivity improves significantly to $m_H = 108.5$ GeV/c^2 which brings the search sensitivity almost to its kinematical limit ($m_H = 108.8$ GeV/c^2).

The lower part of figure 8.14 shows the luminosity needed to discover a SM Higgs boson in 50% of signal + background experiments at the 5σ level as a function of the Higgs boson mass. One can see from the plot that the discovery sensitivity for the SM Higgs boson saturates with an integrated luminosity of 100 pb^{-1}. It is also seen that the average discovery sensitivity when collecting 200 pb^{-1} at $\sqrt{s} = 198$ GeV ($m_H = 104.5$ GeV/c^2) is comparable to that obtained if one trades the last 100 pb^{-1} at $\sqrt{s} = 198$ GeV with 50 pb^{-1} collected at $\sqrt{s} = 200$ GeV ($m_H = 104.2$ GeV/c^2). However if one can provide higher luminosity at $\sqrt{s} = 200$, the search sensitivity is improved. For example, if the additional luminosity collected at $\sqrt{s} = 200$ GeV is 100 pb^{-1} rather than 50 pb^{-1}, the discovery sensitivity improves from $m_H = 104.2$ GeV/c^2 to $m_H = 105.8$ GeV/c^2. Collecting 200 pb^{-1} at $\sqrt{s} = 200$ GeV can discover a Higgs up to $m_H = 106.9$ GeV/c^2.

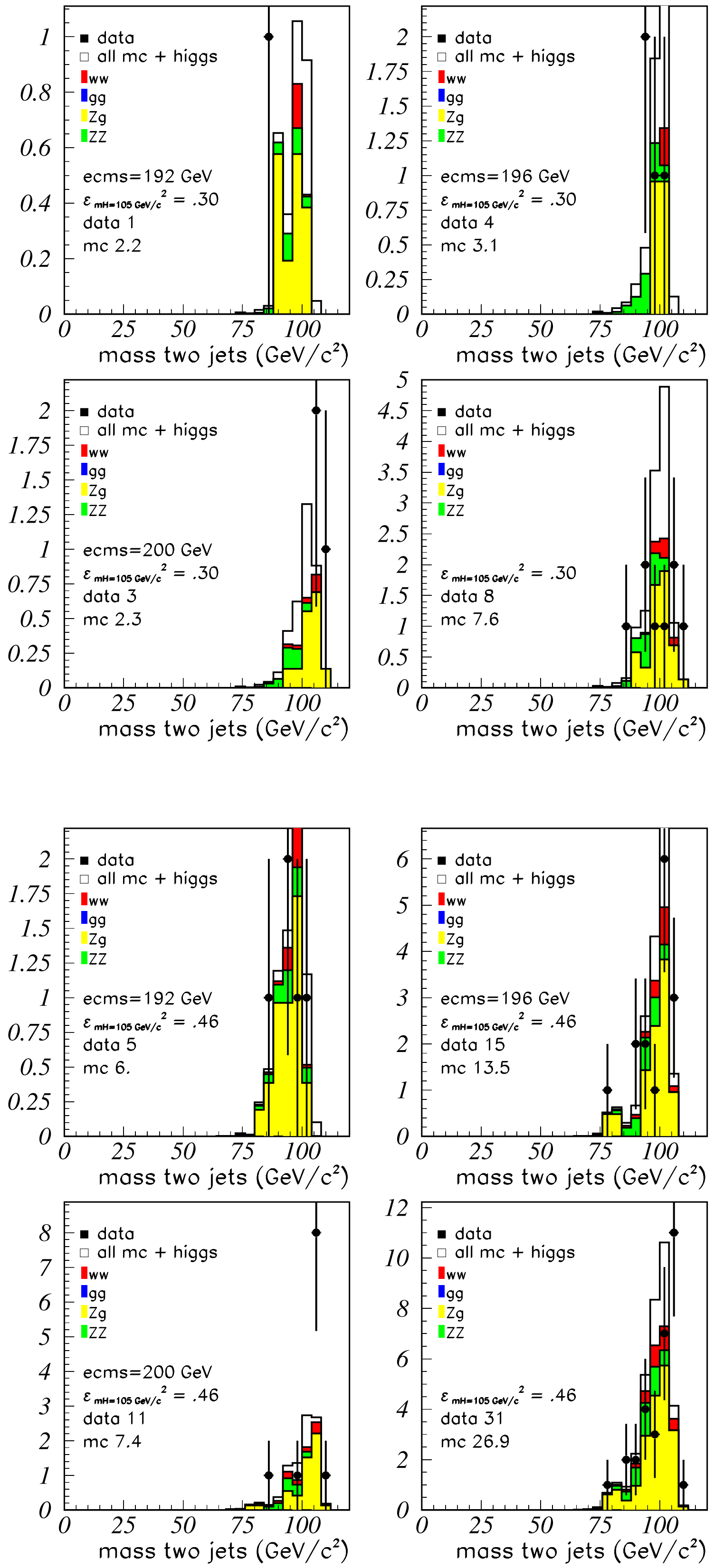

Figure 8.12: *Two jets invariant mass distribution at Higgs efficiency of 30% (four upper plots) and 46% (four lower plots). The samples of data are at three centre of mass energies of 192, 196, 200 GeV and the three sets together.*

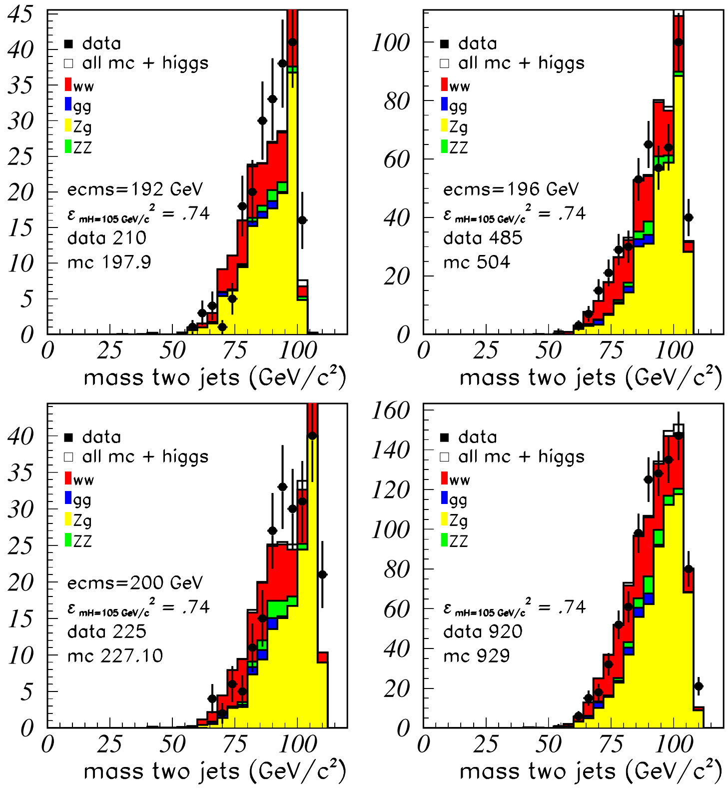

Figure 8.13: *Two jets invariant mass distribution at Higgs efficiency of 74%. The samples of data are at three centre of mass energies of 192, 196, 200 GeV and the three sets together.*

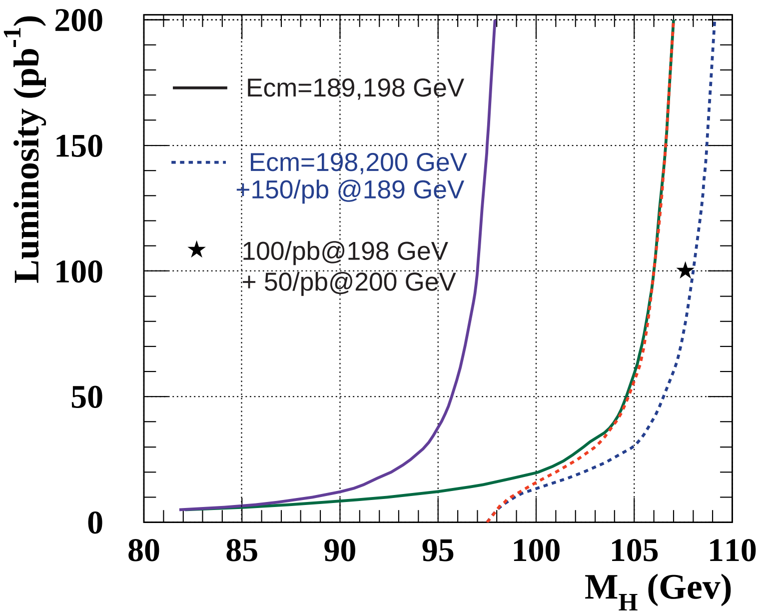

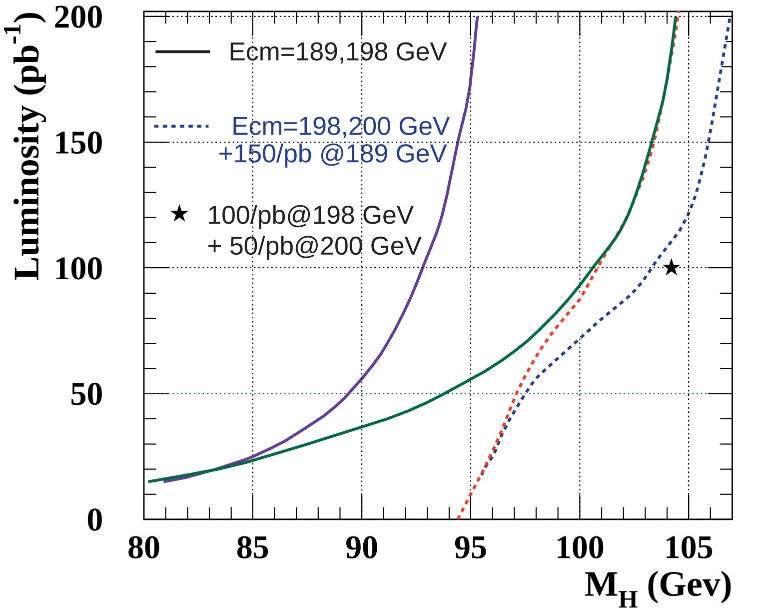

Figure 8.14: *Up:The luminosity required in order to exclude the SM Higgs boson at the 95% CL at the indicated centre of mass energies of 189, 198 GeV and combining the luminosity collected at 198 and 200 GeV with 150 pb^{-1} collected at 189 GeV. The star indicates the exclusion sensitivity if one stops collecting data after 100 pb^{-1} at $\sqrt{s} = 198$ GeV and upgrades to $\sqrt{s} = 200$ GeV where an additional 50 pb^{-1} are collected. Down: The luminosity required in order to discover the SM Higgs boson at the 5σ level at the indicated centre of mass energies of 189, 198 GeV and combining the luminosity collected at 198 and 200 GeV with 150 pb^{-1} collected at 189 GeV. The star indicates the discovery sensitivity if one stops collecting data after 100 pb^{-1} at $\sqrt{s} = 198$ GeV and upgrades to $\sqrt{s} = 200$ GeV where an additional 50 pb^{-1} are collected.*

"Est, qui non potuit dicere, dixit erit"
Medioeval proverb

Conclusions

A search for the Higgs boson in $e^+e^- \to H\nu\overline{\nu}$ final states has been presented. The branching ratio of this channel is 20% and its signature is a high value of missing energy and the presence of two acoplanar jets.

Data collected with the DELPHI detector at LEP were used. A complete analysis has been done on the sample of 158 pb^{-1} collected at a centre of mass energy of 189 GeV and a preliminary analysis on 1999 data has been performed. The complete analysis consists of three steps:

- a sequential series of cuts has been applied in order to reduce the bulk of background coming from $e^+e^- \to e^+e^-$, $e^+e^- \to e^+e^-\gamma\gamma X$, $e^+e^- \to q\overline{q}\gamma$ and $e^+e^- \to W^+W^-$. The bulk of these events has a distribution in phase space with low overlap with the signal, and the sequential cuts can be used to remove them without affecting the signal efficiency.

- The likelihood ratio method has been adopted to further discriminate between remaining background and signal. After the cuts, the remaining events are basically $e^+e^- \to q\overline{q}n(\gamma)$ with ISR photons in the beam pipe, $e^+e^- \to Z^0Z^0$ with one $Z^0 \to \nu\overline{\nu}$ and $e^+e^- \to W^+W^-$ with semileptonic decay of one W. The distribution in phase space of these events has a non-negligible overlap with the Higgs signal, and in such a situation the likelihood ratio is one of the most powerful methods to discriminate between signal and background.

- The statistical significance required to establish the discovery has been defined. Since no Higgs evidence has been found, only a limit on the Higgs mass was derived. A detailed analysis of possible sources of systematic uncertainty has been performed, and the limit on the Standard Model Higgs has been derived (both in data: observed limit, and in simulation: expected limit) taking into account the total systematic error. The following results were found for the Standard Model Higgs:

  - **expected limit** :
  $$m_H \geq 81.9 GeV/c^2 \tag{8.1}$$
  - **observed limit** :
  $$m_H \geq 81.7 GeV/c^2 \tag{8.2}$$

A scan on the parameters of the Minimal Supersymmetric extension of Standard Model has been shown. The analysis described in this thesis is particularly useful to increase the exclusion region in the $\tan\beta$, m_h plane at high value of $\tan\beta$. The results are summarised in figures 7.17 and 7.19

Since one of the irreducible backgrounds consists in $e^+e^- \rightarrow q\bar{q}\gamma\gamma$ with two γs in the beam pipe, and since there were no other analyses dedicated to the study of this background, I was motivated to pursued a detailed analysis on $e^+e^- \rightarrow q\bar{q}\gamma\gamma$ events. In this thesis the cross section has been derived for the first time, both at 189 and 196 GeV centre of mass energy:

Energy	cross section [pb]		
	2 γ visible	1 γ lost	2 γ lost
	$3^\circ \leq \theta_\gamma \leq 177^\circ$		$\theta_\gamma \leq 3^\circ, \geq 177^\circ$
189 GeV	0.298± 0.066	0.599 ± 0.158	0.683 ± 0.155
196 GeV	0.229± 0.050	0.702 ± 0.192	0.725 ± 0.165

A preliminary search for the Higgs boson has been performed on the data collected during the first months of 1999 data taking. No statistically significant signal for Higgs boson events has been found.

The keyword for the discovery is clearly the energy. An increase to 204 GeV in centre of mass energy is foreseen for next year at LEP. If at least 150 pb^{-1} per experiment are collected a discovery can be made up to a Higgs mass of $\simeq$ 109 GeV/c^2 or the Higgs excluded for masses below 112 GeV/c^2.

Acknowledgements

This is the end of a wonderful journey. It was wonderful because wanderful is exploring the particle's world and wandering toward the understanding of how we are made by. But it was wonderful especially because I met so many people and all they gave me so much.

The journey begun in Milano, where I stayed for half of my PhD. First of all I have to thanks prof. Guido Vegni who gave me the possibility to join the DELPHI microvertex group of Milano. I'm in debt of gratitude with all the group. Thanks to Chiara Meroni. She helped me in all what I have done. She was near to me in so many occasions, opening many streets and always the right ones. Thanks to Massimo Caccia who knows the microvertex detector better than his pockets and tried to explain me all its secrets.

If Milano was not so grey was thanks to Marco Paganoni. He spotted many colours in obscure days. Milano from the 14^{th} floor of his apartment is not so bad...

The journey continued at CERN (Geneve) where I stayed for the other half of my PhD, but always having the support of my group in Milano who promoted me to get a scientific experience at CERN. I worked here with a lot of people and from all them I learned a lot. Thanks to: Alberto Benvenuti, Tiziano Camporesi, Paula Collins, Fabio Cossutti, Jan van Eldik, Markus Elsing, Vincent Hedberg, Niels Kjaer, Maria Catarina Espirito Santo, Dietrik Liko, Kenneth Ostenberg, Pierpaolo Rebecchi. They were important for all the useful discussions but also because the time I spent with them was always a nice time.

In particular I want to thanks Attilio Andreazza who explained me everything concerning the alignment procedure.

An enormous grazie to Chiara Mariotti. It was with Chiara that this analysis has been done. We spent many hours in discussion, but at the end the result was not so bad...isn't it Chiara? Pat, pat...

Merci beaucoup à Daniel Treille for the continuous support and all the hints during the analysis.

I'm in debt of gratitude with John Wickens who leads the work on the data processing at DELPHI. Thanks for all the suggestions on the alignment and thanks because he was extremely kind in reading this thesis and improving my english. I hope it was not too much boring!

This is the end of a marvellous journey, but all these people will always be in my story. At the end of it the special thank is for Federica who decided to stay with me for *all the other journeys of my life and make them better. "...e alla fine di un viaggio, c'è sempre un viaggio da ricominciare..." (Francesco de Gregori).*

References

[1] S. Weinberg, *The quantum theory of fields*

[2] A.G.Cohen, D.B.Kaplan and A.E.Nelsen, Phys. Rev. **B263** (1991) 86

[3] U. Amaldi et al., Phys. Rev. **D36** (1987) 1385

[4] A. G. Akeroyd, Phys. Lett. **B353** (1995) 519

[5] R.M.Burnett et al., Particle Data Book, Phys. Rev. **D54** (1996) 1

[6] S.L.Glashow and S.Weinberg, Phys. Rev. **D15** (1977) 1958

[7] M.Sher, Phys. Rep. **179** (1989) 273

[8] Y.Grossmman, Nuc. Phys. **B426** (1994) 355

[9] Y.L.Wu and L. Wolfestein, Phys. Rev. Lett. **73** (1994) 1762

[10] S. Dawson, Introduction to the physics of Higgs bosons, hep-ph/9411325

[11] N.Cabibbo, L. Maiani, G. Parisi, and R. Petronzio, Nucl. Phys. **B158** (1979) 295;
M. Sher, Phys. Rev. **179** (1989) 273;
L. Maiani, G. Parisi, and R. Petronzio, Nucl. Phys. **B136** (1978) 115;
M.Lindner, Z. Phys. **C31** (1986) 295; M. Lindner, M. Sher, and H. Zaglauer, Phys. Lett. **228** (1989) 139.

[12] T. Cheng, E. Eichten and L. Li, Phys. Rev. **D9** (1974) 2259;
B. Pendleton and G. Ross, Phys. Lett. **B98** (1981) 291;
C. Hill, Phys. Rev. **D24** (1981) 691;
J. Bagger, S. Dimopoulos and E. Masso, Nucl. Phys. **B253** (1985) 397;
M. Beg, C. Panagiotakopoulos, and A. Sirlin, Phys. Rev. Lett. **52** (1984) 883;
M. Duncan, R. Philippe, and M. Sher, Phys. Lett. **B153** (1985) 165;
K. Babu and E. Ma, Phys. Rev. Lett. **55** (1985) 3005.

[13] M. Chanowitz and M. Gaillard, Nucl. Phys. **B261** (1985) 379.

[14] N. Cabibbo *et.al.*, Nucl. Phys. **B158** (1979) 295.

[15] M. Sher, Phys. Lett. **B317** (1993)159; addendum, **B331** (1994) 448.

[16] E. Braaten and J. Leveille, Phys. Rev. **D22** (1980) 715;
N. Sakai, Phys. Rev. **D22** (1980) 2220;
T. Inami and T. Kubota, Nucl. Phys. **B179** (1981) 171;
M. Drees and K.Hikasa, Phys. Lett. **B240** (1990) 455;
E. Gross, B. Kniehl and G. Wolf, Z. Phys. **C63** (1994) 417;
C66 (1995) 321 **E**.

[17] B. Kniehl, Phys. Rept. **240** (1994) 211.

[18] J. Gunion *et.al.*, *The Higgs Hunter's Guide* (Addison Wesley, Menlo Park, 1990.)

[19] Degrassi et al., *Costraints on the Higgs boson mass from direct searches and precision measurements*, hep-ph/9902226

[20] W.-Y. Keung and W. Marciano, Phys. Rev. **D30** (1984) 248.

[21] A. Vainshtein, M. Voloshin, V. Zakharov, and M. Shifman, Sov. J. Nucl. Phys. **30** (1979) 711;
M. Okun, *Leptons and Quarks*, (North-Holland, Amsterdam, 1982).

[22] D. Jones and S. Petcov, Phys. Lett. **B84** (1979) 440.

[23] S. Dawson and J. Rosner, Phys. Lett. **B148** (1984) 497.

[24] A. Djouadi, Int. Journ. Mod. Phys. **A10** (1995) 1, hep-ph/9406430.

[25] J. Wess and J. Bagger, *Supersymmetry and Supergravity*, (Princeton University Press, Princeton, N.J. 1983);
P. Fayet and S. Ferrara, Phys. Rep. **32** (1977) 249.

[26] D. Gross and R. Jackiw, Phys.Rev. **D6** (1972) 477;
C. Bouchiat, J. Iliopoulos and P. Meyer, Phys. Lett. **B38** (1972) 519;
H. Georgi and S. Glashow, Phys. Rev. **D6** (1972) 429; L. Alvarez-Gaume and E. Witten, Nucl. Phys. **B234** (1983) 269.

[27] E. Witten, Nucl. Phys. **B185** (1981) 513; M. Dine, W. Fischler, and M. Srednicki, Nucl. Phys. **B189** (1981) 575;
S. Dimopoulos and S. Raby, Nucl. Phys. **B192** (1981) 353;
J. Polchinski and L. Susskind, Phys. Rev. **D26** (1982) 3661;
L. Ibanez and G. Ross, Phys. Lett. **B105** (1981) 439.

[28] M. Drees, Contribution to Inauguration Conference of the Asia Pacific Center for Theoretical Physics, Seoul, Korea, June, 1996, hep-ph/9611409.

[29] H.E. Haber and R. Hempfling, Phys. Rev. Lett. **66** (1991) 1815;
Y. Okada, M. Yamaguchi and T. Yanagida, Prog. Theor. Phys. **85** (1991) 1;
J. Ellis, G. Ridolfi and F. Zwirner, Phys. Lett. **B257** (1991) 83.

[30] H.E. Haber, R. Hempfling, and A.H. Hoang, Z. Phys. **C75** (1997) 539.

[31] M. Carena, J.R. Espinosa, M. Quiros and C.E.M. Wagner, Phys. Lett. **B355** (1995) 209;
M. Carena, M. Quiros and C.E.M. Wagner, Nucl. Phys. **B461** (1996) 407.

[32] DELPHI Collaboration, *The DELPHI detector at LEP* NIM **A303** (1991) 233-276

[33] DELPHI Collaboration, *Performance of the DELPHI detector* NIM **A378** (1996) 57-100

[34] DELPHI Collaboration, *DELANA user's guide*, DELPHI-89-44 PROG/137(1989)

[35] D. Bertrand and L. Pape, *TANAGRA, Track Analysis and Graphics Package*, DELPHI-87-95 PROG/98(1987)

[36] V. Chabaud et al., *Alignment of the DELPHI vertex detector*, DELPHI 95-177 MVX 10.

[37] Joerg Wenninger, private comunication.

[38] This procedure for the forward alignment has originally been developed by H. Wahlen, M. Elsing (University of Wuppertal and CERN) and R. Fruhwirth (University of Wien): it has been adapted and included in the central alingment procedure in 1995.

[39] P. Billoir and Y. Sacquin *The DELPHI TPC distortions*, DELPHI 92-16 PROG 182 TRACK 68;
A. Andreazza, transparencies presented at the DSTFIX/Alignment meeting of 30/01/1996

[40] The VFT alignment is performed by V. Vrba (University of Prague) starting from ntuples we produce at the end of the alignment procedure.

[41] DELPHI collaboration *Measurement of the mass of W boson using direct reconstruction at* $\sqrt{s} = 183\ GeV$, CERN-EP99-79.

[42] REMCLU, F.Cossutti, F.Mazzucato, A.Tonazzo, DELPHI note in preparation.

[43] G. Altarelli, T. Sjostrand and F. Zwirner *Phisics at LEP2* CERN 96-1

[44] DELPHI collaboration *Measurement and Interpretation of Fermion-Pair Production at LEP energies from 130 to 172* GeV, CERN-EP-99-005

[45] DELPHI collaboration *W pair production cross sections and W branching fractions in* e^+e^- *interactions at 183* GeV CERN-EP/99-47

[46] DELPHI collaboration *DELSIM, DELPHI event generation and detector simulation. Reference Manual* DELPHI 90-35 PROG 152

[47] T. Sjostrand, Comp. Phys. Comm. **82** (1994) 74

[48] M.L. Mangano and G. Ridolfi, *Event generators for discovery physics* CERN 96-01

[49] E. Accomando and A. Ballestrero, *A program for ww, Higgs and 4 fermions physics at e^+e^- colliders* DFTT16/96

[50] S. Cattanei et al., Phys. Lett. **B269** (1991) 432; N. Brown and W.J. Stirling, Z. Phys. **C53** (1992) 629.

[51] A. Grefrath *Measurement of event shape distribution, their avarages and jet rates at $\sqrt{s} = 161$ and 172 GeV*, DELPHI 97-28 Phys 681

[52] T. Sjöstrand, Comp. Phys. Comm. **39** (1986) 347.

[53] S. Nova, A. Olchevski and T. Todorov, in CERN Report 96-01, Vol. 2, p. 224 (1996).

[54] F.A. Berends, P.H. Daverveldt and R. Kleiss, Nucl. Phys. **B253** (1985) 421; Comp. Phys. Comm. **40** (1986) 271, 285 and 309.

[55] F.A. Berends, R. Kleiss, W. Hollik, Nucl. Phys. **B304** (1988) 712.

[56] DELPHI Collaboration, P. Abreu et al., Nucl. Inst. Meth. **A378** (1996) 57.

[57] S. Bethke, *JETS in Z^0 decays*, Workshop on QCD: 20 years later, Aachen QCD wkshp. 1992:43-72

[58] DELPHI collaboration *A precise measurement of the partial decay width ratio* $R_b^0 = \Gamma_b\bar{b}/\Gamma_{had}$,CERN-EP-98-180.

[59] V. Hedberg, DELPHI note in preparation.

[60] P. Abreu et al., *SPRIME A package for estimating the effective $\sqrt{s'}$ centre of mass energy in $q\bar{q}\gamma$ events* DELPHI 96-124 PHYS 632.

[61] A. Read *Optimal statistical analysis of search results based on the likelihood ratio and its application to search for the MSM Higgs boson at $\sqrt{s} = 161$ and $\sqrt{s} = 172$ GeV*, DELPHI 97-158 PHYS 737.

[62] *Review of particle physics* The European Physical Journal **3** (1998)

[63] M. Espirito Santo *Search for composite and exotic leptons with the DELPHI detector at LEP 2*, PhD thesis.

[64] V Obraztsov, Nucl. Instr. Methods **A316** (1992) 388;
V Obraztsov, Nucl. Instr. Methods **A399** (1997) 500

[65] E. Gross, A.L. Read and D. Lellouch, *Prospects for the Higgs boson search in e^+e^- collisions at LEP 200* , CERN-EP-98-094.

[66] A. Benvenuti algorithm, private comunication.

[67] J. Ellis, G. Ridolfi and F. Zwirner, Phys. Lett. **257B** (1991) 83;
H.E. Haber and R. Hempfling, Phys. Rev. Lett. **66** (1991) 1815;
Y. Okada, M. Yamaguchi and T. Yanagida, Phys. Lett. **262B** (1991) 54;
R. Barbieri, M. Frigeni and M. Caravaglios, Phys. Lett. **258B** (1991) 167.

[68] J. Ellis, G. Ridolfi and F. Zwirner, Phys. Lett. **262B** (1991) 477;
R. Barbieri and M. Frigeni, Phys. Lett. **258B** (1991) 395;
A. Brignole, J. Ellis, G. Ridolfi and F. Zwirner Phys. Lett. **271B** (1991) 123.

[69] M. Carena, K. Sasaki and C.E.M. Wagner, Nucl. Phys. **381B** (1992) 66;
R. Hempfling, Phys. Lett. **296B** (1992) 121;
H.E. Haber and R. Hempfling, Phys. Rev. **48B** (1993) 4280.

[70] P.H. Chankowski, S. Pokorski and J. Rosiek, Phys. Lett. **281B** (1992) 100.

[71] P.H. Chankowski, S. Pokorski and J. Rosiek, Phys. Lett. **274B** (1992) 191; **286B** (1992) 307; Nucl. Phys. **423B** (1994) 437; **423B** (1994) 497.

[72] A. Brignole, Phys. Lett. **281B** (1992) 284.

[73] Z. Kunszt and F. Zwirner, Nucl. Phys. **385B** (1992) 3.

[74] A.V. Gladyshev et al., Nucl. Phys. **498B** (1997) 3.

[75] G. Borisov and C. Mariotti, Nucl. Inst. Meth. **A372** (1996) 181.
G. Borisov and C. Mariotti, *Tuning of the Track Impact Parameter Resolution of the Upgraded DELPHI Detector*, ISS-INFN 97/14 (also DELPHI note, DELPHI 97-95 PHYS 717).

[76] D. Cousins and V. Highland, Nucl. Inst. Meth. **A320** (1992) 331.